Charm production in proton–proton collisions with ALICE at the LHC and light nuclei synthesis via coalescence in heavy-ion collisions

Ph.D. Thesis

by

Yoshini Bailung

Department of Physics
Indian Institute of Technology Indore
Khandwa Road, Simrol, Indore - 453552, India

CERN-THESIS-2024-354
11/02/2025

Charm production in proton–proton collisions with ALICE at the LHC and light nuclei synthesis via coalescence in heavy-ion collisions

A THESIS

Submitted in partial fulfillment of the requirements for the award of the degree

of

DOCTOR OF PHILOSOPHY
by

Yoshini Bailung

Department of Physics
Indian Institute of Technology Indore
Khandwa Road, Simrol, Indore - 453552, India

INDIAN INSTITUTE OF TECHNOLOGY INDORE

I hereby certify that the work which is being presented in the thesis entitled **Charm production in proton–proton collisions with ALICE at the LHC and light nuclei synthesis via coalescence in heavy-ion collisions** in the partial fulfillment of the requirements for the award of the degree of **DOCTOR OF PHILOSOPHY** and submitted in the **Department of Physics**, **Indian Institute of Technology Indore**, is an authentic record of my own work carried out during the time period from **July 2019** to **July 2024** under the supervision of **Prof. Ankhi Roy**, Professor, Indian Institute of Technology Indore.

The matter presented in this thesis has not been submitted by me for the award of any other degree of this or any other institute.

Signature of the student with date
Yoshini Bailung

This is to certify that the above statement made by the candidate is correct to the best of my knowledge.

Signature of Thesis Supervisor with date
Prof. Ankhi Roy

Mr. Yoshini Bailung has successfully given his Ph.D. Oral Examination held on **11/02/2025**.

Signature of Thesis Supervisor with date
Prof. Ankhi Roy

Dedicated

to

my parents

Acknowledgements

As I prepare to print my thesis, I find myself reflecting on the many individuals who have shaped this journey. To those acknowledged below, whether knowingly or unknowingly, you have been an integral part of this long, challenging, yet rewarding PhD experience. I am forever grateful for your support, guidance, and encouragement, which have helped bring this work to fruition.

I thank my parents, whose patience, perseverance, and belief in me have been the foundation of my strength. The values you instilled in me, define the person I am today. In the moments of doubt, thank you for believing in me. Thank you for shaping my life with positivity, passion, and a relentless pursuit of success.

I express my deepest gratitude to my supervisor, Prof. Ankhi Roy, for her support, guidance, and encouragement throughout my research journey. You have been a constant pillar of support, patience and mentorship. To Prof. Neha Shah, I thank you for your constant guidance, insightful feedback and expertise which were invaluable in curating the projects. I am equally grateful to my thesis progress committee members, Prof. Subhendu Rakshit and Prof. Bhargav Vaidya, for their constructive criticism and suggestions throughout my PhD. Your viewpoints significantly improved my outlook and approach to research. I also thank Dr. Biplab Ghosh for his availability and for being there to always lend a helping hand.

My time in the lab was enriched by incredible colleagues who made this experience memorable. To Sudhir, thank you for being an exemplary mentor, an inspiring senior, and a great friend. Your resilience and work ethic set a benchmark I aspired to reach. Sumit, more than a labmate, you have been a brother since day one. Thank you for your unconditional help and reliability. Ravindra, your camaraderie and impactful presence in our group were invaluable. Swapnesh, working alongside you was a joy; I will always cherish our brainstorming sessions and shared love for indulgent snacks. Rohit and Shankar, thank you for reinforcing my mentorship skills and patiently enduring my counsel. To, Ayan, Rashi, Anurag, Diksha, Garvit, Praveen, Tarun and Yatharth, it was truly a pleasure to share my research journey with all of you.

To my colleagues from the ALICE Collaboration, Marco and Randhir, working with you has been an absolute pleasure. I will always cherish the sleepless nights before ALICE preliminaries, the relentless deadlines, and the constant teamwork that kept us moving forward. To my mentors in D2H PAG, Fabrizio and Cristina, I am indebted to you for guiding me through the initial days of data analysis. To my AOT colleagues, Binti and Felix, thank you for making my time during ALICE service work truly enjoyable. Special thanks to Vivek, Dibakar, Prottay and Swati for making my stay at CERN super fun and

memorable.

To all the friends I met throughout the years, a massive thank you! To Sarvesh, thank you for being the best roommate one could get. Thank you for bestowing your pop culture knowledge and literature and for being a person I could truly count on. Jay, your presence during the uncertainty of COVID times was a pillar of strength. Sayan Kundu and Sayan Poddar, my later-found roommates, made my hostel life a cherished memory. Arghya, our super cooking sessions and your care during my illness will always be remembered. To my remaining astronomy mates, Sriya, Akriti, Parul, and Unnati, thank you for being a constant source of joy and laughter.

Finally, I extend my sincere appreciation to the staff of the Department of Physics at the Indian Institute of Technology Indore for their constant support and assistance. To anyone I may have unintentionally missed, please know that your contributions have been invaluable in this journey. Thank you all for being a part of this milestone.

Yoshini

Abstract

Ultrarelativistic heavy-ion collisions in experimental facilities are conducted to investigate the dynamics of strongly interacting matter. These laboratories produce a dense soup of deconfined quarks and gluons called the quark-gluon plasma (QGP). The ALICE experiment at the LHC is dedicated to studying this exotic state of matter that probes its formation from the aftermath of heavy-ion collisions. Heavy quarks (charm and beauty) are interesting probes to examine the QGP medium. Because of their large masses, they produce at the initial stages of the collision and get to traverse the entire evolution of the medium. Their production mechanisms in proton–proton (pp) collisions are of great interest, providing stringent tests to perturbative quantum chromodynamic (pQCD) calculations. Interestingly, heavy-quark production is also correlated to event properties. Studies have shown a strong correlation between charm production and the event multiplicity in pp collision, where a significant role of multiparton interactions is suspected. The role of auto-correlation effects between charm production and multiplicity is also weighed in. Moreover, with identifiable QGP signatures in high multiplicity pp collisions, the participation of charm in collective-like effects is also worth investigating. In addition, with event shapes, charm production can be categorized into the hard and soft components that allow unfolding of the production mechanisms with event activity. This thesis outlines the studies performed in charm production via D-meson production as a function of event-multiplicity and -shapes in pp collisions at $\sqrt{s} = 13$ TeV.

The second focus of this thesis is on light nuclei (d, ^{3}H, ^{3}He) production in collision experiments. Light nuclei are clusters of nucleons that survive temperatures of $O(100\ \text{MeV})$ in heavy-ion collisions, orders higher than its binding energy. Understanding their 'puzzling' production mechanism is a contentious topic in the community, with the coalescence of nucleons being one of the popular phenomenological models. It is based on the overlap principle between the nucleon phase-space distribution and the nuclei probability distribution. The nucleon phase space generally relies upon an event generator, to which coalescence is appended in an afterburner mode. The coalescence model is initially designed with a box nuclei distribution prescription, which is studied on d, ^{3}H, ^{3}He production in RHIC and LHC energies. The model is revamped with the nuclei's Wigner distribution, inspired by its quantum mechanical wavefunction. With this update, finer details can be added in terms of a common nucleon emission source. This connects the nucleon-nucleon (NN) interactions during the inception of the light cluster formation in these collision experiments. Furthermore, investigation with strong, Coulombic and quantum statistical corrections will capture the femtoscopic details in these NN interactions. This thesis includes all the stages of developing an 'in-situ' coalescence model discussed above and its implementation.

List of Publications

A. Published:

1. **Probing coalescence of light nuclei via femtoscopy and azimuthal anisotropies**
   Authors: **Yoshini Bailung**, Sudhir Pandurang Rode, Neha Shah, Ankhi Roy
   Published in *Phys.Rev.C* 111 (2025) 1, 014911 · DOI · e-Print

2. **Searching for enhancement in coalescence of in-jet (anti-)deuterons in proton–proton collisions**
   Authors: **Yoshini Bailung**, Neha Shah, Ankhi Roy
   Published in *Phys.Rev.C* 109 (2024) 4, 044908 · DOI · e-Print

3. **Exploring light nuclei production at RHIC and LHC energies with A Multi-Phase Transport model and a coalescence afterburner**
   Authors: **Yoshini Bailung**, Neha Shah, Ankhi Roy
   Published in *Nucl.Phys.A* 1037 (2023) 122701 · DOI · e-Print

B. ALICE Analysis Notes:

1. **Measurement of D-meson** $(\mathrm{D}^0, \mathrm{D}^+, \mathrm{D}^{*+})$ **production as a function of event shapes in proton–proton collisions at** $\sqrt{s}$ = 13 **TeV**
   Authors: **Yoshini Bailung**, Randhir Singh, Marco Giacalone
   ALICE Analysis Note; ID number: ANA-1240

2. **Measurement of D-meson** $(\mathrm{D}^0, \mathrm{D}^+, \mathrm{D}^{*+})$ **production versus charged particle multiplicity in proton-proton collisions at** $\sqrt{s}$ = 13 **TeV**
   Authors: **Yoshini Bailung**, Randhir Singh, Marco Giacalone
   ALICE Analysis Note; ID number: ANA-1167

N.B: Entries A1, A2, A3, B1, and B2 are parts of my thesis.

D. Conference proceedings:

1. **Production of light nuclei in heavy-ion collisions via a coalescence mechanism**
   Authors: **Yoshini Bailung**, Sudhir P. Rode, Neha Shah, Ankhi Roy
   Published in *DAE Symp.Nucl.Phys.* 67 (2024) 1149-1150

2. **Heavy-flavour production as a function of charged-particle multiplicity with ALICE at the LHC**
   Authors: **Yoshini Bailung**, on behalf of ALICE Collaboration
   Submitted to *MDPI Proc.*

3. **Dependence of anisotropic flow and particle production on particlization models and nuclear equation of state**
   Authors: Sumit K. Kundu, **Yoshini Bailung**, Sudhir P. Rode, Partha P. Bhaduri, Ankhi Roy
   Published in *Int.J.Mod.Phys.E* 31 (2022) 12

4. **Dependence of anisotropic flow of net-protons on particlization model for various nuclear equation of state**
   Sumit Kumar Kundu, **Yoshini Bailung**, Sudhir Pandurang Rode, Partha Pratim Bhaduri, Ankhi Roy
   Published in *DAE Symp.Nucl.Phys.* 65 (2021) 650-651

5. **Measurements of heavy-flavor production as a function of multiplicity with ALICE at the LHC**
   Authors: **Yoshini Bailung**, on behalf of ALICE Collaboration
   Published in *SciPost Phys.Proc.* 10 (2022) 033

6. **Measurement of** D**-meson production as a function of charged-particle multiplicity in proton-proton collisions at $\sqrt{s}$ = 13 TeV with ALICE at the LHC**
   Authors: **Yoshini Bailung**, on behalf of ALICE Collaboration
   Published in *PoS LHCP2021* (2021) 190

E. Publications outside of the thesis work:

1. **Jet fragmentation via azimuthal angular correlations of electrons from heavy flavor decay in pp, p-Pb, and Pb-Pb collisions using PYTHIA8+Angantyr calculations**
   Authors: Ravindra Singh, **Yoshini Bailung**, Sumit K. Kundu, Ankhi Roy
   Published in *Phys.Rev.C* 107 (2023) 2, 024911 · DOI · e-Print

2. **Effect of various particlization scenarios on anisotropic flow and particle production using UrQMD hybrid model**
   Authors: Sumit K. Kundu, **Yoshini Bailung**, Sudhir P. Rode, Partha P. Bhaduri, Ankhi Roy
   Published in *Nucl.Phys.A* 1030 (2023) 122574 · DOI · e-Print

3. **Dynamics of particle production in Pb–Pb collisions at $\sqrt{s_{NN}}$ = 2.76 TeV using PYTHIA8 Angantyr model**
   Authors: Ravindra Singh, **Yoshini Bailung**, Ankhi Roy
   Published in *Phys.Rev.C* 105 (2022) 3, 035202 · DOI · e-Print

4. **Dependence on beam energy and nuclear equation of state of anisotropic flow and particle production in low-energy heavy-ion collisions**
   Authors: Sumit K. Kundu, **Yoshini Bailung**, Sudhir P. Rode, Partha P. Bhaduri, Ankhi Roy
   Published in *Phys.Rev.C* 104 (2021) 2, 024907 · DOI · e-Print

Contents

Abstract **xi**

List of Publications **xiii**

List of Figures **xxi**

List of Tables **xxxi**

1 Introduction **1**

1.1 The standard model of particle physics 1

1.2 Quantum chromodynamics 3

1.3 The QCD phase diagram 5

1.4 Ultrarelativistic heavy-ion collisions 6

1.5 Signatures of QGP 10

1.5.1 Charged-particle multiplicity 10

1.5.2 Strangeness enhancement 11

1.5.3 Jet quenching 12

1.5.4 Quarkonia suppression 14

1.5.5 Anisotropic flow 16

1.6 Open heavy-flavours 17

1.6.1 Heavy-flavours in pp collisions 17

1.7 Light (anti-)nuclei production 19

1.7.1 Statistical Hadronization Model 20

1.7.2 Coalescence model 21

1.8 Thesis motivation 22

2 ALICE: A Large Ion Collider Experiment **25**

2.1 The Large Hadron Collider 25

2.2 The ALICE Detector 27

2.2.1 Inner Tracking System 28

2.2.2 Time Projection Chamber 29

2.2.3 Time-Of-Flight Detector 30

2.2.4 V0 31

2.3 Triggers 31

2.4 ALICE offline framework 32

2.5 Primary vertex and track reconstruction 33

2.6 Particle identification 35

2.6.1 Particle identification in the ITS 35

2.6.2 Particle identification in the TPC 36

2.6.3 Particle identification in the TOF 37

3 Monte Carlo event generators **39**

3.1 Overview 39

3.2 The Lund string model 40

3.3 PYTHIA8 42

3.3.1 Hard process 42

3.3.2 Initial and final state radiations 43

3.3.3 Multiparton interactions 43

3.3.4 Hadronization 44

3.4 AMPT 45

3.4.1 Initial conditions 46

3.4.2 Parton cascade 48

3.4.3 Hadronization 49

3.4.4 Hadron cascade 49

3.5 SMASH . . . 50
3.5.1 Initial conditions . . . 50
3.5.2 Hybrid treatment . . . 51
3.5.3 Hadron sampler . . . 52
3.5.4 Mean-field potentials . . . 53

4 Charm production in proton–proton collisions **55**
4.1 Physics motivation . . . 55
4.2 Datasets and event selection . . . 57
4.3 Event variables . . . 58
4.3.1 Charged-particle multiplicity . . . 58
4.3.2 Transverse spherocity . . . 59
4.4 Analysis strategy and signal extraction . . . 64
4.5 Acceptance and efficiency corrections . . . 67
4.6 Systematic uncertainties . . . 69
4.6.1 Raw yields extraction . . . 69
4.6.2 Selection efficiency . . . 70
4.6.3 Particle identification . . . 71
4.6.4 Feed-down . . . 72
4.6.5 Monte Carlo p_{T}-shape . . . 73
4.6.6 Multiplicity weights . . . 74
4.6.7 Primary vertex resolution . . . 74
4.6.8 Spherocity dependence on dataset . . . 76
4.6.9 Summary of systematic uncertainties . . . 76
4.7 Results . . . 76
4.7.1 D-mesons vs charged-particle multiplicity . . . 78
4.7.2 D-mesons vs transverse spherocity . . . 83

5 Light nuclei synthesis via coalescence **89**
5.1 Physics motivation . . . 89

5.2 Coalescence model 90
5.3 Coalescence afterburner 92
5.3.1 Box coalescence 92
5.3.2 Wigner coalescence 93
5.3.2.1 Wave function formalism 94
5.3.2.2 The nucleon source function 96
5.4 Femtoscopy 99
5.4.1 The correlation afterburner 100
5.4.2 Lednický-Lyuboshits approach 101
5.5 Light (anti-)nuclei production with AMPT 102
5.5.1 Transverse momentum spectra 103
5.5.2 Particle yield ratios 106
5.5.3 Coalescence parameter 108
5.6 Enhancement of deuteron coalescence probability in jets 111
5.6.1 Transverse momentum spectra 112
5.6.2 Coalescence parameter 114
5.7 Probing light nuclei formation with femtoscopy and anisotropic flow . . . 117
5.7.1 Correlation functions 118
5.7.2 Anisotropic flow 121

6 Summary **127**

Bibliography **153**

List of Figures

1.1 Elementary particles of the standard model. Figure taken from [1] 2

1.2 Summary of measurements of the running coupling constant $\alpha_s(Q^2)$ as a function of the energy scale Q compared to computations from five loops as an input the current PDG average, $\alpha_s(m_Z^2) = 0.1180 \pm 0.0009$. Figure taken from [20]. 4

1.3 A layout of the QCD phase diagram illustrating different regions of hadronic matter. Figure taken from [31]. 5

1.4 Space-time evolution diagram of ultrarelativistic hadronic and heavy-ion collisions in the longitudinal direction without and with a QGP. 7

1.5 Representation of different stages of a heavy-ion collision; (a) the incoming Lorentz contracted heavy-ion beams, (b) the initial stage of collision that marks the onset of pre-equilibrium formation, (c) longitudinal expansion of the formed QGP medium with formation time $\tau \approx 1/\Lambda_{\mathrm{QCD}}$, (d) expansion of the medium in all directions leading to a spherical evolution with radial flow, (e) cooldown stage of the collision, when particle production stops at chemical freezeout. Figure taken from [31]. 8

1.6 (Left) Charged-particle densities per number of participants pair at mid-rapidity ($|y| < 0.5$) in different collision systems and center of mass energies. (Right) Charged-particle densities per number of participants pair at mid-rapidity in pp, p–Pb and Pb–Pb collisions at $\sqrt{s_{\mathrm{NN}}} = 2.76$ TeV, 5.02 TeV as a function of number of participants $\langle N_{\mathrm{part}} \rangle$ [47]. 10

1.7 Relative yields of strange hadrons to pions ($\pi^+ + \pi^-$) as a function of charged-particle multiplicity density at mid-rapidity in pp, p–Pb, and Pb–Pb collisions at $\sqrt{s} = 7$ TeV, $\sqrt{s_{\mathrm{NN}}} = 5.02$ and $\sqrt{s_{\mathrm{NN}}} = 2.76$ TeV, respectively [45]. 12

1.8 (Left) Nuclear modification factor as a function of p_{T} for charged-particles in p–Pb and central Pb–Pb collisions at $\sqrt{s_{\mathrm{NN}}} = 5.02$ TeV by the ALICE [52] and CMS collaboration [53, 54]. (Right) Nuclear modification factor as a function of p_{T} for charged-jets by the ALICE collaboration [55], compared to inclusive jets from ATLAS [56] and CMS collaboration [57] in central Pb–Pb collisions at $\sqrt{s_{\mathrm{NN}}} = 2.76$ TeV. 13

1.9 (Left) Invariant mass distribution of muon pairs in Pb–Pb collisions at $\sqrt{s_{\mathrm{NN}}} = 5.02$ TeV from the CMS experiment [60]. (Right) R_{AA} as a function of $\langle N_{\mathrm{part}} \rangle$ of J/ψ reconstructed in the $\mu^+\mu^-$ channel measured by the ALICE [61] and PHENIX [62] experiments in Pb–Pb collisions at $\sqrt{s_{\mathrm{NN}}} = 2.76$ TeV and Au–Au collisions at $\sqrt{s_{\mathrm{NN}}} = 200$ GeV, respectively. . 14

1.10 Elliptic flow coefficients of different charged hadron species as a function of p_{T} for different centralities in Pb–Pb collisions at $\sqrt{s_{\mathrm{NN}}} = 5.02$ TeV [69]. 15

1.11 p_{T}-differential cross-section of prompt D^0 mesons in pp collisions at $\sqrt{s} = 5.02$ TeV measured by ALICE [82], compared to pQCD calculations from FONLL [78] (left) and GM-VFNS [80] (right). 18

1.12 (Left) p_{T}-differential cross-section of Λ_{c}^+ baryons in pp collisions at $\sqrt{s} = 5.02$ TeV measured by ALICE [83], compared to pQCD calculations from GM-VFNS [80], and POWHEG [86] with CT14NLO PDFs [73]. (Right) Ratio of charm baryon-over-meson $\Lambda_{\mathrm{c}}^+/\mathrm{D}^0$ as a function of p_{T} in pp collisions at $\sqrt{s} = 5.02$ TeV measured by ALICE, compared to pQCD calculations and Monte Carlo model predictions [80, 86, 88, 89]. 19

1.13 Thermal model fits of different hadron species in central Pb–Pb collisions at $\sqrt{s_{\mathrm{NN}}} = 2.76$ TeV [95], with implementations from THERMUS [96], GSI-Heidelberg model [97], and SHARE [98]. 20

1.14 (Left) Measured coalescence parameter B_2 of anti-deuterons as a function of p_{T} in high multiplicity pp collisions at $\sqrt{s} = 7$ TeV, compared to a single parameter coalescence model [102]. (Right) The ratio between the p_{T} spectra of triton and helion ($^3\mathrm{H}/^3\mathrm{He}$) in high multiplicity pp collisions at $\sqrt{s} = 13$ TeV compared with the prediction of thermal and coalescence models [103]. 21

2.1 An illustration of the CERN accelerator complex depicting all the facilities and the injection systems. Image taken from [121]. 26

2.2 Schematic of the ALICE detector. Image taken from ALICE Figure Repository [122]. 27

2.3 The schematic of the ITS detector and its different layers. Figure taken from [123]. 28

2.4 (Left) TPC detector schematic. Figure taken from [125]. (Right) A section of the TPC endplate shows the inner and outer regions. Figure taken from [126]. 30

2.5 Schematic of the TOF detector and the MRPC supermodule. (Right) Cross-section of the MRPC module. Figures taken from [128]. 31

2.6 VZERO detector modules (Left) V0A and (Right) V0C. Figure taken from [129]. 32

2.7 Track reconstruction procedure followed at ALICE with a step-by-step representation. Figure taken from [126]. 34

2.8 Resolution of the interaction vertex position as a function of charged-particle multiplicity density in pp collisions at $\sqrt{s}$ = 7 TeV [139]. 35

2.9 Specific energy loss ($\mathrm{d}E/\mathrm{d}x$) of charged-particles as a function of momentum for the ITS (left) and the TPC detector (right) in pp collisions at $\sqrt{s}$ = 13 TeV. Figure taken from [122]. 36

2.10 Charged-particles β as a function of momentum for TOF detector in pp collisions at $\sqrt{s}$ = 13 TeV [122]. 37

3.1 Representation of Lund string fragmentation zoomed in at (a) mid-rapidity and (b) forward rapidity regions. 41

3.2 Stages of string fragmentation model at work; (a) stretching of the string leading to (b) meson formation, (c) baryon formation through di-quarks, and (d) multiple di-quark fragmentation in the popcorn model. 42

3.3 An illustration of all major processes in a pp $\rightarrow$ $\mathrm{t\bar{t}}$ event in the PYTHIA8 event generator. Figure taken from [149]. 43

3.4 String colour reconnection topologies of (Left) leading colour and (Right) beyond leading colour approximations implemented in PYTHIA8. Figure taken from [145]. 45

3.5 A working flowchart of the AMPT model in default mode (Left) and string melting mode (Right). Figures take from [156]. 46

3.6 Stages of an Au–Au collision along the beam axis at E_{kin} = 0.8 AGeV, with impact parameter b = 3 fm in the SMASH transport model at different time stamps of the collision. Figure taken from [167]. 51

4.1 2D correlation distributions of N_{tracklet} and z_{vtx} superimposed by the average N_{tracklet} profile (in black) for 2018 MB triggered data sample before (Left) and after (Right) z_{vtx} correction. 57

4.2 (Left) Ratio of uncorrected N_{tracklet} distributions in 2016, 2017, 2018 MB triggered sample to 2016 N_{tracklet} distribution. (Center) Ratio of N_{tracklet} distributions after z_{vtx} correction. (Right) Comparison of N_{tracklet} distribution from 2018 MB (black) and HMSPD (blue) triggered sample. . 59

4.3 (Top) 2D correlation distribution between N_{tracklet} and physical primary charged-particles from general purpose MC samples with a global linear fit (black). (Bottom) Charged-particle multiplicity distribution with the limits corresponding to N_{tracklet} intervals obtained from individual linear fits to every N_{tracklet} interval. 60

4.4 (Top) Visualization of an event with jetty-like (red) and isotropic topologies (blue). (Bottom) $S_{\text{O}}^{p_{\text{T}}=1}$ distributions in the $20 < N_{\text{tracklet}} < 30$, $31 < N_{\text{tracklet}} < 81$, and $20 < N_{\text{tracklet}} < 81$ intervals representing reconstructed and generated samples, along with D-meson candidate selection. 62

4.5 Cubic splines calculated from the unweighted spherocity distributions on the $20 < N_{\text{tracklet}} < 81$ interval for data (Green), MC generated (Red), and MC reconstructed (Blue) samples. 63

4.6 2D correlation of generated rapidity (y) and p_{T} of D^0 mesons in pp collisions at $\sqrt{s} = 13$ TeV. 64

4.7 2D correlation distribution of true and measured $S_{\text{O}}^{p_{\text{T}}=1}$, with hybrid tracks (Left) and TPC-only + TPC refit tracks (Right). 66

4.8 D^0 invariant mass distributions in different p_{T} intervals for $60 < N_{\text{tracklet}} < 99$. Data points are fitted with a Gaussian signal function (blue) and an exponential background function (red), superimposed with the reflected spectra (green). The dashed and solid lines represent the background before and after subtracting the contribution of reflected signal. 67

4.9 Acc $\times \mathcal{E}$ of prompt D^0 mesons as a function of p_{T} in different N_{tracklet} intervals (Left) and in different N_{tracklet} and S_{O}-Quantile intervals (Right). 68

4.10 Summary of an output of the multi-trial fitter in the $20 < N_{\text{tracklet}} < 30$ and $1 < p_{\text{T}} < 2$ GeV/c interval. Top three panels (left to right) represent illustrate the Gaussian sigma (σ), mean, and the reduced-χ^2 of the fit. The bottom left and center panels show the ratio of the extracted raw yields in the give N_{tracklet} interval to the integrated one, and the right panel shows the test results of bin counting. 70

4.11 Ratio of D^0 meson yields with central topological selections and two loose and tight selections as a function of S_{O}-Quantiles in different p_{T} intervals. The assigned systematic (magenta) is estimated from the RMS of the deviation from unity per S_{O}-Quantile interval. 71

4.12 Ratio of D^0 meson yields with and without PID selection criteria as function of N_{tracklet} in different p_T intervals. The deviation from unity is negligible, except for $60 < N_{\text{tracklet}} < 99$ interval for $1 < p_T < 2$ GeV/c which is deemed as an outlier. 72

4.13 Ratio of $f_{\text{non-prompt}}/f^{\text{MB}}_{\text{non-prompt}}$ (Left) and $f^{S_O}_{\text{non-prompt}}/f^{S_O-\text{int}}_{\text{non-prompt}}$ (Right) as a function of $\mathrm{d}N_{\text{ch}}/\mathrm{d}\eta/\langle \mathrm{d}N_{\text{ch}}/\mathrm{d}\eta \rangle$ and S_O-Quantiles, respectively. The values correspond to different PYTHIA8 tunes used to account for the systematic variation. 73

4.14 (Left) Ratio of correction efficiencies with PYTHIA8 and FONLL weights for D^0 in MB triggered sample as a function of p_T. (Right) Ratio of correction efficiencies performed on a given S_O-Quantile sample over the integrated one with PYTHIA8 and FONLL weights for D^0 in $20 < N_{\text{tracklet}} < 81$ as a function of p_T. 74

4.15 (Top Left) N_{tracklet} distributions with different S_O-Quantile selections. (Top Right) The efficiency ratios vs p_T computed with and without a spherocity selection. (Bottom Center) Efficiency ratios with anchored MC data sample over general purpose sample as a function of p_T. 75

4.16 D^0-meson self-normalized yields as a function of relative charged-particle multiplicity density at mid-rapidity in different p_T intervals in pp collisions at $\sqrt{s} = 13$ TeV. The statistical and systematic uncertainties are represented as vertical bars and boxes respectively. 77

4.17 (Left) Average D-meson self-normalized yields as a function of relative charged-particle multiplicity density at mid-rapidity in different p_T intervals in pp collisions at $\sqrt{s} = 13$ TeV. The feed-down fractions are displayed in the bottom panel. (Right) The ratios of self-normalized yields to self-normalized multiplicity as a function of relative charged-particle multiplicity. The statistical and systematic uncertainties are represented as vertical bars and boxes respectively. 78

4.18 Comparison of average D-meson self-normalized yields in pp collisions at $\sqrt{s} = 7$ TeV [184] and $\sqrt{s} = 13$ TeV as a function of relative charged-particle multiplicity density at mid-rapidity in three p_T intervals. The statistical and systematic uncertainties are represented as vertical bars and boxes, respectively. 79

4.19 Comparison of self-normalized yields of average D-meson, J/ψ [207], and electrons from heavy-flavour hadron decays ($c, b \rightarrow e$) [186] as a function of relative charged-particle multiplicity density at mid-rapidity in three p_T intervals in pp collisions at $\sqrt{s} = 13$ TeV. The double ratios for the same are presented in the bottom panels. 80

4.20 Comparison of self-normalized yields of average D-meson and model predictions from EPOS3 [208] with (dark green) and without (light green) hydrodynamics, and a 3-Pomeron CGC model [209] (blue) as a function of relative charged-particle multiplicity density at mid-rapidity in three p_{T} intervals in pp collisions at $\sqrt{s}$ = 13 TeV. 81

4.21 Comparison of self-normalized yields of average D-meson with Monash and CR Modes 0, 2, and 3 tunes of PYTHIA8 as a function of relative charged-particle multiplicity density at mid-rapidity in all p_{T} intervals in pp collisions at $\sqrt{s}$ = 13 TeV. 82

4.22 Comparison of self-normalized yields of average D-meson with different combinations of MPI and CR with PYTHIA8 as a function of relative charged-particle multiplicity density at mid-rapidity in all p_{T} intervals in pp collisions at $\sqrt{s}$ = 13 TeV. 83

4.23 D^0-meson self-normalized yields as a function of S_{O}-Quantiles at mid-rapidity in different N_{tracklet} intervals (left: $20 < N_{\mathrm{tracklet}} < 30$, right: $31 < N_{\mathrm{tracklet}} < 81$, and below: $20 < N_{\mathrm{tracklet}} < 81$,) and p_{T} intervals in pp collisions at $\sqrt{s}$ = 13 TeV. The statistical and systematic uncertainties are represented as vertical bars and boxes respectively. 84

4.24 Average D-meson self-normalized yields as a function of S_{O}-Quantiles at mid-rapidity in different N_{tracklet} intervals (left: $20 < N_{\mathrm{tracklet}} < 30$, right: $31 < N_{\mathrm{tracklet}} < 81$, and below: $20 < N_{\mathrm{tracklet}} < 81$,) and p_{T} intervals in pp collisions at $\sqrt{s}$ = 13 TeV. The statistical and systematic uncertainties are represented as vertical bars and boxes respectively. 85

4.25 Comparison of self-normalized yields of average D-meson with Monash and CR Modes 0, 2, and 3 tunes of PYTHIA8 as a function of S_{O}-Quantiles at mid-rapidity in three N_{tracklet} intervals and all p_{T} intervals in pp collisions at $\sqrt{s}$ = 13 TeV. 87

5.1 Deuteron wave functions using Gaussian form (solid orange), Hulthén (dashed green) and Double Gaussian (dashed magenta) fitted to the Hulthén distribution. 94

5.2 Pictorial depiction of the resonance source model to describe the emission of (anti-)nucleon pairs in pp collisions. The distance r_{core} refer to the primordial nucleons or resonance pair emission described by a Gaussian source, while r_0 is the p-n source size described by a modified Gaussian distribution, arising due to effects from resonance decay [111]. 97

5.3 (Left) Source radius (r_0 and r_{core}) as a function of pair transverse mass ($\langle m_{\text{T}} \rangle$) extracted from ALICE measurements [237]. (Right) Source functions for p-p for primordial r_{core} = 1.2 fm and from decay emission r_0 = 1.28 fm. The markers are extracted from the ALICE measurement that shows p − p sources with one proton coming from a resonance decay. The points are fitted using a modified exponential Gaussian function (solid red line) [111, 237]. 99

5.4 Transverse momentum spectra of (Left) protons and (Right) anti-protons in central Au–Au collisions at $\sqrt{s_{\text{NN}}}$ = 19.6 GeV, 39 GeV ($|y| < 0.1$), 200 GeV ($|y| < 0.5$) and central Pb–Pb collisions at $\sqrt{s_{\text{NN}}}$ = 2.76 TeV ($|y| < 0.5$) from "Coalescence" or "Transport OFF" (solid lines) and "Transport ON" (dashed lines) mode. Experimental results (symbols) are taken from STAR and ALICE experiments [251–253]. The lower panels show the ratio of the experimental results to the model predictions. 103

5.5 Transverse momentum spectra of (Left) deuterons and (Right) anti-deuterons in central Au–Au collisions at $\sqrt{s_{\text{NN}}}$ = 19.6 GeV, 39 GeV, 200 GeV ($|y| < 0.3$) and central Pb–Pb collisions at $\sqrt{s_{\text{NN}}}$ = 2.76 TeV ($|y| < 0.5$) from "Coalescence" (solid lines) and "Transport" (dashed lines) mode. Experimental results (symbols) are taken from the STAR and ALICE measurements [212, 213]. The lower panels show the ratio of the experimental results to the model predictions. 104

5.6 Transverse momentum spectra of triton in central Au–Au collisions at $\sqrt{s_{\text{NN}}}$ = 19.6, 39, 200 GeV ($|y| < 0.5$) and helium-3 in central Pb–Pb collisions at $\sqrt{s_{\text{NN}}}$ = 2.76 TeV ($|y| < 0.5$) from the "Coalescence" mode (solid lines). Experimental results (symbols) are taken from the STAR and ALICE measurements [213, 216]. The lower panels show the ratio of the experimental results to the model predictions. 105

5.7 Particle ratios for anti-deuterons over deuterons as a function of center of mass energies from "Coalescence" and "Transport" modes. Experimental measurment of $\bar{\text{d}}/\text{d}$ ratios from the STAR and ALICE experiments for the central Au–Au collisions at $\sqrt{s_{\text{NN}}}$ = 19.6 GeV, 39 GeV, 200 GeV and central Pb–Pb collisions at $\sqrt{s_{\text{NN}}}$ = 2.76 TeV are also shown [212, 213] . . 106

5.8 Particle ratios for deuterons over protons and anti-deuterons over anti-protons as a function of the center of mass energies from "Coalescence" and "Transport" modes. Solid lines are predictions from the PHQMD model [223]. Experimental measurement of d/p and $\bar{\text{d}}/\bar{\text{p}}$ ratios from the STAR and ALICE experiments for the central Au–Au collisions at $\sqrt{s_{\text{NN}}}$ = 19.6 GeV, 39 GeV, 200 GeV and central Pb–Pb collisions at $\sqrt{s_{\text{NN}}}$ = 2.76 TeV are also shown [212, 213]. 107

5.9 Particle ratios from the "Coalescence" mode for triton over proton and deuteron for 0-10% central Au–Au and Pb–Pb collisions, helium-3 over deuteron for 0-10% central Pb–Pb collisions and helium-3 over proton for 0-20% central Pb–Pb collisions. Experimental measurement of ^{3}H/p, ^{3}H/d, ^{3}He/p, ^{3}He/d ratios from the STAR and ALICE experiments for the central Au–Au collisions at $\sqrt{s_{\rm NN}}$ = 19.6 GeV, 39 GeV, 200 GeV and central Pb–Pb collisions at $\sqrt{s_{\rm NN}}$ = 2.76 TeV are also shown [213, 216]. . 108

5.10 (Left) The B_2 parameter versus $p_{\rm T}$ of deuterons and anti-deuterons in central (0-10%) Au–Au collisions at $\sqrt{s_{\rm NN}}$ = 39 GeV and central Pb–Pb collisions at $\sqrt{s_{\rm NN}}$ = 2.76 TeV from "Coalescence" (solid lines) and "Transport" (dashed lines) modes. Predictions from the PHQMD model are superimposed [223]. (Right) The B_3 parameter versus $p_{\rm T}$ for triton and helium-3 in central (0-10%) Au–Au collisions at $\sqrt{s_{\rm NN}}$ = 200 GeV and central (0-20%) Pb–Pb collisions at $\sqrt{s_{\rm NN}}$ = 2.76 TeV from "Coalescence" (solid lines) mode. The results are compared to experimental measurements (symbols) from STAR and ALICE [212, 213, 254]. 109

5.11 Coalescence parameter B_2 and $\sqrt{B_3}$ as a function of $\sqrt{s_{\rm NN}}$ for $p_{\rm T}/A$ = 0.65 GeV/c in central (0-10%) Au–Au and Pb–Pb collisions for "Coalescence" and "Transport" modes. Solid lines are predictions from the PHQMD model [223]. The results are compared with measurements from the STAR and ALICE experiments. [212, 213, 254]. 110

5.12 (Left) Charged-particle multiplicity distributions from PYTHIA8 + Monash (dotted lines) for pp collisions at $\sqrt{s}$ = 13 TeV. Data from ALICE (solid lines) for the midrapidity multiplicity estimator ($N^{|\eta|<0.8}_{\rm tracklet}$) and the V0M detector are presented for comparison [206, 257]. (Right) Transverse sphericity distributions from PYTHIA8 + Monash (lines) for pp collisions at $\sqrt{s}$ = 13 TeV. Data points from ALICE (markers) in the 0-1% multiplicity for the midrapidity estimator ($N^{|\eta|<0.8}_{\rm tracklet}$ I) and the V0M detector (V0M I) with events having $N_{\rm ch} > 10$ are presented for comparison [202]. 112

5.13 Transverse momentum spectra of (anti-)protons from PYTHIA8, and deuterons and anti-deuterons from pp collisions at $\sqrt{s}$ = 13 TeV with PYTHIA8 + Coalescence in MB I and HM I class at midrapidity ($|y| < 0.5$) in two detector acceptances; (Left) Predictions from PYTHIA8 Monash in MB I and HM I multiplicity classes; (Center) Predictions from a single Gaussian deuteron wave function scaled twice to their actual values; (Right) Predictions from a two-Gaussian deuteron wave function. Results are compared to measurements from ALICE in respective multiplicity intervals [103, 258, 259]. 113

5.14 Transverse momentum spectra of (anti)-protons with PYTHIA8 and (anti-)deuterons with PYTHIA8 + Coalescence in "jetty", "isotropic", and S_O-integrated intervals at midrapidity ($|y| < 0.5$) in pp collisions at $\sqrt{s} = 13$ TeV. Predictions from the model are presented in (Left) MB I and (Right) HM I multiplicity interval. 115

5.15 Coalescence parameter of (anti-)deuterons B_2 as a function of proton transverse momentum at midrapidity ($|y| < 0.5$) in pp collisions at $\sqrt{s} = 13$ TeV in (Left) MB I and (Right) HM I multiplicity interval. Solid and dashed lines represent the predictions from single and double Gaussian wave functions respectively. The results are compared to experimental measurements from ALICE [103, 259]. 116

5.16 Momentum correlation of (Bottom) p – d and (Top) d – d pairs in Au–Au collisions at $\sqrt{s_{\rm NN}} = 3$ GeV with a single Gaussian function as the deuteron wavefunction in different centralities from SMASH + Coal + CRAB, compared to STAR preliminaries [262]. Predictions are presented for hydro and hard EoS SMASH fitted with the LL model shown in solid and dashed red lines, respectively. 119

5.17 Momentum correlation of (Bottom) p – d and (Top) d – d pairs in Au–Au collisions at $\sqrt{s_{\rm NN}} = 3$ GeV with a double Gaussian function as the deuteron wavefunction in different centralities from SMASH + Coal + CRAB, compared to STAR preliminaries [262]. Predictions are presented for hydro and hard EoS SMASH fitted with the LL model shown in solid and dashed red lines, respectively. 120

5.18 Source radius extracted from LL fits to p – d and d – d correlation functions from STAR preliminaries [262], and from two cluster formation times in hydro (solid lines) and hard EoS (dashed lines) SMASH + Coal and two choices of the deuteron wave function. 121

5.19 (Left) Elliptic flow (v_2) and directed flow (v_1) of deuterons, tritons and helium-3 produced in non-central Au–Au collisions as function of rapidity using SMASH + Coal. (Right) dv_1/dy of deuterons, tritons and helium-3 produced in non-central Au–Au collisions using SMASH + Coal. Results are compared to experimental measurements from STAR [278]. 122

5.20 Directed flow (v_1) as function of p_T of (Bottom) deuterons, (Middle) tritons and (Top) helium-3 produced in non-central Au–Au collisions using SMASH and their comparison with experimental measurements from STAR [278]. 123

5.21 Elliptic flow (v_2) as function of p_T of (Bottom) deuterons, (Middle) tritons and (Top) helium-3 produced in non-central Au–Au collisions using SMASH and their comparison with experimental measurements from STAR [278]. 124

List of Tables

2.1 Details of the ITS and properties of each layer. 29

4.1 Summary of N_{tracklet} intervals, the corresponding charged-particle multiplicity density intervals, the average charged-particle multiplicity density, and the self-normalized multiplicity used in the D-meson vs multiplicity analysis. The associated statistical and systematic uncertainties are also quoted along with the respective triggers for each N_{tracklet} interval. 61

4.2 Summary of general track selection criteria. 65

4.3 Strong and conservative PID selection criteria with the TPC based on different p_{T} momentum intervals of the decay tracks. 65

4.4 Topological variables and their selections in different p_{T} intervals applied to the D^0 meson decay daughter tracks. 66

4.5 Variations in fitting strategies used in the multi-trials for raw yield systematic uncertainty extraction of D^0 meson. 70

4.6 Summary of systematic uncertainties in $20 < N_{\text{tracklet}} < 30$ interval as a function of p_{T} for the D^0 meson. 76

4.7 Summary of systematic uncertainties in $20 < N_{\text{tracklet}} < 81$ interval for 50-75% S_{O}-Quantile as a function of p_{T} for the D^0 meson. 77

4.8 Charged-particle multiplicity density classes corresponding to the N_{tracklet} intervals relevant in the spherocity dependent analysis. 85

5.1 Parameters (Δp^{max} and Δr^{max}) used in coalescence of deuterons, tritons and helium-3. 93

5.2 S_{O} selection for "jetty" and "isotropic" class on different multiplicity classes at midrapidity. 114

Chapter 1

Introduction

This thesis sets sights on exploring two aspects of ultra-relativistic hadronic and heavy-ion collisions. The first objective is rooted in experimental data analysis of *heavy-flavour* production in proton-proton collisions, performed in collaboration with the ALICE experiment at the LHC, CERN. The other aspect is based on the phenomenology of the production mechanism of light nuclei in collision experiments via *coalescence*. Both aspects explore the interactions predicted by the theory of strong interactions but provide a divided view of the energy regimes of the quantum chromodynamic scale. This introduction supplies an understanding of the fundamentals necessary to deconstruct this thesis. The first few sections provide a general introduction to particle physics and the theory of strong interactions. The stages of heavy-ion collision and formation of the quark-gluon-plasma are discussed, followed by the experimental observables for its detection. A description of heavy-flavour and light nuclei production and production is laid out at the end.

1.1 The standard model of particle physics

The standard model of particle physics provides the fundamental picture of interactions in the universe and classifies elementary particles. At the heart of this model lies the theory of quantum electrodynamics, an abelian gauge theory based on the U(1) symmetry [2], following the concept of gauge theories in quantum fields. Sheldon Glashow moved on to formulate the electroweak theory [3, 4], to which Steven Weinberg and Abdus Salam incorporated the Higgs mechanism (also known as the Glashow-Weinberg-Salam model), leading to the electroweak symmetry breaking [5–9]. The model suggests that we exist in a universe with broken symmetries. For a short moment after the Big Bang, the universe

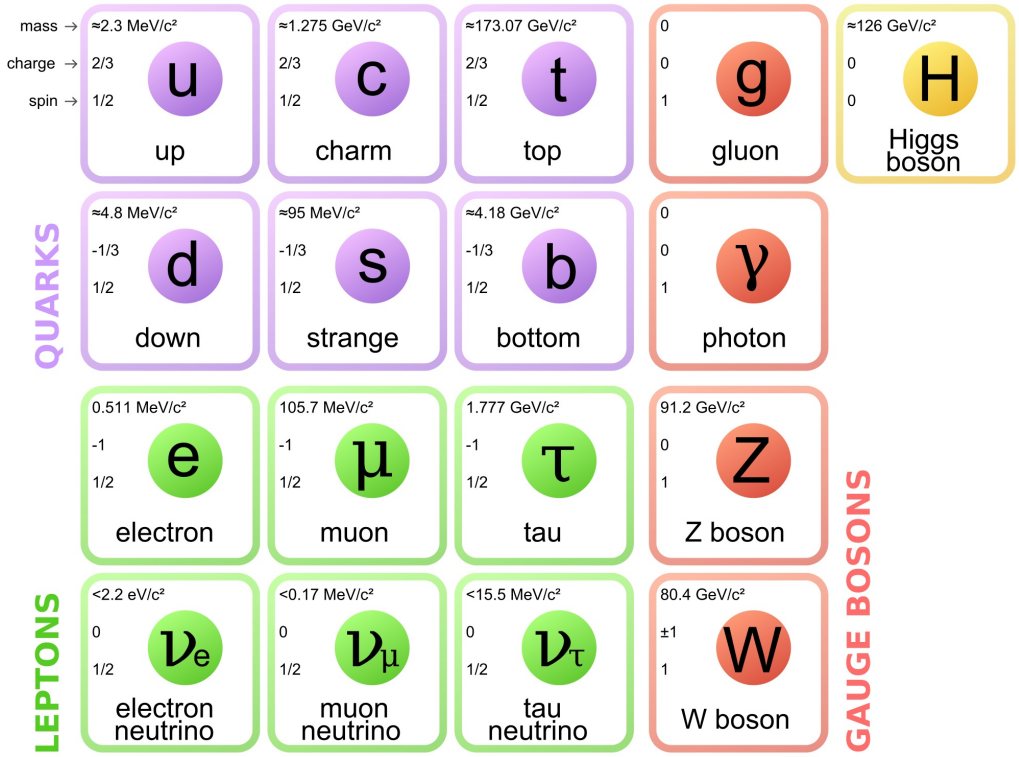

Figure 1.1: Elementary particles of the standard model. Figure taken from [1]

manifests a local $SU(2)_L \otimes U(1)_Y$ symmetry, which undergoes a symmetry breaking phase transition. The phase transition leads to the initially massless fermions, $W^{\pm}$, and Z boson fields acquire mass when the non-zero Higgs field permeates the vacuum. Upon discovering neutral weak currents associated with the Z boson at CERN [10], Glashow, Weinberg, and Salam were awarded the Nobel Prize in 1979. The model successfully predicted the masses of $W^{\pm}$ and Z, later discovered at CERN [11]. The model was further extended with the theory of strong interactions from quantum chromodynamics, which brought in asymptotic freedom of quarks and led to experimental evidence that hadrons are composed of bound quarks mediated by the exchange gluons [12, 13].

The elementary particles are classified into four classes: quarks, leptons, gauge bosons, and the Higgs scalar boson. The fundamental field associated with the Higgs boson is responsible for the generation of the mass of all elementary particles. In 2012, CERN reported the discovery of the Higgs boson [14] for which Peter Higgs and François Englert were awarded the Nobel Prize in 2013. The gauge bosons serve as the mediators or the force carriers, each belonging to the underlying interactions of the model. The gauge boson for strong interactions is the gluon, the $W^{\pm}$, Z boson for weak interactions, and the photon for electromagnetic interactions. The quarks and leptons fall into the same

family of spin 1/2 fermions but constitute different aspects in their interactions. Based on their masses, they are each grouped into three generations. The quarks with fractional charges are fundamentally heavier than leptons. They are divided into two classes based on their electric charge, with up-like quarks carrying +2/3e and down-like quarks with -1/3e. The up-like category contains up, charm, and top (truth) quarks (u, c, t), while the down-like contains the down, strange, and bottom (beauty) quarks (d, s, b). Additionally, quarks also carry a colour charge, which allows them to interact via strong interactions in addition to electromagnetic and weak interactions. Unlike the quarks, leptons can only interact via electromagnetic and weak interactions. Based on their charges, the charged lepton constitute the massive leptons, namely electrons, muons, and tauons (e, μ, τ), and the neutral and massless family of neutrinos (ν_e, ν_μ, ν_τ). A summary of all elementary particles in the standard model is reported in Figure 1.1.

The model proves to be inadequate for certain aspects of particle physics. The standard model considers the neutrino to be massless, disproved by the neutrino flavour oscillation experiments accounting for its non-zero mass [15]. The standard model does not explain the baryon asymmetry of the universe [16] and the possible existence of a particle for dark matter [17]. The model's shortcomings lead to physicists exploring modern avenues of particle physics. They are collectively termed Beyond Standard Model (BSM) theories that constitute effective field theories, extra dimensions, and auxiliary symmetries [18, 19].

1.2 Quantum chromodynamics

The theory of quantum chromodynamics (QCD) encompasses the dynamics of strong interactions. It is a non-abelian theory following a local $SU(3)_C$ symmetry [13, 21]. The symmetry leads to the conservation of the colour charges that the quark and gluon fields carry. The QCD Lagrangian is written in the form [22, 23]

$$\mathcal{L}_{\text{QCD}} = -\frac{1}{4} G^{\mu\nu}_{\alpha} G^{\alpha}_{\mu\nu} + \sum_f \bar{q}_i{}^f (i\gamma_\mu D^{\mu}_{ij} - m_f \delta_{ij}) q^f_j \tag{1.1}$$

where f are the quark flavours with mass m_f and i is the colour charge. The 8 gluon fields $G_{\mu\nu}$ over α are related to the covariant derivative D^{μ}_{ij} by

$$D^{\mu}_{ij} = \partial^\mu \delta_{ij} - i g_s \left(\frac{\lambda^{\alpha}_{ij}}{2} \right) G^{\mu\nu}_{\alpha} \tag{1.2}$$

where, $g_s = \sqrt{4\pi\alpha_s}$ is the strong coupling constant and λ^{α}_{ij} are the Gell-Mann matrices [24]. The coupling constant is a running constant that is dependent on the energy scale of the

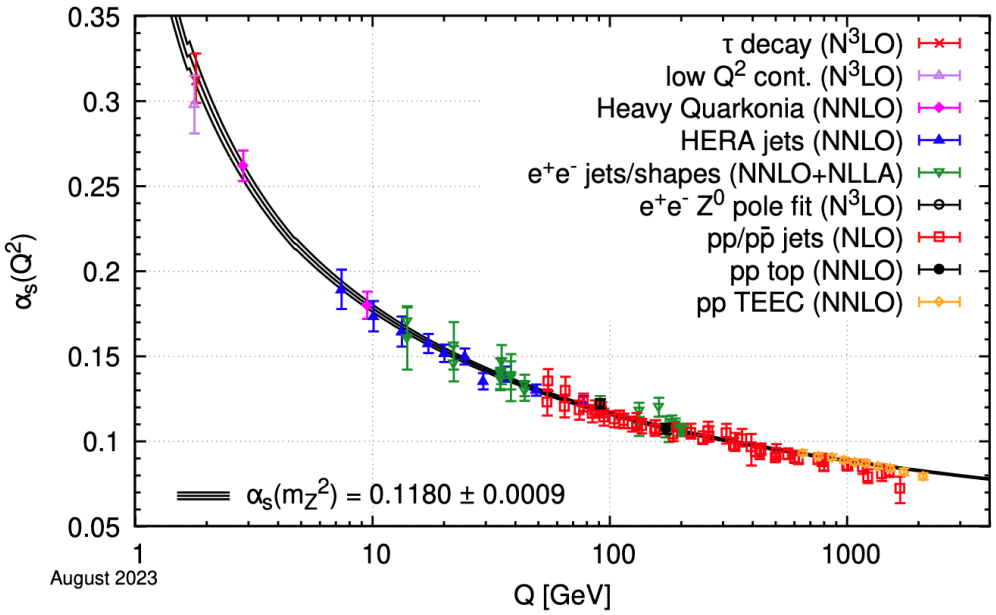

Figure 1.2: Summary of measurements of the running coupling constant $\alpha_s(Q^2)$ as a function of the energy scale Q compared to computations from five loops as an input the current PDG average, $\alpha_s(m_Z^2) = 0.1180 \pm 0.0009$. Figure taken from [20].

interaction. For a process with momentum transfer Q, the running coupling constant $\alpha_s(Q^2)$ is defined as

$$\alpha_s(Q^2) = \frac{\alpha_s(\mu^2)}{1 + \alpha_s(\mu^2)\frac{33-2n_f}{12\pi}\ln\frac{Q^2}{\mu^2}} \tag{1.3}$$

where μ is the renormalization mass scale and n_f is the number of flavours. Figure 1.2 shows the trend of α_s as a function of Q, which show that α_s tends to zero at large Q. This limit of α_s allows the existence of free quarks and gluons (partons), a property of QCD known as asymptotic freedom [25–27]. At decreasing Q, the large α_s leads to the strong binding partons into hadrons, generally known as colour confinement [28]. In between the extremes of Q a transition occurs between confined strongly interacting to weakly interacting free partons. The interaction potential between a quark anti-quark pair ($q\bar{q}$) is given by the Cornell potential [29]

$$V(r) = \kappa r - \frac{\alpha}{r}. \tag{1.4}$$

The first linear term consists of a string tension constant κ, and a Coulomb like potential with constant α. This potential defines the two regimes and treatments of QCD; at small r (or large Q), the interactions are diluted by the anti-screening nature of colour interactions. This is a consequence of the self-interacting nature of gluons, where a perturbative approach is preferred. At large r (small Q), the confinement effects take over until the connecting string breaks to form a new $q\bar{q}$ pair. The asymptotic freedom of strong interactions can be exploited to create a state of deconfined quarks and gluons. This is achieved either by hitting large temperatures or densities in the QCD vacuum, which leads to a free-flowing plasma of quarks and gluons. This results in a phase transition of QCD matter, a colour deconfined state of asymptotically free partons also known as the *quark-gluon plasma* [30].

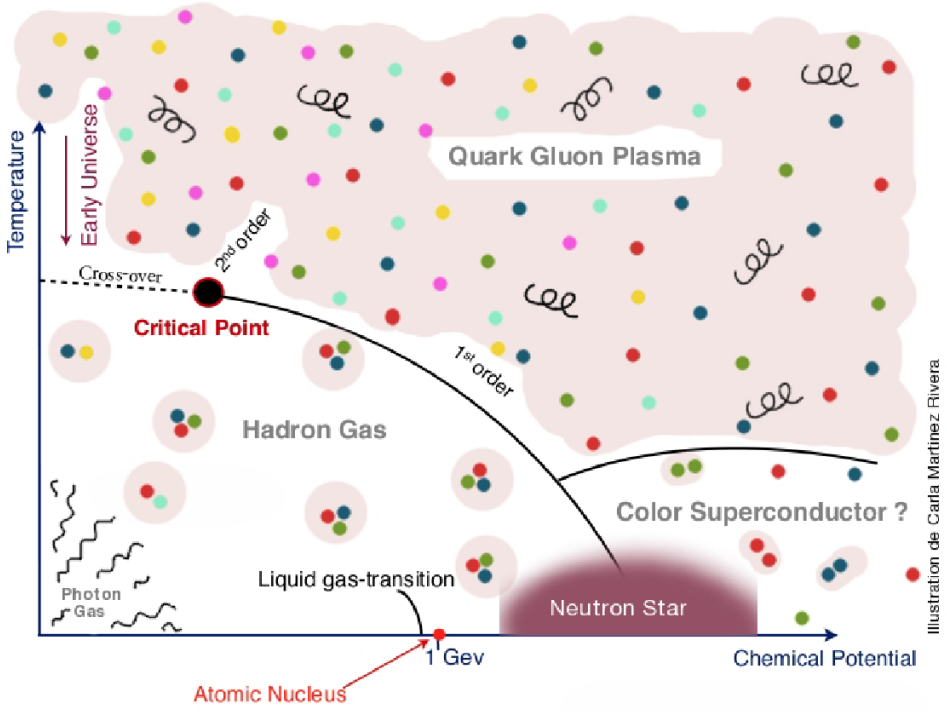

Figure 1.3: A layout of the QCD phase diagram illustrating different regions of hadronic matter. Figure taken from [31].

1.3 The QCD phase diagram

Temperature and density can be controlled to scan the thermodynamic phase space of the QCD vacuum. Also known as the QCD phase diagram, the temperature (T) and baryon chemical potential (μ_B) form the conjugate variables of the QCD vacuum [32]. The phase

diagram in Figure 1.3 presents the different states of strongly interacting matter. At higher temperatures $T \approx 154 - 174$ MeV and low values of μ_B ($\mu_B \approx 0$), a phase transition of a cross-over kind occurs from a hadronic gas state to a quark-gluon plasma [33]. However, at finite μ_B, the phase transition is believed to be a first-order type, implying the existence of a *critical point* [34]. As temperature reduces and μ_B increases, the pressure rises so high that a degenerate system of low temperature quarks forms a state of a *colour superconductor* [35]. As the temperature reaches zero, the hadronic degrees of freedom are recovered, leading to a degenerate state of neutrons that resembles the core of a neutron star [36].

The nature of the QCD phase transition is rooted in the internal symmetries of the QCD Lagrangian. In Equation 1.1, the Lagrangian is chirally symmetric for massless quarks. At low temperatures, this results in a null expectation value in the QCD order parameter $\langle q\bar{q}\rangle$ [37, 38]. The order parameter can be written as the sum of left and right handed quark fields as

$$\langle q\bar{q}\rangle = \langle \bar{q}_L q_R\rangle + \langle \bar{q}_R q_L\rangle \tag{1.5}$$

The chiral symmetry in Equation 1.1 is broken spontaneously $\langle q\bar{q}\rangle \neq 0$ similar to an explicit symmetry breaking, that leads to confinement of quarks into hadrons. The chiral symmetry is restored at high temperatures (QCD vacuum), often regarded as the phase transition of QCD [30].

To create this state of deconfinement, the requisite conditions in the phase diagram can be met using experimental facilities that collide heavy-ions at ultra-relativistic energies. For an instant, these collision events can generate high temperatures or large baryon densities, favourable to create this dense medium of strongly coupled quarks and gluons [38, 39].

1.4 Ultrarelativistic heavy-ion collisions

The dense soup of free partons can be created in a laboratory in experimental facilities worldwide [40]. The primary facilities are at the Brookhaven National Laboratory (BNL) and the European Organization for Nuclear Physics (CERN). The Alternating Gradient Synchrotron (AGS) at BNL and Super Proton Synchrotron (SPS) conducted 'fixed target' experiments to carry out heavy-ion collisions [41, 42]. These experiments collided Au and Pb beams operating at center of mass energies in the range of 7.7 - 17.3 GeV, lying at a non-zero μ_B, leading to a baryon-rich regime. With SPS, the first circumstantial evidence of QGP was achieved. With the beginning of collider experiments, the observations narrowed down to smaller net-baryon densities and higher temperatures to achieve the phase transition. The Relativistic Heavy-Ion Collider (RHIC) [43] provided the first

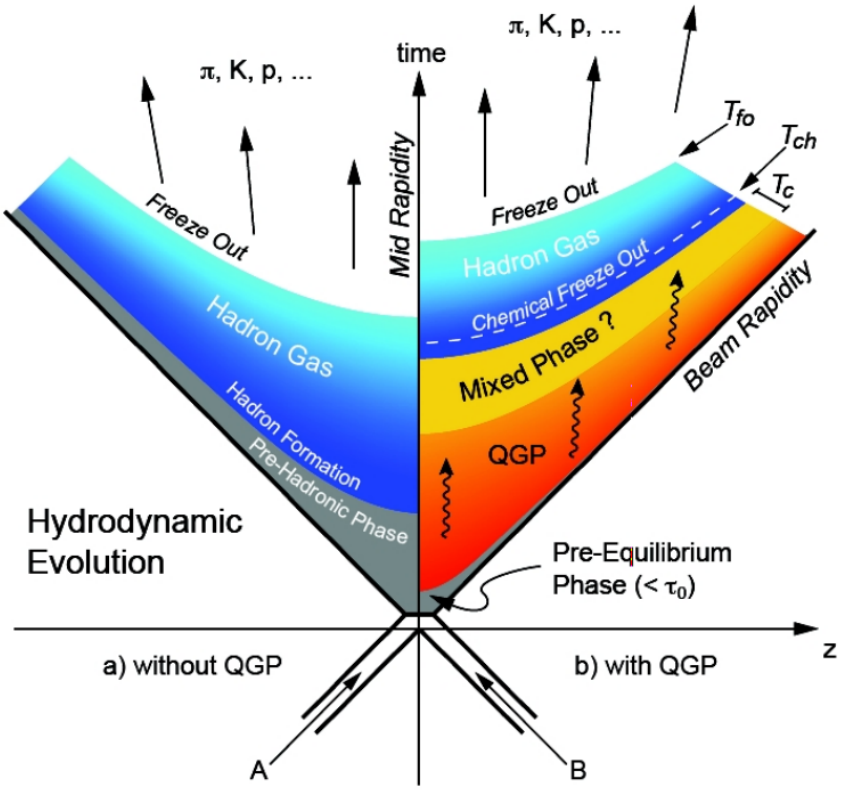

Figure 1.4: Space-time evolution diagram of ultrarelativistic hadronic and heavy-ion collisions in the longitudinal direction without and with a QGP.

conclusive results of the existence of QGP, with substantial extension of the knowledge at the Large Hadron Collider (LHC) at CERN [44], colliding Au and Pb ion beams at center of mass energies per nucleon up to 200 GeV and 5.5 TeV, respectively. The generated QGP lies at $\mu_B = 0$, causing a crossover phase transition with a nearly transparent collision region. Figure 1.4 shows the space-time evolution diagram of ultrarelativistic hadronic and heavy-ion collisions in the Bjorken picture, where all transverse dynamics are neglected, and the evolution is described in terms of proper time (τ) and the beam axis (z) [39].

Each stage of the evolution of a heavy-ion collision can be understood from the illustration in Figure 1.5. The stages can be divided as follows:

- At ultrarelativistic energies, Lorentz contracted colliding beams of radius R, cross for time $\tau_{\text{cross}} = 2R/\gamma$, where γ is the Lorentz factor. The crossing time is less than $\tau_0 = 1/\Lambda_{\text{QCD}} \approx 1$ fm.

- The energy density deposited from the collision can be estimated via the Bjorken

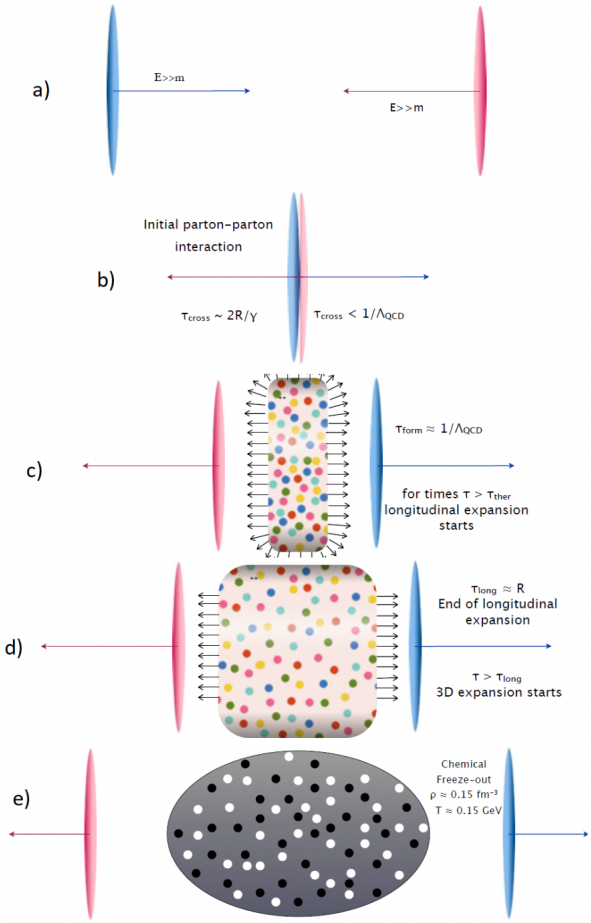

Figure 1.5: Representation of different stages of a heavy-ion collision; (a) the incoming Lorentz contracted heavy-ion beams, (b) the initial stage of collision that marks the onset of pre-equilibrium formation, (c) longitudinal expansion of the formed QGP medium with formation time $\tau \approx 1/\Lambda_{\rm QCD}$, (d) expansion of the medium in all directions leading to a spherical evolution with radial flow, (e) cooldown stage of the collision, when particle production stops at chemical freezeout. Figure taken from [31].

relation at mid-rapidity[1] where $\mu_{\rm B} = 0$, which is given by

$$\epsilon_{\rm BJ} = \frac{1}{\mathcal{A}\tau_o}\frac{{\rm d}E_{\rm T}}{{\rm d}y}\bigg|_{y=0}. \tag{1.6}$$

[1] rapidity is a particle kinematic variable related to its to four-momentum as $y = \frac{1}{2}\ln\left(\frac{E+p_z}{E-p_z}\right)$

Here E_T is the transverse energy[2], $\mathcal{A} = \pi R^2$ is the transverse area, with rapidity y. This marks the onset of a pre-equilibrium phase where a local thermalization is achieved. The deposited energy density is high enough to reach the critical conditions for QGP.

- Local thermal equilibrium marks QGP formation; the produced medium can be treated with its thermal properties and relativistic hydrodynamic expansion. The expansion is longitudinally dominant from the large pressure carried by the heavy-ion beams. At pressure P and energy density ϵ, the hydrodynamic equation [39] can be written as

$$\frac{d\epsilon}{d\tau} + \frac{\epsilon + P}{\tau} = 0 \tag{1.7}$$

  This expansion is guided by an equation of state (EoS), which can be based on the assumption of the type of medium formed. For an ideal gas, the EoS is $3P = \epsilon$, providing a energy density and temperature dependence relation $\epsilon \propto 1/\tau^{4/3}$ and $T \propto 1/\tau^{1/3}$ respectively.

- At a certain critical temperature ($T < T_c$), the expanding system no longer exists in partonic degrees of freedom. *Hadronization* of quarks and gluons take place, followed by an expansion of a hadron gas.

- In the final stages of this evolution, the hadron interactions die off; firstly, the inelastic collisions cease to exist, stopping particle production. This is the point of *chemical freezeout*. At *kinetic freezeout*, all elastic collisions stop, fixing the momentum spectra of the final state particles.

Unlike heavy-ions, the RHIC and the LHC also accelerate and collide proton beams. A proton–proton (pp) collision system sets a baseline for the heavy-ion measurements, allowing for comparative measurements to quantify the modifications due to the nuclear environment from heavy-ion collision systems. A pp system is also a great playground to test a variety of perturbative calculations, where the required energy scale (Q) is high and achievable via hard scattered processes. Furthermore, pp collisions with a large number of ensuing particles (high multiplicity) can show similarities with heavy-ion systems. Measurements by ALICE and CMS collaboration have established that certain signatures of QGP formation [45, 46], such as 'collective-like' effects, can be achieved through high multiplicity pp collisions.

[2] Transverse energy is a kinematic variable relating the total energy E and the polar angle θ of a particle with respect to the beam axis by $E_T = E \sin\theta$

1.5 Signatures of QGP

QGP is impossible to probe directly because of its short-lived nature. However, it leaves traces in various observables that can be extracted from the ensuing particle production. The understanding of the QGP, its dynamics, and its properties is reported by analyzing these observables. The upcoming sections discuss a few key experimental observables that weigh into QGP detection in heavy-ion collisions, namely charged-particle multiplicity, strangeness enhancement, jet quenching, quarkonia suppression, and anisotropic flow of produced particles [40].

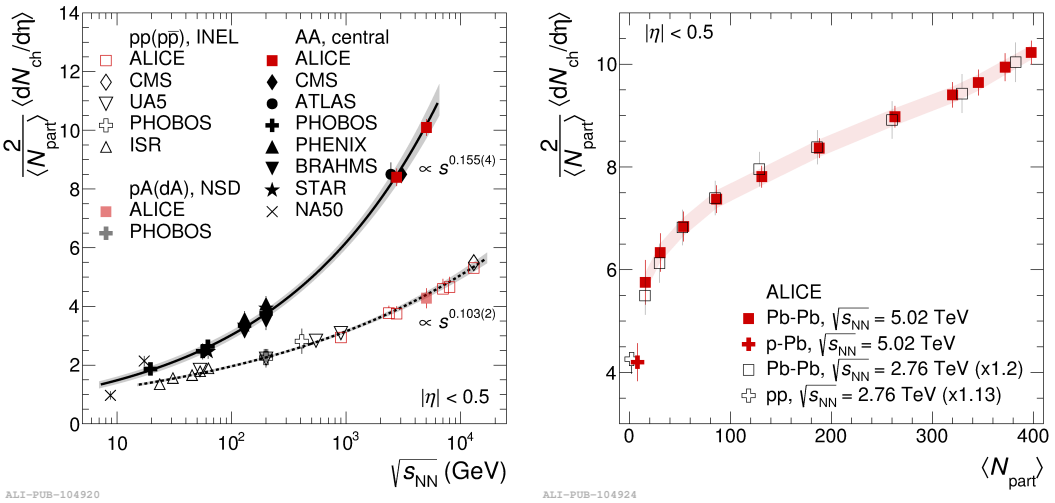

Figure 1.6: (Left) Charged-particle densities per number of participants pair at mid-rapidity ($|y| < 0.5$) in different collision systems and center of mass energies. (Right) Charged-particle densities per number of participants pair at mid-rapidity in pp, p–Pb and Pb–Pb collisions at $\sqrt{s_{\mathrm{NN}}}$ = 2.76 TeV, 5.02 TeV as a function of number of participants $\langle N_{\mathrm{part}} \rangle$ [47].

1.5.1 Charged-particle multiplicity

Charged-particle multiplicity is defined as the number of charged particles produced in a collision event. Depending on the energy density of the collision, the partonic scatterings at the pre-equilibrium stage become the deciding parameter for the multiplicity of the event. In a way, charged-particle multiplicity becomes a proxy for the energy density of the collision. This can be estimated from the rapidity or pseudo-rapidity[3] distribution

[3] In the massless limit, rapidity can be replaced with pseudo-rapidity defined in terms of the particle polar angle as $\eta = -\ln \tan \frac{\theta}{2}$. While pseudo-rapidity measurement does not require any information about the particle, rapidity requires the knowledge of the particle's mass.

of charged-particles. The left panel of Figure 1.6 shows the pseudo-rapidity densities $\langle \mathrm{d}N_{\mathrm{ch}}/\mathrm{d}\eta \rangle$ at mid-rapidity scaled to per pair participating nucleons N_{part}[4] as a function of the center of mass energy for different collision systems. There is a visible difference in the trends between the systems, the pp and p–A and d–A systems with a smaller slope (b) from a power law fit of the form (as^b), while a much steeper slope seen for A–A systems. This signifies that, in addition to participating nucleon-nucleon interactions, there is a significant portion of interactions leading to increased multiplicities in A–A systems, contrary to small systems where a saturation of the parton densities occurs leading to lower multiplicities. The right panel of Figure 1.6 reports the scaled pseudo-rapidity densities as a function of $\langle N_{\mathrm{part}} \rangle$ in pp, p–Pb, and Pb–Pb collisions measured by the ALICE collaboration [47]. The trend shows a quick increase in the charged-particle density from pp to p–Pb collisions and peripheral Pb–Pb collisions. After $\langle N_{\mathrm{part}} \rangle \approx 50$, the slope reduces and increases linearly with $\langle N_{\mathrm{part}} \rangle$ for Pb–Pb collisions. The drop in charged-particle multiplicity densities in small systems is explained by models that incorporate gluon saturation at the initial state that limits particle production.

1.5.2 Strangeness enhancement

In a QGP, the quarks lose their bare masses, restoring the chiral symmetry and reducing the threshold for the strangeness production. The increased gluon density generated in a QGP, favours strangeness production via gluon fusion processes ($\mathrm{g\bar{g}} \rightarrow \mathrm{s\bar{s}}$). This leads to a significant enhancement of strange quarks and, in turn, a relative increase in the strange hadron yield at the final state [48]. An interesting approach to understanding strangeness enhancement is via *canonical suppression* in small systems. Unlike heavy-ion systems, a small collision system cannot be treated with a grand canonical ensemble approach, forcing it to locally conserve the conservation of strangeness. In a larger system, strangeness conservation is not limited to nearby points but can be anywhere in the produced medium. In this way, the enhancement of strangeness can be considered a removal of canonical suppression.

Measurements at RHIC [49] and LHC [50, 51] confirmed the effect of strangeness enhancement. Results from high multiplicity pp collisions by ALICE also show similar effects hinting at the possible formation of QGP droplets in these systems, which are in tandem with results from p–Pb and Pb–Pb collisions [45]. These results are presented in Figure 1.7 show the ratios of strange hadrons ($2\mathrm{K}^0_{\mathrm{s}}$, $\Lambda + \bar{\Lambda}$, $\Xi^- + \bar{\Xi}^+$, $\Omega^- + \bar{\Omega}^+$) to pions ($\pi^+ + \pi^-$) yields for a given multiplicity interval in pp, p–Pb, and Pb–Pb collisions at mid-rapidity. The $\Omega^-(\mathrm{sss})$ baryon shows a faster rise (by a factor of 5) with respect to multiplicity, which can be seen to decrease with the decreasing strangeness content among the hadrons.

[4] This scaling accounts for different collision systems.

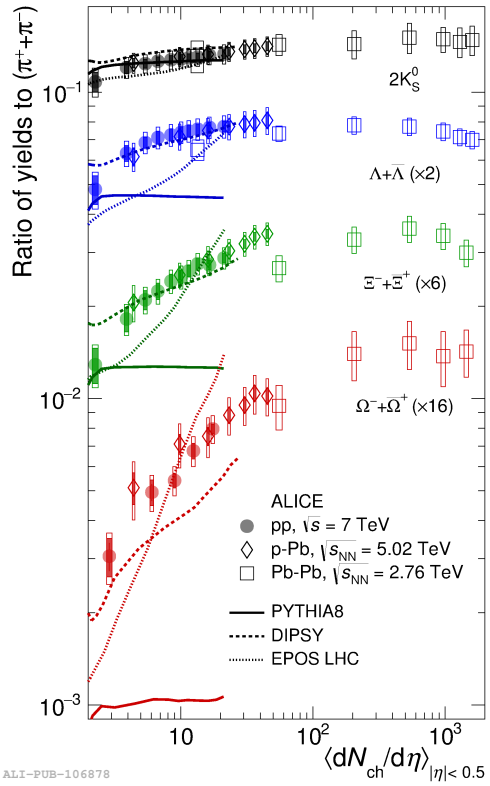

Figure 1.7: Relative yields of strange hadrons to pions ($\pi^+ + \pi^-$) as a function of charged-particle multiplicity density at mid-rapidity in pp, p–Pb, and Pb–Pb collisions at $\sqrt{s}$ = 7 TeV, $\sqrt{s_{\rm NN}}$ = 5.02 and $\sqrt{s_{\rm NN}}$ = 2.76 TeV, respectively [45].

1.5.3 Jet quenching

Jets are collimated beams of hadrons originating from hard scattered partons. The general jet topology at leading order leads to a back-to-back topology, often modified in the presence of a QGP. The modification is reflected in the energy spectrum of the jet, which is modified due to in-medium energy loss in the form of gluon radiation. This energy loss phenomenon is known as *jet-quenching*, measured by comparing yields of identified particles in heavy-ion and pp systems. This is quantified by the *nuclear modification factor* $R_{\rm AA}$, defined as

$$R_{\rm AA}(p_{\rm T}) = \frac{1}{\langle N_{\rm coll} \rangle} \frac{{\rm d}^2 N_{\rm AA}/{\rm d}p_{\rm T}{\rm d}y}{{\rm d}^2 N_{\rm pp}/{\rm d}p_{\rm T}{\rm d}y} \tag{1.8}$$

where the numerator represents hadron yields scaled to the number of binary collisions $\langle N_{\rm coll} \rangle$ in the A–A system. The $\langle N_{\rm coll} \rangle$ is determined from a geometric interpretation of the

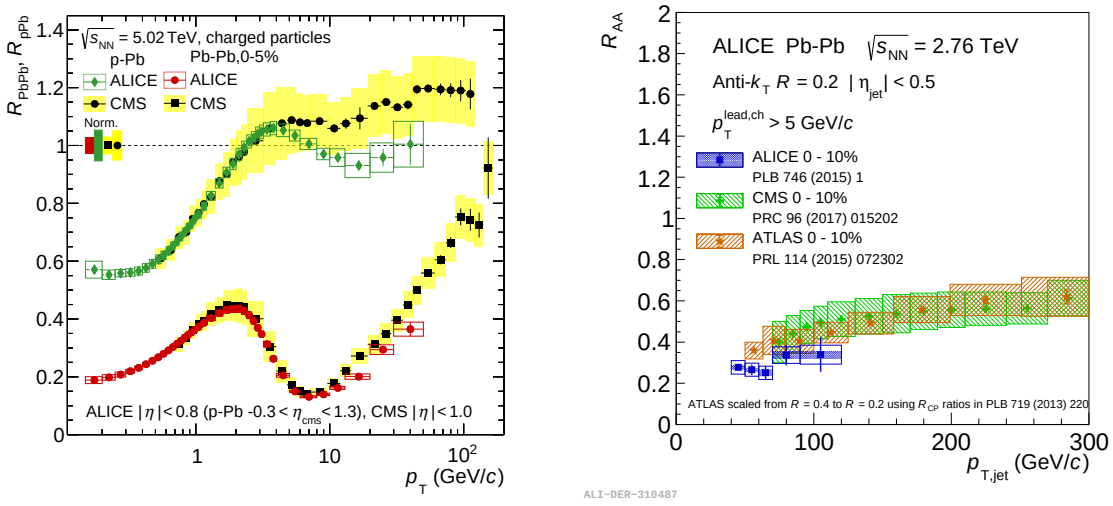

Figure 1.8: (Left) Nuclear modification factor as a function of p_T for charged-particles in p–Pb and central Pb–Pb collisions at $\sqrt{s_{NN}}$ = 5.02 TeV by the ALICE [52] and CMS collaboration [53, 54]. (Right) Nuclear modification factor as a function of p_T for charged-jets by the ALICE collaboration [55], compared to inclusive jets from ATLAS [56] and CMS collaboration [57] in central Pb–Pb collisions at $\sqrt{s_{NN}}$ = 2.76 TeV.

A–A collision by semi-classical collision models such as the Glauber model [58, 59]. The denominator is the hadron yield measured in pp collisions. R_{AA} is expected to be unity where no significant modifications are expected in the produced momentum distribution of the hadrons. In p–Pb collisions, effects of *cold nuclear matter effects* can be noticed, causing a deviation from unity, while in high energy heavy-ion systems, the presence of QGP can lead to significant modifications.

The left panel of Figure 1.8 shows the R_{AA} measurements from ALICE [52] and CMS collaboration [53, 54] in central Pb–Pb and p–Pb collisions at $\sqrt{s_{NN}}$ = 5.02 TeV. At high p_T ($p_T > 3$ GeV/c), the R_{AA} of charged-particles is significantly suppressed for Pb–Pb collisions as a consequence of in-medium energy loss, while being close to unity for p–Pb systems within 1.5σ between the two measurements. At very high momentum ranges, the charged-particle R_{AA} closes to unity. This is not observed for jets, shown on the right panel of Figure 1.8, where the R_{AA} of charged-jets in central Pb–Pb collisions at $\sqrt{s_{NN}}$ = 2.76 TeV [55] are compared to inclusive jets measured by the CMS [57] and ATLAS [56] collaboration. The increasing trend with p_T could arise due to modification of the fragmentation function in Pb–Pb collisions.

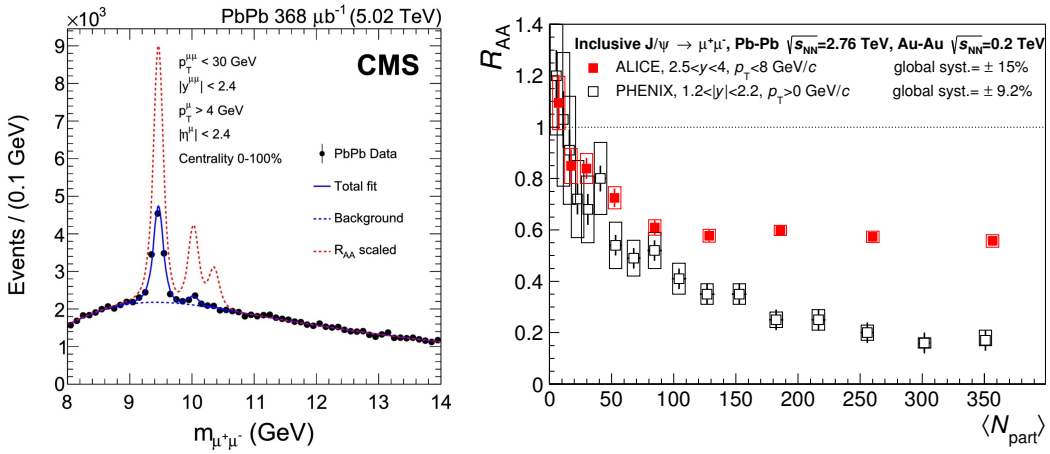

Figure 1.9: (Left) Invariant mass distribution of muon pairs in Pb–Pb collisions at $\sqrt{s_{\mathrm{NN}}}$ = 5.02 TeV from the CMS experiment [60]. (Right) R_{AA} as a function of $\langle N_{\mathrm{part}} \rangle$ of J/ψ reconstructed in the $\mu^+\mu^-$ channel measured by the ALICE [61] and PHENIX [62] experiments in Pb–Pb collisions at $\sqrt{s_{\mathrm{NN}}}$ = 2.76 TeV and Au–Au collisions at $\sqrt{s_{\mathrm{NN}}}$ = 200 GeV, respectively.

1.5.4 Quarkonia suppression

Quarkonia are bound states of charm or beauty ($c\bar{c}$, $b\bar{b}$) that are considered to be good probes of QGP formation. First coined by Matsui and Satz [63], quarkonia suppression refers to a sequential melting of the bound states in a hot and dense system of quarks and gluons. The melting can be understood from the Cornell potential, discussed in Section 1.2; the finite temperature reduces the string tension (κ) between the $q\bar{q}$ pair. At a critical temperature T_c, the linear term of the potential (Equation 1.4) vanishes as $\kappa = 0$. With the remaining term, the colour charges experience a screening effect, which prevents a $q\bar{q}$ formation. With a similar analogy to electrodynamics, at a distance beyond a certain *Debye* screening length[5], the $q\bar{q}$ pairs do not survive in the QGP. This combined effect of a high-temperature medium and screening of colour charges leads to a depletion of the quarkonia yields in heavy-ion collisions. The melting of the bound states is dependent on their binding energies, which allows for a sequential melting for the different quarkonia states (excited states melt earlier due to their lower binding energies). This dissociated form can act as a thermometer of the QGP, which can provide significant information on the thermal properties of the medium.

Quarkonia suppression was originally observed for J/ψ in the di-muon decay channel by SPS in Pb–Pb collisions at $\sqrt{s_{\mathrm{NN}}}$ = 17.4 GeV [64] and at RHIC in Au–Au collisions at

[5] Debye length represents a characteristic distance over which the electric fields and the charges are screened in a plasma, which amounts to $1/e$ of the electric field value.

$\sqrt{s_{\mathrm{NN}}}$ = 200 GeV [65], and later confirmed at the LHC in Pb–Pb collisions. The left panel of Figure 1.9 shows the invariant mass distribution of $\mu^+\mu^-$ pairs in Pb–Pb collisions at $\sqrt{s_{\mathrm{NN}}}$ = 5.02 TeV, measured by the CMS collaboration [60]. The highlight of this result is the bottomonia states $\Upsilon(1S)$, $\Upsilon(2S)$ and $\Upsilon(3S)$ at their rest masses with their raw yield extraction fits (in solid blue lines) and the respective yields without a QGP medium obtained by scaling the R_{AA} values (in dashed red lines). The $\Upsilon(1S)$ states show a 50% depletion and complete disappearance of the higher excited states. This result is a testament to the pronounced colour screening effects at play in the medium and the sequential melting of the quarkonia states. The right panel reports the R_{AA} as a function of $\langle N_{\mathrm{part}} \rangle$ of J/ψ mesons in Au–Au, and Pb–Pb collisions measured by PHENIX [62] and ALICE collaboration [61] at $\sqrt{s_{\mathrm{NN}}}$ = 200 GeV and 2.76 TeV, respectively. The J/ψ mesons at RHIC are seen to be suppressed more than at the LHC for the same $\langle N_{\mathrm{part}} \rangle$, which is counter-intuitive to the effects of color screening. This is possible because of an underlying regeneration process coming from statistical recombination of c$\bar{\mathrm{c}}$ pairs coming from unrelated hard scatterings that counterbalance the screening effects [66–68]. At higher center of mass energies, these regeneration effects are prevalent due to a larger occupation number of c$\bar{\mathrm{c}}$ pairs. The regeneration process destroys the interpretation of the sequential dissociation of charmonia states as a medium thermometer.

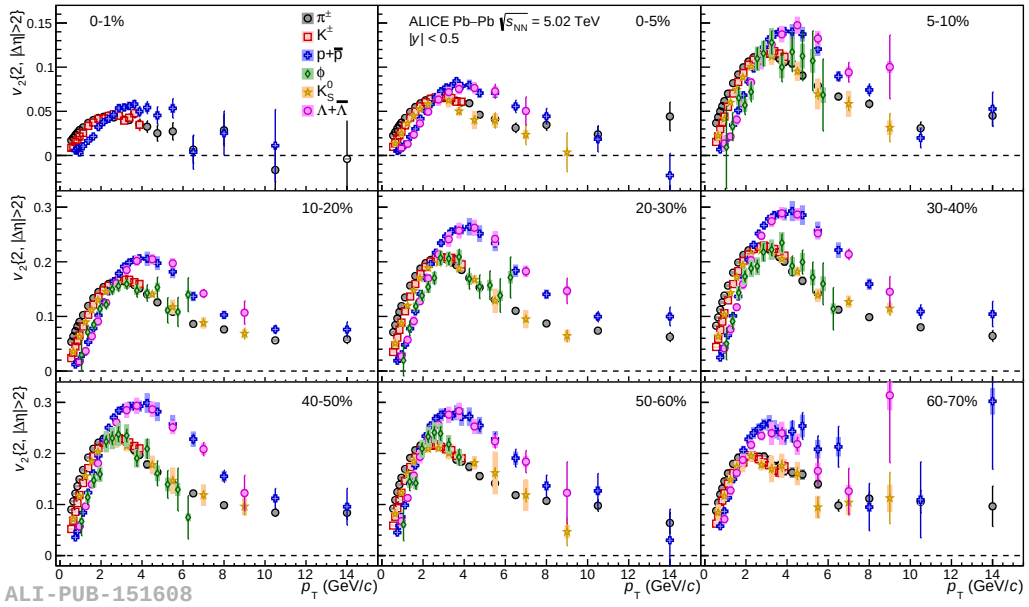

Figure 1.10: Elliptic flow coefficients of different charged hadron species as a function of p_{T} for different centralities in Pb–Pb collisions at $\sqrt{s_{\mathrm{NN}}}$ = 5.02 TeV [69].

1.5.5 Anisotropic flow

The momentum distribution of the final-state particles is sensitive to the collision geometry of the two nuclei. Collisions can be classified based on their overlap region, quantified by the impact parameter of the collision. Experimentally, event centrality obtained from measured charged-particle multiplicities is a proxy for the collision impact parameter. For a non-central collision, an initial spatial anisotropy in the collision geometry gets converted to a final state momentum anisotropy. This is created by the pressure gradients generated from the anisotropic collective emission of partons from the collision region, which is reflected in the azimuthal angle (φ) of the emitted hadrons at the final state. The azimuthal distribution can be decomposed via a Fourier expansion [70] of the form

$$E\frac{\mathrm{d}^3N}{\mathrm{d}p^3} = \frac{1}{2\pi}\frac{\mathrm{d}^2N}{p_\mathrm{T}\mathrm{d}p_\mathrm{T}\mathrm{d}y}\left(1 + 2\sum_{n=1}^{\infty} v_n(p_\mathrm{T})\cos\left[n(\varphi - \Psi_n)\right]\right). \tag{1.9}$$

Here, n denotes the harmonic order, and Ψ_n is called the n^{th} harmonic symmetry plane of the collision. The Fourier coefficients, also called flow coefficients (v_n), are defined as

$$v_n(p_\mathrm{T}) = \langle\cos\left[n(\varphi - \Psi_n)\right]\rangle \tag{1.10}$$

The dominant flow component comes from the second harmonic coefficient, known as the *elliptic flow*. Non-zero elliptic flow arises directly from the collective anisotropic expansion of the partons, which measures the degree of collectivity in the system. Figure 1.10 shows the elliptic flow of identified hadrons as a function of p_T from the ALICE collaboration for several centrality classes [69]. A rise in v_2 is seen from most central (0-1%) to mid-central classes (30-40%) as the collision geometry starts becoming less and less isotropic. With increasing centrality (more peripheral), the pressure gradients are not strong enough to generate a stronger elliptic flow due to smaller overlap regions. Among the hadrons species, we also see a mass ordering at $p_\mathrm{T} < 3$ GeV/c that is a direct consequence of the hydrodynamics of the collective expansion of the system. At intermediate p_T ($3 < p_\mathrm{T} < 8$ GeV/c), the rules of constituent quark scaling take over, and we see the baryon v_2 to be higher than that of mesons. This can be explained by the models invoking quark coalescence at hadronization. High p_T region is reserved mostly for hard scattered partons that get to traverse the collective medium expansion and lose energy via fragmentation or multiple scattering.

1.6 Open heavy-flavours

Heavy-flavours, viz., charm and beauty (c, b), as their name suggests, are heavy, with masses $m_c = 1.27 \pm 0.02$ GeV/c^2 and $m_b = 4.18^{+0.03}_{-0.02}$ GeV/c^2 respectively [20], are excellent probes of the QGP. Due to their large masses, they are typically produced in the initial hard scatterings at time scales ($\tau \propto 1/Q$) shorter than the QGP formation time. This allows them to freely traverse the entire evolution and interact with partons in the plasma. These quarks hadronize with a light quark, forming an open heavy-flavour hadron, which can be experimentally reconstructed to extract the relevant information of the medium. The participation of heavy-flavours in the QGP help disentangle the induced effects by the medium. However, studying the production of the heavy-flavours is favourable in circumstances where external effects do not modify its dynamics. In this thesis, measurements pertaining to heavy-flavour production in pp collisions at $\sqrt{s} = 13$ TeV are drawn out, with differential studies in event properties, which will be discussed in detail in Chapter 4.

1.6.1 Heavy-flavours in pp collisions

Due to their early production via hard scatterings, the production of heavy-flavour lies in the perturbative QCD (pQCD) regime, valid at large momentum transfer (Q^2) between the partons of the colliding protons where the strong coupling constant (α_s) becomes less than unity, allowing the production cross-section to become a geometric sum in α_s. Measuring heavy quark production in pp collisions is an ideal tool to probe the pQCD regime and provide stringent tests to theoretical calculations. The production cross-section of heavy-flavour hadrons in a pQCD approach is given by the factorization theorem [71]

$$\sigma_{pp\to H_Q+X} = \sum_{i,j=q,\bar{q},g} f_1(x_i;Q_i^2) \otimes f_2(x_j;Q_j^2) \otimes \sigma^{hard}_{ij\to Q\bar{Q}} \otimes D(z_Q;Q^2). \tag{1.11}$$

$f_{1,2}(x_i;Q_i^2)$ is the *parton distribution function* (PDF), describing the number density of partons as a function of the fraction of momentum of the proton x_i carried by the parton [72, 73], and $D(z_Q;Q^2)$ is the *fragmentation function* (FF), which define the probability of a heavy quark hadronizing into a hadron H_Q carrying z_Q of the initial parton momentum [74]. Both PDF and FF values depend on the virtuality (Q^2) of the processes, which is linked to the factorization scale (μ_F). PDFs are generally obtained via deep inelastic scattering measurements [75], which are parametrized for a fixed energy scale (Q_0^2), evolved via the Dokshitzer-Gribov-Lipatov-Altarelli-Parisi (DGLAP) equations for different virtualies [25]. The FF is obtained from the hadron production measurements in e^+e^- collisions [76] (assuming a universality of FF among collision systems). The perturbative part of the factorization theorem is given by the hard scattering cross-section

($\sigma^{\text{hard}}_{ij\to \text{Q}\bar{\text{Q}}}$), which is calculated as a perturbative series in α_s, which is dependent on the energy scale. The factorization and normalization scales are usually set to the same order of the momentum transfer of the process. Theoretically, pQCD calculations handle the heavy quark production cross-sections from FONLL ("Fixed Order + Next-to-Leading Log") [77, 78] and GM-VFNS ("General Mass Variable Flavour Number Scheme") [79, 80] that can perform up to next-to-leading terms $O(\alpha_s^3)$ and at fixed order with the next-to-leading-log resummation. These calculations have also been extended to next-to-next-to-leading order (NNLO) terms with QCD radiative corrections [81].

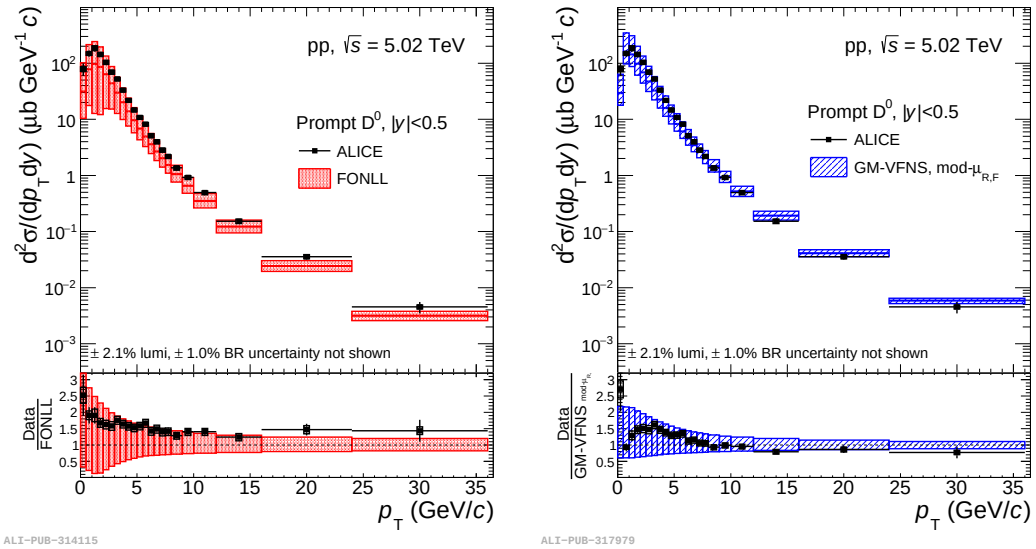

Figure 1.11: p_T-differential cross-section of prompt D^0 mesons in pp collisions at $\sqrt{s}$ = 5.02 TeV measured by ALICE [82], compared to pQCD calculations from FONLL [78] (left) and GM-VFNS [80] (right).

The pQCD calculations by FONLL and GM-VFNS are tested with measurements of open heavy-flavour cross-section measurements by ALICE [82], reported in Figure 1.11 for the *prompt*[6] D^0-meson ($c\bar{u}$) in pp collisions at $\sqrt{s}$ = 5.02 TeV. The mass values for the charm quark are taken as m_c = 1.5 GeV/c^2 in FONLL and m_c = 1.3 GeV/c^2 in GM-VFNS. The PDF, FF and uncertainties in quark masses introduce the uncertainty bands in the predictions by the two calculations. Both predictions describe the D^0 cross-section, with FONLL calculations lying on the upper edge of the uncertainties. In contrast to the meson sector, the heavy-flavour baryon measurements differ from the factorization approach predictions. The left panel of Figure 1.12 show the predictions from GM-VFNS [80] deviating from the Λ_c^+ baryon production cross-section measurements in pp collisions at $\sqrt{s}$ = 5.02 TeV by ALICE [83]. The FFs in this calculation are taken from the OPAL

[6] prompt charm quarks are produced directly from hard scattering and not from decays of beauty quarks

data fits for e^+e^- collisions at $\sqrt{s}$ = 10 GeV [84] and Belle experiment at $\sqrt{s}$ = 10.52 GeV [85]. Predictions from the POWHEG framework, coupled with the PYTHIA6 event generator [86, 87], are also unable to reproduce the measurements. The right panel of Figure 1.12 presents the ALICE measurements [83] for p_T-differential charm baryon-to-meson Λ_c^+/D^0 ratios, along with an assortment of theoretical models that use fragmentation functions based on e^+e^- experiments [80, 86, 88, 89]. The predictions fail to describe the enhancement seen from the ratios, which hint at a possible breaking in the universality of charm fragmentation in different collision systems.

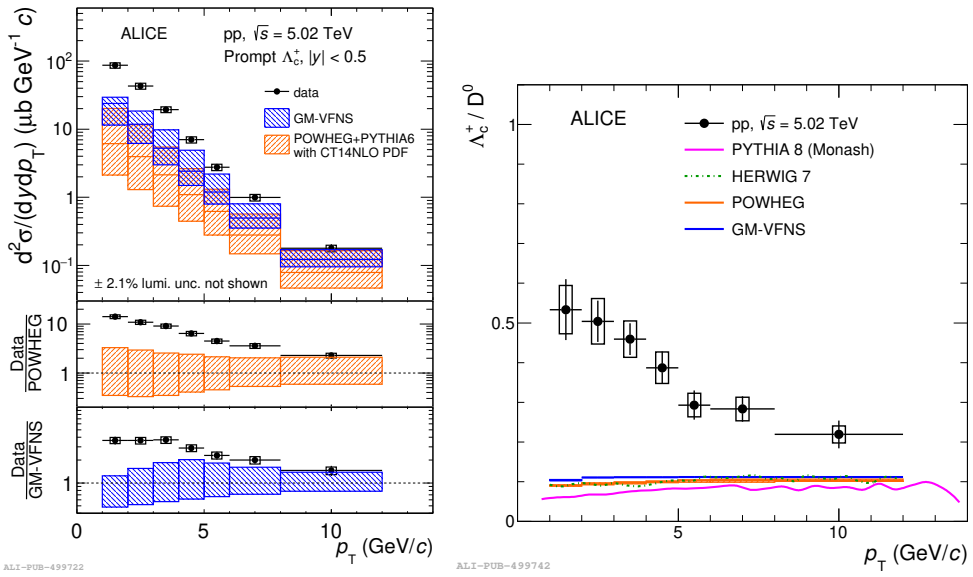

Figure 1.12: (Left) p_T-differential cross-section of Λ_c^+ baryons in pp collisions at $\sqrt{s}$ = 5.02 TeV measured by ALICE [83], compared to pQCD calculations from GM-VFNS [80], and POWHEG [86] with CT14NLO PDFs [73]. (Right) Ratio of charm baryon-over-meson Λ_c^+/D^0 as a function of p_T in pp collisions at $\sqrt{s}$ = 5.02 TeV measured by ALICE, compared to pQCD calculations and Monte Carlo model predictions [80, 86, 88, 89].

1.7 Light (anti-)nuclei production

Light (anti-)nuclei are bound states or clusters of nucleons, with typical energies of O(2 MeV) [90, 91]. They are produced in collision experiments during the hadronic evolution, where the temperatures are of O(100 MeV). Their survival in the hot evolving hadron gas is a mystery and remains an open problem among physicists. Theoretical models attempt to describe how light (anti-)nuclei and hyper (anti-)nuclei are produced. Unlike heavy-flavours, the interactions between the nucleons are governed by non-perturbative effects, generally occurring at lower energies than the QCD scale, where the QCD la-

grangian cannot be solved analytically [92]. These short-range NN interactions are key to understanding the formation of light nuclei [93, 94]. Phenomenological approaches taken by the statistical hadronization model or the coalescence model provide alternate description of their production mechanisms.

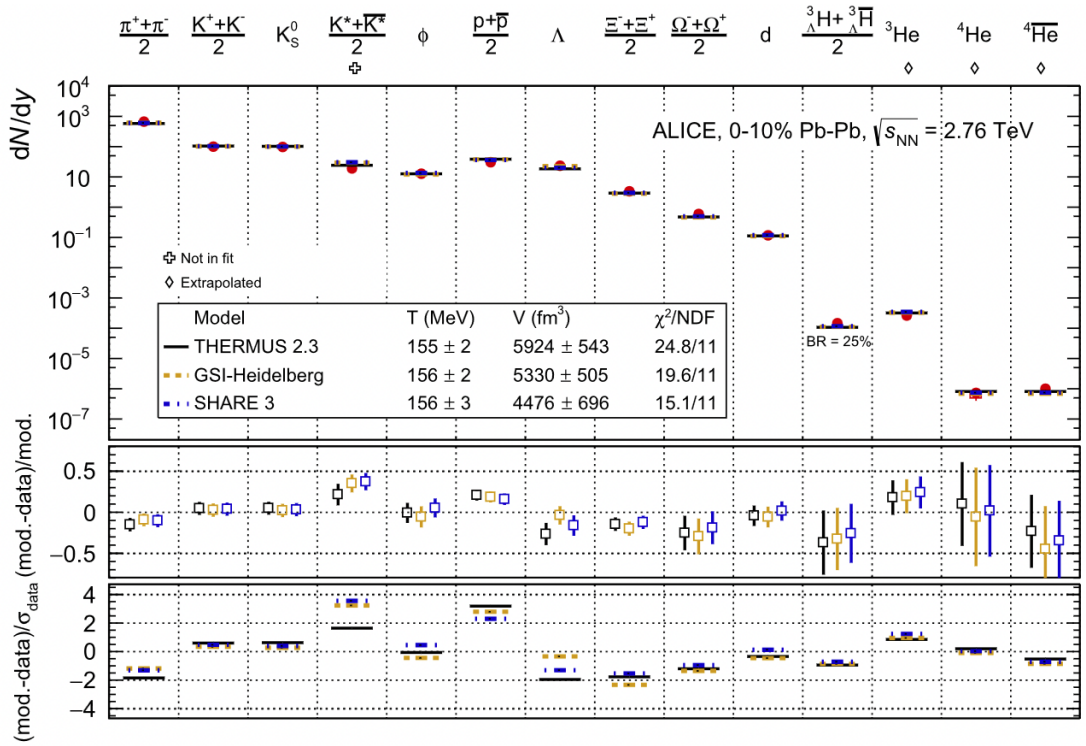

Figure 1.13: Thermal model fits of different hadron species in central Pb–Pb collisions at $\sqrt{s_{NN}}$ = 2.76 TeV [95], with implementations from THERMUS [96], GSI-Heidelberg model [97], and SHARE [98].

1.7.1 Statistical Hadronization Model

The *Statistical Hadronization Model* (SHM) or the Thermal Model [97, 99] is a complete framework that generates the relative abundances of hadrons based on the chemical freeze-out temperature (T_c). SHM works with an ensemble approach, which represents the collision system. In heavy-ion systems, SHM assumes a grand-canonical ensemble, while for a small system, invoking local conservation laws allows a canonical ensemble approach. In general, the grand canonical partition function at thermal equilibrium would be

$$Z(T,V,\mu) = \mathrm{Tr}\left[\exp\left(-\frac{H+\sum_i \mu_i \mathcal{Q}_i}{T}\right)\right], \quad \text{with } \mu = \sum_i \mu_i \mathcal{Q}_i, \tag{1.12}$$

where T, V, μ are the temperature, volume, and chemical potential of the system with a Hamiltonian H. Parameters $\hat{Q}_i$ and μ_i are the conserved charges and chemical potentials, respectively, of particle species i. The chemical potential can be divided into individual components μ_s, μ_B, and $\mu_{\hat{Q}}$, where μ_s and $\mu_{\hat{Q}}$ are fixed due to net strangeness and isospin symmetry. The baryon chemical potential μ_B is decided by the collision energy, and the volume V is cancelled out when the relative yields are taken, leaving temperature T as the only free parameter. For absolute yields, the temperature T and volume V are the free parameters in the model, obtained from fitting experimental measurements or via Lattice QCD calculations. Figure 1.13 reports different thermal model fits to different charged and neutral hadrons, light, and hyper-nuclei species in central Pb–Pb collisions at $\sqrt{s_{NN}} = 2.76$ TeV [95]. For smaller systems such as pp or e^+e^-, the use of canonical statistical models (CSM) is preferred due to local quantum number conservation. This leads to suppression of particle yields, also known as canonical suppression [100, 101].

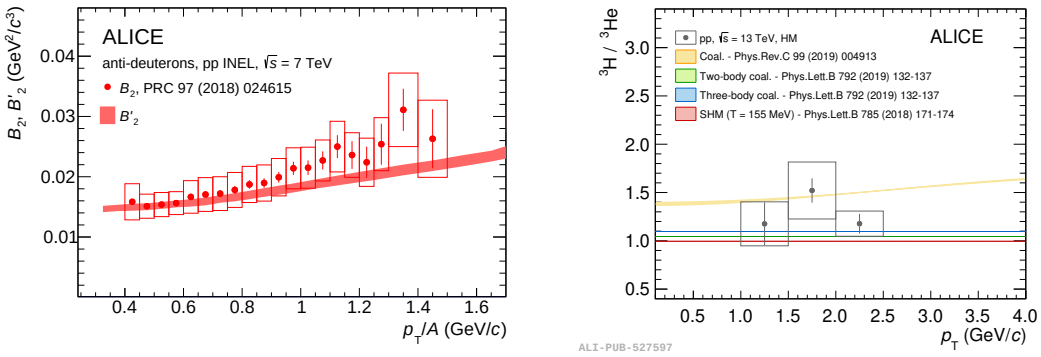

Figure 1.14: (Left) Measured coalescence parameter B_2 of anti-deuterons as a function of p_T in high multiplicity pp collisions at $\sqrt{s} = 7$ TeV, compared to a single parameter coalescence model [102]. (Right) The ratio between the p_T spectra of triton and helion (^{3}H/^{3}He) in high multiplicity pp collisions at $\sqrt{s} = 13$ TeV compared with the prediction of thermal and coalescence models [103].

1.7.2 Coalescence model

Coalescence models are based on the hypothesis that nucleons in close proximity in phase space come together, bind, and form a cluster. The origins of this model are often based on a very simple approach involving momentum correlations between the nucleons, where (anti-)nucleons close momentum space and coalesce together to form light (anti-)nuclei. This version of coalescence ignores the spatio-temporal coordinates of the nucleons having a single parameter dependence, an assumption that may work in small system collisions [104, 105]. However, in heavy-ion systems where the system size is much larger than the dimensions of the produced nuclei, the space-time effects cannot be

ignored. A single parameter coalescence model fails to describe the light nuclei production versus system size or charged-particle multiplicity. This is corrected by considering the overlap between the phase-space of the nucleons and the nuclei distribution. As a simple approach, the nuclei distribution can be of a *box* form, where a fixed condition for relative position and momentum is used, often referred to as *box* coalescence [106–108]. Modern coalescence methods invoke a physical picture of the nuclei by taking a wave function approach and building a Wigner probability distribution for the nuclei [109–111]. The left panel of Figure 1.14 shows the measured coalescence parameter (B_2) as a function p_{T} for anti-deuterons in pp collisions at $\sqrt{s} = 7$ TeV by the ALICE collaboration [102, 103]. The coalescence parameter quantifies the probability of the nucleons to coalesce into a light nuclei, which depends on the nucleon correlation size or volume. The results show that B_2 has an increasing dependence with the scaled deuteron p_{T}, showing a positive correlation between nucleon momentum and the deuteron formation probability via coalescence. More details on the coalescence parameter and its calculation are put forward in Chapter 5. The results are compared with the predictions from a single parameter coalescence model, which describes the increasing trend of B_2 with scaled deuteron transverse momentum. On the right panel, the triton to helium-3 ratios ($^3\mathrm{H}/^3\mathrm{He}$) as a function of p_{T} are reported for high multiplicity pp collisions at $\sqrt{s} = 13$ TeV, compared with different versions of coalescence model and the statistical hadronization model.

1.8 Thesis motivation

The goal of this work is to probe the different regimes of strong interactions with two different approaches of study. The first approach touches on the pQCD regime, with experimental data analysis of measuring the heavy quark production in pp collisions at the LHC as a function of event variables. The second aspect falls in a non-perturbative regime aimed at understanding the production mechanism of light nuclei via the coalescence of nucleons in collision experiments.

The first objective of this work is to perform differential studies of heavy-flavour production, in particular, charm production in pp collisions, by means of event variables/classifiers that quantify the level of 'activity' of a collision event. In addition to testing pQCD calculations, variables such as event-multiplicity or -shapes enhance the understanding of heavy-flavour production with respect to the microscopic details of particle production in pp collisions. The production of charm in pp collisions is performed by measuring the D-meson yields and reconstructing them from their hadronic decay channels. Their production is studied as a function of charged-particle multiplicity in pp collisions at $\sqrt{s} =$ 13 TeV, which adds to the previous measurement at $\sqrt{s} = 7$ TeV. With improved statistics and more precise measurements, studying the D-meson production with multiplicity will inspect the role of multiparton interactions (MPI) and colour reconnection (CR) mechanisms in hadronization. The analysis is extended with transverse spherocity (the event

shape variable) will disentangle the hard and soft components of particle production in pp collisions, allowing the categorization of charm production in different event topologies while studying its interplay with multiplicity.

The second objective is based on the foundations and development of the coalescence model, circling around light nuclei production in collision experiments. The model is deployed as an afterburner in two distinct stages. A simple 'box' form is initially tested for deuteron, triton, and helium production in heavy-ion collisions at RHIC and LHC energies. Through an afterburner mode, the model is coupled to the AMPT event generator, allowing for a comparative measurement with deuterons production via kinetic processes such as pion catalysis. The next step involves improving the coalescence mechanism to a Wigner formalism inspired by the nuclei wave function. The intention is also to introduce a sense of realism through an emission source model for nucleons, with resonance effects that work in tandem with coalescence. This complete treatment allows for a reliable estimation of light nuclei production in collision experiments. Moreover, the framework can be extended onto femtoscopy calculations, and check the viability of coalescence as a primary production mechanism of light nuclei. This will lead to insight into the spatial extent of emission in the collisions with insight into nucleon-nucleon interactions.

The thesis is arranged in the following manner:

As discussed in this chapter, a brief introduction to the fundamentals of strong interactions is provided. A description of deconfinement and phase transition in QCD, leading to the formation of QGP in a heavy-ion collision, is put forward. Chapter 1 also introduces open-heavy flavours and light nuclei that encapsulate the topics of motivation of this thesis.

The details of the ALICE apparatus, with the description of the detectors relevant to experimental data analysis of open heavy-flavour production, are reported in Chapter 2. The techniques of track and vertex reconstruction are laid out, with the methods employed by the detectors for particle identification.

In Chapter 3, the Monte Carlo methods utilized in modern-day event generators are discussed. An assortment of event generators, such as PYTHIA8, AMPT, and SMASH, which are extensively used in the studies performed in this thesis, are discussed.

The study of charm production in pp collisions at $\sqrt{s}$ = 13 TeV, is drawn out in Chapter 4. Here, a detailed structure of the methodology of the two analyses is described, pointing out the specific selections, the analysis strategies to reconstruct the D-meson, the corrections, and systematic uncertainties. The results are presented with a comprehensive comparison with different model calculations.

Chapter 5 discusses the second motivation of the thesis, dealing with coalescence models for light nuclei formation. A well-rounded explanation of the development of the model is put forward. Tools used for femtoscopy studies are described before discussing the results from three unique studies related to the production and dynamics of light nuclei in

collision experiments.

Chapter 2

ALICE: A Large Ion Collider Experiment

A major aspect of this thesis is analyzing pp collision data collected by the ALICE detector during Run-2 of the LHC. The ALICE detector is specially designed to analyze and study the properties of QGP. This chapter describes the ALICE apparatus, the tools and methodology for vertex and track reconstruction, and the performance of the sub-detectors relevant to the analyses presented in this thesis.

2.1 The Large Hadron Collider

The Large Hadron Collider (LHC) supersedes the Large Electron Positron (LEP) collider [112], located at the European Organisation for Nuclear Research (CERN) near the border of France and Switzerland, next to the city of Geneva, Switzerland. The LHC is the world's largest particle accelerator, dug 50-175 meters underground. It is comprised of two superconducting rings housed in one cryostat with a circumference of 26.7 km that can accelerate proton and lead (Pb) beams up to $\sqrt{s}$ = 14 TeV with peak luminosity $\mathcal{L} = 10^{34}$ cm^{-2}s^{-1} and $\sqrt{s_{\rm NN}}$ = 5.52 TeV with peak luminosity $\mathcal{L} = 10^{27}$ cm^{-2}s^{-1}, respectively.

The LHC houses four mega detectors, which constitute the major experiments at CERN. Figure 2.1 shows different points and the sites where the experiments are located, where the ATLAS (A Toroidal LHC Apparatus [113]) at Point 1, and CMS (Compact Muon Solenoid [114]) at Point 5 are built for Higgs Physics and searches for physics beyond SM. These two experiments are designed to handle pp collisions with the highest interaction rates at the LHC. The LHCb (Large Hadron Collider beauty [115]) experiment is located at Point 8, which is designed to study the CP violation in the beauty sector and baryon asymmetry. At Point 2, the ALICE (A Large Ion Collider Experiment [44]) apparatus

is located, a special detector built for the purpose of studying heavy-ion collisions and its entailing hot and dense strongly interacting matter. The collider operation begins at LINAC2 (LINear ACcelerator 2 [116]), right after the electrons are *stripped off* off hydrogen atoms such that the protons remains. The LINAC2 accelerates the proton beams up to $\approx$ 50 MeV and then injected into the PSB (Proton Synchrotron Booster [117]), followed by the PS (Proton Synchrotron [118]) that further accelerates up to $\sim$ 25 GeV. Prior to the LHC, the protons are accelerated in the SPS (Super Proton Synchrotron) till an energy of 450 GeV. The Pb ions are initially accelerated through the LINAC3 (LINear ACcelerator 3 [119]), which reaches an energy of $\approx$ 4.2 MeV/nucleon. This is fed into the LEIR (Low Energy Ion Ring [120]), reaching an energy of $\sim$ 72 MeV/nucleon, and injected into the PS ($\approx$ 5.9 GeV/nucleon) and through the SPS ($\approx$ 177 GeV/nucleon) and finally into the LHC.

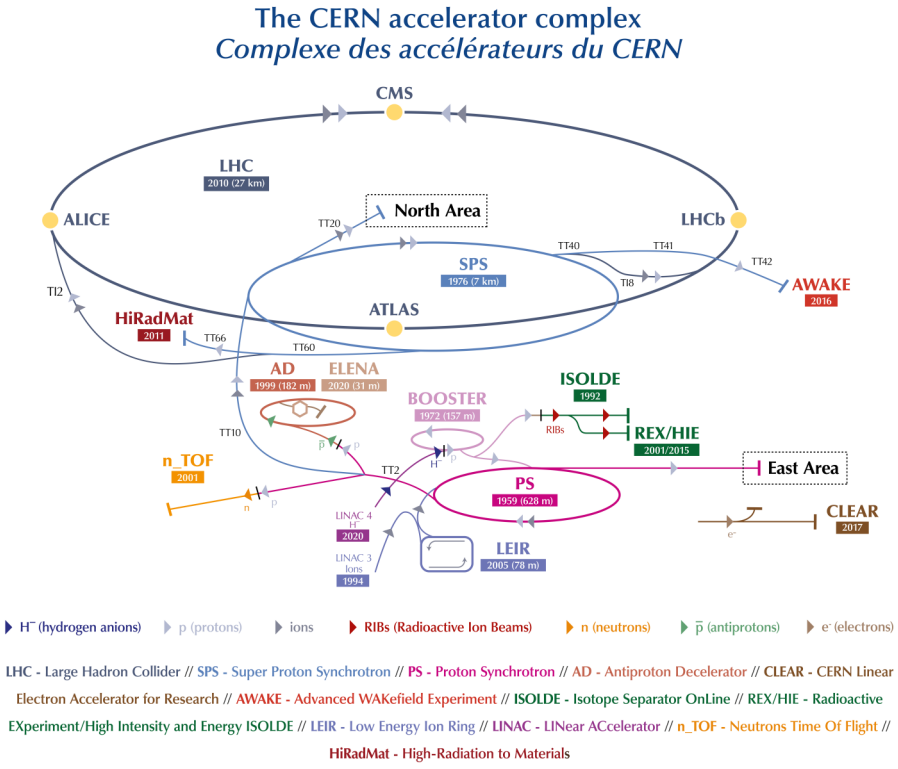

Figure 2.1: An illustration of the CERN accelerator complex depicting all the facilities and the injection systems. Image taken from [121].

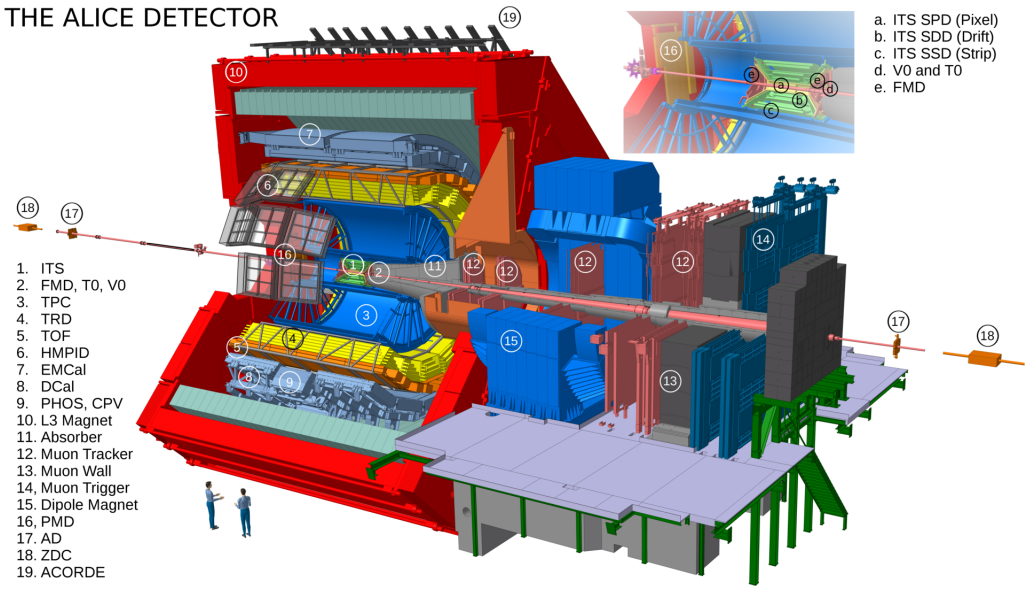

Figure 2.2: Schematic of the ALICE detector. Image taken from ALICE Figure Repository [122].

2.2 The ALICE Detector

The ALICE apparatus is built to study the physics of the QCD phase diagram and the produced strongly interacting matter in ultra-relativistic hadronic and heavy-ion collisions [44]. The detector is designed to capture charged-particles up to very low momentum while handling very large multiplicities. The charged-particle multiplicities in a typical Pb–Pb event can reach upto $\mathrm{d}N_{\mathrm{ch}}/\mathrm{d}\eta = 8000$ at mid-rapidity. The detectors are designed with high granularities and low material budget to cover a wide range of particle momentum and excellent particle identification capabilities.

Figure 2.2 shows a full schematic of the Run-2 ALICE detector [122]. It is 26 meters long, 16 meters high, and 16 meters wide, weighing more than 10000 tons. Based on acceptance, the detector is divided into the central barrel ($|\eta| < 0.9$) and the muon spectrometer ($-4.0 < \eta < -2.4$). The central barrel is designed with a cylindrical geometry, embedded in a large solenoidal magnet (L3), which generates a maximum magnetic field of B = 0.5 T. The nominal interaction point is surrounded by the Inner Tracking System (ITS), followed by the Time Projection Chamber (TPC), the Transition Radiation Detector (TRD), and the Time-of-Flight (TOF) detector. Other detectors that cover either partly or in segments of the entire ALICE acceptance are the High Momentum Particle Identification Detector (HMPID), a Ring Imaging Cherenkov detector, and two electromagnetic calorimeters, PHOS and EMCal. In the muon spectrometer arm, fourteen layers of Resistive Plate Chambers (RPC) trigger events with muons present. Other peripherals in forward and

backward rapidities are the V0, T0, FMD, PMD, and ZDC, designed to collect and interpret event properties. A series of scintillators are placed outside the L3 solenoid to trigger the entry of cosmic rays for removal. The experimental analyses covered in this thesis are performed using detector information from ITS, TPC, TOF, and V0 detectors, which are described in detail in the following sections.

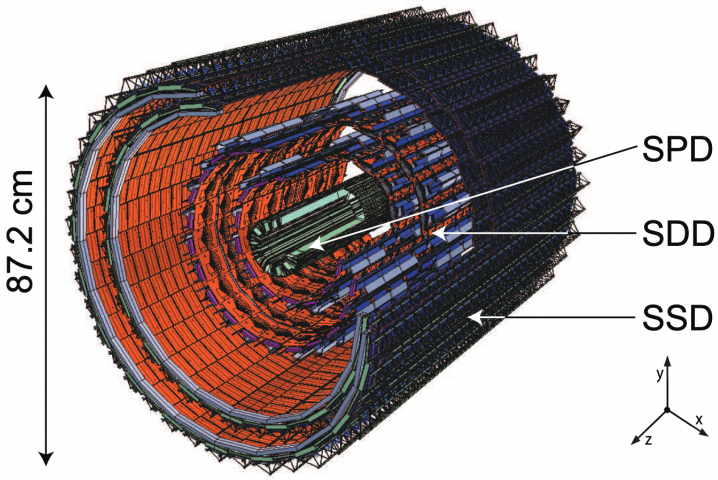

Figure 2.3: The schematic of the ITS detector and its different layers. Figure taken from [123].

2.2.1 Inner Tracking System

The Inner Tracking System is a silicon detector placed closest to the interaction point [123]. It is comprised of 3 individual detectors, each with 2 having layers for tracking purposes. The 3 detectors collectively operate for track and secondary vertex reconstruction near the interaction point while handling large charged-particle multiplicities. Each detector's technologies differ; as shown in Figure 2.3 the first two layers make the *Silicon Pixel Detector* (SPD). It is based on a five-cell bi-dimensional sensors matrix formed by 256×160 pixels, of dimensions 50 μm$(r\phi)$ × 425 μm(z). Four matrices are mounted together, two in the longitudinal direction, and two are attached head-to-head along the z-direction on a carbon fiber support that aids cooling. This contraption is known as a *stave*, which is attached in the ten azimuthal sectors having two staves each. The two layers of the SPD are located 3.9 cm and 7.9 cm from the beam pipe, with acceptances $|\eta| < 2$ and $|\eta| < 1.4$, respectively. The pixel matrices provide a spatial resolution of $\sim$ 12 μm in the radial direction and $\sim$ 100 μm along z. The *Silicon Drift Detector* (SDD) forms the next two layers after the SPD, comprising of two drift regions divided by a central cathode of a 500 V/cm electric field. Each module is a 72.5 × 75.3 mm sized silicon sensor mounted on linear supports called *ladders*. The two layers are placed at 15 cm and 24 cm from the

Layer	r (cm)	$\pm z$ (cm)	Material Budget ($\%X_0$)	Active area per module $r\phi \times z$ (mm^2)	Resolution $r\phi \times z$ ($\mu\mathrm{m}^2$)
SPD	3.9	14.1	1.14	12.8×70.7	12×100
SPD	7.6	14.1	1.14	12.8×70.7	12×100
SDD	15.0	22.2	1.13	70.17×75.26	35×25
SDD	23.9	29.7	1.26	70.17×75.26	35×25
SSD	38.0	43.1	0.83	73×40	20×830
SSD	43.0	48.9	0.86	73×40	20×830

Table 2.1: Details of the ITS and properties of each layer.

beam pipe, with both within acceptance $|\eta| < 0.9$. The first layer consists of 14 ladders with six modules each, while the second layer has 22 ladders with 8 modules, providing a spatial resolution of ~ 35 μm in the radial direction and ~ 25 μm along z. The final two layers comprise the *Silicon Strip Detector* located 38 and 46 cm from the beam pipe with pseudo-rapidity acceptance of $|\eta| < 0.9$. The modules are double sided arrangements of 768 segmented parallel strips of silicon sensors with a pitch of 95 μm. The SSD shares a similar ladder support technology, with 34 ladders with 22 modules for the first layer along the beam axis. This ensures a spatial resolution of ~ 20 μm in the radial direction. The second layer is fitted with 38 ladders with 25 modules in the radial direction with a resolution of ~ 830 μm along z. Table 2.1 reports a summary of the numbers discussed above.

2.2.2 Time Projection Chamber

The *Time Projection Chamber* (TPC) is the largest detector in ALICE and is the primary tracking detector [124, 125]. It measures the momentum of the charged-particles, performs particle identification via specific energy loss, and participates in the interaction vertex reconstruction. The detector covers the entire azimuth ($0^\circ < \phi < 360^\circ$) and pseudo-rapidity acceptance $|\eta| < 0.9$. It is a cylindrical detector, ~ 510 cm long, with an internal radius of ~ 85 cm, and an external radius of ~ 247 cm and a total active volume of ~ 88 m^3. It is divided into two sectors, with a central high voltage electrode in the middle operating at a ~ 100 kV potential, generating a constant electric field of $\mathrm{E} \simeq 500$ V/cm. The chamber is filled up with a $\mathrm{Ne/CO_2N_2}$ mixture in the proportions of 90/10/5 to achieve a high electron drift time of ~ 90 μs from the central cathode to the endcaps of TPC, with drift velocity ~ 3 cm/μs. The TPC also requires proper thermal stability to control the balance of the velocity of the electrons and the temperature. Electrons from the ionization of the gas by the charged-particle tracks drift to the ends of the cylinder. Each end plate is segmented in 18 trapezoidal sections (total 36), divided in an inner and an outer region,

each fitted with a Multi Wire Proportional Chamber (MWPC). Figure 2.4 shows the design of the TPC and the configuration of one segment of the MWPC. The inner and outer regions together form 159 readout *pad rows*, cathodes that collect the drifting electron signal. The reconstructed signal gives the $x-y$ projection of the charged-particle track, while the drift time gives the track information along z direction. The TPC can provide resolutions up to 1% for low momentum particles leading up to 3.5% for large momentum tracks. The TPC is also used extensively for particle identification, a discussion dedicated in Section 2.6.2.

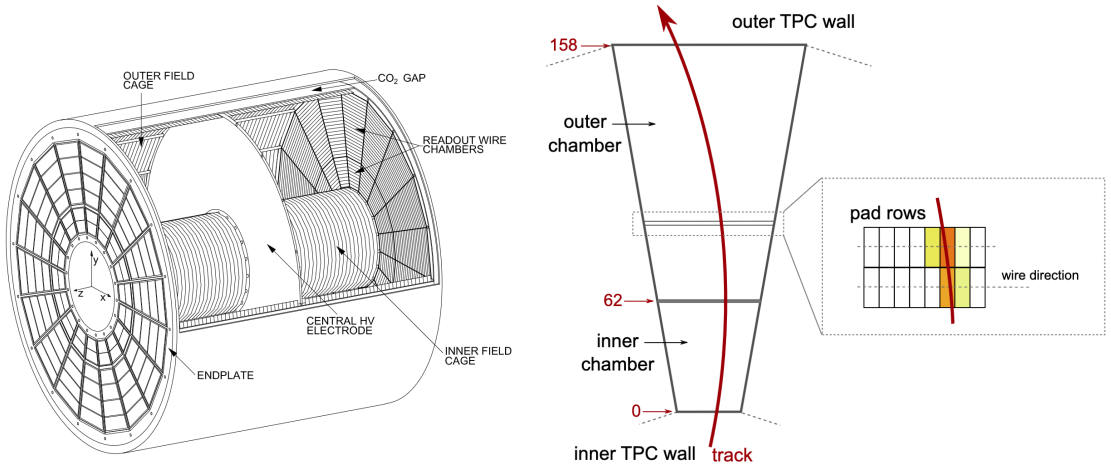

Figure 2.4: (Left) TPC detector schematic. Figure taken from [125]. (Right) A section of the TPC endplate shows the inner and outer regions. Figure taken from [126].

2.2.3 Time-Of-Flight Detector

The *Time-Of-Flight* detector follows the TPC cylindrical geometry with complete azimuthal coverage and a pseudorapidity coverage of $|\eta| < 0.9$ [127]. The inner and outer radii are $\sim$ 370 cm and $\sim$ 399 cm, respectively. The detecting element is a Multi-gap Resistive Plate Chamber (MRPC) designed in 10 layers of double stacked strips. The entire detector is made out of 1593 MRPCs and is divided into 18 sectors. In the vacuum region between the two plates, an electron avalanche is produced from the ionizing particle. The final signal reaching the electrode of TOF is a sum of signals coming from every vacuum space between the plates. The MRPCs are, therefore, placed in a transverse direction to the traversing charged tracks to suppress the oblique paths and avoid the mixture from adjacent elements. The optimization of the MRPCs allows the TOF to reach time resolutions close to 50 ps in Pb–Pb collisions and 100 ps in pp collisions. Its primary purpose is to identify charged-particles in the intermediate momentum range, which it does via the information of the particles' measured velocity (β) as a function of the measured momentum. The schematic of TOF and a single MRPC module is presented in Figure 2.5. A detailed description of particle identification by TOF is presented in Section 2.6.3.

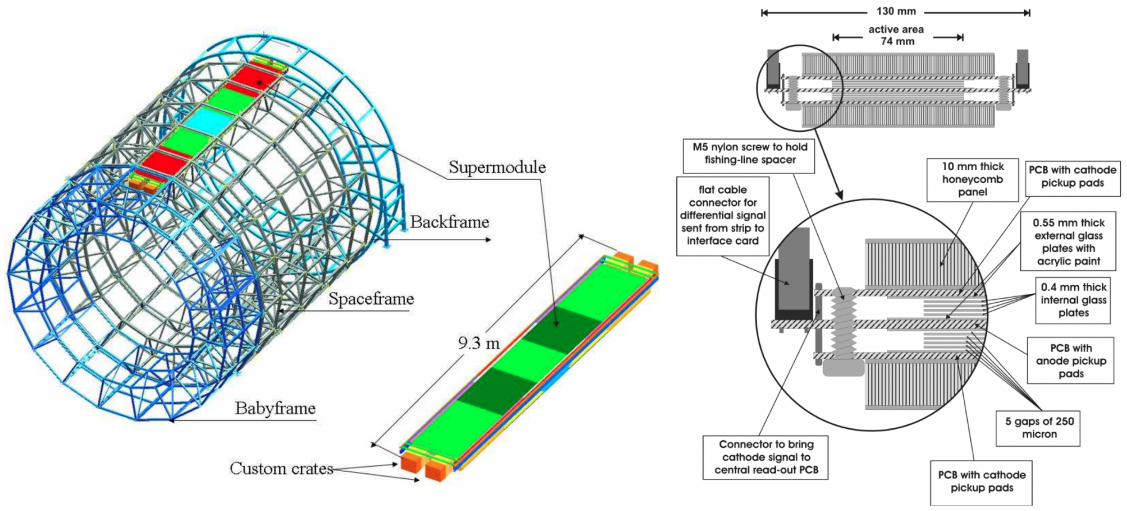

Figure 2.5: Schematic of the TOF detector and the MRPC supermodule. (Right) Cross-section of the MRPC module. Figures taken from [128].

2.2.4 V0

The V0 detectors (V0A and V0C) are scintillator detectors made up of two arrays of 32 plastic scintillators placed along the beamline on both sides of the interaction point [129]. The V0A and V0C are located at 390 cm and 90 cm from the nominal interaction point, with acceptances in the pseudorapidity range $2.8 < \eta < 5.1$ and $-3.1 < \eta < -1.7$, respectively, with a complete azimuthal coverage. Figure 2.6 shows the design of V0A and V0C, both consisting of 4 rings placed in increasing radial distances and are individually divided into 8 sectors, each covering 45°. The detector is primarily used for triggering and defining event multiplicities, which are collected from the scintillation light signal amplitude.

2.3 Triggers

A centralized system of selecting collision events in pp, p–Pb, and Pb–Pb collisions is carried out by the Central Trigger Processor (CTP). The CTP receives inputs from various trigger detectors, which are managed in terms of logical conditions, which are categorized in *classes*. The hardware trigger classes are generally subdivided into Level 0 (L0), Level 1 (L1), and Level 2 (L2). The CTP analyses trigger inputs every $\sim$ 25 ns, corresponding to the LHC clock cycle, and execute the L0 trigger $\sim$ 0.9 ns after the collision. Here, the fast detectors, namely SPD, T0, V0, EMCal, PHOS, and the Muon Triggers, are used for *event selection*. The L1 trigger is executed $\sim$ 6.5 μs after the L0 trigger, invoking a delay of 260 LHC clock cycles (caused by the computing time of TRD and EMCal detectors). The L2 trigger decision is made after L1, with a global delay of $\sim$ 100 μs, which accounts

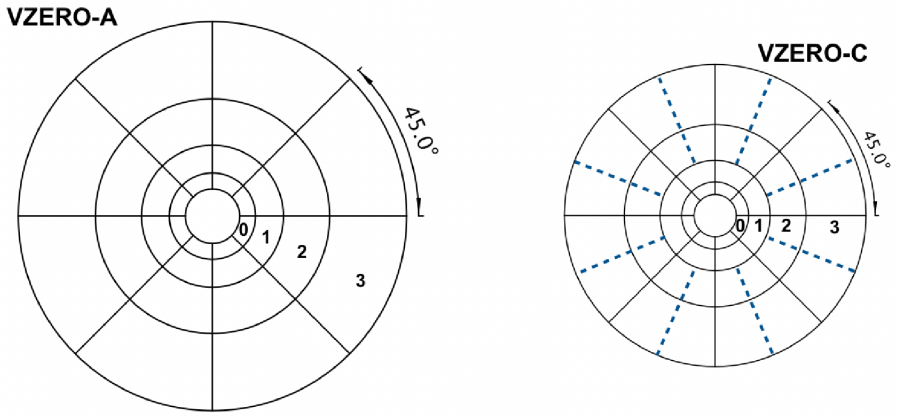

Figure 2.6: VZERO detector modules (Left) V0A and (Right) V0C. Figure taken from [129].

for the drift time of electrons in the TPC. This delay is also utilized by the past-future protection circuits to filter out the pile-up events. The accepted event from the L2 decision is sent to the Data Acquisition System (DAQ) [130] and the High-Level Trigger (HLT) system [131], where the storing of the events and data compression is performed.

At the DAQ level, the trigger selections are based on different physics goals of ALICE. The Minimum Bias trigger (MB) [132] is the most commonly applied trigger scheme that involves fewer biasing conditions for data acquisition. The trigger was originally designed (Run-1) to follow an $\mathrm{MB_{OR}}$ logic, where a hit in the SPD or either one of the V0 arrays was required. This was replaced by a high purity $\mathrm{MB_{AND}}$ trigger, which required the coincidence between the V0A and V0C arrays. This choice was adapted for higher luminosity in Run-2.

The High Multiplicity trigger strategy for the 2018 data taking period is to increase the number of events with a larger number of tracks in the SPD. The trigger is based on the number of fast-OR chips fired online, which is strongly correlated to the number of SPD tracklets. This was termed as the HMSPD trigger, and only applied on the periods LHC18f/h/j/k/l/m/o/p. The analyses presented in the thesis will consist of data samples triggered with both MB and HMSPD schemes, which are important to reach high precision at large multiplicities in pp collisions.

2.4 ALICE offline framework

The ALICE computing model is based on the Worldwide LHC Computing Grid (WLCG), which is the world's largest computing facility operated by CERN [133, 134]. It connects 170 computing centers across 42 countries, allowing the handling, processing, and storage

of about 1 EB of data. The framework is highly optimized so that the computing resources provide real-time access to LHC data, regardless of the location. During Run-1 and Run-2, a typical year of data taking, ALICE collects up to 12 PB of data that carry information from 10^9 pp collisions and 10^8 Pb–Pb collisions. The physical form of the data in its entirety is stored as Event Summary Data (ESD) files, which go through multiple filtering stages. At the analysis level, the data is kept in Analysis Object Data (AOD) files. The ALICE Environment (Alien) [135] provides real-time access, analysis, and simulation task execution to the collected data. The tool to access and analyze the data is a C++-based object-oriented interpreter tool called `ROOT` [136], developed and maintained at CERN. The ALICE analysis framework is built around `ROOT`, divided into two major components; (i) `AliROOT` forms the construct for the various analysis tools [137], which include detector development, alignment and calibrations, Monte Carlo simulations and data reconstruction, and (ii) `AliPhysics` carries all the analysis codes and tasks that are essential to carry out the different physics analyses, which are executed over the processed data. The analyses pertaining to this thesis are performed in this set of ALICE computing tools. However, ALICE has a new analysis framework called the Online-Offline (O^2) framework [138], designed for the Run-3 of the LHC and data collection for ALICE.

2.5 Primary vertex and track reconstruction

The primary vertex and track reconstruction follow a common workflow [139]. The first step is to have a preliminary determination of the primary vertex. This is done with information from the ITS, in particularly with the SPD clusters[7] (one cluster per layer), which is termed as a *tracklet*. A primary vertex is assigned to a point where a maximum number of tracklets converge.

The reconstruction of charged-particle tracks begins at the TPC detector, at its outermost layer. Track *seeds* are defined according to two TPC clusters and the preliminary primary vertex, and then with three consequent clusters without a vertex requirement. The seeds are then propagated inward using *Kalman filtering* [140], where the track is iteratively updated based on the proximity of the clusters. The propagation is continued to the inner layer of the TPC, and the tracks with at least 20 out of 159 possible clusters are accepted. The tracks are then prolonged to the outer layer of the ITS, where a similar track propagation method is applied until the inner layer of ITS is reached. According to the reduced-χ^2 from the Kalman filter algorithm, only the highest quality tracks are chosen. However, for low p_{T} tracks, the TPC reconstruction efficiency drops, caused by deflection of the expected helical path due to the magnetic field, which is due to multiple scatterings and energy loss of the charged-particles in the detector material. This effect is counterbalanced by the

[7] A cluster is a collection of data characterized by position, signal amplitudes, signal times, etc. from a detector

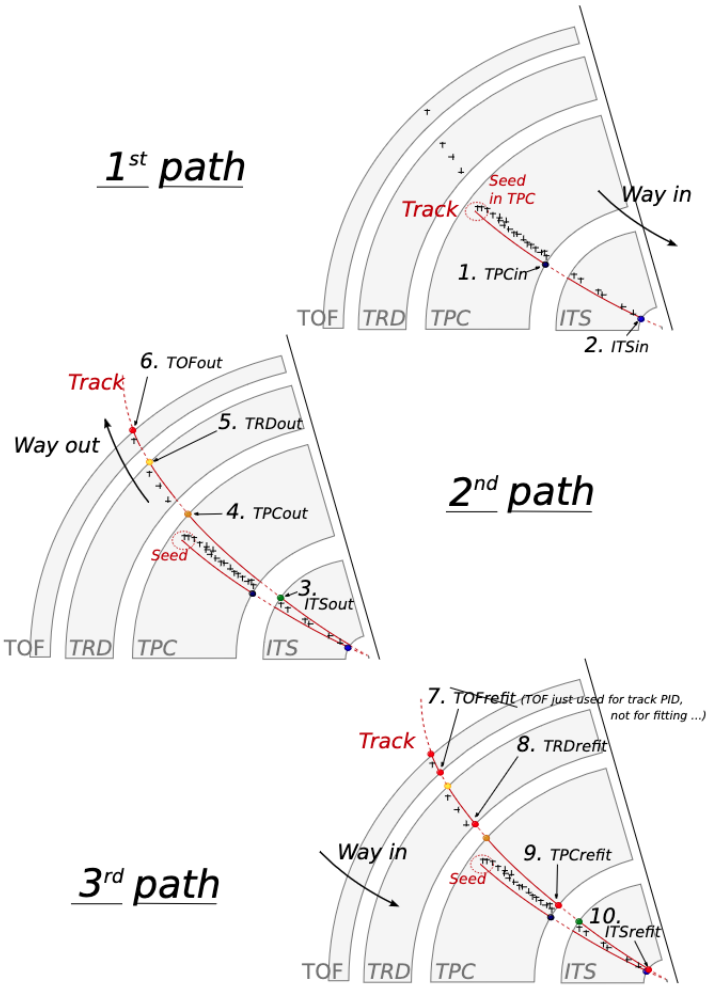

Figure 2.7: Track reconstruction procedure followed at ALICE with a step-by-step representation. Figure taken from [126].

ITS standalone tracking procedure, where a reversal of the track propagation as discussed above is followed, by defining helical seed in the innermost ITS layer and propagating outwards. The best quality track is chosen from the lowest reduced–χ^2 from the Kalman filter procedure, and track efficiency is optimized by repeating the procedure multiple times and maximizing the opening angle of the track prolongation procedure. Once the standalone procedure is done, the tracks are propagated towards the preliminary primary vertex and stopped at the point of closest approach. The outward refitting procedure begins with the clusters used during the inward propagation, termed sequentially as ITS and TPC-*refit* procedures until the outer layer of the TPC is reached. The final fit provides the *global* reconstructed tracks, which are used to definitively determine the interaction vertex. A step-by-step representation of the track reconstruction procedure is shown in

Figure 2.7.

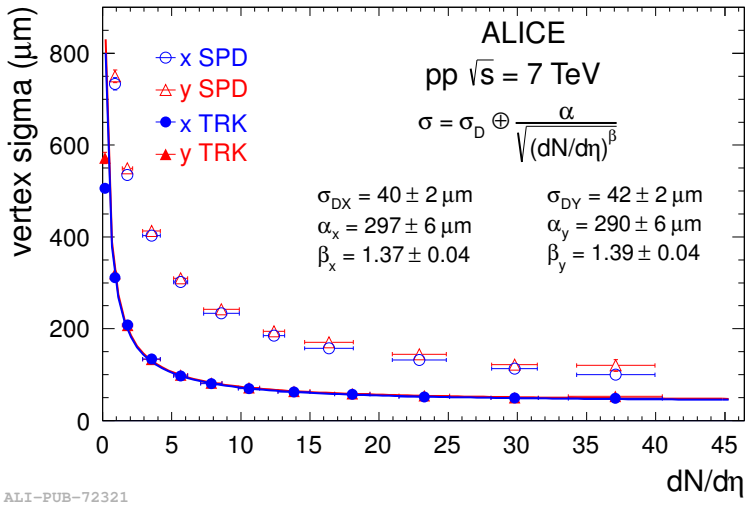

Figure 2.8: Resolution of the interaction vertex position as a function of charged-particle multiplicity density in pp collisions at $\sqrt{s}$ = 7 TeV [139].

Finally, the primary vertex determination is performed by propagating the global tracks inward to a point of closest approach. A more precise vertex fitting procedure is performed using track-weighting procedure [141] to prevent the participation of outliers. The precision of determination improves with the number of global tracks involved. Figure 2.8 shows the resolution of interaction vertex position as a function of the charged-particle multiplicity density in pp collisions at $\sqrt{s}$ = 7 TeV [139]. It is observed that the vertex resolution improves significantly with the increase in charged-particle tracks, which can be parametrized with a power law function of the form $\alpha/\sqrt{(\mathrm{d}N/\mathrm{d}\beta)^{\beta}}$.

2.6 Particle identification

ALICE detectors are designed to identify particles, in ITS and TPC via the measurement of specific energy loss and from the time of flight in the TOF detector. This section is dedicated to discuss the particle identification techniques, which are used in the analyses of this thesis.

2.6.1 Particle identification in the ITS

The outer two detectors (or four layers) of the ITS (SDD, SSD) are employed for particle identification, that extracts the ionization charge of the electrons that come from the ionization of the detector material. The specific energy loss of each charged-particle track

($\mathrm{d}E/\mathrm{d}x$) is calculated from the weighted mean of the values of each layer. The left panel of Figure 2.9 shows the charged-particle $\mathrm{d}E/\mathrm{d}x$ as a function of the measured momentum for pp collisions at $\sqrt{s}$ = 13 TeV [122]. The ITS allows for a good distinction between the charged-particles at low momentum [123].

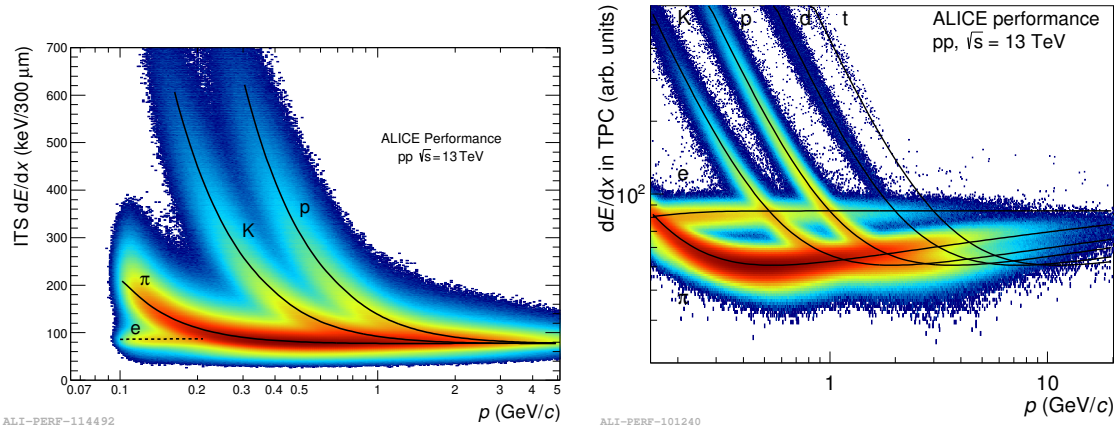

Figure 2.9: Specific energy loss ($\mathrm{d}E/\mathrm{d}x$) of charged-particles as a function of momentum for the ITS (left) and the TPC detector (right) in pp collisions at $\sqrt{s}$ = 13 TeV. Figure taken from [122].

2.6.2 Particle identification in the TPC

The TPC shares a majority of the particle identification workload of ALICE [125]. The TPC measures the ionization charge of the drifting electrons on the 159 pad rows of the TPC endplate. The $\mathrm{d}E/\mathrm{d}x$ of the corresponding charged-particle tracks are taken from the 65% of the lowest amplitude signals, in order to avoid the contributions from secondary ionizations. Figure 2.9 (right panel) shows the measured $\mathrm{d}E/\mathrm{d}x$ as a function of measured momentum in pp collisions at $\sqrt{s}$ = 13 TeV [122]. The measured values are compared to the expected values given by the Bethe-Block equation, which after a data driven parametrization, looks like

$$f(\beta\gamma) = \frac{P_1}{\beta^{P_4}}\left[P_2 - \beta^{P_4} - \ln\left(P_3 + \frac{1}{(\beta\gamma)^{P_5}}\right)\right] \tag{2.1}$$

where, P_{1-5} are free parameter, β is the particle velocity and $\gamma = 1/\sqrt{1-\beta^2}$ is the Lorentz boost factor. The solid lines in Figure 2.9 represent the expected $\mathrm{d}E/\mathrm{d}x$ trends of different charged-particle species. At different cut-off momentum values, the different hadron species are separable, which decreases with increasing p, due to relativistic rise.

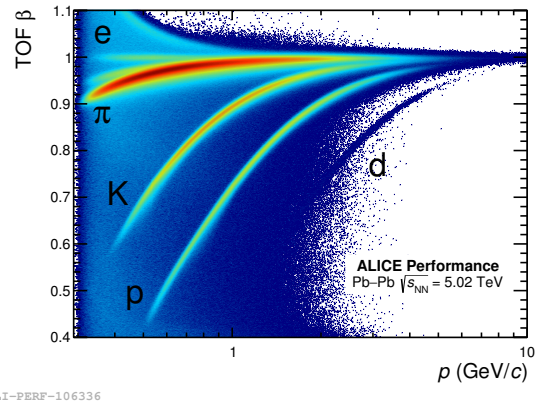

Figure 2.10: Charged-particles β as a function of momentum for TOF detector in pp collisions at $\sqrt{s}$ = 13 TeV [122].

2.6.3 Particle identification in the TOF

The particle identification methodology in the TOF detector is carried out via the flight time of the charged-particle [127]. The flight time of a particle of mass m, traversing with momentum p in a path length L, is given by

$$t = L \cdot \frac{\sqrt{m^2c^4 + p^2c^2}}{pc^2} \tag{2.2}$$

TOF measures the charged-particle velocities via measuring their flight times, $t_{\text{flight}} = t_{\text{hit}} - t_0$, where the start time t_0 is triggered by the T0 detector or via the arrival time of the charged-particle tracks at TOF, and t_{hit} when the track hits the detector. Figure 2.10 reports the measured charged-particle velocities as a function of the measured momentum in pp collisions at $\sqrt{s}$ = 13 TeV, ensuring particle separation upto $p \simeq 4.5$ GeV/c.

Chapter 3

Monte Carlo event generators

This chapter is dedicated to the discussion of Monte Carlo event generators, relevant in experimental data analysis and phenomenological studies. A description of the Lund string model, which forms the backbone of the event generators, is provided. The details of the event generators, namely PYTHIA8, AMPT, and SMASH, which are relevant to the studies in this thesis, are discussed in the following sections.

3.1 Overview

The experimental measurements in hadronic and heavy-ion collisions, standalone, provide a limited understanding of the underlying physics unless compared to theory. Conversely, theoretical predictions are futile if they fail to describe the experimental results. This creates a consonance between theory and experiment, involving measurements with experimental data and comparisons with theoretical predictions. The use of Monte Carlo methods is considered a popular approach to computationally simulate or "generate" the collision events and attempt to describe the physics of the experimental measurement as closely as possible. Moreover, before an experimental measurement can be delivered, the detector responses and the measuring equipment require checks, corrections, and unfolding, achieved with full Monte Carlo simulations. The Monte Carlo event generators, therefore, serve two purposes: first being a theoretical tool to design and obtain physics results/predictions to compare them with experimental results and as a practical tool for simulation and tuning of experimental signals and their responses.

Modern Monte Carlo event generators exploit the phenomenology of strong interactions. The principle of colour confinement in a hadron is simulated with a *string* motion analogy. In this approach, the quarks are present at the two ends of a string, and the gluon is considered to carry the property of string force. Baryons, which are made up of three

quarks, can be imagined as a string consisting of three ends or be treated like mesons, i.e., made up of two quarks. The string model is considered to be a strongbox for many event generators. In the studies described in this thesis, event generators are used to simulate pp and heavy-ion collisions for both data analysis and phenomenological aspects. This chapter is dedicated to the working principles of modern Monte Carlo event generators, with a detailed description of the Lund string model put forward in Section 3.2. A selection of event generators, namely, PYTHIA8, AMPT, and SMASH, are used in the studies of this thesis, which are discussed in Sections 3.3 to 3.5.

3.2 The Lund string model

The Lund string model [142–144] is a non-perturbative hadronization model widely employed in modern Monte Carlo event generators. The model applies the $q\bar{q}$ confining component of the Cornell potential [29] (Equation 1.4), where a colour string of string tension κ connects the moving away quark anti-quark pair. As the pair moves farther away, the string extends, storing the potential energy, which at a certain point translates into kinetic energy. At this point, the $q\bar{q}$ is turned around and accelerated in the reverse direction till they meet, and this process is repeated. This process, or the *yo-yo* mode, causes a gradual stretching of the string from the linear increase of the energy stored in the string. The yo-yo motion is the simplest case of the string model, with complex structures being implemented with new models. A case of single *junction* or a *T-junction* is when strings are arranged between three quarks. Double junctions can also form, where two T-junctions are combined with a common string. The formation of junctions can later lead to the formation of baryons [145].

The hadronization process begins as the strings begin to fragment. Once the energy stored in the string exceeds the energy required to form a new $q\bar{q}$, the string breaks into two $q\bar{q}$ pairs. In this process, multiple strings may break, causing new $q\bar{q}$ pairs to form, which becomes a hadron or generate more hadrons, until only hadrons remain. The formation of hadrons is also decided by the area spanned by the string, corresponding to its potential energy. The left panel of Figure 3.1 shows the string fragmentation model at work, whereas massless $q\bar{q}$ pair moves in opposite direction, with colour strings breaking at different positions in space-time. At $x = 0$, the trajectories are back to back (yo-yo), which gets elongated with Lorentz boost at larger x values. The symmetric fragmentation function of the Lund string model [142] is given by

$$f(z) \propto z^{-1}(1-z)^{a} \exp(-bm_{\mathrm{T}}^{2}/z) \tag{3.1}$$

where, z denotes the light cone momentum fraction of a produced hadron with respect to that of the fragmentation string, m_{T} is the transverse mass of the hadron, and a and b are

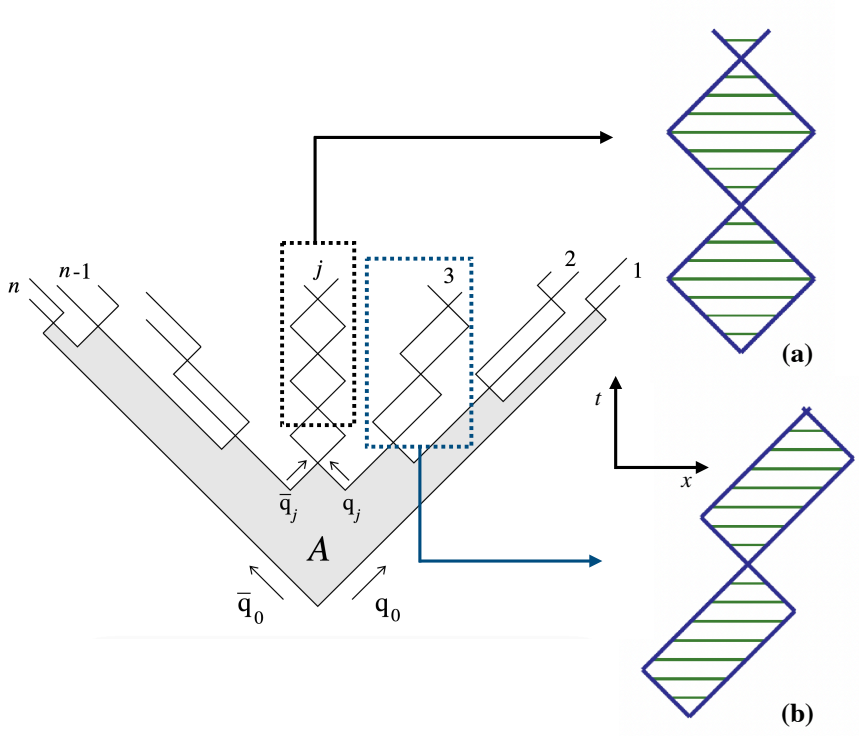

Figure 3.1: Representation of Lund string fragmentation zoomed in at (a) mid-rapidity and (b) forward rapidity regions.

the Lund fragmentation parameters. The $q\bar{q}$ string breaking probability [142], decreases exponentially with the square of the quark transverse mass in the following form

$$\mathcal{P}(\text{string breaking}) = \exp\left(-\frac{\pi m_{\text{q}}^2}{\kappa}\right)\exp\left(-\frac{\pi p_{\text{T,q}}^2}{\kappa}\right) \tag{3.2}$$

For heavy quarks, the probability to produce a $c\bar{c}$ pair is insignificant compared to $u\bar{u}$ and $d\bar{d}$ pairs. This suppresses heavy-flavour production with soft string fragmentation. Although, throughout this discussion, the fragmentation and hadronization of Lund strings have led to the formation of mesons, the production of baryons via Lund strings also follows a similar prescription. Baryon formation is regarded as a quark combining with a di-quark state, making it a colour anti-triplet (following SU(3) algebra). Another production mechanism of immediate baryon production is the *popcorn* mechanism [146], a consequence of multiple string breaking. Figure 3.2 shows the formation of meson and baryon pairs

produced via different string breaking mechanisms, as well as multiple breaking through the popcorn mechanism.

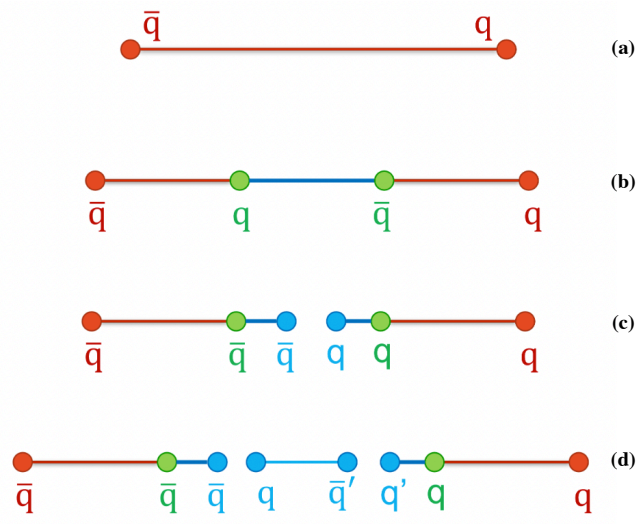

Figure 3.2: Stages of string fragmentation model at work; (a) stretching of the string leading to (b) meson formation, (c) baryon formation through di-quarks, and (d) multiple di-quark fragmentation in the popcorn model.

3.3 PYTHIA8

PYTHIA8 is a popular QCD inspired event generator that can be applied to a large set of phenomenological problems in high-energy as well as astroparticle physics [147–149]. It has a collection of individual physics models that tend to different stages of evolution. It is based on the Lund string model that is widely used to simulate electron-proton and proton–proton collisions. PYTHIA8 provides a wide range of processes and a variety of control parameters suitable for generating hard and soft scatterings, initial and final state radiations in parton scatterings, parton fragmentations, multi-parton interactions, and color-reconnection mechanisms in hadronization. The primary components are described in the following sections.

3.3.1 Hard process

The initial scattering of the partons from the incoming protons is referred to as the hard scattering. The scattering process involves a large momentum transfer, that leads to two

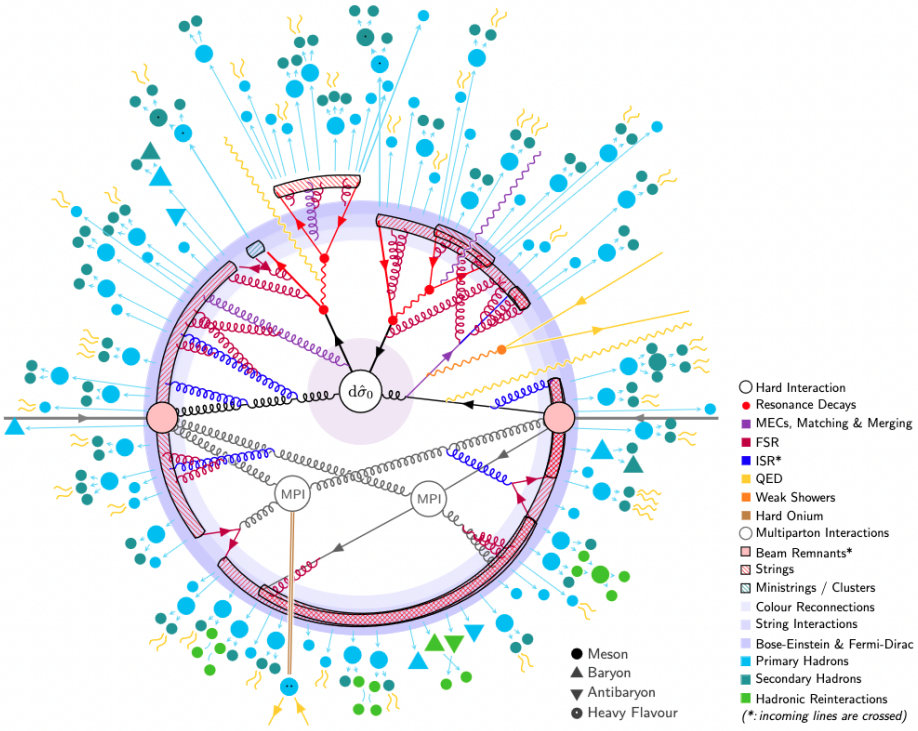

Figure 3.3: An illustration of all major processes in a pp → $t\bar{t}$ event in the PYTHIA8 event generator. Figure taken from [149].

or more outgoing particles. This can be treated with a pQCD or electroweak process. In PYTHIA8, several phase space cuts are applied to remove the contributions from infrared singularities while calculating the hard process cross-sections.

3.3.2 Initial and final state radiations

The incoming partons can split and create several branching, leading to initial state radiations (ISR). Similarly, the outgoing partons may also go through final-state radiations (FSR). The evolution of these parton showers are carried out via the DGLAP equations [25]. The parton radiations or splitting processes such as q → qg are tended by splitting functions, that are ordered according to the virtuality (Q^2) of the process.

3.3.3 Multiparton interactions

The incoming proton beams in PYTHIA8, contain several partons that can interact via additional soft processes; they are termed as multiparton interactions (MPI) [150]. The

soft processes in PYTHIA are modelled using the Regge theory [151], where the scattering of the partial waves is extended onto the complex angular momentum (l) plane. The poles in the complex plane (known as Regge poles) are traced out by Regge trajectories ($\alpha(t)$), forming a relationship as

$$l = \alpha(t). \tag{3.3}$$

The force carriers are referred to as *reggeons* or *Pomerons* [151], that mediate elastic and inelastic collisions. In a 2→2 scattering process, the MPI cross-section function can be written as

$$\frac{d\sigma_{2\to2}}{dp_{\mathrm{T}}^2} \propto \frac{\alpha_{\mathrm{s}}^2}{p_{\mathrm{T}}^4} \to \frac{\alpha_{\mathrm{s}}^2(p_{\mathrm{T}}^2 + p_{\mathrm{T0}}^2)}{(p_{\mathrm{T}}^2 + p_{\mathrm{T0}}^2)^2} \tag{3.4}$$

where, p_{T} is the transverse momentum of the outgoing partons, and p_{T0} is a tunable parameter that regulates the MPI cross-section. One can estimate the approximate number of MPIs in an event with non-diffractive[8] scattering cross-section (σ_{ND}) as

$$\langle n_{\mathrm{MPI}} \rangle (p_{\mathrm{T0}}) = \frac{\sigma_{2\to2}(p_{\mathrm{T0}})}{\sigma_{\mathrm{ND}}} \tag{3.5}$$

3.3.4 Hadronization

PYTHIA8 uses the Lund model as the standard hadronization model for all collision systems. The Monash tune in PYTHIA8 has the complete deployment of the Lund model [143]. The traditional Lund string model in PYTHIA8 utilizes a *leading colour* (LC) approximation to trace the colour flow for each event [88]. In this scenario, each quark and anti-quark pair are uniquely connected to a gluon (both carrying one colour and anti-colour charge) via two colour strings. This approximation is good enough for e^+e^- collisions but faces shortcomings in hadronic collision systems. This happens due to the background of colour charges from the initial state, and the beam remnants, and also from MPI in pp systems [150]. A typical pp event can hold between 4-6 MPIs, essential to explain the underlying event and soft interactions, even higher for high multiplicity events. In the leading colour approximation, a higher rate of MPIs leads to a flattening of the $\langle p_{\mathrm{T}} \rangle$ of charged-particles as a function of event multiplicities, which was disproved by

[8] depending on the exchange of internal quantum numbers, a collision can be defined into diffractive, when no quantum numbers are exchanged, and non-diffractive where colour charges are exchanged via Pomerons.

experimental results. This led to the requirement of *colour reconnections beyond leading colour* (CR-BLC) models to be constructed [145].

The CR-BLC model extends the string recombinations among partons in different MPIs and colour charges from beam remnants. The $SU(3)_c$ group allows for 9 quark colour combinations and 72 gluon combinations, which allows for additional string topologies to undergo hadronization. These combinations are also known as *junctions*, shown in the right panel of Figure 3.4, compared to the LC topologies presented on the left. The reconnection is dictated by minimizing the *string-length measure* (λ), while its invariant mass should overcome a certain threshold m_0. The $C_j = m_{0j}/m_0$ parameter decides the amount of reconnections, where a high m_{0j} corresponds to a low λ and C_j greater than unity. The string topologies are also influenced by *causal connections*, where the time dilation effects due to the relative boost come into play. The string formation proper time $\tau_{\text{form}} \sim 1/m_{\text{string}}$ can be causally connected to the hadronization time $\tau_{\text{had}} \sim 1/\Lambda_{\text{QCD}}$ by

$$\gamma\tau_{\text{form}} < C_{\text{time}}\tau_{\text{had}} \tag{3.6}$$

where C_{time} is a tunable parameter. The CR-BLC modes are defined according to different causal contacts. Mode-0 refers to no time dilation constraint and only defined by the invariant mass criterion. Mode-2 considers a strict condition of causal contact. At the same time, Mode-3 has a relaxed version of the same with the first reconnection to agree with the causal contact, even if further reconnections take place later.

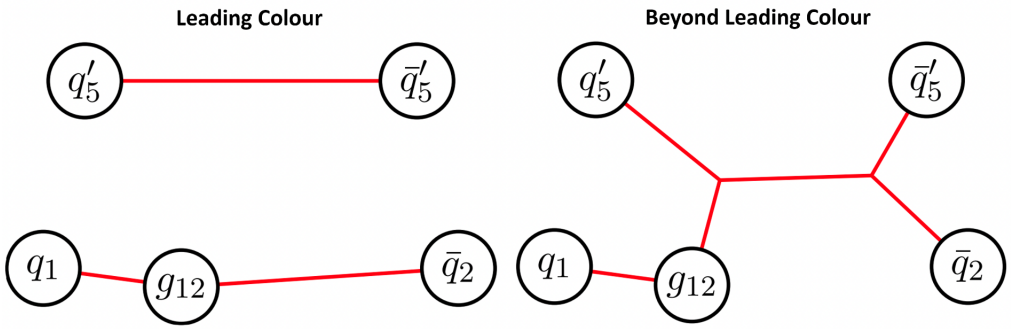

Figure 3.4: String colour reconnection topologies of (Left) leading colour and (Right) beyond leading colour approximations implemented in PYTHIA8. Figure taken from [145].

3.4 AMPT

Unlike pp collisions, simulation of heavy-ion collisions requires a significant deal of complex many-body dynamics. Various theoretical models have attempted to reproduce the

heavy-ion results from RHIC and LHC. They comprise statistical hadronization models [96, 98], hydrodynamic models with local thermal equilibrium formation [152, 153], and transport approaches that involve non-equilibrium dynamics [154, 155]. A popular transport model that addresses non-equilibrium many-body dynamics is 'A Multi-Phase Transport' (AMPT) model [156]. AMPT includes partonic and hadronic degrees of freedom in its evolution of heavy-ion collisions with a transition between the two phases. AMPT is designed to simulate p–A and A–A collisions at center of mass energies $\sqrt{s_{\mathrm{NN}}}$ = 5 GeV to 5.5 TeV. AMPT consists of a hybrid framework of four primary components: the initial conditions, parton-level interactions, a hadronization mechanism, and the hadronic scatterings. The individual components are described in the following sections.

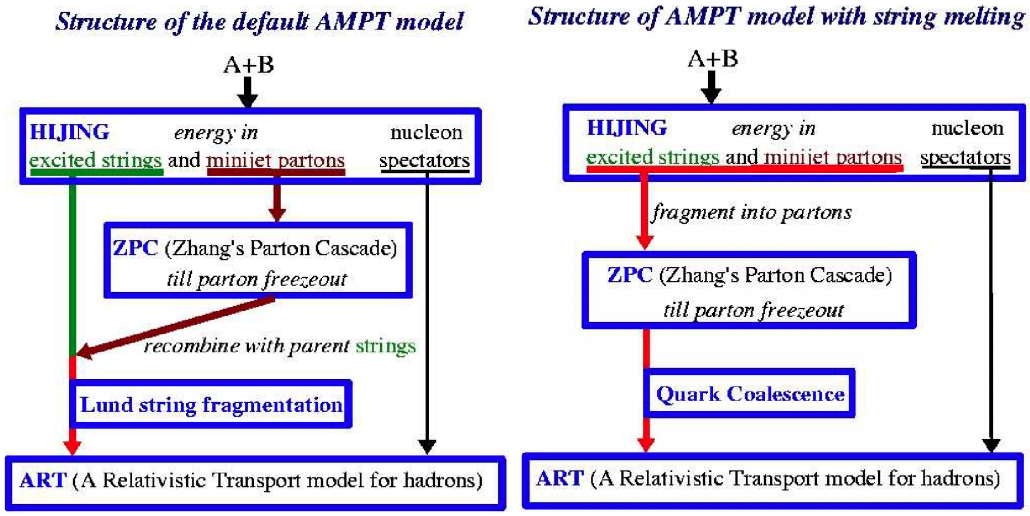

Figure 3.5: A working flowchart of the AMPT model in default mode (Left) and string melting mode (Right). Figures take from [156].

3.4.1 Initial conditions

The default model

The initial conditions in AMPT for heavy-ion collisions are obtained from the "Heavy-Ion Jet INteraction Generator" (HIJING) model [157]. The nuclear densities are parameterized via the Woods-Saxon distribution of the form

$$\frac{\mathrm{d}N}{\mathrm{d}^3 r} = \frac{\rho_0}{1 + \exp\left(r - r_0/d\right)} \tag{3.7}$$

where, $\rho = 0.168\ \mathrm{fm}^{-3}$ is the nuclear ground state density and r_0 is the nuclear radius. d = 0.584 is the diffusiveness parameter. The particle production is divided into hard and soft

components from HIJING [157]; (i) the hard scatterings via minijet partons are decided by a cut-off momentum parameter treated with PYTHIA [158], (ii) while the soft processes follow the Lund fragmentation model [142]. The cut-off parameter 'p_0' is chosen to be 2 GeV/c, which fits the experimental data of $\sigma_{\text{elastic}}/\sigma_{\text{total}}$ for pp and p$\bar{\text{p}}$ cross-sections in the energy range $20 < \sqrt{s} < 1800$ GeV, with an additional soft nucleon-nucleon cross-section $\sigma_s(s) = 57$ mb. These two independent parameters are inspired by the Duke-Owens set 1 for parton distribution functions in the nucleon [159]. For high energy A–A collisions, the number of hard scatterings scales as $A^{4/3}$ with rapid increase in collision energy, while the number of strings roughly scales as A [158, 160]. This leads to an increased production of mini-jets at high collision energies, showing sensitivity to the cut-off parameter.

The parton distribution functions in the colliding nuclei are modified due to nuclear shadowing effects from a superposition of individual contribution of the nucleons. This effect is included in AMPT via HIJING following an impact parameter dependent, and virtuality (Q^2) and flavour independent parameterization [157], given by the nuclear shadowing function as,

$$\begin{aligned} R_A(x,r) &= \frac{f_a^A(x,Q^2,r)}{A f_a^N(x,Q^2,r)} \\ &= 1 + 1.19\ln^{1/6} A(x^3 - 1.2x^2 + 0.21x) - \left[\alpha_A(r) - \frac{1.08(A^{1/3}-1)\sqrt{x}}{\ln(A+1)}\right] \end{aligned} \tag{3.8}$$

where x is the fraction of light cone momentum carried by a parton in the nucleon N, and f_a, is the parton distribution function. The impact parameter dependent nuclear shadowing effect is given by

$$\alpha_A(r) = 0.133(A^{1/3} - 1)\sqrt{1 - r^2/R_A^2} \tag{3.9}$$

where r is the transverse distance of an interacting nucleon from the center of the nucleus A with radius $R_A = 1.2A^{1/3}$.

String melting model

The partonic energy densities at the initial evolution of the collision can be an order higher than the critical energy density (~ 1 GeV/fm^3) in the QCD phase transition for central Au–Au collisions at $\sqrt{s_{\text{NN}}} = 200$ GeV. In these conditions, the strings at high energy densities lead to underestimation of the partonic effects [39]. In order to reproduce the effects of high energy density regimes, AMPT employs a string melting technique to introduce partonic degrees of freedom to the strings without any interactions [161]. This means that

a meson melts into a quark and anti-quark, and a baryon into a diquark and a quark. The melting occurs according to the flavour and spin structures of the valence quarks. The melting is initiated at formation times $t_f = E_{\rm H}/m^2_{\rm T,H}$, with energy $E_{\rm H}$ and transverse mass $m_{\rm T,H}$ of the parent hadron.

3.4.2 Parton cascade

The final state interactions among partons are modeled with a transport approach. Also termed the cascade method, the equations of motion of the Wigner distributions of the partons are obtained by solving the Boltzmann transport equations in a semi-classical prescription [156]. The parton cascade mode is tended to by the Zhang Parton Cascade (ZPC) [162] model, where the interactions among the partons are described by the equations of motion of their Wigner distributions. The Boltzmann transport equations, which for 2 body interactions are given by

$$p^\mu \partial_\mu f(\mathbf{x}, \mathbf{p}, t) \propto \int \sigma f(\mathbf{x_1}, \mathbf{p_1}, t) f(\mathbf{x_2}, \mathbf{p_2}, t) \tag{3.10}$$

where σ is the 2-body scattering cross-section, and $f(\mathbf{x}, \mathbf{p}, t)$ is the distribution function of parton at time t in the phase space. The ZPC model is used to solve the Boltzmann transport equations, where the partons undergo interactions when they approach a distance of $\sqrt{\sigma/\pi}$. The ZPC model allows 2-body parton scattering processes supported by pQCD calculations. For instance, the gluon scattering elastic cross-section, at leading order, is given by

$$\frac{{\rm d}\sigma_{\rm gg}}{{\rm d}t} \simeq \frac{9\pi\alpha_{\rm s}^2}{2}\left(\frac{1}{t^2} + \frac{1}{u^2}\right) \tag{3.11}$$

where $\alpha_{\rm s}$ is the strong coupling constant, and t, u are the Mandelstam variables. By taking the scattering angle range between 0 and π, and assigning a Debye screening mass μ to the cross-section singularity, one can get

$$\frac{{\rm d}\sigma_{\rm gg}}{{\rm d}t} \simeq \frac{9\pi\alpha_{\rm s}^2}{2(t^2-\mu^2)^2} \tag{3.12}$$

$$\sigma_{\rm gg} = \frac{9\pi\alpha_{\rm s}^2}{2\mu^2}\frac{1}{1+\mu^2/s} \tag{3.13}$$

Since $s >> \mu^2$ at very high temperatures, the relation is simplified to

$$\sigma_{gg} \approx \frac{9\pi\alpha_s^2}{2\mu^2} \tag{3.14}$$

This relation is tunable in AMPT with the parton screening mass in the default as well as the string melting model.

3.4.3 Hadronization

Based on the initial condition prescription, there are two hadronization mechanisms employed in AMPT. The Lund string model is employed for the default mode [142], while a quark coalescence model is deployed for the string melting mode. The Lund string model is implemented exactly as described in Section 3.2. A suppression factor of 0.3 is introduced for strange anti-strange ($s\bar{s}$) production relative to light $q\bar{q}$ pairs. The fragmentation function given by Equation 3.1 is employed for $q\bar{q}$ formation. The parameters a and b can be related to the average transverse momentum of the particle, which is proportional to the string constant as

$$\langle p_T^2 \rangle \propto \kappa = \frac{1}{b(2+a)} \tag{3.15}$$

For the string meting scenario, the free melted partons are hadronized via a simple coalescence model. The coalescence is invoked when the partons freeze-out, and based on their phase space proximity are combined into mesons or baryons. Conserving quark flavours and three momentum during coalescence, the coalescence probability of two and three (anti-)quark states are treated differently based on the population of formed mesons and baryons. The coalescence covers the formation of all particles listed in the HIJING program. The hadronization process takes place for 0.7 fm/c before the hadron cascade begins.

3.4.4 Hadron cascade

The final state hadron interactions are handled by the "A Relativistic Transport" (ART) [163] model, based on solving the equations of motion of the hadrons via a transport approach. The model includes a variety of elastic and inelastic scatterings between baryons and mesons. The model also produces resonances via these scatterings with cross-sections given by standard Breit-Wigner form, including the K^* resonance [164]. The baryon-baryon interactions also include $N\bar{N}$ and $(N\Delta N^*)(\bar{N}\bar{\Delta}\bar{N}^*)$ annihilation and pair production processes [164]. The ART model also include multi-strange baryons and ϕ meson production and decay processes. Multi-strange baryons occur via strangeness-exchange reactions

such as $\bar{K}(\Lambda\Sigma) \leftrightarrow \pi\Xi$, $\pi\Xi \leftrightarrow \pi\Omega$ [165]. The ϕ meson formation and decay to $K\bar{K}$ pair are considered by taking the cross-sections from a standard Breit Wigner form [166].

3.5 SMASH

The hadronic transport model SMASH, or "Simulating Many Accelerated Strongly interacting Hadrons" is a many-interaction model developed to extend the exploration of the QCD phase diagram to the low and intermediate beam energies [167]. In this regime, the prevailing degrees of freedom are that of hadrons. The interactions in SMASH are modeled by solving the non-equilibrium dynamics of hadrons. The relativistic Boltzmann equation

$$p^{\mu}\partial_{\mu}f_i(\mathbf{x},\mathbf{p}) + m_i F^{\alpha}\partial^{p}_{\alpha} f_i(\mathbf{x},\mathbf{p}) = C^{i}_{\text{coll}} \tag{3.16}$$

where f_i is the single particle distribution for species i that operates as test particles. F^{α} is the force experienced by individual particles with mass m_i, C^{i}_{coll} is the collision term. At low collision energies, $F^{\alpha} = -\partial^{\alpha}U(\mathbf{x})$ where $U(\mathbf{x})$ is the mean-field potential, while at high energies $F^{\alpha} = 0$. The collision criterion is similar to the one employed in the "Ultrarelativistic Quantum Molecular Dynamics" (UrQMD) approach [155], defined as

$$d_{\text{trans}} < d_0 = \sqrt{\frac{\sigma_{\text{tot}}}{\pi}} \tag{3.17}$$

where the total cross-section σ_{tot} depends on the center of mass energy of the colliding species, d_{trans} is the relative distance between the two colliding beams. Figure 3.6 shows the stages of evolution along the beam axis of an Au–Au collision at $E_{\text{kin}} = 0.8$ AGeV.

In the following sections, the general setup of the SMASH model is provided. SMASH can be operated in a hybrid mode, where an initial condition of the collision can be created, followed by a hydrodynamic evolution [168, 169]. In addition, SMASH also allows mean-field potential interactions which are sensitive to low energy collisions [167, 170].

3.5.1 Initial conditions

The treatment of the colliding nuclei species in SMASH is similar to AMPT, given by a Woods-Saxon distribution given by Equation 3.7. However, unlike AMPT, SMASH does not offer partonic degrees of freedom. The string model from PYTHIA8 is employed here to convert colliding nucleons to excited strings, which undergo fragmentation to produce further hadrons. Moreover, initial conditions [167, 169] in SMASH can be generated for a constant proper time τ_0, given by

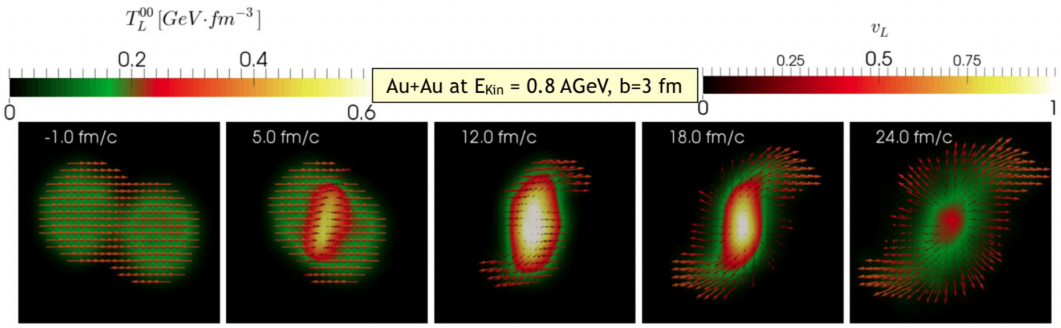

Figure 3.6: Stages of an Au–Au collision along the beam axis at $E_{\rm kin} = 0.8$ AGeV, with impact parameter $b = 3$ fm in the SMASH transport model at different time stamps of the collision. Figure taken from [167].

$$\tau_0 = \frac{R_p + R_t}{\sqrt{\left(\frac{\sqrt{s_{\rm NN}}}{2m_{\rm N}}\right)^2 - 1}} \tag{3.18}$$

where R_p and R_t are the radii of projectile and target respectively, $\sqrt{s_{\rm NN}}$ is the collision energy and $m_{\rm N}$ is the nucleon mass. τ_0 corresponds to the passing time of the colliding nuclei, which marks the time when local thermal equilibrium is achieved. This hypersurface can be later utilized for a hybrid treatment with hydrodynamic evolution.

3.5.2 Hybrid treatment

Hybrid treatment in SMASH is carried out by the 3+1D viscous hydrodynamic model, vHLLE [171]. The model solves the energy-momentum tensor relations while conserving net-baryon ($N_{\rm B}$), net-charge ($N_{\rm Q}$), and net-strangeness ($N_{\rm S}$) as,

$$\partial_\nu T^{\mu\nu} = 0 \tag{3.19}$$

$$\partial_\nu N^\nu_{\rm B} = 0, \quad \partial_\nu N^\nu_{\rm Q} = 0 \quad , \partial_\nu N^\nu_{\rm S} = 0 \tag{3.20}$$

leading to the complete relation as

$$T^{\mu\nu} = \epsilon u^\mu u^\nu - \Delta^{\mu\nu}(p + \Pi) + \pi^{\mu\nu} \tag{3.21}$$

where $T^{\mu\nu}$ is the energy-momentum tensor, ϵ is the local energy density in the rest frame, p and Π are the equilibrium and bulk pressures respectively, and $\pi^{\mu\nu}$ is the shear stress tensor. vHLLE solves the relativistic viscous hydrodynamic equations in the second-order Israel-Stewart framework in a 14-momentum approximation [172, 173], with shear-bulk coupling terms. The relaxation type equations for viscous corrections can be written as

$$\begin{aligned} D\Pi &= \frac{-\zeta\theta - \Pi}{\tau_\Pi} - \frac{\delta_{\Pi\Pi}}{\tau_\Pi}\Pi\theta + \frac{\lambda_{\Pi\pi}}{\tau_\Pi}\pi^{\mu\nu}\sigma_{\mu\nu}, \\ D\pi^{\langle\mu\nu\rangle} &= \frac{2\eta\sigma^{\mu\nu} - \pi^{\mu\nu}}{\tau_\pi} - \frac{\delta_{\pi\pi}}{\tau_\pi}\pi^{\mu\nu}\theta + \frac{\phi_7}{\tau_\pi}\pi_\alpha^{\langle\mu}\pi^{\nu\rangle\alpha} - \frac{\tau_{\pi\pi}}{\tau_\pi}\pi_\alpha^{\langle\mu}\sigma^{\nu\rangle\alpha} + \frac{\lambda_{\pi\Pi}}{\tau_\pi}\Pi\sigma^{\mu\nu} \end{aligned} \tag{3.22}$$

where θ is the expansion scalar, $\sigma^{\mu\nu}$ is the stress tensor, τ_π and τ_Π are the relaxation times for the shear and bulk corrections, and $\Lambda_{\Pi\pi}$, $\Lambda_{\pi\Pi}$, $\delta_{\pi\pi}$, $\tau_{\pi\pi}$ and ϕ_7 are higher order couplings. The evolution with SMASH is computed on fixed values of shear viscosity over entropy density, with initialization from the particle list of initial conditions created by SMASH. Two Gaussian smearing parameters, $R_\perp$, and R_η are used to tune the Gaussian smearing kernel, in order to prevent shocks during the evolution. The fluid elements are treated with a chiral EoS [174], which is matched with a hadron resonance gas EoS at low energy densities. The evolution is performed until the energy density of the fluid drops below a critical value $\epsilon_{\text{crit}} = 0.5$ (GeV/fm^3). The CORNELIUS subroutine [175] is used to create the corresponding freezeout hypersurface.

3.5.3 Hadron sampler

The fluid elements from the hydrodynamic evolutions are transformed to hadrons via a particlization technique. The smash-hadron-sampler [176] is employed for this purpose, which invokes the properties of a hadron resonance gas EoS. A grand canonical ensemble approach is used, so that each fluid surface element is particlized independently. Cooper-Frye formula [177] is applied to sample the momentum of each hadron based on its relative abundances (N) from the thermal average of the ensemble.

$$\frac{\mathrm{d}N}{\mathrm{d}\mathbf{p}} = \frac{d}{(2\pi)^3}\int_\Sigma [f_0(x,\mathbf{p}) + \delta f_{\text{shear}}(x,\mathbf{p}) + \delta f_{\text{bulk}}(x,\mathbf{p})]\frac{p^\mu \mathrm{d}\Sigma_\mu}{E_\mathbf{p}} \tag{3.23}$$

where $\mathbf{p}$, p^μ are the 3- and 4-momentum, with energy $E_\mathbf{p}$, d is the degeneracy factor, $\mathrm{d}\Sigma_\mu$ is the normal vector to a particlization hypersurface path, f_0 is a single particle distribution in vacuum, and $\delta f_{\text{shear/bulk}}$ are the viscous and bulk corrections respectively.

3.5.4 Mean-field potentials

SMASH provides the ability to tune the interaction potentials between the colliding nucleons via Skyrme parameterizations of the EoS [178, 179]. The parameterizations are achieved by tuning the stiffness of the EoS [170]. These methods provide a realistic simulation of low energy collisions. The general collision setup of SMASH is adopted with a test particle ansatz. However, to create mean field potentials, the number of test-particles can be increased to generate "local" effects [167]. The Skyrme and symmetry potential in SMASH is expressed as

$$U = U_{\rm sk} + U_{\rm sym} \tag{3.24}$$

which, individually, are written as

$$U_{\rm sk} = A\left(\frac{\rho_B}{\rho_0}\right) + B\left(\frac{\rho_B}{\rho_0}\right)^{\tau} \tag{3.25}$$

$$U_{\rm sym} = \pm 2 S_{\rm pot} \frac{\rho_{I_3}}{\rho_0} \tag{3.26}$$

where ρ_B is the net baryon density, $\rho_0 = 0.168$ fm^{-3} is the nuclear ground state density, ρ_{I_3} is the density of the relative isospin projection. A (soft) hard EoS corresponds to a (smaller) larger value of compressibility (K), which is tuned via the parameters A, B, and τ, the values for which are studied and used in references [170, 179].

Chapter 4

Charm production in proton–proton collisions

This chapter is focused on a multi-differential study of D-meson production with event properties in pp collisions. The analysis is carried out on the data collected by ALICE during Run-2 of the LHC, at the center of mass energy $\sqrt{s}$ = 13 TeV. The production of heavy-flavours, which is a 'hard' process is investigated as a function of event observables such as charged-particle multiplicity and transverse spherocity. The contents of the chapter are adapted from two approved analyses in the ALICE collaboration where D-mesons viz., D^0, D^+, and D^{*+} are collectively studied, which allows for a comprehensive measurement of D-meson species lying in the same mass range. The work done in this thesis pertains to measurement of the D^0 meson, which is combined with two separate analyses for D^+ and D^{*+} performed by collaborators from ALICE.

4.1 Physics motivation

Differential measurements in heavy-flavour production with event variables lead to further insight into the interplay of hard and soft components of particle production. Event variables such as charge-particle multiplicity and transverse spherocity allow classification of hard processes and the underlying event (UE). Studies at NA27 collaboration suggested a strong correlation between charm production with the event activity for 400 GeV/c proton–proton collisions, showing a 20% rise in event multiplicities that have charm hadrons [180]. The collision centrality was considered a deciding factor here, leading to larger multiplicities and higher rates of hard processes. However, it was later believed that multiparton interactions (MPIs) could play a major role at higher multiplicities. A typical pp collision event at the LHC can have around 4-6 MPIs [150], which has a defining role in describing the charged-particle multiplicity in pp collisions. Although

MPI is independent of heavy-flavour production, some studies hinted at a possible role of a hard scale MPI in charm production [181]. String fragmentation models like PYTHIA6, PYTHIA8, and HERWIG [89, 147, 148] that involve MPI, validated the experimental findings of its contribution to the UE and ultimately, charged-particle multiplicity [182, 183]. Measurements from ALICE showed a *stronger than linear* rise of charm meson yields as a function of charged-particle multiplicities in pp collisions at $\sqrt{s}$ = 7 TeV [181, 184]. Until recently, arguments on *auto-correlation* effects and their role in the trends of charm hadron yields have been heavily discussed [185, 186]. Generally, charged-particle production also correlates to the same hard scattering from which the heavy-flavours are produced. The components of such effects appear in the form of initial- or final-state radiations, decays of heavy-flavour hadrons, and jet-fragmentation, which generate an auto-correlation between the heavy-flavour yields and charged particles in the pp collision. The presence of these effects drives the heavy-flavour yields in a stronger than linear behavior with charged-particle multiplicities.

The interest in looking into the intricacies of particle production in pp collisions is enhanced with event classifiers that allow the disentangling of the charm production processes from the UE. Event shapes provide information on the energy distribution in an event, which means particle production could be classified into hard and soft events based on the azimuthal topology of the charged tracks in an event [187–189]. Generally, an event with one or more hard scatterings will produce back-to-back jets, which can be explained by pQCD approaches. In contrast, the UE with multiple soft scatterings will lead to an isotropic azimuthal topology. As heavy-flavours are produced via hard scatterings, scanning its production across events with *jet-likelihoods* to isotropic distributions allows the categorization of the production in pQCD and non-pQCD regimes of particle production while examining its interplay with event multiplicity. First measurements on jet production with event shapes were performed at the CERN Inner Storage Rings (ISR) and the proton anti-proton collider (Sp$\bar{\text{p}}$S) [190–192], followed by deep inelastic collision experiments aimed to extract α_{s} and perform tests to pQCD calculations [193–195]. Experiments at the LHC have also performed jet and particle production measurements utilizing event shape variables such as sphericity or transverse thrust [183, 196, 197].

In this thesis, charm production is measured via D-mesons in pp collisions with ALICE to perform a differential study with event multiplicity and transverse spherocity. The D-mesons are reconstructed using particle identification (PID) techniques at mid-rapidity, in the central barrel region of ALICE. The extracted yields are corrected for the selection efficiencies and detector acceptances while considering the systematic effects. The upcoming sections are dedicated to discussing the general strategies pertaining specifically to the measurement of the D^0 meson.

4.2 Datasets and event selection

The multiplicity and transverse spherocity dependent analyses in pp collisions at $\sqrt{s}$ = 13 TeV are performed on the data collected by ALICE during the Run-2 of the LHC during the years 2016, 2017, and 2018. The available statistics amounts to 1.82×10^9 MB triggered events, corresponding to an integrated luminosity of $\mathcal{L}_{\rm int}$ = 32 nb^{-1} with a total cross-section of $\sigma_{\rm MB}$ = 57.95 mb. Apart from the MB-triggered events [132], the multiplicity analysis requires a high multiplicity dataset, obtained from the HMSPD triggered, which constitutes a total of 300×10^6 events. The Monte Carlo (MC) datasets, anchored to the Run-2 periods, are used for the efficiency corrections. Two types of MC datasets are used; one that is enriched with heavy-flavour pairs ($c\bar{c}$, $b\bar{b}$) and the other is a general-purpose kind.

Events with a reconstructed primary vertex and global tracks are used for both analyses. The selected events need to have the reconstructed primary vertex within ±10 cm from the nominal position of the beam line ($|z_{\rm vtx}| < 10$ cm). A condition to reject multiple interactions vertices in a collision, also known as in-bunch *pile-up* events is applied.

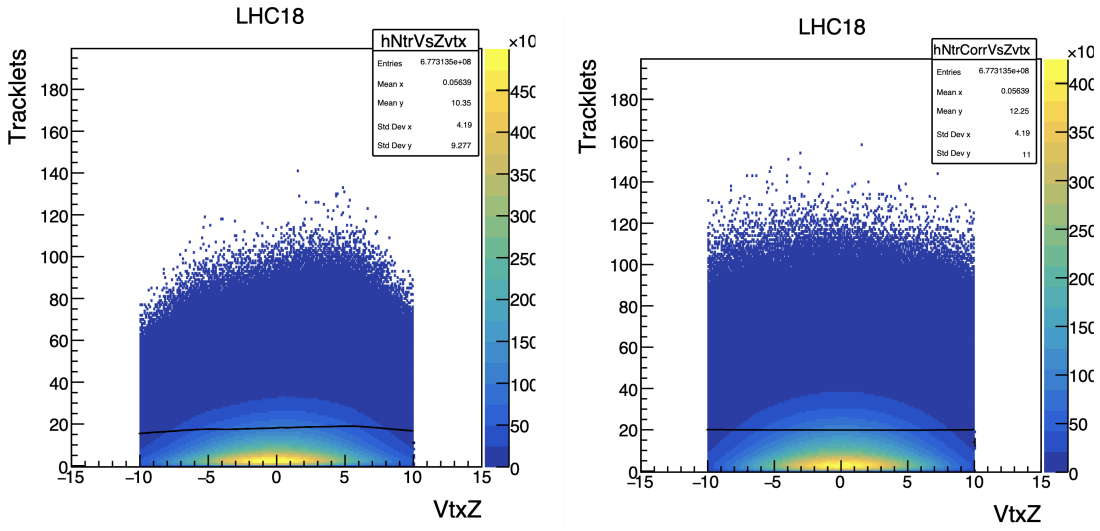

Figure 4.1: 2D correlation distributions of $N_{\rm tracklet}$ and $z_{\rm vtx}$ superimposed by the average $N_{\rm tracklet}$ profile (in black) for 2018 MB triggered data sample before (Left) and after (Right) $z_{\rm vtx}$ correction.

4.3 Event variables

4.3.1 Charged-particle multiplicity

The charged-particle multiplicity is estimated with the number of reconstructed tracklets[9] (N_{tracklet}) of the SPD within the pseudorapidity interval $|\eta| < 1$. Due to inefficiencies of the detector, the N_{tracklet} distributions show a dependence with the reconstructed z_{vtx}. This is corrected by taking the yearwise profile of each run period and weighing it to the run with the highest efficiency [181, 184]. Due to detector aging, 2016 showed the highest efficiency, gradually decreasing by 2018. The uncorrected N_{tracklet} values (N_{raw}) are corrected event by event with the formula

$$N_{\text{corr}} = N_{\text{raw}} \frac{\langle N_{\text{ref}} \rangle}{\langle N_{\text{period}(z)} \rangle} \tag{4.1}$$

where $\langle N_{\text{ref}} \rangle$ is the mean number of N_{tracklet} from LHC16h, which takes the values 12.25 for MB triggered selection and 55.05 for the HMSPD triggered sample. $\langle N_{\text{period}(z)} \rangle$ is the mean N_{tracklet} for events with vertex at a given value of z for the run period under consideration. Following Poisson statistics, an integer value of N_{corr} is obtained from Equation 4.1. The corrected profiles, in contrast to the uncorrected ones as a function of z_{vtx} for each year and triggered sample, are reported on the right and left panel of Figure 4.1, respectively. The corrected N_{tracklet} profiles are rid of the z_{vtx} dependence, showing a flat dependence. In Figure 4.2, the ratio of N_{tracklet} distributions of 2017 and 2018 distributions to 2016 are shown before and after z_{vtx} correction for the MB triggered sample. The HM N_{tracklet} distribution is shown together with the 2018 distribution in the same figure, showing the shift in the mean N_{tracklet} value.

The definition of multiplicity till this point is not a physical observable that can be used for a global understanding. The physical primary observable is the charged-particle multiplicity density ($\mathrm{d}N_{\text{ch}}/\mathrm{d}\eta$). The conversion is performed with MC simulations on the general purpose dataset choosing the physical-primary charged particles (N_{ch}) and drawing a 2D correlation with the N_{tracklet} distribution within $|\eta| < 1$ [181, 184]. The correlation distribution of N_{ch} vs N_{tracklet} is shown in Figure 4.3, which presents a positive linear correlation. The N_{tracklet} intervals considered for the multiplicity-dependent analysis are reported in Table 4.1. The $\mathrm{d}N_{\text{ch}}/\mathrm{d}\eta$ intervals are extracted by performing a global first-order polynomial fit to a profile weighted by the RMS of the projected N_{ch} distribution in the respective N_{tracklet} intervals. The fit parameters are used to convert the N_{tracklet} to N_{ch}. Corresponding to each N_{tracklet} interval, the corresponding limits of $\mathrm{d}N_{\text{ch}}/\mathrm{d}\eta$, the $\langle \mathrm{d}N_{\text{ch}}/\mathrm{d}\eta \rangle$, and the relative or self-normalized multiplicity and the associated statistical and systematic errors are reported in Table 4.1. The self-normalized multiplicity is

[9] Two subsequent hits in the SPD joined to reconstructed primary vertex constitute a tracklet

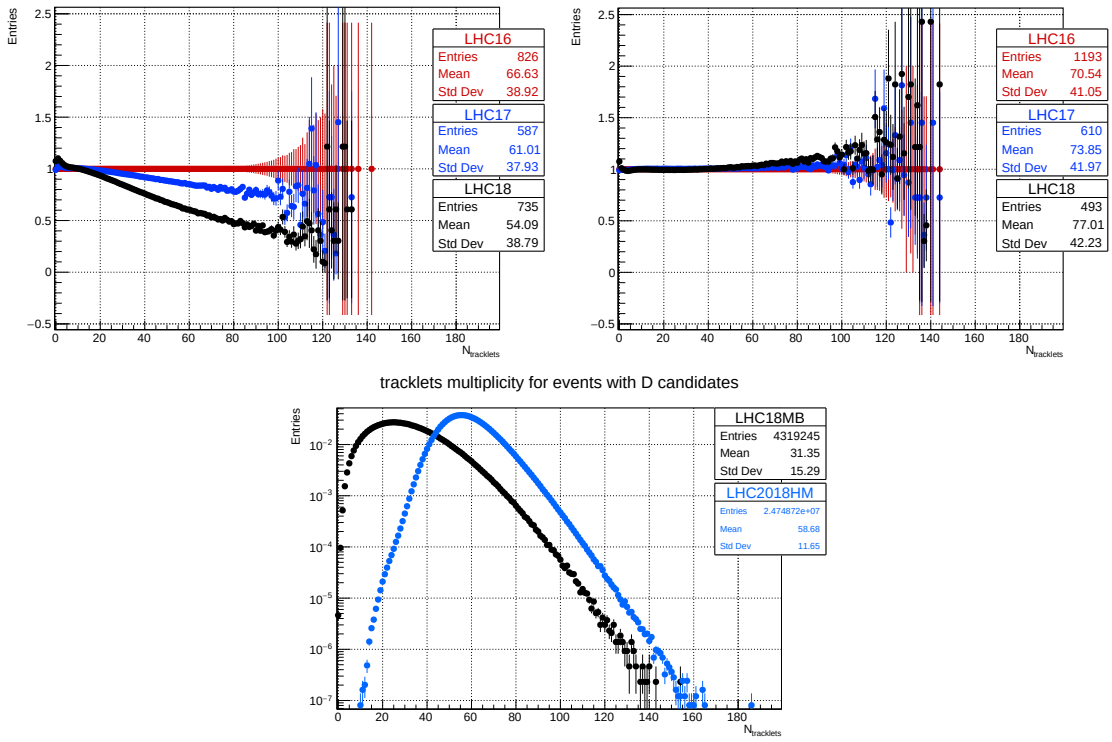

Figure 4.2: (Left) Ratio of uncorrected N_{tracklet} distributions in 2016, 2017, 2018 MB triggered sample to 2016 N_{tracklet} distribution. (Center) Ratio of N_{tracklet} distributions after z_{vtx} correction. (Right) Comparison of N_{tracklet} distribution from 2018 MB (black) and HMSPD (blue) triggered sample.

the $\langle \mathrm{d}N_{\text{ch}}/\mathrm{d}\eta \rangle$ for a corresponding N_{tracklet} interval, normalized by the multiplicity of the MB or multiplicity integrated ($1 < N_{\text{tracklet}} < 199$) sample. The $\langle \mathrm{d}N_{\text{ch}}/\mathrm{d}\eta \rangle_{\text{INEL}>0}$ corresponding to the integrated multiplicity sample is $7.42 \pm 0.02\,(\text{stat}) \pm 0.001\,(\text{syst})$ [198, 199].

4.3.2 Transverse spherocity

Based on the geometrical p_{T} distribution of charged hadrons in an event, an event's energy flow can be measured using event shape variables [187–189]. An event dominated by hard scattered processes will have a jetty-like or pencil-like topology, while the underlying event comprising soft scatterings gives an isotropic topology. One of the first event shape observables is *transverse thrust* [200], defined as

$$T_{\perp} = \max_{\hat{n}_{\text{T}}} \frac{\sum_i |\vec{p}_{\text{T}_i} \cdot \hat{n}_{\text{T}}|}{\sum_i p_{\text{T}_i}} \tag{4.2}$$

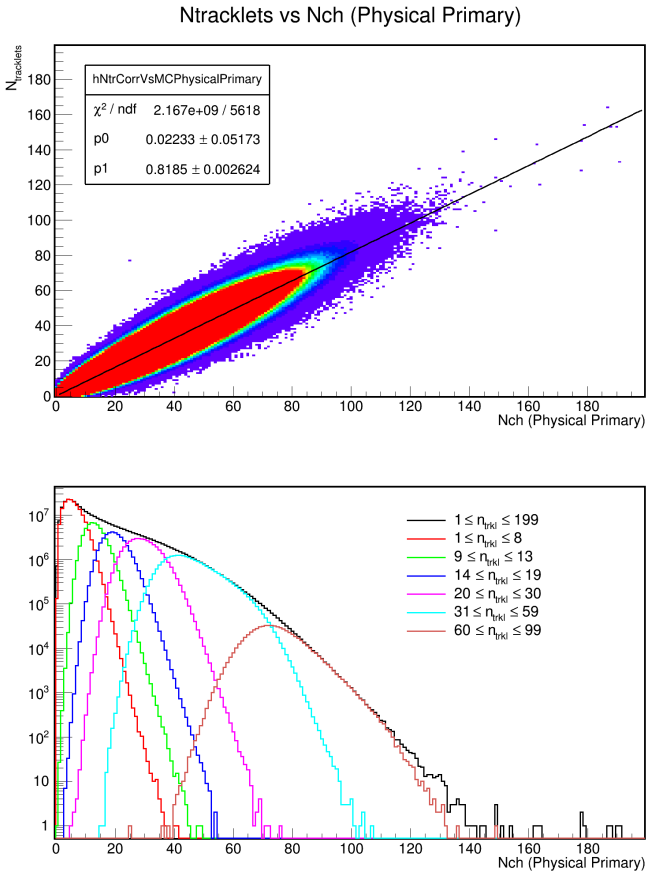

Figure 4.3: (Top) 2D correlation distribution between N_{tracklet} and physical primary charged-particles from general purpose MC samples with a global linear fit (black). (Bottom) Charged-particle multiplicity distribution with the limits corresponding to N_{tracklet} intervals obtained from individual linear fits to every N_{tracklet} interval.

where p_{T} represents the transverse momentum of a track, and $\hat{n}_{\text{T}}$ is the unit vector along the thrust axis which is perpendicular to the beam axis. The transverse thrust axis $\hat{n}_{\text{T}}$ and the beam axis together form the event plane, and then the to-be-maximized ratio defines the out-of-plane energy flow. This concept can be reformulated into *transverse spherocity* [201–203], where the energy flow can be measured in the direction mutually perpendicular to the direction of the event plane.

$$S_{\text{O}} = \frac{\pi^2}{4} \min_{\vec{n}=(n_x,n_y,0)} \left(\frac{\sum_i |\vec{p}_{\text{T}_i} \times \hat{n}|}{\sum_i p_{\text{T}_i}} \right)^2, \quad S_{\text{O}} = \begin{cases} 0, & \text{“ jetty” limit (hard events)} \\ 1, & \text{“ isotropic” limit (soft events)} \end{cases} \tag{4.3}$$

N_{tracklet}	$\mathrm{d}N_{\text{ch}}/\mathrm{d}\eta^{\text{max}}_{\text{min}}$	$\langle \mathrm{d}N_{\text{ch}}/\mathrm{d}\eta \rangle$ ± stat	$\langle \mathrm{d}N_{\text{ch}}/\mathrm{d}\eta \rangle / \langle \mathrm{d}N_{\text{ch}}/\mathrm{d}\eta \rangle_{\text{INEL>0}}$ ± stat ± syst	Trigger
1-8	0.55 - 4.86	2.87 ± 0.02	0.39 ± 0.003 ± 0.03	MB
9-13	5.47 - 7.93	6.59 ± 0.04	0.89 ± 0.006 ± 0.01	MB
14-19	8.55 - 11.62	9.88 ± 0.06	1.33 ± 0.009 ± 0.01	MB
20-30	12.23 - 18.38	14.59 ± 0.10	1.97 ± 0.014 ± 0.02	MB
31-59	19.23 - 36.21	22.64 ± 0.17	3.05 ± 0.024 ± 0.03	MB
60-99	36.83 - 60.8	37.77 ± 0.47	5.10 ± 0.065 ± 0.03	HMSPD

Table 4.1: Summary of N_{tracklet} intervals, the corresponding charged-particle multiplicity density intervals, the average charged-particle multiplicity density, and the self-normalized multiplicity used in the D-meson vs multiplicity analysis. The associated statistical and systematic uncertainties are also quoted along with the respective triggers for each N_{tracklet} interval.

where $\hat{n}$ is the direction that minimizes the entire quantity for an event. The factor $(\pi^2/4)$ normalizes the minimized ratio from 0 to 1, from a jetty-like to an isotropic structure. A pictorial depiction of the two limits of transverse spherocity is shown on the top panel of Figure 4.4. Due to its design in the transverse plane, transverse spherocity is collinear and infrared safe, which is essential to perform perturbative QCD calculations [204].

Equation 4.3 is subjected to a neutral p_{T} bias in an event. This refers to the neutral tracks present in the event, which can be overlooked during the spherocity calculation. To remove this, an "unweighted"-p_{T} definition of spherocity is introduced [202]. The quantity is measured similarly to S_{O} with only the azimuthal angular component of the tracks

$$S_{\text{O}}^{p_{\text{T}}=1.0} = \frac{\pi^2}{4} \min_{\vec{n}=(n_x,n_y,0)} \left(\frac{\sum_i |\hat{p}_{\text{T}_i}|_{p_{\text{T}}=1.0} \times \hat{n}|}{N_{\text{tracks}}} \right)^2 \tag{4.4}$$

Keeping a statistical advantage, the spherocity dependent analysis is performed on three MB triggered multiplicity (N_{tracklet}) classes. The normalized $S_{\text{O}}^{p_{\text{T}}=1.0}$ distributions in each N_{tracklet} interval are presented on the bottom panel of Figure 4.4, where the reconstructed and true $S_{\text{O}}^{p_{\text{T}}=1.0}$ distributions, along with the corresponding distributions with D-meson candidate selections are shown. These $S_{\text{O}}^{p_{\text{T}}=1.0}$ distributions are calculated on a dataset with a 'TPC-only + TPC-refit' track selection criteria, which will be discussed in the upcoming sections. The $S_{\text{O}}^{p_{\text{T}}=1}$ distributions present the archetype regions of jetty and isotropic regions, with higher occupancy lying for the latter. Without any candidate selection, the distributions differ between the multiplicity selections, with increased entries

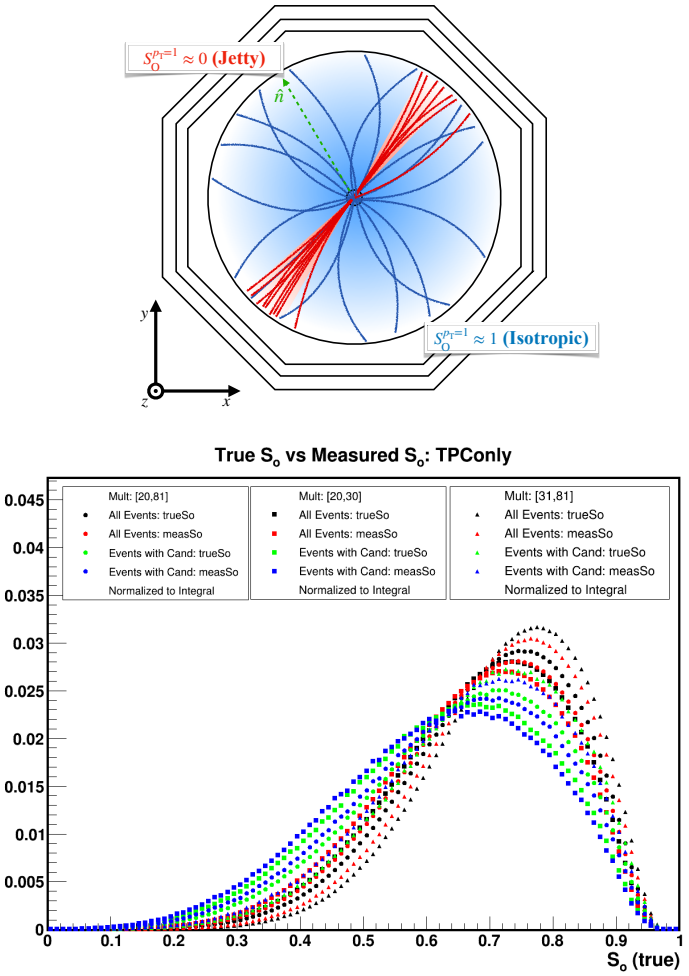

Figure 4.4: (Top) Visualization of an event with jetty-like (red) and isotropic topologies (blue). (Bottom) $S_{\mathrm{O}}^{p_{\mathrm{T}}=1}$ distributions in the $20 < N_{\mathrm{tracklet}} < 30$, $31 < N_{\mathrm{tracklet}} < 81$, and $20 < N_{\mathrm{tracklet}} < 81$ intervals representing reconstructed and generated samples, along with D-meson candidate selection.

in the isotropic class for high multiplicity events. The events with a D-meson candidate selection, the number of entries on the jetty side increases, as these events are almost always accompanied by a hard scattered $\mathrm{c\bar{c}}$ pair.

Spherocity quantiles calculation

The spherocity distributions between the reconstructed and the generated data contain an inherent asymmetry. To overcome this, the spherocity values are eventually converted to

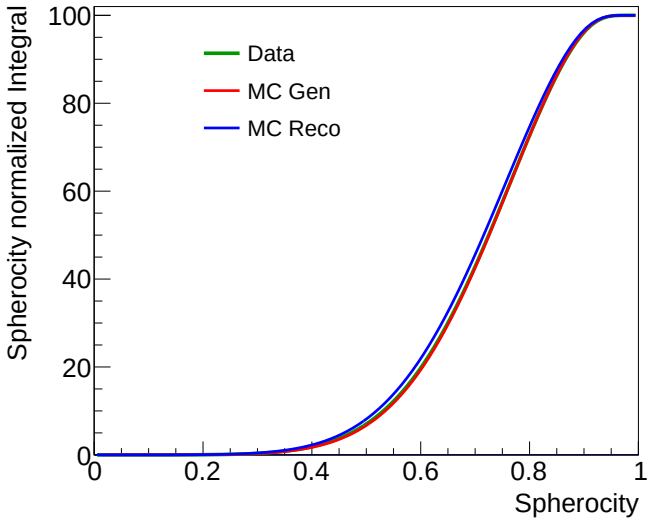

Figure 4.5: Cubic splines calculated from the unweighted spherocity distributions on the $20 < N_{\text{tracklet}} < 81$ interval for data (Green), MC generated (Red), and MC reconstructed (Blue) samples.

spherocity quantiles, which removes these efficiency biases by providing a coherent comparison between reconstructed and generated data. The spherocity values are converted to *cubic splines* with extremely fine intervals to reproduce the full shape of the interpolation. Three splines are defined to convert the spherocity distribution in each N_{tracklet} interval of the pp raw data and the general purpose MC reconstructed and generated samples. The conversion to splines is performed per multiplicity interval because the spherocity distributions are sensitive to the N_{tracklet} selection. In the MB triggered sample, this would cause a bias in the balance of the quantiles[10]. The conversion is performed with the following relation

$$y_i^{\text{spl}} = 100 \cdot \frac{h_0^i}{h_{\text{int}}}, \tag{4.5}$$

where h_0^i is the sum of the calculated spherocity values of selected events from 0 to i^{th} spherocity and h_{int} is the integral of the distribution. The splines obtained from pp data and MC samples are shown in Figure 4.5 for the $20 < N_{\text{tracklet}} < 81$ interval. For the analyses, the spherocity quantile (S_{O}-Quantile) intervals are defined into uniform intervals 0–25%, 25–50%, 50–75%, 75–100%.

[10] This has been tested with the number of events in spherocity quantile intervals of same bin width are not the same using multiplicity independent splines.

4.4 Analysis strategy and signal extraction

D^0 mesons are reconstructed in the central rapidity region from its charged hadronic decay channel $D^0 \rightarrow K^-\pi^+$ (BR 3.89 ± 0.04%) [20]. The signal extraction strategy of D^0 is based on displaced decay topologies, which refer to the decay topology of D^0. Before this, a standard selection criteria is applied to select the reconstructed charged tracks [205]. These generally involve selections at the level of detector clusters, acceptance, and track reconstruction. A summary of the general selections is presented in Table 4.2. These tracks are selected to be in the acceptance $|\eta| < 0.8$ with $p_T > 0.3$ GeV/c. However, as shown in Figure 4.6 the selection criteria reduce the D^0 meson acceptance, which drops steeply to zero for $|y_{lab}| > 0.5$ at low p_T and for $|y_{lab}| > 0.8$ at $p_T > 5$ GeV/c. A p_T-dependent *fiducial* acceptance region is therefore defined as $|y_{lab}| < y_{fid}(p_T)$, with $y_{fid}(p_T)$ increasing from 0.5 to 0.8 in the transverse momentum range $0 < p_T < 5$ GeV/c according to a second order polynomial function, and $y_{fid} = 0.8$ for $p_T > 5$ GeV/c.

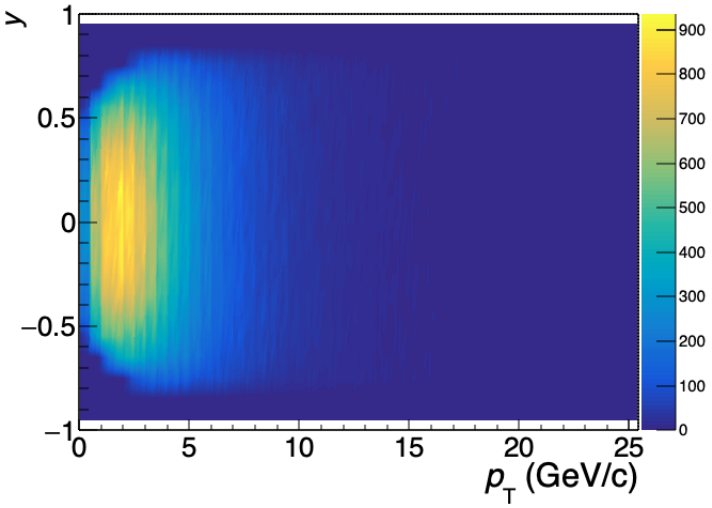

Figure 4.6: 2D correlation of generated rapidity (y) and p_T of D^0 mesons in pp collisions at $\sqrt{s} = 13$ TeV.

The PID selection strategy uses the information on specific energy deposit (dE/dx) in the Time Projection Chamber (TPC) [125] and on the time of flight measured by the Time-of-Flight (TOF) [127] detector. The TOF detector allows a reliable identification of kaons and pions in a wide momentum range up to 2 GeV/c. A combination of strong and conservative cuts are applied to the kaon and pion tracks decaying from D^0. The strategies are shown in Table 4.3, where a response of -1, 0 or +1 is assigned to each mass hypothesis, based on the comparison of the measured value of Nσ to $N_\sigma^{\text{TPC, max}}$. Moreover,

Variable	Condition
$\|\eta\|$	<0.8
p_{T} (GeV/c)	>0.3
Number of TPC crossed rows	$\geq$ 70
TPC crossed rows/ findable clusters	$\geq$ 0.8
TPC χ^2/ndf	<2
Minimum number of ITS layers	2
ITS refit	Yes
TPC refit	Yes

Table 4.2: Summary of general track selection criteria.

p_{T} range (GeV/c)	$N_{\sigma}^{\mathrm{TPC,\ max}}$	
	Strong	Conservative
p_{T} < 0.6	2	3
0.6 <p_{T} < 0.8	1	3
p_{T} > 0.8	2	3

Table 4.3: Strong and conservative PID selection criteria with the TPC based on different p_{T} momentum intervals of the decay tracks.

a 3σ compatibility cut is applied to the D^0 daughters for both TPC and TOF. These tasks are based on an optimization of the *topological* and kinematic cuts and application of the PID selection to the D^0 candidates and decay daughter distributions.

The yield extraction is performed with a topological selection strategy with high efficiency and high statistical significance for the D^0 meson signal. Topological variables are p_{T} dependent due to the large combinatorial background from the low p_{T} tracks, while the D^0 signal is significant at high p_{T} (before applying the topological selections). The D^0 measurement is performed by reconstructing pairs of Kπ tracks with the correct charge-sign combination. A detailed description of the p_{T} dependent selection cuts and values are shown in Table 4.4.

The general set of track selections are common for both analyses, independent of multiplicity and transverse spherocity. Before obtaining the final results, the spherocity analysis is checked with two track selections, a *hybrid* approach, where the tracks reconstructed with both TPC and ITS are considered, and a *TPC-only + TPC-refit* scenario, where only the TPC-refit tracks are taken for the calculation of spherocity. With the generated and reconstructed spherocity distributions, both the track selection criteria are checked with a correlation distribution of true and measured spherocity, as shown in Figure 4.7. At large values of spherocity, the hybrid tracks deviate from the diagonal, causing a drop in

Topological quantity	p_{T} interval (GeV/c)				
	1-2	2-4	4-6	6-12	12-24
p_{T}^{K} (GeV/c)	>0.5	>0.7	>0.7	>0.7	>0.6
p_{T}^{π} (GeV/c)	>0.5	>0.7	>0.7	>0.7	>0.6
$\cos\theta_{\mathrm{pointing}}$	>0.7	>0.9	>0.85	>0.85	>0.8
$d_0 \times d_0(\mu\mathrm{m}^2)$	<-2000	<-2000	<-5000	<-5000	–
DCA (cm)	<350	<300	<300	<300	<300
$\cos\theta^*$	<0.8	<0.8	<0.8	<0.9	<1

Table 4.4: Topological variables and their selections in different p_{T} intervals applied to the D^0 meson decay daughter tracks.

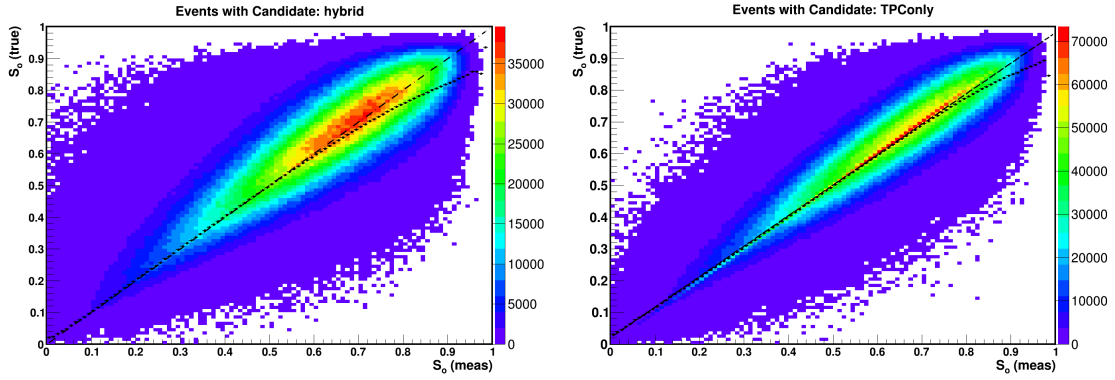

Figure 4.7: 2D correlation distribution of true and measured $S_{\mathrm{O}}^{p_{\mathrm{T}}=1}$, with hybrid tracks (Left) and TPC-only + TPC refit tracks (Right).

the measured spherocity, possibly due to asymmetrical statistical distribution at the edges. The TPC-only tracks show a narrower correlation and a comparatively low deviation between the diagonal and the most probable value, ultimately being the choice of spherocity track selections.

The D^0 yields are extracted with a fit to the invariant mass distribution of the $\mathrm{K}^-\pi^+$ tracks, corresponding to the true D^0 candidates with a nominal value of $m_{\mathrm{inv}} = 1.866 \pm 0.20$ GeV/c^2 [20]. The fitting function of D^0 contains an exponential term for the background and a Gaussian function for the signal. The standard deviation for all fits is fixed from the fit from the MB sample. The D^0 yield is corrected for the reflected Kπ signal to account for the wrong mass hypothesis. The amount of reflected Kπ concerning the D^0 signal is taken from the Monte Carlo analysis, the invariant mass distribution of which is fitted with two Gaussian functions. The reflected spectra can change the shape of the background and increase the width of the Gaussian signal, which makes a difference in signal extraction. In Figure 4.8, an example of the invariant mass distributions from the multiplicity dependent

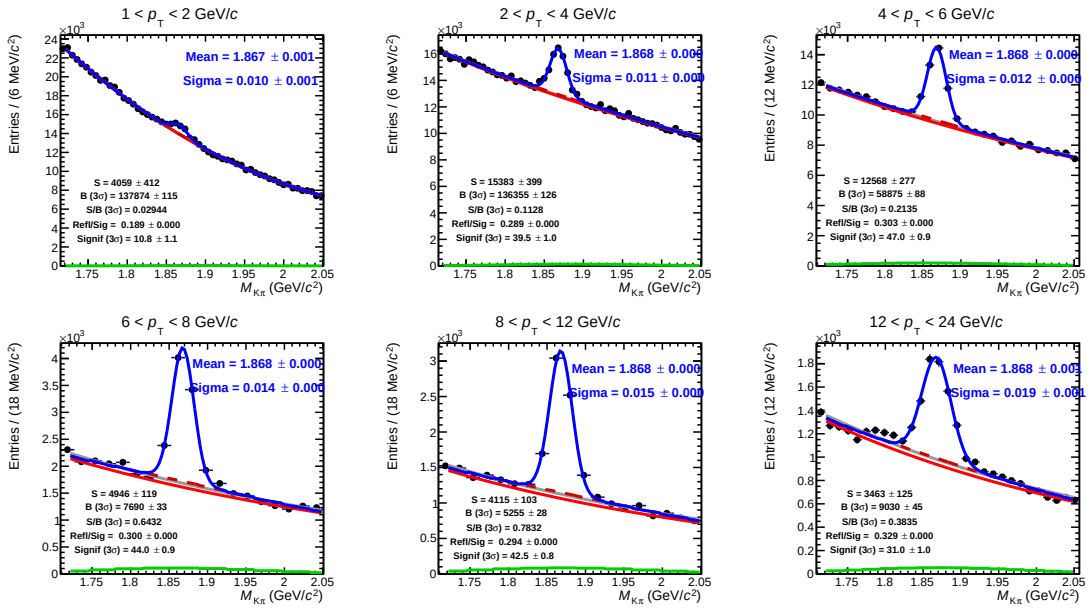

Figure 4.8: D^0 invariant mass distributions in different p_T intervals for 60 $< N_{\text{tracklet}} <$ 99. Data points are fitted with a Gaussian signal function (blue) and an exponential background function (red), superimposed with the reflected spectra (green). The dashed and solid lines represent the background before and after subtracting the contribution of reflected signal.

analysis is shown; the blue lines are the Gaussian fits of the signal, and the red (solid) lines are the fitted background subtracted with the contribution from the reflected spectra. The red (dashed) lines represent the un-subtracted background due to the contribution from the reflections, which are shown in green. The raw yields are extracted in 6 p_T intervals between 1 to 24 GeV/c, divided into intervals as 1-2, 2-4, 4-6, 6-8, 8-12, 12-24 GeV/c for each N_{tracklet} interval in the multiplicity dependent analysis and for each N_{tracklet} and S_O-Quantile interval in the spherocity dependent analysis. The $1 < p_T < 2$ GeV/c interval is discarded for the spherocity analysis due to poor signal extraction in all D-mesons.

4.5 Acceptance and efficiency corrections

The raw yields extracted from the fits to the invariant-mass distributions of D^0 meson candidates are later used to obtain the self-normalized yields (Equation 4.10) of prompt D^0 mesons. The yields must be corrected with the selection efficiencies employed to reconstruct the D^0 mesons. The raw counts of D^0 mesons extracted in each p_T, multiplicity, and spherocity interval are corrected for the reconstruction and selection efficiency and detector acceptance. The reconstruction and selection efficiency depend on the multiplicity of charged particles produced in the collision since the primary vertex resolution and

the resolution on the topological selection variables improve at high multiplicity. As a consequence, the resolution of the topological selection variables (track impact parameter, particle decay length, pointing angle) that make use of the primary vertex position also improves with increasing multiplicity, introducing a multiplicity dependence in the selection efficiency. On the other hand, the corrections are sensitive to spherocity selections, which improve for jetty-like events than isotropic ones.

Efficiency and acceptance of D^0 are defined as

$$\mathcal{E} = \frac{N_{\mathrm{reco}}|_{|y|<y_{\mathrm{fid}}}}{N_{\mathrm{gen}}^{\mathrm{dau\ in\ acc}}|_{|y|<y_{\mathrm{fid}}}} \tag{4.6}$$

where, $N_{\mathrm{reco}}|_{|y|<y_{\mathrm{fid}}}$ is the number of reconstructed D^0 mesons after all the selections, $N_{\mathrm{gen}}^{\mathrm{dau\ in\ acc}}|_{|y|<y_{\mathrm{fid}}}$ is the number of generated D^0 mesons decaying in the decay channel of interest, having $|y| < y_{\mathrm{fid}}$, with two daughters that fulfil the acceptance requirements of $|\eta| < 0.9$ and $p_{\mathrm{T}} > 0.1$ GeV/c, belonging to the events with $|z_{\mathrm{vtx}}^{\mathrm{gen}}| < 10$ cm. Similarly, acceptance is defined as

$$\mathrm{Acc} = \frac{N_{\mathrm{gen}}^{\mathrm{dau\ in\ acc}}|_{|y|<y_{\mathrm{fid}}}}{N_{\mathrm{gen}}|_{y<0.5}} \tag{4.7}$$

where, $N_{\mathrm{gen}}|_{y<0.5}$ is the number of generated D^0 mesons in events with $|z_{\mathrm{vtx}}^{\mathrm{gen}}| < 10$ cm decaying in the decay channel of interest with $|y| < 0.5$. The product of acceptance and efficiency is computed per p_{T} bin for each multiplicity interval and used to correct the extracted D^0 raw yields.

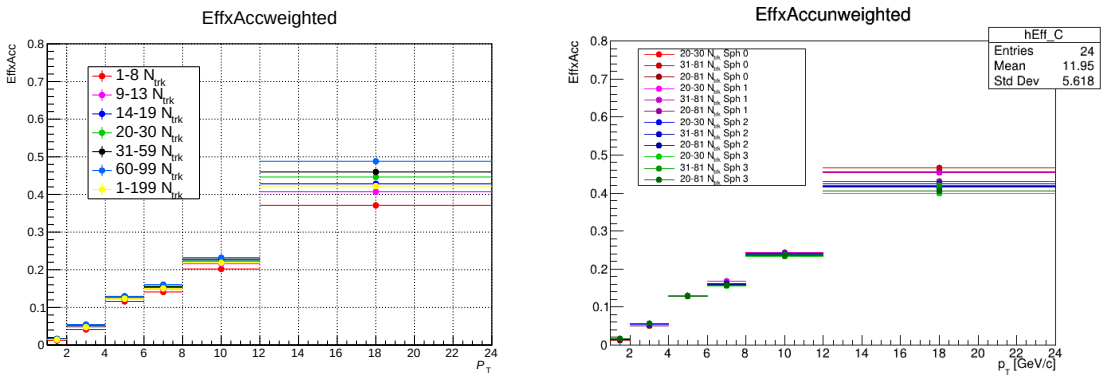

Figure 4.9: Acc $\times\, \mathcal{E}$ of prompt D^0 mesons as a function of p_{T} in different N_{tracklet} intervals (Left) and in different N_{tracklet} and S_{O}-Quantile intervals (Right).

The acceptance and efficiency correction factors, (Acc $\times\, \mathcal{E}$), are determined for the D-

meson using Monte Carlo simulations of pp collisions generated with the PYTHIA8 event generator with the Perugia-0 tune. The particles are propagated through the apparatus using the GEANT3 transport codes. The luminous region distribution and the conditions (active channels, gain, noise level, and alignment) of all the ALICE detectors are included in the simulations, also considering their evolution with time during the 2016, 2017, and 2018 LHC data taking periods. The anchored MC productions used to compute the Acc $\times \mathcal{E}$ only events containing a $c\bar{c}$ or a $b\bar{b}$ pair are transported through the apparatus and reconstructed. Moreover, the simulated N_{tracklet} distribution is weighted with the ratio of the N_{tracklet} distribution observed in data over that of MC's, accordingly. The weights are computed by selecting MC and data events with at least one D^0 meson candidate in the D^0 mass range. The weights are computed separately for each year, ensuring that they are compatible with each other. The prompt efficiencies versus p_T are calculated in the different N_{tracklet} and S_O-Quantile selections, as shown in Figure 4.9.

4.6 Systematic uncertainties

The analysis methods employed at various stages can lead to possible anomalies and biases that can cause a systematic effect on the results. In this section, the different sources of systematic uncertainties and their estimation procedure for multiplicity and spherocity dependent analyses are presented in detail. The common sources for both analyses include (i) raw yield extraction (ii) selection efficiencies (iii) feed-down (iv) MC p_T-shape, while (v) PID selection (vi) multiplicity weights are sources specific for multiplicity dependent analysis, while (vii) resolution of the primary vertex and (viii) dataset dependence are centered on the spherocity analysis. The estimation of the systematic uncertainties for the spherocity analysis is carried out in the 'wide' $20 < N_{\text{tracklet}} < 81$ interval and assigned the same for the individual N_{tracklet} intervals, to avoid large statistical fluctuations.

4.6.1 Raw yields extraction

The yield extraction systematic uncertainties are evaluated with a multi-trial approach, where the yields are extracted by varying the background fit function, the range of the invariant mass spectra, and variations in fit conditions. Among the variations, two methods of bin counting are considered: one in which the signal is extracted as the difference between the total histogram and the fit function of the background in the signal region and one in which the same procedure is performed considering the entire invariant mass region. Only fits with a reduced χ^2 below two for the D^0 meson were considered as a variation. The variations in the fit strategy for D^0 are reported in Table 4.5.

The summary of results from a multi-trial fitting shows the variation of the fit parameters (mean and sigma), along with the χ^2 and the ratio of the extracted yield in $14 < N_{\text{tracklet}} < 19$ over the $1 < N_{\text{tracklet}} < 199$ sample in $1 < p_T < 2$ GeV/c interval is presented in

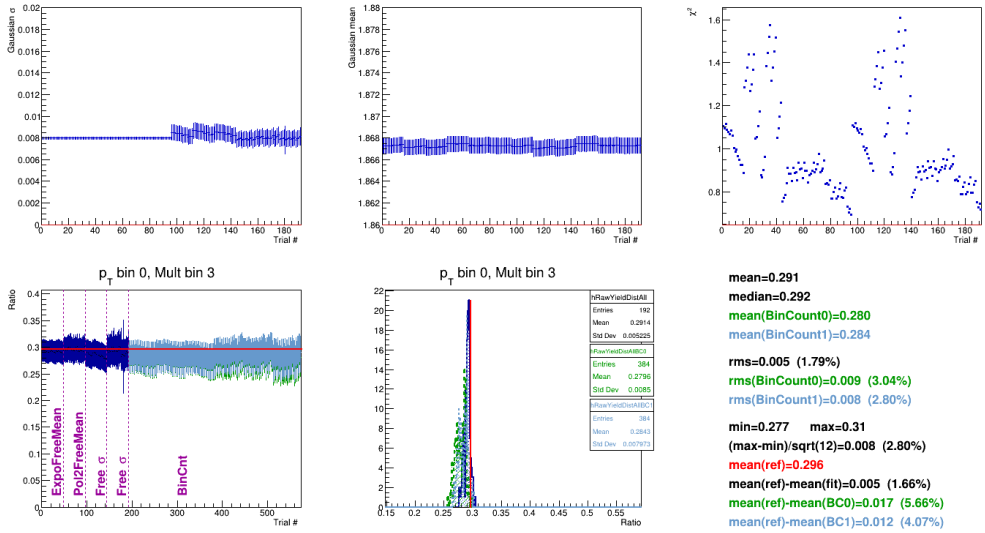

Figure 4.10: Summary of an output of the multi-trial fitter in the $20 < N_{\text{tracklet}} < 30$ and $1 < p_{\text{T}} < 2\,\text{GeV}/c$ interval. Top three panels (left to right) represent illustrate the Gaussian sigma (σ), mean, and the reduced-χ^2 of the fit. The bottom left and center panels show the ratio of the extracted raw yields in the give N_{tracklet} interval to the integrated one, and the right panel shows the test results of bin counting.

Lower bound Fit range (GeV/c^2)	(1.68, 1.70, 1.72, 1.74)
Upper bound Fit range (GeV/c^2)	(2.02, 2.04, 2.06, 2.08)
Rebin values	1, 2, 3
Background functions	Polynomial-2, Exponential

Table 4.5: Variations in fitting strategies used in the multi-trials for raw yield systematic uncertainty extraction of D^0 meson.

Figure 4.10. For the spherocity analysis, the ratio is considered for a given S_{O}-Quantile interval over the integrated one. The systematic is assigned to the relative RMS of the ratios to the central value.

4.6.2 Selection efficiency

The kinematic selections used for the reconstruction of D^0 are subject to biases which need to be taken into account. These selection criteria with respect to the central values are made looser and tighter, generally done by varying the cosine of the pointing angle ($\cos\theta_{\text{pointing}}$) and the cross product of the distance of closest approach ($d_0 \times d_0$). The ratios are taken on the self-normalized yields from the cut variations to the central results. The

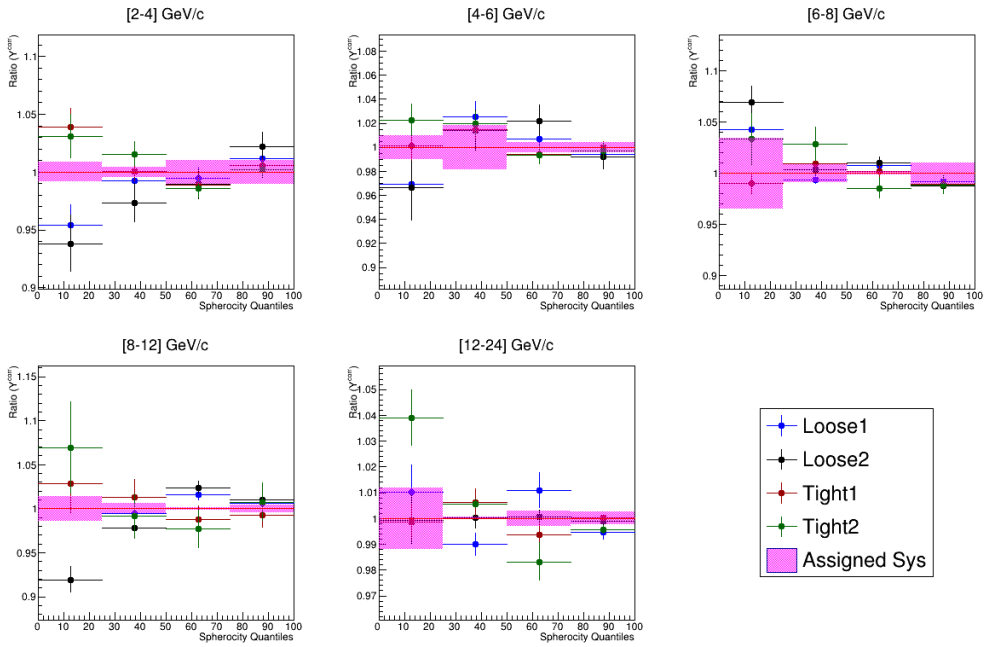

Figure 4.11: Ratio of D^0 meson yields with central topological selections and two loose and tight selections as a function of S_O-Quantiles in different p_T intervals. The assigned systematic (magenta) is estimated from the RMS of the deviation from unity per S_O-Quantile interval.

ratios are reported in the Figure 4.11 as function of S_O-Quantiles for two different sets of loose and tight cuts in different p_T intervals for 20 $<N_{\text{tracklet}} <$ 81.

4.6.3 Particle identification

The D^0 meson reconstruction uses PID strategies for the daughter tracks from the information of the TOF and TPC detector. The systematic uncertainty is estimated in the multiplicity dependent analysis from the ratios of self-normalized yields obtained with and without PID. These ratios cancel out for the spherocity dependent analysis. The ratios are shown in Figure 4.12, compatible with unity in almost all p_T and multiplicity bins, which states that there is no influence of the PID response. As a consequence, no systematic uncertainty related to the PID response is considered. For $1 < p_T < 2$ GeV/c and $60 < N_{\text{tracklet}} < 99$, the value of the ratio is high due to a poor signal extraction for the non PID case. Considering the particular p_T and N_{tracklet} bin to be a non-suitable configuration, the given point is considered to be an outlier and ignored.

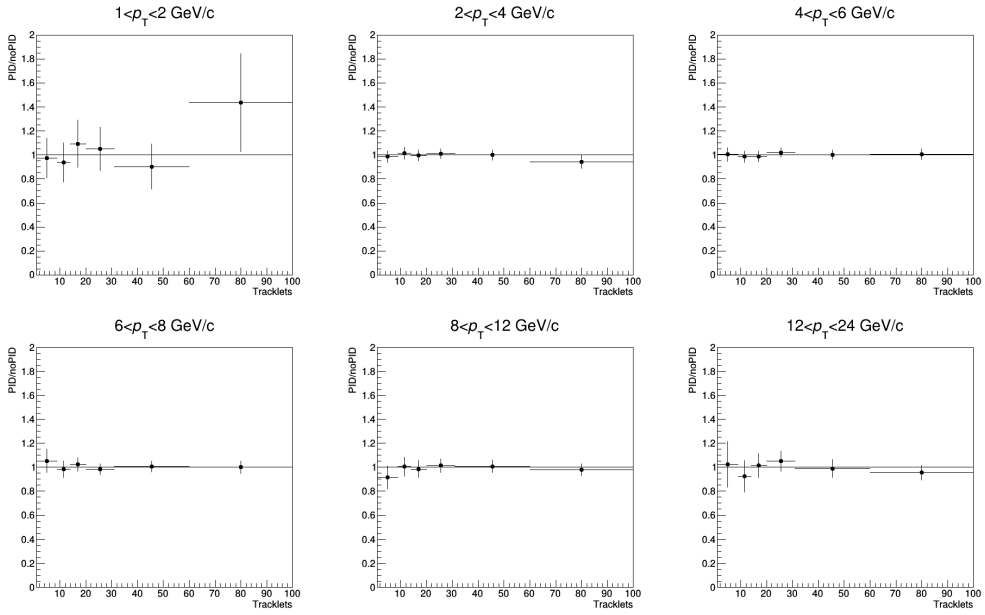

Figure 4.12: Ratio of D^0 meson yields with and without PID selection criteria as function of N_{tracklet} in different p_{T} intervals. The deviation from unity is negligible, except for $60 < N_{\text{tracklet}} < 99$ interval for $1 < p_{\text{T}} < 2$ GeV/c which is deemed as an outlier.

4.6.4 Feed-down

Feed-down refers to contribution coming from the *non-prompt* D-mesons, i.e., D coming from B-meson decays. The prompt D^0 production yields are corrected from feed-down using the beauty production cross-section, typically obtained from the FONLL calculation [77, 78], and with the efficiencies calculated for feed-down D^0 mesons. It is assumed that the relative contribution of beauty hadron decays to the D yields in the different multiplicity or spherocity intervals is constant and equal to that of the multiplicity and spherocity integrated sample. Organically, the self-normalized yields would cancel the feed-down contributions. However, a systematic effect is needed to account for the previous assumption. The procedure to calculate the systematic for both analyses is carried out with a PYTHIA8 driven approach. The PYTHIA8 simulations are performed with different tunes: Monash, CR modes 0, 2 and 3 and 4Cx[11] [88, 145, 149], where the self-normalized non-prompt fractions $f_{\text{non-prompt}}/f^{\text{MB}}_{\text{non-prompt}}$ are calculated as a function of charged-particle multiplicity or S_{O}-Quantiles. The left panel of Figure 4.13 shows the PYTHIA8 predictions of $f_{\text{non-prompt}}/f^{\text{MB}}_{\text{non-prompt}}$ from different tunes as a function of charged-particle multiplicities. The f_{prompt} is obtained from FONLL predictions, obtained

[11] 4Cx is chosen for multiplicity analysis only

with the N_b method[12]. The relative lower and upper systematic uncertainties $\sigma(f_{\text{prompt}})$ are assigned as

$$\sigma(f_{\text{prompt}})^{\text{rel}}_{\text{low/up}} = \frac{(1 - f_{\text{prompt}}) \cdot \sigma(f_{\text{non-prompt}})^{\text{rel}}_{\text{low/up}}}{f_{\text{prompt}}}. \tag{4.8}$$

The feed-down systematic dependence with spherocity is calculated in a similar manner. The self-normalized non-prompt fractions $f_{\text{non-prompt}}/f^{\text{MB}}_{\text{non-prompt}}$ from PYTHIA are estimated as a function of S_O-Quantiles, reported in right panel of Figure 4.13. The relative systematic uncertainties are estimated using Equation 4.8 in the $20 < N_{\text{tracklet}} < 81$ interval.

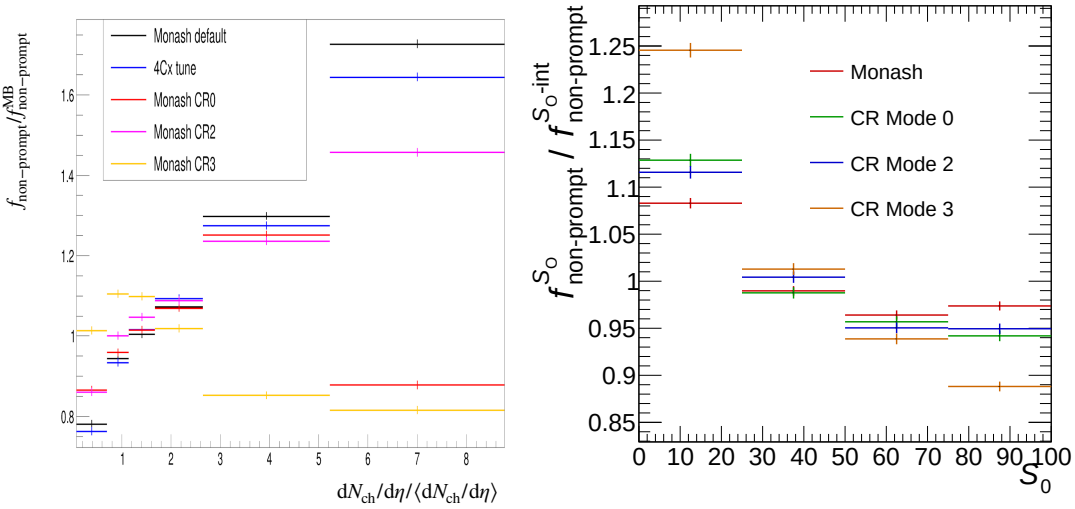

Figure 4.13: Ratio of $f_{\text{non-prompt}}/f^{\text{MB}}_{\text{non-prompt}}$ (Left) and $f^{S_O}_{\text{non-prompt}}/f^{S_O-\text{int}}_{\text{non-prompt}}$ (Right) as a function of $dN_{ch}/d\eta/\langle dN_{ch}/d\eta\rangle$ and S_O-Quantiles, respectively. The values correspond to different PYTHIA8 tunes used to account for the systematic variation.

4.6.5 Monte Carlo p_T-shape

The acceptance times efficiency in each p_T interval is sensitive to the generated MC p_T distribution. The effects are estimated by reweighting the efficiencies with a FONLL calculation [77, 78] based p_T-shape to account for the difference in the trend obtained from PYTHIA8 [88] MC datasets. The systematic uncertainties for the two analyses are estimated in the integrated multiplicity and S_O-Quantile intervals. The ratio of the

[12]The N_b method refers to the f_{prompt} calculation from the feed-down cross-section from FONLL, where the raw yield of charm hadrons are considered equal for particles and anti-particles

efficiencies is used (as shown in Figure 4.14) with and without FONLL p_{T}-weights and the systematics are assigned as

$$\sigma^{\mathrm{MC}}_{p_{\mathrm{T}}-\mathrm{shape}} = 1 - \frac{\mathcal{E}^{\mathrm{FONLL}}}{\mathcal{E}^{\mathrm{PYTHIA}}} \tag{4.9}$$

4.6.6 Multiplicity weights

The efficiency corrections are performed by applying a weight on the D-meson candidate selection. An associated systematic uncertainty is computed by considering weights where the D-meson candidates (at least one per event) are chosen without a selection on its PDG mass. This is calculated only for the multiplicity analysis, where the uncertainties are estimated in the ratios of the self-normalized yields of the differently weighted efficiencies. The ratios showed no significant deviation from unity and are neglected for D^0 mesons. The same systematic uncertainty is not considered for the spherocity dependent analysis, as the efficiency ratios in the self-normalized yields would cancel out.

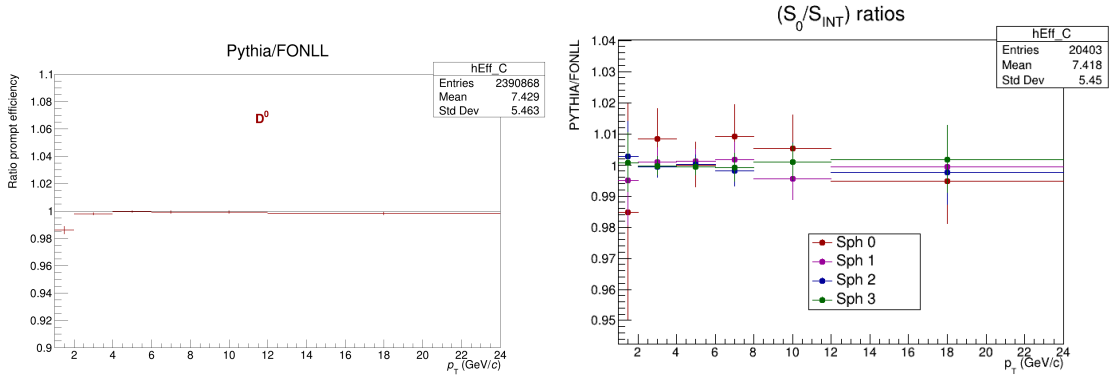

Figure 4.14: (Left) Ratio of correction efficiencies with PYTHIA8 and FONLL weights for D^0 in MB triggered sample as a function of p_{T}. (Right) Ratio of correction efficiencies performed on a given S_{O}-Quantile sample over the integrated one with PYTHIA8 and FONLL weights for D^0 in $20 < N_{\mathrm{tracklet}} < 81$ as a function of p_{T}.

4.6.7 Primary vertex resolution

The reconstruction efficiency for heavy-flavour particles has a dependence on the primary vertex resolution, which depends on the charged-particle multiplicity. Due to the specific multiplicity selection on the spherocity distribution, a systematic is assigned on the S_{O}-Quantiles. This is done by re-calculating the efficiencies which are weighted by the ratios of $20 < N_{\mathrm{tracklet}} < 81$ distribution per S_{O}-Quantile to the one in the integrated S_{O}-Quantile.

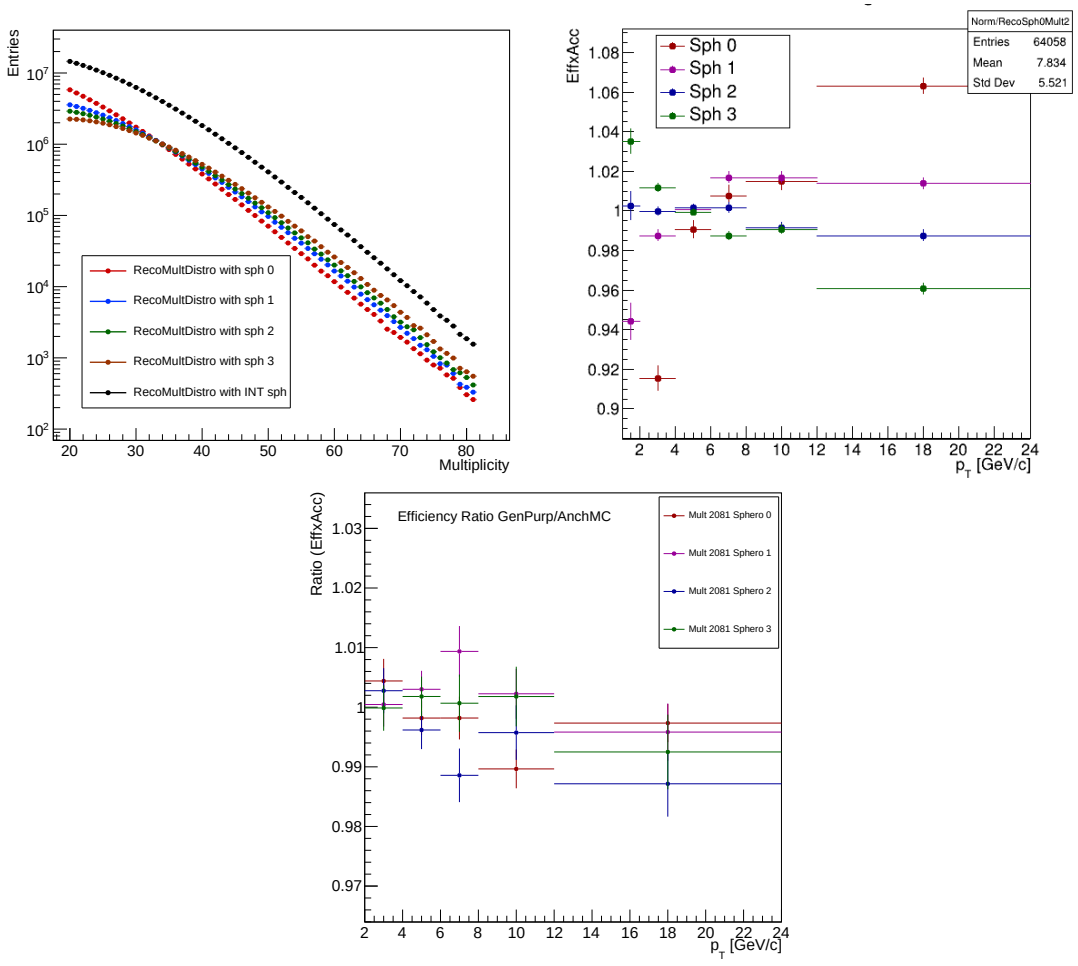

Figure 4.15: (Top Left) N_{tracklet} distributions with different S_{O}-Quantile selections. (Top Right) The efficiency ratios vs p_{T} computed with and without a spherocity selection. (Bottom Center) Efficiency ratios with anchored MC data sample over general purpose sample as a function of p_{T}.

This method removes the spherocity selection dependence on the multiplicity distribution. The multiplicity distributions corresponding to each S_{O}-Quantile is shown on the top left panel of Figure 4.15. At high multiplicities, the distributions are quite comparable while a significant sensitivity on the quantiles can be seen at low multiplicities. The final systematic error is assigned to the ratio of the efficiencies calculated with and without the spherocity selection (shown on the top right panel of Figure 4.15), the former being the central values.

4.6.8 Spherocity dependence on dataset

The cubic splines used for the S_O-Quantiles are calculated on the general purpose Monte Carlo samples. However, the efficiency corrections in the analysis are done on the anchored Monte Carlo datasets. The choice of Monte Carlo samples needs to considered as a systematic uncertainty on the calculation of the spherocity distributions, which may affect the S_O-Quantiles. In order to check this, the splines are calculated using the anchored datasets, followed by the calculation of the efficiencies. The systematics are assigned by taking the ratio of the efficiencies with the recalculated splines over the central ones. The ratio of efficiencies for D^0, as a function of p_T in different S_O-Quantiles for the $20 < N_{tracklet} < 81$ interval is reported on the bottom panel of Figure 4.15. The small deviations from unity reveal a negligible dependence, with the overall systematic uncertainty assigned to be at a maximum of 1%.

4.6.9 Summary of systematic uncertainties

The estimated systematic uncertainties are refined and smoothed for each $N_{tracklet}$ interval (multiplicity dependent analysis) and S_O-Quantile interval (spherocity dependent analysis) across all p_T intervals. Summary tables reporting the systematic uncertainties for the $20 < N_{tracklet} < 30$ and $20 < N_{tracklet} < 81$ in $25 < S_O-$Quantile < 50 are shown in Table 4.6 and 4.7, for the multiplicity- and spherocity-dependent analysis, respectively.

Source of systematic	Transverse momentum intervals (GeV/c)					
	$1<p_T<2$	$2<p_T<4$	$4<p_T<6$	$6<p_T<8$	$8<p_T<12$	$12<p_T<24$
Raw yield extraction	5%	1%	1%	1%	2%	3%
Selection efficiency	2%	1%	1%	1%	1%	1%
Particle identification	0%	0%	0%	0%	0%	0%
Feed-down Upper	2%	1%	1%	1%	1%	1%
Feed-down Lower	0%	0%	0%	0%	0%	0%
MC p_T shape	1%	0%	0%	0%	0%	0%
Multiplicity weights	0%	0%	0%	0%	0%	0%

Table 4.6: Summary of systematic uncertainties in $20 < N_{tracklet} < 30$ interval as a function of p_T for the D^0 meson.

4.7 Results

The final results are presented in the form of self-normalized yields of D-mesons (D^0, D^+, D^{*+}) versus multiplicity and transverse spherocity (as S_O-Quantiles). The measurements

Source of systematic	Transverse momentum intervals (GeV/c)				
	$2<p_{\mathrm{T}}<4$	$4<p_{\mathrm{T}}<6$	$6<p_{\mathrm{T}}<8$	$8<p_{\mathrm{T}}<12$	$12<p_{\mathrm{T}}<24$
Raw yield extraction	1%	1%	1%	2%	3%
Selection efficiency	1%	0%	0%	0%	0%
Feed-down Upper	0%	1%	1%	1%	1%
Feed-down Lower	0%	0%	1%	1%	1%
MC p_{T} shape	0%	0%	0%	0%	0%
Primary vertex resolution	0%	0%	2%	1%	4%
Anchored MC dependence	0%	0%	1%	0%	1%

Table 4.7: Summary of systematic uncertainties in $20 < N_{\mathrm{tracklet}} < 81$ interval for 50-75% S_{O}-Quantile as a function of p_{T} for the D^0 meson.

on D^0 meson, which is the focus of this thesis, are combined with similar calculations with D^+ and D^{*+}. A detailed set of results and their comparisons with model predictions are presented in this section.

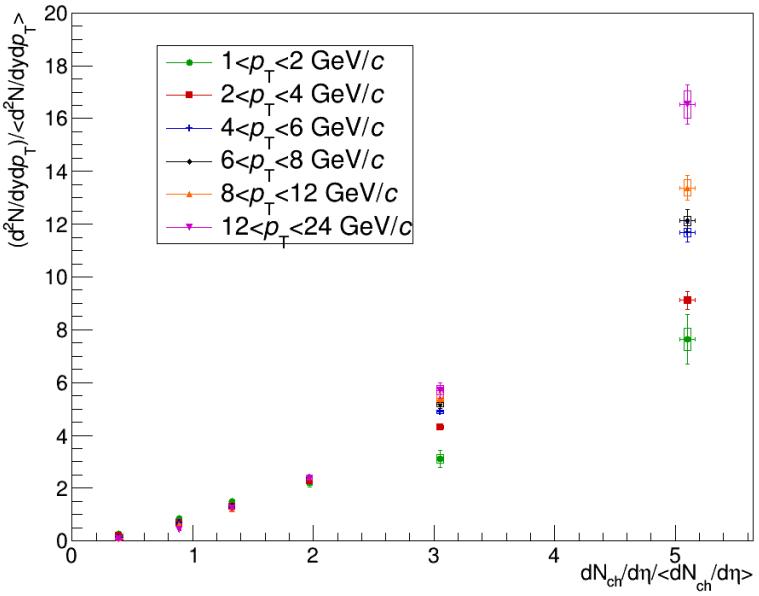

Figure 4.16: D^0-meson self-normalized yields as a function of relative charged-particle multiplicity density at mid-rapidity in different p_{T} intervals in pp collisions at $\sqrt{s} = 13$ TeV. The statistical and systematic uncertainties are represented as vertical bars and boxes respectively.

4.7.1 D-mesons vs charged-particle multiplicity

Self-normalized yields are calculated as the raw D-meson yield in a given multiplicity and p_{T} interval corrected by the Acc $\times\, \mathcal{E}$ over the corresponding quantity in the multiplicity integrated interval.

$$\mathrm{Y}^{\mathrm{mult}}_{\mathrm{corr}} = \left(\frac{\mathrm{Y}^{\mathrm{mult}}}{(\mathcal{E}^{\mathrm{mult}}_{\mathrm{prompt}} \times N^{\mathrm{mult}}_{\mathrm{event}})/\mathcal{E}^{\mathrm{mult}}_{\mathrm{trigger}}} \right) \Bigg/ \left(\frac{\mathrm{Y}^{\mathrm{mult}}_{\mathrm{int}}}{(\mathcal{E}^{\mathrm{mult\ int}}_{\mathrm{prompt}} \times N^{\mathrm{mult\ int}}_{\mathrm{event}})/\mathcal{E}^{\mathrm{mult\ int}}_{\mathrm{trigger}}} \right) \tag{4.10}$$

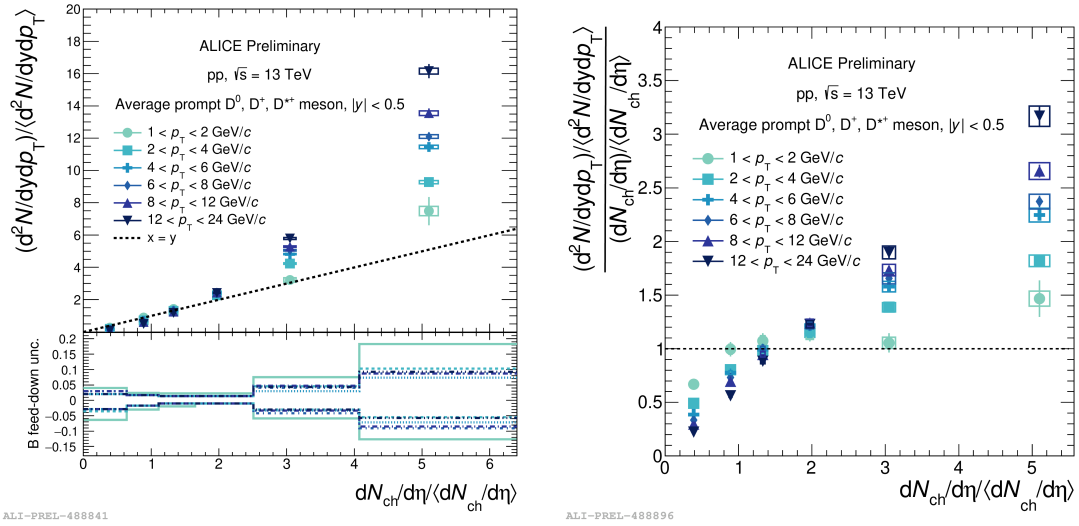

Figure 4.17: (Left) Average D-meson self-normalized yields as a function of relative charged-particle multiplicity density at mid-rapidity in different p_{T} intervals in pp collisions at $\sqrt{s}$ = 13 TeV. The feed-down fractions are displayed in the bottom panel. (Right) The ratios of self-normalized yields to self-normalized multiplicity as a function of relative charged-particle multiplicity. The statistical and systematic uncertainties are represented as vertical bars and boxes respectively.

where $\mathcal{E}_{\mathrm{prompt}}$ is the correction from the Acc $\times\, \mathcal{E}$ of prompt D-mesons and N_{events} are the number of events in the given N_{tracklet} interval. The $\mathcal{E}^{\mathrm{mult}}_{\mathrm{trigger}}$ is the trigger inefficiency factor, which is 92% for MB triggered events, 87% for $1 < N_{\mathrm{tracklet}} < 8$, 98% for $9 < N_{\mathrm{tracklet}} < 13$ and 100% in the rest of the intervals [199, 206]. The D^0 self-normalized yields as a function of relative charged-particle multiplicity are reported in Figure 4.16 in 6 p_{T} intervals. The self-normalized yields of the three D-meson species are combined in the final version of the results. On the left panel of Figure 4.17, the weighted mean of the corrected yields of D^0, D^+ and D^{*+} as a function of relative charged-particle multiplicity for different p_{T} intervals at mid-rapidity are shown. The weighted mean is taken as

$$Y_{\text{mean}} = \frac{\sum_i w_i Y_i}{\sum_i w_i} \tag{4.11}$$

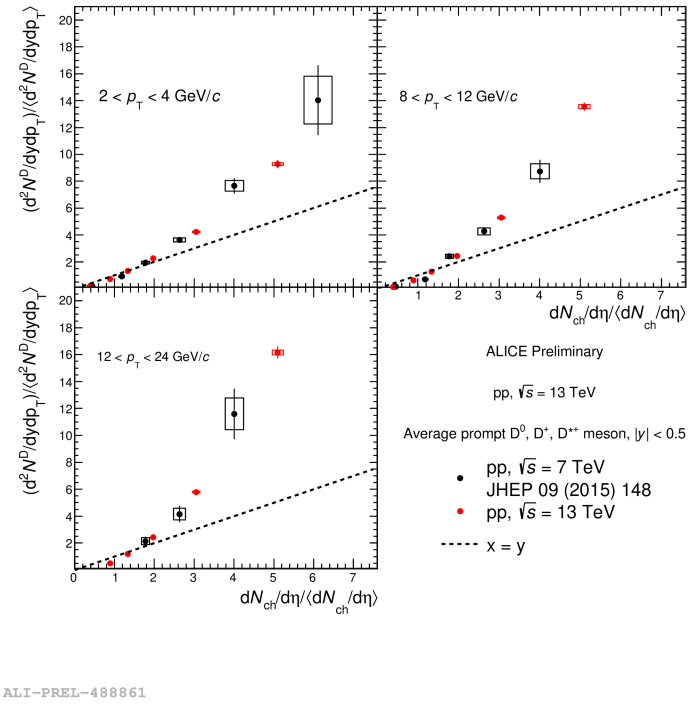

Figure 4.18: Comparison of average D-meson self-normalized yields in pp collisions at $\sqrt{s}$ = 7 TeV [184] and $\sqrt{s}$ = 13 TeV as a function of relative charged-particle multiplicity density at mid-rapidity in three p_T intervals. The statistical and systematic uncertainties are represented as vertical bars and boxes, respectively.

where weights for the i^{th} D-meson with corrected yields Y_i and associated standard deviation σ_i are defined as $w_i = (Y_i/\sigma_i)^2$. The statistical and systematic errors on the mean are propagated as

$$\sigma^{\text{stat/sys}}_{\text{mean}} = \frac{\sqrt{(\sum_i w_i \sigma_i^{\text{stat/sys}})^2}}{\sum w_i} \tag{4.12}$$

The self-normalized yields of D-mesons show a stronger than linear trend as a function of relative charged-particle multiplicity. With increasing p_T, the rise of the D-meson yields becomes steeper with multiplicity. A similar observation is made from the double ratio trends of the self-normalized yields to the relative charged-particle multiplicity as a

function of relative charged-particle multiplicity, shown on the right panel of Figure 4.17. The increase in the multiplicity trend is accredited to auto-correlation effects between heavy-flavour production and the multiplicity of an event. The charged-particle production accompanies the charm hard scattering process through components such as initial- or final-state radiations, heavy flavour hadron decays or fragmentation process and lead to this stronger than linear behavior [185, 186].

The results in pp collisions at $\sqrt{s}$ = 13 TeV are compared to the previous measurements at $\sqrt{s}$ = 7 TeV [184]. One of the ultimate goals of this measurement is to achieve more precision at higher multiplicities, illustrated in Figure 4.18, by comparing these two measurements at three p_{T} intervals. The D-meson self-normalized yields are also compared with similar heavy-flavour measurements in pp collisions at $\sqrt{s}$ = 13 TeV. The comparisons are performed with self-normalized yields of J/ψ mesons [207] and heavy-flavour decay electrons (c, b $\rightarrow$ e) [186] at low and high p_{T} ranges. The comparisons show a good agreement of the trend with charged-particle multiplicity between the different species, as shown in Figure 4.19. The lower panel of the figures report the double ratios of the yields for each species (similar to Figure 4.17).

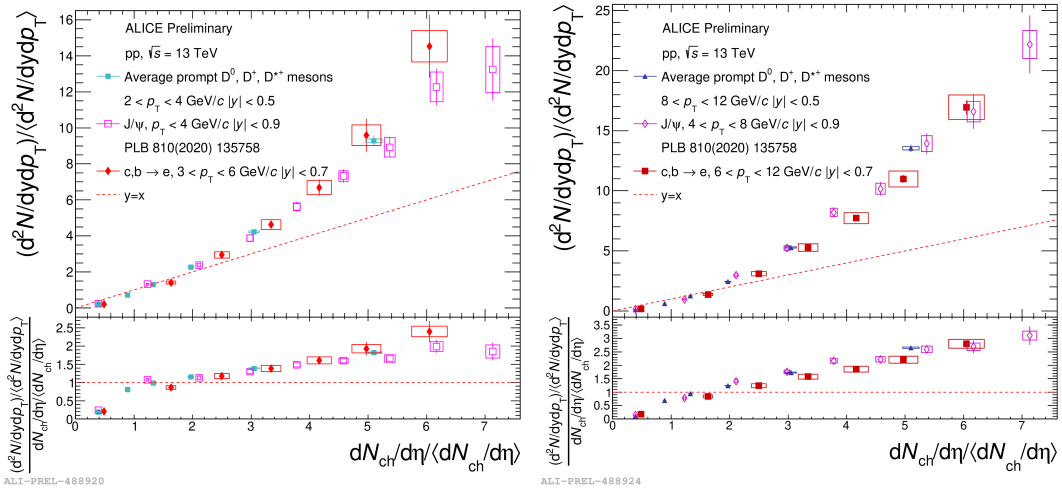

Figure 4.19: Comparison of self-normalized yields of average D-meson, J/ψ [207], and electrons from heavy-flavour hadron decays (c, b $\rightarrow$ e) [186] as a function of relative charged-particle multiplicity density at mid-rapidity in three p_{T} intervals in pp collisions at $\sqrt{s}$ = 13 TeV. The double ratios for the same are presented in the bottom panels.

Model predictions

To gain insight into charm production with charged-particle multiplicity, the final results are compared with different model calculations. The EPOS3 [208] approach utilizes a Gribov-Regge multiple scattering framework, designed to generate pp, p–Pb, Pb–Pb colli-

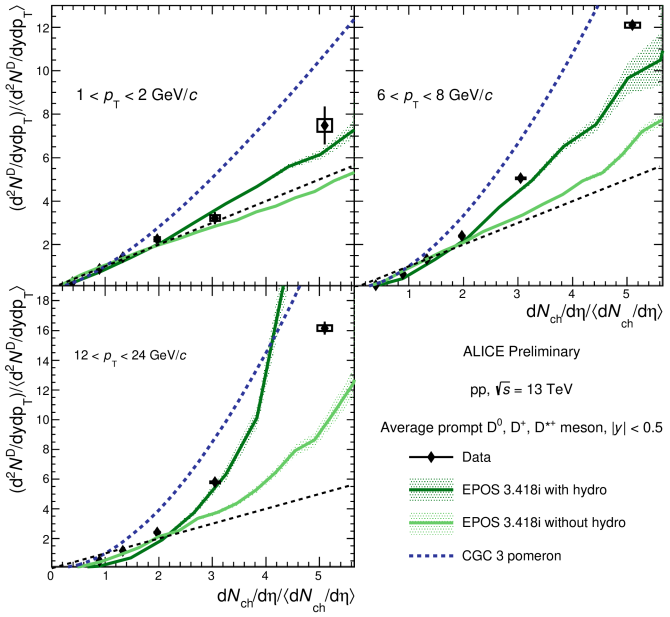

Figure 4.20: Comparison of self-normalized yields of average D-meson and model predictions from EPOS3 [208] with (dark green) and without (light green) hydrodynamics, and a 3-Pomeron CGC model [209] (blue) as a function of relative charged-particle multiplicity density at mid-rapidity in three p_T intervals in pp collisions at $\sqrt{s}$ = 13 TeV.

sions. The hard scattering element of this framework is a Pomeron, identified with a parton ladder, which show up as *colour flux tubes* or strings. The particle production is continued via fragmentation with the addition of a 3+1D viscous hydrodynamic evolution. Another model based on the Colour Glass Condensate (CGC) is added to the comparison [209]. The 3-Pomeron CGC, makes use of a 3-Pomeron fusion correction at the individual hard scatterings for heavy flavour production. The purpose of the 3 Pomeron correction, is due to potential contribution of 3 gluon fusion mechanisms in charm production.

Figure 4.20 show the D-meson self-normalized yields as a function of relative charged-particle multiplicity in three p_T intervals, compared to the model predictions from EPOS3 with and without a hydrodynamic evolution, and the 3-Pomeron CGC approaches [208, 209]. All the models qualitatively show the stronger than linear trend of the D-meson yields with multiplicity. EPOS3 without any hydrodynamic evolution is seen to underestimate the yields, while the hydrodynamic treatment shows a good agreement with the data. A deeper look shows deviation at large multiplicity values, which is accredited to the distribution of the energy in the collision into the hydrodynamic evolution, rather than in

particle production. This bias generates a stronger auto-correlation at larger p_{T} intervals, causing a higher rise than data from the hydrodynamic EPOS3 approach. The 3-Pomeron CGC is seen to highly overestimate the D-meson yields.

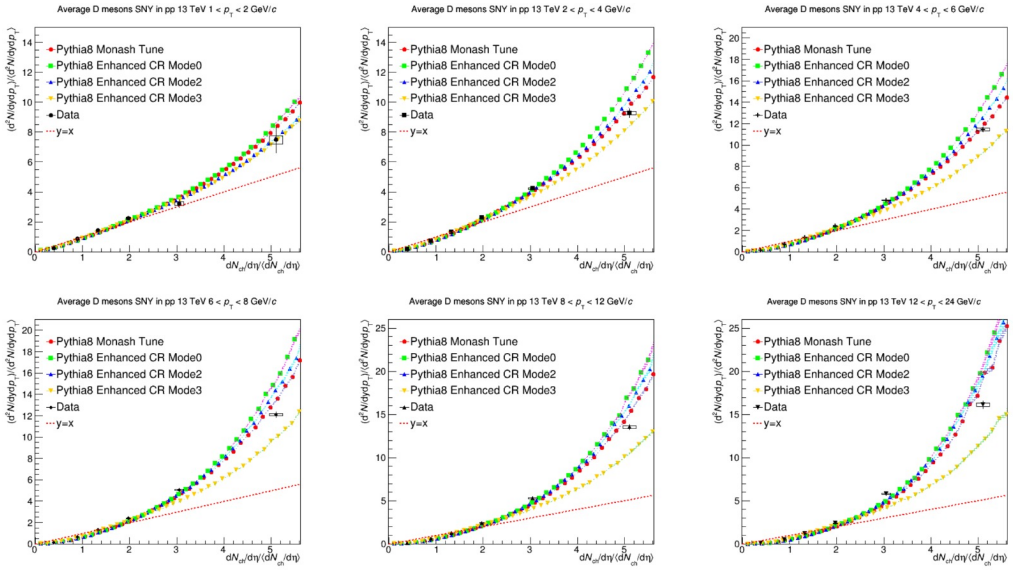

Figure 4.21: Comparison of self-normalized yields of average D-meson with Monash and CR Modes 0, 2, and 3 tunes of PYTHIA8 as a function of relative charged-particle multiplicity density at mid-rapidity in all p_{T} intervals in pp collisions at $\sqrt{s}$ = 13 TeV.

A comprehensive study with PYTHIA8 simulations is carried out for the D-meson yields results obtained in pp collisions at $\sqrt{s}$ = 13 TeV. The Monash tune and the enhanced colour reconnection modes (Mode 0, 2, 3) [88, 145, 149] are deployed to reproduce the self-normalized yields of D-mesons, reported in Figure 4.21. Initial impressions show a deviation of D-meson yields from CR Mode 3, especially at high multiplicities. However, it can be concluded that the other modes slightly deviate from the data at high charged-particle multiplicities. Additionally, affirmed from the Monash predictions, the combination of MPI and CR is essential to reproduce the D-meson yields as a function of multiplicity, or more precisely, the event multiplicities in pp collisions at $\sqrt{s}$ = 13 TeV. This is further confirmed by simulating pp events by enabling or disabling MPI and CR settings in PYTHIA. The summary of these results are shown in Figure 4.22. A large deviation is seen in D-meson yields from turning off MPI, affecting the primary component of particle production in pp collisions. This enhances the auto-correlation, which enhances the yields as a function of multiplicity. On the other hand, disabling CR leads to the agreement of D-meson yields at low multiplicities, but underestimates at higher values, mostly from overestimating event multiplicities.

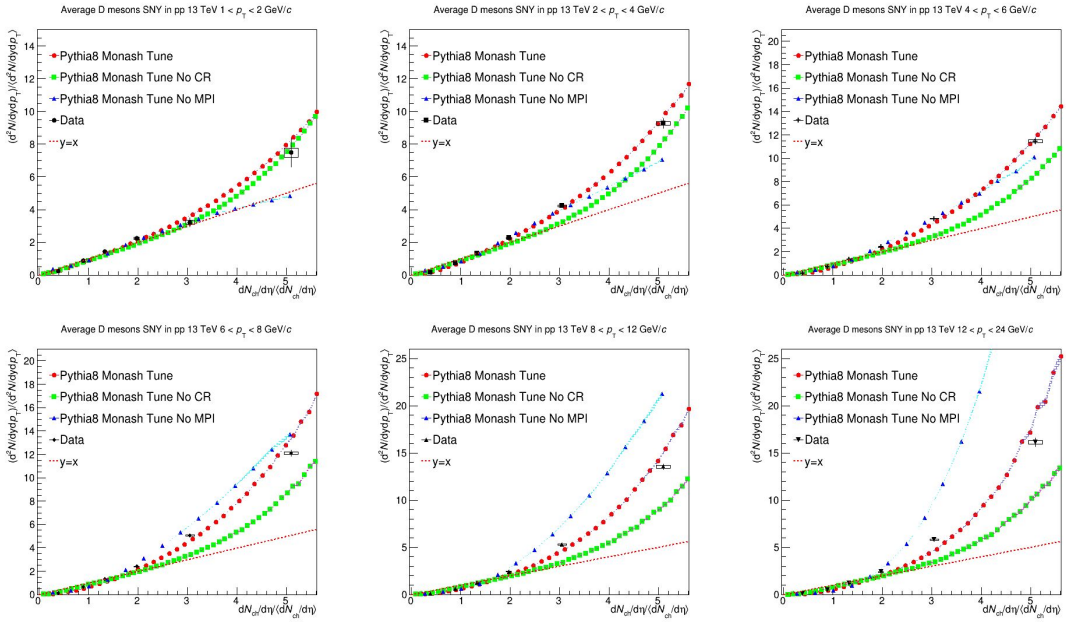

Figure 4.22: Comparison of self-normalized yields of average D-meson with different combinations of MPI and CR with PYTHIA8 as a function of relative charged-particle multiplicity density at mid-rapidity in all p_{T} intervals in pp collisions at $\sqrt{s}$ = 13 TeV.

4.7.2 D-mesons vs transverse spherocity

The results on the transverse spherocity analysis are performed in a similar manner. The self-normalized yields are calculated with the raw D-meson yield (Y) given in a S_{O}-Quantile in a particular multiplicity and p_{T} interval corrected by the respective Acc $\times\, \mathcal{E}$ over the complete S_{O}-Quantile range (0-100%).

$$\mathrm{Y}^{\mathrm{mult}\ S_{\mathrm{O}}}_{\mathrm{corr}} = \left(\frac{\mathrm{Y}^{\mathrm{mult}\ S_{\mathrm{O}}}}{\mathcal{E}^{\mathrm{mult}\ S_{\mathrm{O}}}_{\mathrm{prompt}} \times N^{\mathrm{mult}\ S_{\mathrm{O}}}_{\mathrm{event}}} \right) \Bigg/ \left(\frac{\mathrm{Y}^{\mathrm{mult}\ S_{\mathrm{O}}-\mathrm{int}}}{\mathcal{E}^{\mathrm{mult}\ S_{\mathrm{O}}-\mathrm{int}}_{\mathrm{prompt}} \times N^{\mathrm{mult}\ S_{\mathrm{O}}-\mathrm{int}}_{\mathrm{event}}} \right) \tag{4.13}$$

The D^0 meson self-normalized yields are shown in Figures 4.23 and Figures 4.24 illustrate the average self-normalized yields of D-mesons in different p_{T} intervals as a function of S_{O}-Quantiles. The average D-meson yields are calculated per multiplicity interval, following Equation 4.13. A general trend is observed between the D-meson yields from each p_{T} interval, where the D-mesons coming from harder events tend to dominate in the "jetty" event topology. Here, the soft D-mesons are strongly suppressed, which increases as the event topology becomes more isotropic. On the other hand, the population decreases with a change in event topology from jetty to isotropic for hard D-mesons. Moreover,

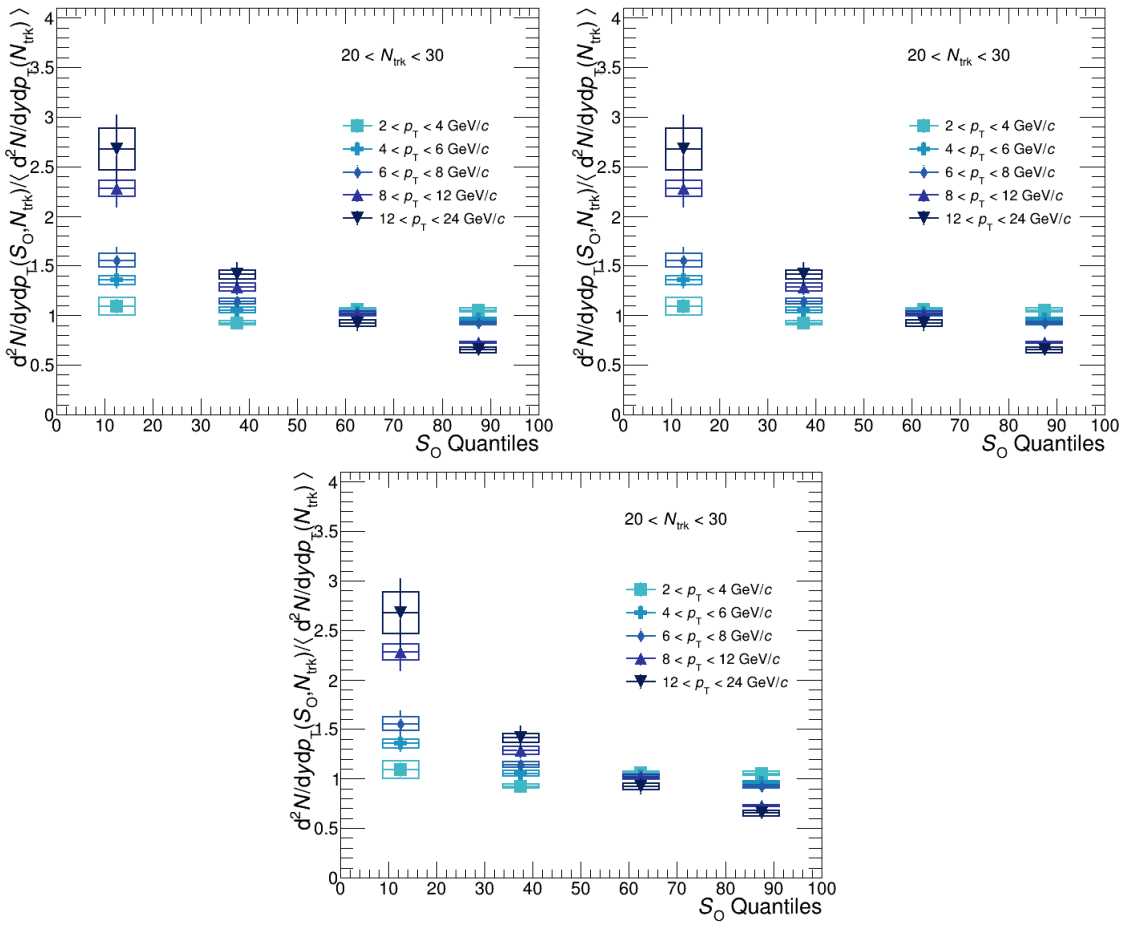

Figure 4.23: D^0-meson self-normalized yields as a function of S_O-Quantiles at mid-rapidity in different $N_{tracklet}$ intervals (left: $20 < N_{tracklet} < 30$, right: $31 < N_{tracklet} < 81$, and below: $20 < N_{tracklet} < 81$,) and p_T intervals in pp collisions at $\sqrt{s} = 13$ TeV. The statistical and systematic uncertainties are represented as vertical bars and boxes respectively.

variations in the D-meson yields amongst the multiplicity intervals are small. This is expected due to the spherocity selection described in Section 4.3.2, which removes the multiplicity biases coming from the MB-triggered data sample during the spherocity calculation.

PYTHIA8 comparisons

Similar to the multiplicity-dependent analysis, PYTHIA8 simulations under the same conditions are performed for D-meson yields versus spherocity. The S_O-Quantile distribution in each multiplicity interval is obtained in PYTHIA8 using the method explained in Sec-

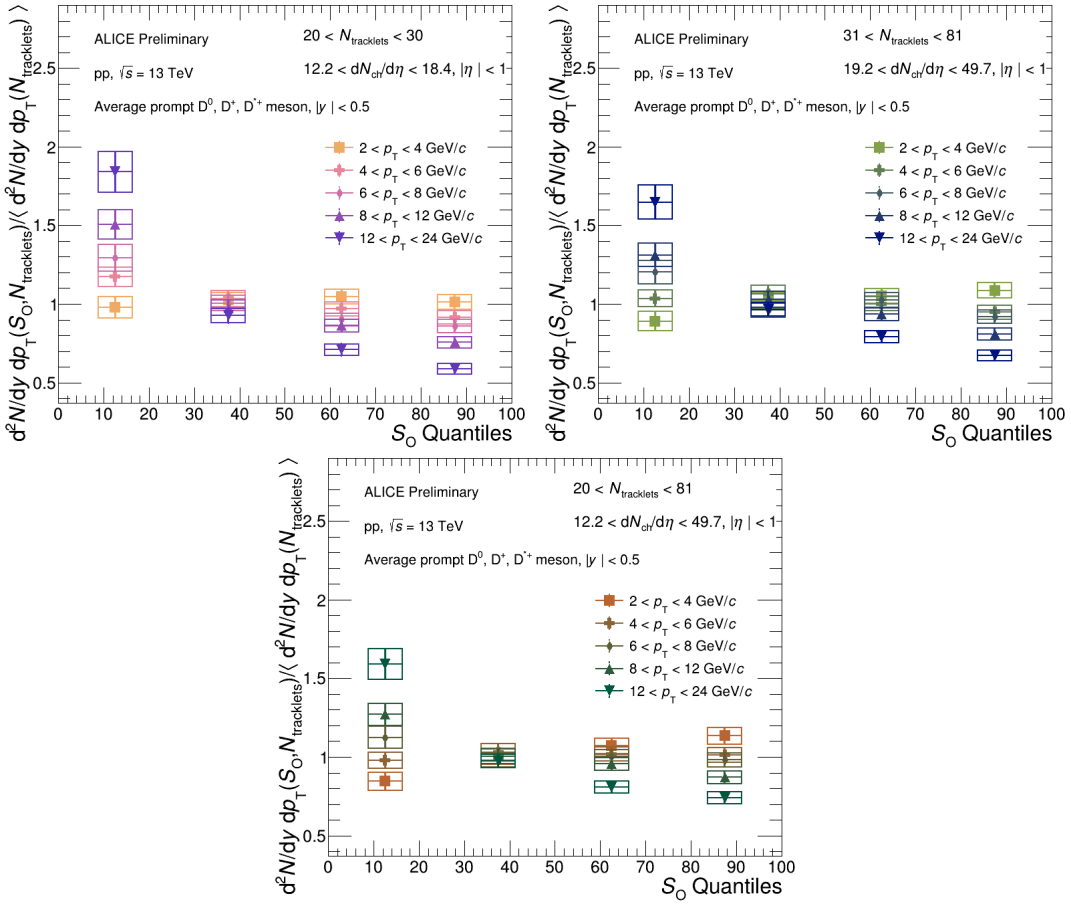

Figure 4.24: Average D-meson self-normalized yields as a function of S_O-Quantiles at mid-rapidity in different N_{tracklet} intervals (left: $20 < N_{\text{tracklet}} < 30$, right: $31 < N_{\text{tracklet}} < 81$, and below: $20 < N_{\text{tracklet}} < 81$,) and p_T intervals in pp collisions at $\sqrt{s} = 13$ TeV. The statistical and systematic uncertainties are represented as vertical bars and boxes respectively.

N_{tracklet}	$dN_{ch}/d\eta$
20-30	12.23-18.38
31-81	19.23-49.73
20-81	12.23-49.73

Table 4.8: Charged-particle multiplicity density classes corresponding to the N_{tracklet} intervals relevant in the spherocity dependent analysis.

tion 4.3.2. To maintain consistency between the N_{tracklet} selections in data, the charged particle multiplicity density ($dN_{ch}/d\eta$) intervals are chosen using the correlation map be-

tween N_{tracklet} and N_{ch} obtained by the results from Monte Carlo samples (summarised in Table 4.8). The PYTHIA8 predictions are presented in Figure 4.25, that show a reasonable comparison with the measured D-meson yields for every p_{T} and N_{tracklet} interval. Monash and CR Mode 0, 2, and 3 calculations [88, 145, 149] lie within uncertainties with each other and the data while reproducing the trends of the yields as a function of S_{O}-Quantile.

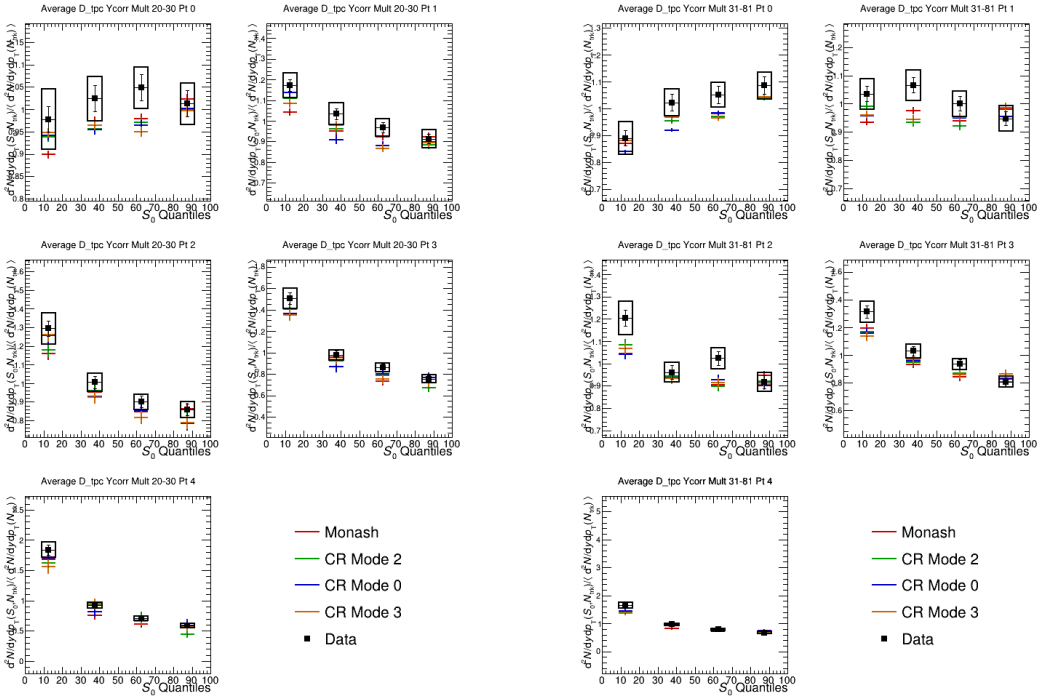

(a) $20 < N_{\text{tracklet}} < 30$ (b) $31 < N_{\text{tracklet}} < 81$

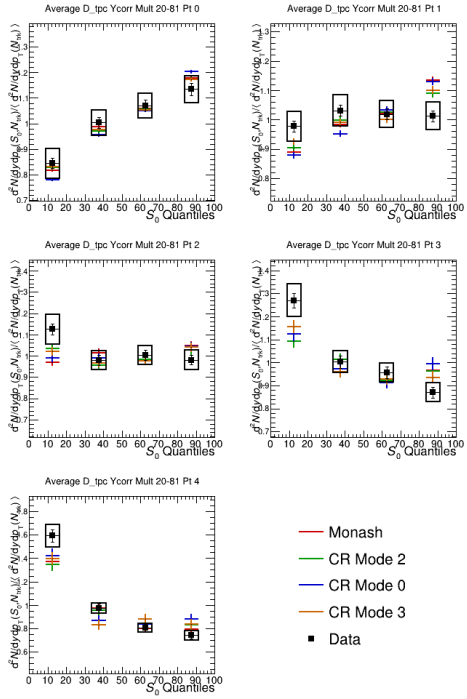

(c) $20 < N_{\text{tracklet}} < 81$

Figure 4.25: Comparison of self-normalized yields of average D-meson with Monash and CR Modes 0, 2, and 3 tunes of PYTHIA8 as a function of S_{O}-Quantiles at mid-rapidity in three N_{tracklet} intervals and all p_{T} intervals in pp collisions at $\sqrt{s}$ = 13 TeV.

Chapter 5

Light nuclei synthesis via coalescence

This chapter is focused on light (anti-)nuclei production in hadronic and heavy-ion collisions via coalescence of (anti-)nucleons. The coalescence model is a well know phenomenological model for explaining the production mechanism of light nuclei. This thesis is centered around an 'in-situ' coalescence model, developed as an afterburner to different transport models or event generators. The chapter is adapted from a collection of articles pertaining to the development and implementation of this model.

5.1 Physics motivation

The first measurements in light (anti-)nuclei production were carried out at the CERN Inner Storage Ring (ISR) experiments [210, 211]. Several measurements that followed at the RHIC and the LHC reported light and hyper nuclei (d, ^{3}H, ^{3}He, ^{4}He, $^{4}_{\Lambda}$H) and their respective anti-nuclei production in pp, Au–Au, p–Pb and Pb–Pb systems in different center of mass energies [212–216]. Their production measurements as a function of center of mass energy are crucial to probe the QCD phase diagram. For instance, fluctuations in nuclei yield ratios, which are a proxy for net baryon density fluctuations are sensitive to QCD phase structure and allows one to locate the *critical end-point*. Additionally, these nucleon clusters allow us to understand the nature of low-energy nucleon-nucleon (NN) interactions that provide insight to the EoS of neutron stars. However, the formation mechanism of light (anti-)nuclei from the aftermath of collision experiments is still a puzzle. These bound states are believed to be formed during the hadronic evolution (T ~100 MeV), while the typical binding energies of light nuclei are of O(2 MeV). Because of this, light nuclei are popularised with the term "snowballs in hell" [217], challenging the phenomenological aspects of its production.

A substantial amount of studies with models have described how light (anti-)nuclei and

hyper (anti-)nuclei are produced in these extreme conditions. The *thermal* model, adopts a statistical hadronization approach, that generates the relative abundances of hadrons based on the chemical freeze-out temperature (T_c) [97, 99, 218, 219]. The model works with an ensemble approach, which represents the collision system, assuming a grand-canonical ensemble for heavy-ion systems, and a canonical ensemble for smaller systems. The model successfully reproduces the relative hadron yields and light and hyper (anti-)nuclei states including (anti-)helium and (anti-)hyper triton [95–98], however, it is not sensitive to the internal structure of the nuclei. On the other hand, coalescence models are based on the closeness or proximity of nucleons in phase space which, given favourable conditions, will form a nuclei state. The phase space is generally defined at kinetic freezeout, allowing decoupled nucleons to come together and coalesce [106–108]. Moreover, kinetic processes or potential interactions during the hadronic evolution also serve as a tangible mechanism for nuclei production. Recent advancements in n-body transport models are allowing detailed and concrete studies in light as well as hyper nuclei cluster formation via potential interactions [220–223].

In this thesis, the focus circles around the development and implementation of a coalescence model, deployed in the form of an *afterburner*. Three studies are covered on the production of light nuclei via coalescence, with different physics goals. Section 5.2 discusses briefly the features of a coalescence model followed by the details of coalescence afterburners in Section 5.3. A brief introduction to femtoscopy and the tools used in the studies are described in Section 5.4. The first study described in Section 5.5, is about d, ^{3}H, and ^{3}He production in heavy-ion collisions at RHIC and LHC energies with a simple coalescence afterburner, utilizing a box formalism. The heavy-ion collisions are generated with the AMPT model [156]. The second objective aims to refine the model and incorporate a Wigner coalescence formalism, while targeting the production of *in-jet* deuterons in high multiplicity pp collisions with PYTHIA8 [149], described in Section 5.6. The final study in Section 5.7 dives into the intricacies of nucleon-nucleon interactions, trying to understand the minute characteristics of coalescence. This is achieved with *femtoscopy* between nucleon and nuclei species, performed by a correlation afterburner (CRAB) model [224], over the nucleon/nuclei phase space generated by the SMASH event generator [167, 168]. The results provide the space-time snapshot of the species, which allows insight into their formation times in the collision.

5.2 Coalescence model

Coalescence models for light-nuclei at their origins, assumed close-by (anti-)nucleon pairs at the kinetic freeze-out hyper-surface, coalesce and form a bound state or a nuclei [104, 105, 225]. This assumption holds strong for relativistically expanding systems, where the nucleons would be ‘de-coupled’ at freeze-out, allowing two or more nucleons in close proximity to coalesce [106–108]. However, further studies unveiled the kinetic processes

that contribute to nuclei formation, particularly the deuteron creation and annihilation processes during hadronic evolution [220–223]. This reiterates our understanding of coalescence, and the possibility of it being a dynamic phenomenon, that is prevalent during the entire hadronic cascade phase. The coalescing nucleons should have non-consequential interactions with the surrounding matter but show affinity towards Coulombic and strong interactions between them. As a simple approach, the probability of finding $A = Z + N$ nucleons is given by the product of individual nucleon probabilities as

$$E_A \frac{\mathrm{d}^3 N_A}{\mathrm{d}p_A^3} = B_A \left(E_\mathrm{p} \frac{\mathrm{d}^3 N_\mathrm{p}}{\mathrm{d}p_\mathrm{p}^3} \right)^Z \left(E_\mathrm{n} \frac{\mathrm{d}^3 N_\mathrm{n}}{\mathrm{d}p_\mathrm{n}^3} \right)^{A-Z} \tag{5.1}$$

where B_A is the coalescence parameter of $Z + N$ nucleons coalescing to a nuclei of mass number A in a small sphere of radius p_0 around one of the nucleon momenta, given by

$$B_A = \left(\frac{4\pi}{3} p_0^3 \right)^{A-1} \frac{g_A m_A}{m_\mathrm{p}^Z m_\mathrm{n}^N}. \tag{5.2}$$

Here, m_A is the mass of the nuclei, m_p, and m_p are masses of the coalescing proton and neutron, respectively, and g_A is the spin factor of the nuclei. The radius parameter p_0 can be reinstated as the coalescence cut-off momentum. The coalescence parameter can be physically interpreted as the nucleon correlation size or volume that depends on the nucleon emission source and quantifies the probability of coalescence. Under the isospin symmetry, Equation 5.1 can be approximated as

$$E_A \frac{\mathrm{d}^3 N_A}{\mathrm{d}^3 p_A} = B_A \left(E_\mathrm{p} \frac{\mathrm{d}^3 N_\mathrm{p}}{\mathrm{d}p_\mathrm{p}^3} \right)^A \quad , \quad \mathbf{p}_\mathrm{p} = \mathbf{p}_A / A \tag{5.3}$$

This is a single-parameter, simple, and empirical version of coalescence [226], that has been used to describe a variety of experimental measurements, especially for small collision systems [102]. For larger systems, Equation 5.2 does not hold as it is independent of the source size of the nucleon emission volume and, more generally, the spatio-momenta correlations between the nucleons. This makes it an incomplete approach to coalescence. An improvement to this would be to take into account the phase space coordinates of the nucleons. More advanced models invoke a quantum mechanical treatment of the deuteron, where a Wigner probability density is assigned to the light (anti-)nuclei species based on an ansatz wave function [109, 227, 228]. Coalescence is achieved when the nucleons' phase space coordinates overlap with the light (anti-)nuclei Wigner probability density. To perform an exhaustive study, realistic modeling of the nucleon source from the emission

volume is helpful [110, 111]. Event generators, although provide the space-time evolution of the collision, experimental measurements are better relied upon to have a accurate description of the nucleon emission. These emission sources are estimated experimentally via femtoscopy methods of like and unlike hadron species, providing a space-time snapshot of the particle emission [229–231].

5.3 Coalescence afterburner

The coalescence criteria can be appended onto a phase-space hyper-surface of nucleons. The nucleon hyper-surface is generally obtained from an event generator or a transport model, which can be dynamically controlled and operated for various colliding systems and energies. In the following subsections, a series of coalescence afterburner implementations are discussed. The collisions are modeled with various event generators, with the goal of achieving insight into the different treatments of the collision dynamics and nuclei production. The underlying physics of these studies are focused on light nuclei production from coalescence, with an effort to improve the physics of coalescence in each study. The version of each coalescence model is tested on experimental measurements of light nuclei production from small to large collision systems, and ranging from low to high collision energies. In the following subsections, methodologies of coalescence models used in the studies of this thesis are discussed in detail.

5.3.1 Box coalescence

As the name suggests, simple coalescence criteria can be deployed by calculating the relative position and momentum coordinates of the nucleons at kinetic freezeout. The coalescence conditions are met when the relative momentum between the nucleons is less than a critical value ($\Delta p^{\max}$), and the distance between the nucleons is less than twice the size of the nuclear charge radius ($\Delta r^{\max} < 2R_0$) [106–108]. R_0 is 1.57 fm for deuterons and 2.09 fm for triton and helium-3. A step-by-step procedure to achieve this phase-space coalescence is described below:

1. The (anti-)nucleon states, which is pn($\bar{\text{p}}\bar{\text{n}}$) for d($\bar{\text{d}}$), pnn for ^{3}H and ppn for ^{3}He are boosted to the center of mass frame.

2. If their relative momentum $\Delta p = |\mathbf{p}_1 - \mathbf{p}_2| < \Delta p^{\max}$, their momenta are combined ($\mathbf{p}_{\text{d}} = \mathbf{p}_{\text{p}} + \mathbf{p}_{\text{n}}$ or $\mathbf{p}_{^3\text{H},^3\text{He}} = \mathbf{p}_{\text{p}} + \mathbf{p}_{\text{n,p}} + \mathbf{p}_{\text{n}}$).

3. The position(s) of the (anti-)nucleon(s) at an earlier freezeout time relative to the candidate (anti-)nucleon(s) are reset to the later freeze-out time. This is done to ensure that the pair of nucleons do not interact between these two times.

Parameters	d($\bar{\text{d}}$)	^{3}H/^{3}He
$\Delta r^{\max}$ (fm)	3.15	4.18
$\Delta p^{\max}$ (MeV/c)	190	350

Table 5.1: Parameters ($\Delta p^{\max}$ and $\Delta r^{\max}$) used in coalescence of deuterons, tritons and helium-3.

4. The relative distances between the pairs are checked so that the condition $\Delta r = |\mathbf{r}_1 - \mathbf{r}_2| < \Delta r^{\max}$ is satisfied.

5. Due to spin-isospin statistics only 3/8 or 1/12 possible nucleon combinations will actually couple to a valid deuteron or triton and helium-3 state, respectively. In this regard, the spin-isospin coupling probabilities are taken into account [107, 232]. The finally chosen deuteron, triton, and helium-3 candidates that fulfill the coalescence conditions are then removed from the phase space distribution.

The set of parameters used for each nuclei species for the study [108] is reported in Table 5.1.

5.3.2 Wigner coalescence

A modern approach for a coalescence afterburner is by incorporating a quantum mechanical treatment of the light nuclei. The nuclei distribution is defined by the wave function of the nuclei and associating it to its Wigner probability distribution, while the nucleon overlap function is decided by nucleon source function (more in Section 5.3.2.2). Coalescence is achieved by checking the level of overlap between the phase space of the nucleons and the nuclei's Wigner probability [109–111, 227, 228]. The yields for deuteron and triton/helium-3 can be expressed in the form [111, 233]

$$\frac{\mathrm{d}^3 N_{\mathrm{d}}}{\mathrm{d}p_{\mathrm{d}}^3} = S_{\mathrm{d}} \int \mathrm{d}^3 r_{\mathrm{d}} \mathrm{d}^3 r \mathrm{d}^3 q \mathcal{D}(\mathbf{r}, \mathbf{q}) W_{\mathrm{np}} \left(\frac{\mathbf{p}_{\mathrm{d}}}{2} \pm \mathbf{q}, \mathbf{r}_{\mathrm{d}} \pm \frac{\mathbf{r}}{2} \right) \tag{5.4}$$

$$\begin{aligned} \frac{\mathrm{d}^3 N_{^3\mathrm{H}/^3\mathrm{He}}}{\mathrm{d}p_{^3\mathrm{H}/^3\mathrm{He}}^3} = S_{^3\mathrm{H}/^3\mathrm{He}} \int \mathrm{d}^3 r_{^3\mathrm{H}/^3\mathrm{He}} \mathrm{d}^3 r \mathrm{d}^3 r' \mathrm{d}^3 q \mathrm{d}^3 q' \mathcal{D}(\mathbf{r}, \mathbf{r}', \mathbf{q}, \mathbf{q}') \\ \times W_{\mathrm{ppn/pnn}} \left(\frac{\mathbf{p}_{\mathrm{d}(^3\mathrm{H}/^3\mathrm{He})}}{2} \pm \mathbf{q}(\mathbf{q}'), \mathbf{r}_{\mathrm{d}(^3\mathrm{H}/^3\mathrm{He})} \pm \frac{\mathbf{r}(\mathbf{r}')}{2} \right) \end{aligned} \tag{5.5}$$

respectively, where the cluster spatio-momenta and the relative coordinates are expressed as

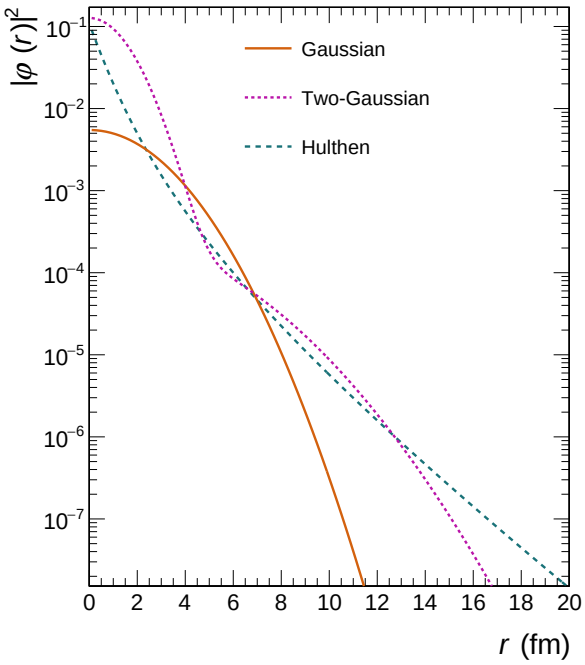

Figure 5.1: Deuteron wave functions using Gaussian form (solid orange), Hulthén (dashed green) and Double Gaussian (dashed magenta) fitted to the Hulthén distribution.

$$\mathbf{r}_{\mathrm{d}} = \frac{1}{2}(\mathbf{r}_1 + \mathbf{r}_2) \quad , \quad \mathbf{r} = \frac{1}{\sqrt{2}}(\mathbf{r}_1 - \mathbf{r}_2)$$
$$\mathbf{r}_{^3\mathrm{H}/^3\mathrm{He}} = \frac{1}{2}(\mathbf{r}_1 + \mathbf{r}_2 + 2\mathbf{r}_3) \quad , \quad \mathbf{r}' = \frac{1}{\sqrt{6}}(\mathbf{r}_1 + \mathbf{r}_2 - 2\mathbf{r}_3)$$
$$\mathbf{p}_{\mathrm{d}} = \mathbf{p}_1 + \mathbf{p}_2 \quad , \quad \mathbf{q} = \frac{1}{\sqrt{2}}(\mathbf{p}_1 - \mathbf{p}_2)$$
$$\mathbf{p}_{^3\mathrm{H}/^3\mathbf{He}} = \mathbf{p}_1 + \mathbf{p}_2 + 2\mathbf{p}_3 \quad , \quad \mathbf{q}' = \frac{1}{\sqrt{6}}(\mathbf{p}_1 + \mathbf{p}_2 - 2\mathbf{p}_3).$$

$S_{\mathrm{d}/^3\mathrm{H}/^3\mathrm{He}}$ is the statistical spin-isospin averaging factor, $W_{\mathrm{ppn/pnn}}$ is the nucleon pair selection probability term which is related to the source function of the two- and three-nucleon cluster, and $\mathcal{D}(\mathbf{r}, \mathbf{q})$ is the Wigner probability density. A detailed description of the individual components of Equation 5.5 are provided in the following sections.

5.3.2.1 Wave function formalism

The light nuclei wave function is crucial to define the Wigner probability density. Generally, a deuteron wave function is approximated to a single Gaussian function [227] of the

form

$$\varphi_{\mathrm{d}}(\mathbf{r}) = \frac{1}{(\pi d^2)^{3/4}} \exp\left(-\frac{r^2}{2d^2}\right) \tag{5.6}$$

with the deuteron scale parameter d. Two different values of this parameter are considered; the RMS point radius $d = 3.2$ fm [234] for the pp collision study, and the RMS charge radius of $d = 2.14$ fm for the heavy-ion collision study. The Wigner density $\mathcal{D}(\mathbf{r}, \mathbf{q})$ in momentum space can be obtained via

$$\begin{aligned} \mathcal{D}(\mathbf{r}, \mathbf{q}) &= \frac{1}{(\pi d^2)^{3/2}} \int \mathrm{d}^3\xi \exp\left(-i\mathbf{r}\cdot\mathbf{q}\right) \varphi\left(\mathbf{r} + \frac{\xi}{2}\right) \varphi^*\left(\mathbf{r} - \frac{\xi}{2}\right) \\ &= \frac{4}{\sqrt{\pi} d^3 q} \int \mathrm{d}\xi \xi \sin\left(q\xi\right) \exp\left(-\frac{4r^2 + \xi^2}{4d^2}\right) \\ &= 8 \exp\left(-\frac{d^4 q^2 + r^2}{d^2}\right) \end{aligned} \tag{5.7}$$

Similarly, for the three-nucleon clusters (^{3}H, ^{3}He), the Wigner probability over a Gaussian wave function [227] becomes

$$\mathcal{D}(\mathbf{r}, \mathbf{q}, \mathbf{r}', \mathbf{q}') = 8^2 \exp\left(-\frac{q^2\sigma^4 + r^2}{\sigma^2}\right) \exp\left(-\frac{q'^2\sigma^4 + r'^2}{\sigma^2}\right). \tag{5.8}$$

where the RMS charge radii are $\sigma = 1.75$ fm, and 1.96 fm, of ^{3}H and ^{3}He, respectively [234].

For the Wigner coalescence based studies [111, 233], a second choice of the deuteron wave function is considered: a parameterized double or "two" Gaussian form. This formalism is adopted from Refs [109, 235, 236], which use parameterized double Gaussian functions to reproduce the Hulthén wave function of the deuteron. The Hulthén wave function,

$$\varphi(\mathbf{r}) = \sqrt{\frac{ab(a+b)}{2\pi(a-b)^2}} \frac{e^{-ar} - e^{-br}}{r} \tag{5.9}$$

with $a = 0.23$ fm^{-1} and $b = 1.61$ fm^{-1}, is based on the Yukawa theory of interactions and provides a good description of the deuteron ground state wave function. The two-Gaussian wave function can be written as

$$\varphi(\mathbf{r}) = \frac{1}{\pi^{3/4}} \left[\frac{\Delta^{1/2}}{d_1^{3/2}} e^{-\frac{r^2}{2d_1^2}} + e^{i\alpha} \frac{(1-\Delta)^{1/2}}{d_2^{3/2}} e^{-\frac{r^2}{2d_2^2}} \right] \tag{5.10}$$

Choosing $e^{i\alpha} = i$, the probability distribution becomes

$$|\varphi(\mathbf{r})|^2 = \frac{1}{\pi^{3/2}} \left[\frac{\Delta}{d_1^3} e^{-\frac{r^2}{d_1^2}} + \frac{(1-\Delta)}{d_2^3} e^{-\frac{r^2}{d_2^2}} \right] \tag{5.11}$$

The parameters $\Delta = 0.247$, $d_1 = 5.343$ fm^{-1}, and $d_2 = 1.81$ fm^{-1} are taken from the references [109, 235, 236], that are extracted by fitting Equation 5.10 to the Hulthén wave function. The probability distributions $|\varphi(\mathbf{r})|^2$ are displayed in Figure 5.1, which shows the single and two-Gaussian distributions and the Hulthén probability distribution.

5.3.2.2 The nucleon source function

The coalescence parameter is strongly correlated to the correlation volume of the nucleon, which is incorporated by the source function of the nucleons. In the context of deuterons, the selection term W_{np} in Equation 5.5 is the probability of selecting (an)a (anti-)proton and (anti-)neutron pair at positions $\mathbf{r}_{\mathrm{d}} \pm \mathbf{r}/2$ and momenta $\mathbf{p}_{\mathrm{d}}/2 \pm \mathbf{q}$. This term can be factorized into spatial and momentum components as

$$W_{\mathrm{np}} = \mathcal{S}(\mathbf{r}_{\mathrm{p}}, \mathbf{r}_{\mathrm{n}}) \cdot Q(\mathbf{p}_{\mathrm{d}}/2 + \mathbf{q}, \mathbf{p}_{\mathrm{d}}/2 - \mathbf{q}). \tag{5.12}$$

$\mathcal{S}(\mathbf{r}_{\mathrm{p}}, \mathbf{r}_{\mathrm{n}})$ is the source function of the p-n pairs. In pp collisions, the PYTHIA8 event generator is not ideal for generating the space-time correlations. To account for realistic experimental conditions, a nucleon-emitting (p-n) source is embedded in PYTHIA8 [111]. Assuming a Gaussian source and neglecting correlations between proton and neutron, the spatial component can be written as

$$\mathcal{S}(\mathbf{r}; r_0) = \frac{1}{(4\pi r_0^2)^{3/2}} \exp\left(-\frac{r^2}{4r_0^2}\right) \tag{5.13}$$

where r_0 is the size of the nucleon pair emitting source or the source radius. Estimation of the source size for a p-n system has been measured by ALICE in pp collisions at $\sqrt{s} = 13$ TeV [237]. These measurements are performed with femtoscopy methods, where the initial spatial correlations are estimated with the help of two-particle momentum correlations. The methods of femtoscopy are discussed in Sections 5.4. The source radius r_0, as

described in Equation 5.13, can be obtained from the fit of the momentum correlation function through the Koonin-Pratt relation [238] (described in Section 5.4). The source function $\mathcal{S}(\mathbf{r})$ is radially symmetric, and the relevant one-dimensional (1D) probability density function of r can be written as

$$\mathcal{S}_{4\pi}(\mathbf{r}) = 4\pi r^2 \mathcal{S}(\mathbf{r}) = \frac{4\pi r^2}{(4\pi r_0^2)^{3/2}} \exp\left(-\frac{r^2}{4r_0^2}\right) \tag{5.14}$$

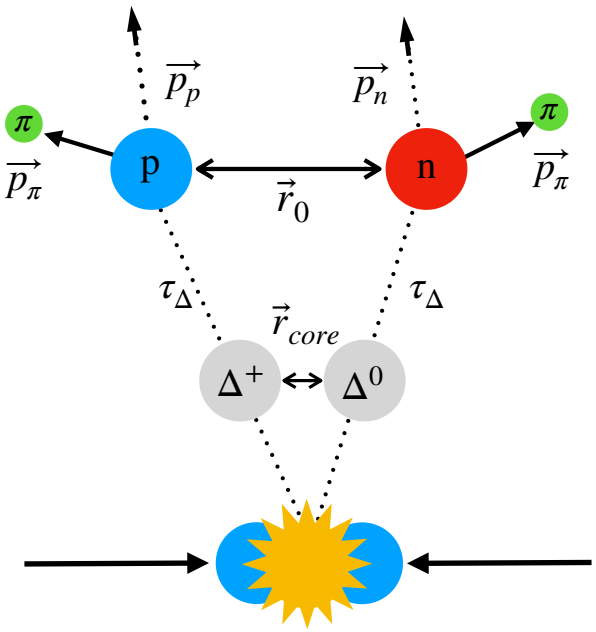

Figure 5.2: Pictorial depiction of the resonance source model to describe the emission of (anti-)nucleon pairs in pp collisions. The distance r_{core} refer to the primordial nucleons or resonance pair emission described by a Gaussian source, while r_0 is the p-n source size described by a modified Gaussian distribution, arising due to effects from resonance decay [111].

ALICE measurements have extracted these parameters extensively for baryon systems, namely for p-p and p-Λ in pp collisions at $\sqrt{s}$ = 13 TeV [237]. These measurements conclude that the source size varies (i) with the pair transverse mass $\langle m_{\text{T}} \rangle$[13] and (ii)

[13] the p-n pair transverse mass is defined as $\langle m_{\text{T}} \rangle = \sqrt{\left(\frac{p_{\text{Tp}}+p_{\text{Tn}}}{2}\right)^2 + \left(\frac{m_{\text{p}}+m_{\text{n}}}{2}\right)^2}$

according to the decay topology of the baryons. For example, a pair of protons coming from the collision (primordial) and another pair of protons coming from the decay of resonances must have different source radii. This resonance source model assumes that the primordial nucleons and resonances are emitted at equal times, independently from a "core" Gaussian source. The resonances are assumed to be free streaming and non-interacting for their short lifetime. Figure 5.2 shows a pictorial representation of the decay topologies of a proton and neutron pair from resonances. The source radii r_{core} belong to the primordial nucleon or resonance pairs coming from the collision, and r_0 represent the source radii of nucleon pairs, where at least one nucleon is from a resonance decay.

Conducting a femtoscopy study to estimate the source sizes with PYTHIA8 is desirable; however, certain discrepancies exist. In PYTHIA8, the source radius of a p-p state can be calculated from the final state momentum correlations with femtoscopic techniques, which in the $\langle m_{\text{T}} \rangle$ range 1.26–1.38 GeV/c, is estimated to be ~1.2 fm (r_{core}). It is also seen in the results from Ref [110] that the source size from PYTHIA8 is relatively non-changing with the $\langle m_{\text{T}} \rangle$, on contrary to ALICE results, which has a decreasing trend of r_{core} (r_0) with $\langle m_{\text{T}} \rangle$. The dynamic nature of r_{core} (r_0) is important to the coalescence formalism as well as to the likelihood of coalescing in-jet nucleons. The source radii from the ALICE measurements are relied upon, to not overlook this microscopic detail. The left panel of Figure 5.3 shows the source radii values as a function of $\langle m_{\text{T}} \rangle$. The source radius of a primordial emission (r_{core}) is more compact than the source with the inclusion of resonance decays. The resonance source model is developed by assigning the emission source radii according to the decay topology of the nucleon pairs and $\langle m_{\text{T}} \rangle$ as shown on the left panel of Figure 5.3. This treatment also reinstates the spatio-momenta correlations broken during the factorization of W_{np} into independent spatial and momentum components, as shown in Equation 5.12. In the right panel of Figure 5.3, an example of the two sources are presented; the primordial nucleon/resonance pairs having r_{core} = 1.2 fm, and a corresponding r_0 from resonance decays for $\langle m_{\text{T}} \rangle$ = 1.25 GeV/c^2. With the inclusion of the resonances, the Gaussian form is modified by an exponential tail, as seen from the ALICE measurements (markers) on the right panel of Figure 5.3. This shape can be described by a modified Gaussian distribution of the form

$$f(r;\mu,\sigma,\lambda) = \frac{\lambda}{2} e^{\frac{\lambda}{2}(2\mu+\lambda\sigma^2-2r)} \text{erfc}\left(\frac{\mu+\lambda\sigma^2-r}{\sqrt{2}\sigma}\right) \tag{5.15}$$

where the fit parameters, $\mu = \sqrt{2}r_0$ and σ is calculated from the Gaussian sources associated to r_0. The decay parameter λ = 0.9 (fixed value) is important to describe the signature tail of the modified source and can be connected to the decay time of the resonance particle.

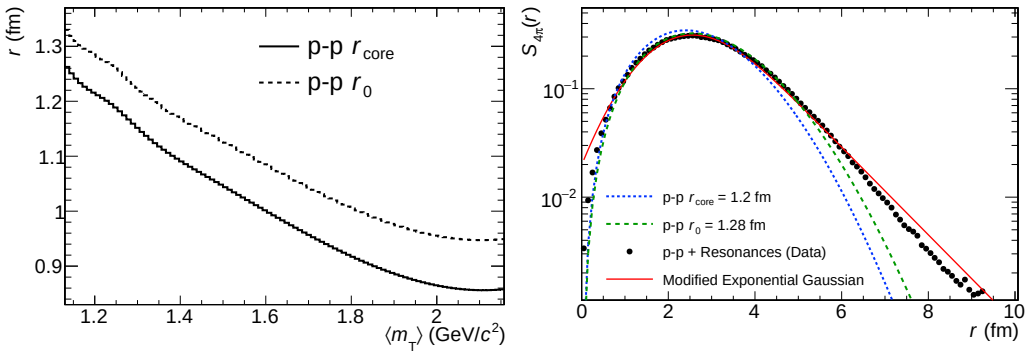

Figure 5.3: (Left) Source radius (r_0 and r_{core}) as a function of pair transverse mass ($\langle m_{\text{T}} \rangle$) extracted from ALICE measurements [237]. (Right) Source functions for p-p for primordial r_{core} = 1.2 fm and from decay emission r_0 = 1.28 fm. The markers are extracted from the ALICE measurement that shows p − p sources with one proton coming from a resonance decay. The points are fitted using a modified exponential Gaussian function (solid red line) [111, 237].

5.4 Femtoscopy

Femtoscopy has its roots in interferometry studies where techniques such as Hanbury-Brown and Twiss (HBT) interferometry were used to measure the angular dimensions of stars [239]. In particle physics, this technique was adopted to study the quantum state of Bose-Einstein condensates via correlations of electrons and identical pion pairs [230, 240]. Femtoscopy is performed using two particle momentum correlations, by building correlation functions from the ratios of correlated and uncorrelated pairs (more in Section 5.4.1). The correlations between identical or non-identical pairs are mostly generated from their final state interactions (FSIs), quantum statistics effects, and Coulomb and strong interactions between the pair [238, 241–243]. The correlation between two particles '1' and '2' with space-time coordinates x_1 and x_2, with final state momentum p_1 and p_2 can be represented in terms of their plane waves $\langle p_i | x_i \rangle = e^{-ip_i \cdot x_i}$. The two particle quantum mechanical amplitude can then be written as

$$|\Psi(x, p)|^2 = \langle p_1 | x_1 \rangle \langle p_2 | x_2 \rangle \pm \langle p_1 | x_2 \rangle \langle p_2 | x_1 \rangle \tag{5.16}$$

For even (odd) total spin the amplitudes would be added (subtracted) to give a (anti-)symmetric wave function of the system. This results in an enhancement (suppression) of the total amplitude from Equation 5.16 at zero momentum separation [244]. The width of this enhancement or suppression is inversely proportional to the space-time separation of the particle emission. This is why the femtoscopic correlation function becomes a

tool to study the space-time properties of the particle emission region, which forms the source of the interfering plane waves. Conversely, such methods are relevant to study the short-range Coulomb and strong interactions for small emission sources. This allows one to extend studying particle interactions, that may not be feasible to perform with scattering experiments.

5.4.1 The correlation afterburner

The two-particle momentum correlations are constructed from the two-particle correlation function. It is defined as the invariant yield of the particle pair, to the product of the individual particle yields. This also translates as the ratio of probabilities of finding the particle pair to the probabilities of finding particles with momentum $\mathbf{p}_1$ and $\mathbf{p}_2$

$$C(\mathbf{p}_1, \mathbf{p}_2) = \frac{E_1 E_2 \mathrm{d}N_{12}/\mathrm{d}p_1^3 \mathrm{d}p_2^3}{E_1 \mathrm{d}N_1/\mathrm{d}p_1^3 \cdot E_2 \mathrm{d}N_2/\mathrm{d}p_2^3} = \frac{\mathcal{P}(\mathbf{p}_1, \mathbf{p}_2)}{\mathcal{P}(\mathbf{p}_1)\mathcal{P}(\mathbf{p}_2)} \tag{5.17}$$

The ratio converges to unity in the absence of any correlations between the particles. Experimentally, the reference frame is chosen as the *pair rest frame* (PRF), wherewith the relative momentum of the particles with PRF momentum ($\mathbf{p}_i^*$), is defined as $k^* = \frac{1}{2}|\mathbf{p}_1^* - \mathbf{p}_2^*|$. This can redefined as

$$C(k^*) = \mathcal{A}\frac{N_{\text{same}}(k^*)}{N_{\text{mixed}}(k^*)}. \tag{5.18}$$

The correlation function converges to unity as $k^* \to \infty$. The N_{same} and N_{mixed} correspond to the measured yield of the correlated pairs *signal* and *reference*, respectively. The normalisation constant $\mathcal{A}$ is chosen so that $C(k^*) = 1$, typically at $k^* > 200$ MeV/c.

In the context of the femtoscopic analysis performed in the thesis, a Correlation After-Burner (CRAB) package is used to construct the two particle correlation function [224]. The CRAB model makes use of a quantum mechanical interpretation, where a wave-function of the particle pair $\psi(\mathbf{q}, \mathbf{r})$, and a source function $\mathcal{S}_i(\mathbf{p_i}, \mathbf{x_i})$, where $\mathbf{q} = \frac{1}{2}[(p_1 - p_2)^\mu - (p_1 - p_2)_\nu \cdot \frac{\mathbf{P}^\nu \cdot \mathbf{P}^\mu}{\mathbf{P}^2}]$ with $\mathbf{P} = \mathbf{p}_1 + \mathbf{p}_2$. The components in Equation 5.18 can be replaced as

$$E_i \mathrm{d}N_i/\mathrm{d}p_i^3 = \int \mathrm{d}^4 x_i \mathcal{S}_i(\mathbf{p}_i, \mathbf{x}_i) \tag{5.19}$$

$$E_1 E_2 \mathrm{d}N_{12}/\mathrm{d}p_1^3 \mathrm{d}p_2^3 = \int \mathrm{d}^4 x_1 \mathrm{d}^4 x_2 \mathcal{S}_1(\mathbf{p}_1, \mathbf{x}_1) \cdot \mathcal{S}_2(\mathbf{p}_2, \mathbf{x}_2) |\psi(\mathbf{q}, \mathbf{r}^*)|^2. \tag{5.20}$$

With this, the correlation function becomes

$$C(\mathbf{P},\mathbf{q}) = \frac{\int \mathrm{d}^4x_1\mathrm{d}^4x_2\mathcal{S}_1(\mathbf{p}_1,\mathbf{x}_1)\cdot\mathcal{S}_2(\mathbf{p}_2,\mathbf{x}_2)|\psi(\mathbf{q},\mathbf{r}^*)|^2}{\int \mathrm{d}^4x_1\mathcal{S}_1(\mathbf{p}_1,\mathbf{x}_1)\cdot\int \mathrm{d}^4x_2\mathcal{S}_2(\mathbf{p}_2,\mathbf{x}_2)} \tag{5.21}$$

The $|\psi(\mathbf{q},\mathbf{r})|^2$ is the Bethe-Salpeter amplitude corresponding to the probability weights of the particle pair. The source function can be decomposed in the PRF by considering $\mathbf{r}^* = \mathbf{x}_1 - \mathbf{x}_2$ and $\mathbf{R} = (\mathbf{x}_1 + \mathbf{x}_2)/2$, where $\mathbf{P} = \mathbf{p}_1 + \mathbf{p}_2 = 0$ and $\mathbf{q} \to k^*$. The Equation 5.21 finally transforms to the Koonin-Pratt relation [238]

$$C(k^*) = \int \mathrm{d}^3r^*|\psi(k^*,\mathbf{r}^*)|^2\mathcal{S}(\mathbf{r}^*). \tag{5.22}$$

5.4.2 Lednický-Lyuboshits approach

The Lednický-Lyuboshits approach [242, 243, 245] takes the two particle wave function from a scattering theory approach. The total wave function is an approximation from the $s-$wave and the strong force given by

$$\psi(\mathbf{k}^*,\mathbf{r}^*) \approx e^{-i\mathbf{k}^*\mathbf{r}^*} + f(k^*)\frac{e^{ik^*r^*}}{r^*} \tag{5.23}$$

where $f(k^*)$ is the scattering amptitude given by,

$$f(k^*) \approx \left(\frac{-1}{a_0} + \frac{1}{2}d_0k^{*2} - ik^*\right)^{-1}. \tag{5.24}$$

The parameters, scattering length a_0, and the effective range d_0 are obtained from scattering cross-section measurements. Using the wave function in the Koonin-Pratt relation (Equation 5.22) and a Gaussian approximation for the source, the correlation function for a non-identical system becomes [242]

$$C_{\mathrm{LL}}(k^*) = 1 + \frac{1}{2}\left|\frac{f}{r_0}\right| + \frac{2\Re(f)F_1(2k^*r_0)}{\sqrt{\pi}r_0} - \frac{2\Im(f)F_2(2k^*r_0)}{r_0} \tag{5.25}$$

Here, the analytic functions are defined as $F_1(z) = \frac{1}{2}e^{-z^2}\int_0^z e^{x^2}dx$, and $F_2(z) = \frac{1}{z}(1-e^{-z^2})$. For identical pairs, the effect of (anti-)symmetrization is considered. Moreover, the Coulombic interactions must be taken into account. The s-wave component of Equa-

tion 5.23 can be written as

$$\psi_{-k^*}(r^*) = e^{i\delta_c}\sqrt{A_c(\eta)}\left[e^{-ik^*r^*}F(-i\eta, 1, i\xi) + f_c(k^*)\frac{\tilde{G}(\rho,\eta)}{r^*}\right] \tag{5.26}$$

where, $\eta = 1/(k^*a_c)$ and a_c is the Bohr radius, $\xi = \rho(1+\cos\theta^*)$, and $\rho = k^*r^*$ are variables. $A_c(\eta) = 2\pi\eta[e^{2\pi\eta}-1]^{-1}$ is the Coulomb penetration factor, also known as the Gamow factor. The term $F(-i\eta, 1, i\xi)$ is a confluent hypergeometric function and $\tilde{G}(\rho,\eta) = \sqrt{A_c}(G_0 + iF_0)$, where G_0 and F_0 are the regular and singular Coulomb functions. This takes the asymptotic form of the Coulombic interaction in the wave function. This gives the final Coulomb corrected scattering amplitude f_c as

$$f_c(k^*) = \left[\frac{1}{-a_0} + \frac{1}{2}d_0k^{*2} - \frac{2}{a_c}h(\eta) - ik^*A_c(k^*)\right]^{-1} \tag{5.27}$$

where, $h(\eta) = \eta^2\sum_{n=1}^{\infty}[n(n^2+\eta^2)]^{-1} - C(=0.5772) - \ln|\eta|$.

5.5 Light (anti-)nuclei production with AMPT

This section presents the implementation of a simple transport + coalescence methodology for producing light nuclei with a simple but effective coalescence model. The box coalescence model, which operates over the (anti-)nucleon freezeout phase space, captures light nuclei (d, $\bar{\text{d}}$, ^{3}H, ^{3}He) production for a broad range of beam energies in heavy-ion collisions. The *string melting* AMPT transport model (version 1.26t9b-v2.26t9b) [156] is utilized to obtain the phase space information of the constituent nucleons. In addition, AMPT deploys kinetic processes for deuteron and anti-deuteron formation during the hadronic transport phase, which gives an opportunity for a comparative study between the two prescriptions ("Transport" vs "Coalescence"). The study is carried out in various center of mass energies $\sqrt{s_{\rm NN}}$ = 19.6, 39, and 200 GeV for central (0-10%) Au–Au collisions and $\sqrt{s_{\rm NN}}$ = 2.76 TeV for central (0-10% and 0-20%) Pb–Pb collisions at mid-rapidity. The results are compared with predictions from the parton-hadron-quantum-molecular-dynamics (PHQMD) model [246] with light nuclei clustering algorithms [223]. In this model, the nuclei clustering is done dynamically in various cluster freezeout times via Simulated Annealing Clustering Algorithm (SACA) and Minimum Spanning Tree (MST) algorithm [246, 247].

The AMPT model is well established in describing various experimental observables obtained at RHIC and the LHC [248–250]. Several interpretations of nuclei formation are covered using AMPT. AMPT natively produces (anti-)deuterons via elementary pion

catalysis interactions of NN $\rightarrow$ dπ, NNN $\rightarrow$ dN, and NNπ $\rightarrow$ dπ during the hadronic evolution. In this study, deuteron production processes in two different modes are investigated. For "Coalescence" mode, the native deuteron processes in AMPT are turned off, to ensure that all (anti-)nucleon pairs are available for the coalescence afterburner. For the "Transport" mode, the hadronic re-scattering processes are on, and afterburner is not implemented on this freeze-out hyper-surface.

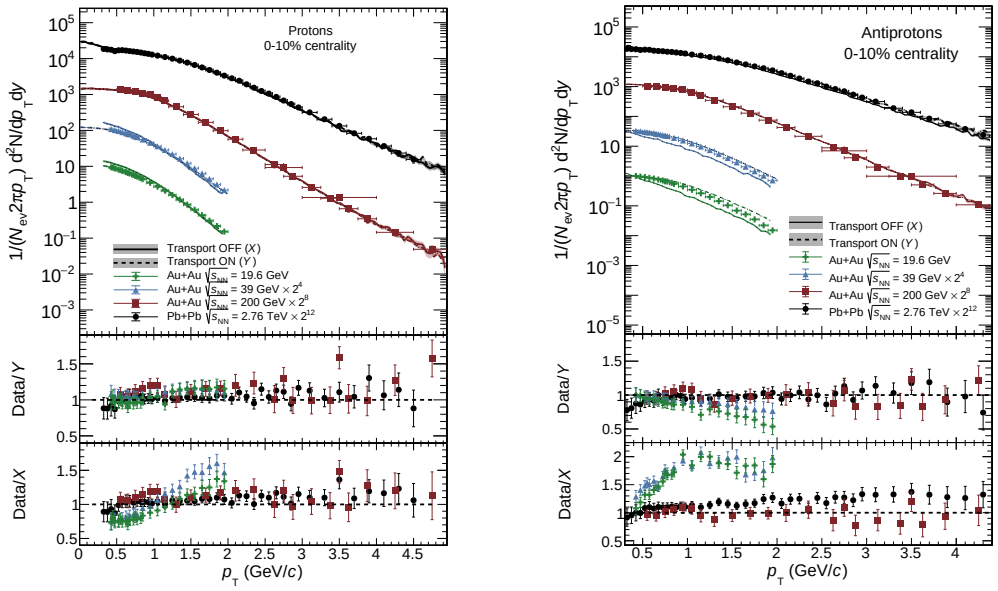

Figure 5.4: Transverse momentum spectra of (Left) protons and (Right) anti-protons in central Au–Au collisions at $\sqrt{s_{\rm NN}}$ = 19.6 GeV, 39 GeV ($|y| < 0.1$), 200 GeV ($|y| < 0.5$) and central Pb–Pb collisions at $\sqrt{s_{\rm NN}}$ = 2.76 TeV ($|y| < 0.5$) from "Coalescence" or "Transport OFF" (solid lines) and "Transport ON" (dashed lines) mode. Experimental results (symbols) are taken from STAR and ALICE experiments [251–253]. The lower panels show the ratio of the experimental results to the model predictions.

5.5.1 Transverse momentum spectra

The transverse momentum spectra ($p_{\rm T}$) for the (anti-)proton and their comparisons to the STAR and ALICE measurements [251–253] at mid-rapidity for $\sqrt{s_{\rm NN}}$ = 19.6, 39 ($|y| < 0.1$), 200 GeV ($|y| < 0.5$) (Au–Au, 0-10%) and 2.76 TeV (Pb–Pb, 0-10%, $|y| < 0.5$) respectively, are shown in Figure 5.4. The "Coalescence" (transport deuterons are OFF) results overestimate the data for protons at $p_{\rm T} < 1$ GeV/c for $\sqrt{s_{\rm NN}}$ = 19.6 and 39 GeV and underestimate at $p_{\rm T} \sim 2$ GeV/c. In this aspect, the "Transport" (transport deuterons are ON) mode provides a better description of the $p_{\rm T}$ spectra for $\sqrt{s_{\rm NN}}$ = 19.6 and 39 GeV [252]. Both the modes show good agreement with the data for protons at $\sqrt{s_{\rm NN}}$ = 200 GeV (Au–Au) and $\sqrt{s_{\rm NN}}$ = 2.76 TeV (Pb–Pb) [251, 253]. However, the "Coalescence"

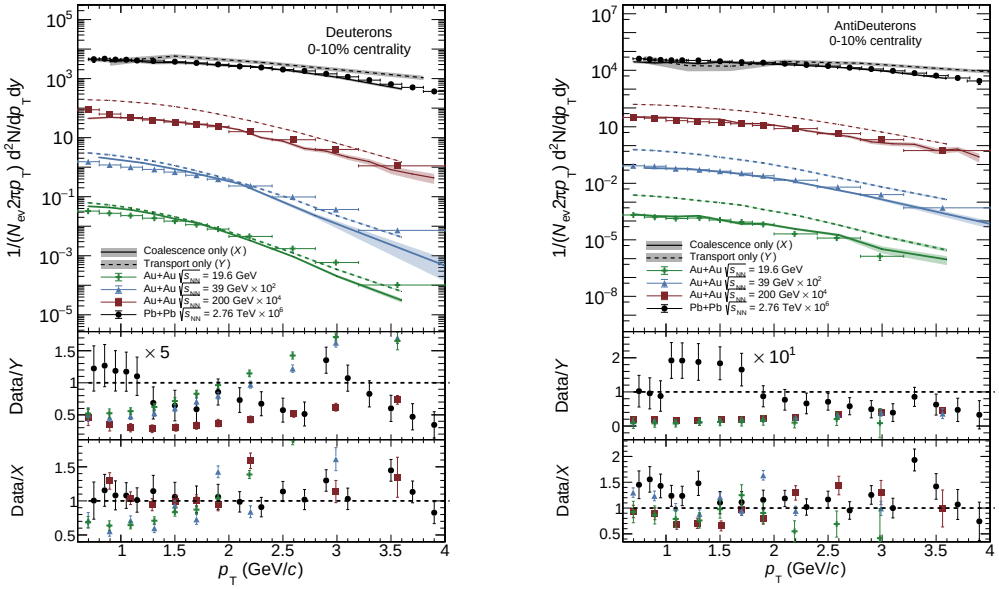

Figure 5.5: Transverse momentum spectra of (Left) deuterons and (Right) anti-deuterons in central Au–Au collisions at $\sqrt{s_{\rm NN}}$ = 19.6 GeV, 39 GeV, 200 GeV ($|y| < 0.3$) and central Pb–Pb collisions at $\sqrt{s_{\rm NN}}$ = 2.76 TeV ($|y| < 0.5$) from "Coalescence" (solid lines) and "Transport" (dashed lines) mode. Experimental results (symbols) are taken from the STAR and ALICE measurements [212, 213]. The lower panels show the ratio of the experimental results to the model predictions.

mode largely underestimate the anti-proton data for Au–Au collisions at $\sqrt{s_{\rm NN}}$ = 19.6 and 39 GeV, but gives a good description at $\sqrt{s_{\rm NN}}$ = 200 GeV and 2.76 TeV. The anti-protons from "Transport" mode provides a slightly harder $p_{\rm T}$ spectra for $\sqrt{s_{\rm NN}}$ = 19.6 and 39 GeV when compared to data, and performs similar to the "Coalescence" mode for $\sqrt{s_{\rm NN}}$ = 200 GeV (Au–Au) and 2.76 TeV (Pb–Pb).

Figure 5.5 displays the (anti-)deuteron $p_{\rm T}$ spectra for "Coalescence" and "Transport" modes, which are compared to experimental measurements at midrapidity for Au–Au collisions at $\sqrt{s_{\rm NN}}$ = 19.6, 39, 200 GeV ($|y| < 0.3$), as well as Pb–Pb collisions at $\sqrt{s_{\rm NN}}$ = 2.76 TeV ($|y| < 0.5$). While the deuterons produced via "Coalescence" accurately reproduce the experimental data at $\sqrt{s_{\rm NN}}$ = 200 GeV (Au–Au) [212] and 2.76 TeV (Pb–Pb) [213] at all $p_{\rm T}$ values, they tend to overestimate the data at low $p_{\rm T}$ and underestimate it at high $p_{\rm T}$ in Au–Au collisions at $\sqrt{s_{\rm NN}}$ = 19.6 and 39 GeV [212]. This disagreement is attributed to the softer proton $p_{\rm T}$ spectra from AMPT. The "Coalescence" anti-deuteron spectra show minor deviations across $p_{\rm T}$, and fit well with the experimental measurements for Au–Au and Pb–Pb collisions. [212, 213]. In contrast, the deuterons and anti-deuteron yields from "Transport" mode significantly deviates from the experimental results. In particular, the anti-deuteron yields are largely overestimated for Au–Au collisions. While,

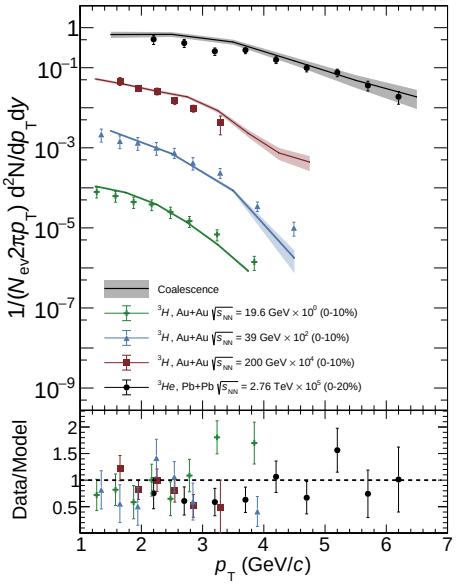

Figure 5.6: Transverse momentum spectra of triton in central Au–Au collisions at $\sqrt{s_{\rm NN}}$ = 19.6, 39, 200 GeV ($|y| < 0.5$) and helium-3 in central Pb–Pb collisions at $\sqrt{s_{\rm NN}}$ = 2.76 TeV ($|y| < 0.5$) from the "Coalescence" mode (solid lines). Experimental results (symbols) are taken from the STAR and ALICE measurements [213, 216]. The lower panels show the ratio of the experimental results to the model predictions.

the "Transport" deuteron spectra for Au–Au collision at $\sqrt{s_{\rm NN}}$ = 19.6 and 39 GeV sits close to the "Coalescence" spectra, the yields are overestimated for $\sqrt{s_{\rm NN}}$ = 200 GeV. In Pb–Pb collisions, the "Transport" (anti-)deuteron yields are underestimated, with a visible drop at low $p_{\rm T}$.

The results shown in Figure 5.4 and 5.5 clearly demonstrate a trade-off between (anti-)proton and (anti-)deuteron production in the AMPT model. This trade-off likely contributes to the observed differences in (anti-)proton yields between the "Coalescence" and "Transport" modes, especially for anti-proton yields in Au–Au collisions at $\sqrt{s_{\rm NN}}$ = 19.6 GeV and 39 GeV. The overestimation of anti-deuteron yields when using the "Transport" mode suggests that there might be an inherent imbalance in the cross-sections governing anti-deuteron production and dissociation processes. This imbalance directly impacts the anti-proton yields when these processes are turned OFF. In the "Coalescence" mode, where these kinetic processes are absent, the production of anti-protons is underestimated, particularly at collision energies where the net proton number is non-zero.

The triton and helium-3 $p_{\rm T}$-spectra results from "Coalescence" mode are presented and compared to experimental results in Figure 5.6 for central (0-10%) Au–Au collisions at $\sqrt{s_{\rm NN}}$ = 19.6, 39, 200 GeV [216] and central (0-20%) Pb–Pb collisions at $\sqrt{s_{\rm NN}}$ = 2.76 TeV [213] at mid-rapidity ($|y| < 0.5$). For tritons in Au–Au collisions at $\sqrt{s_{\rm NN}}$ = 19.6

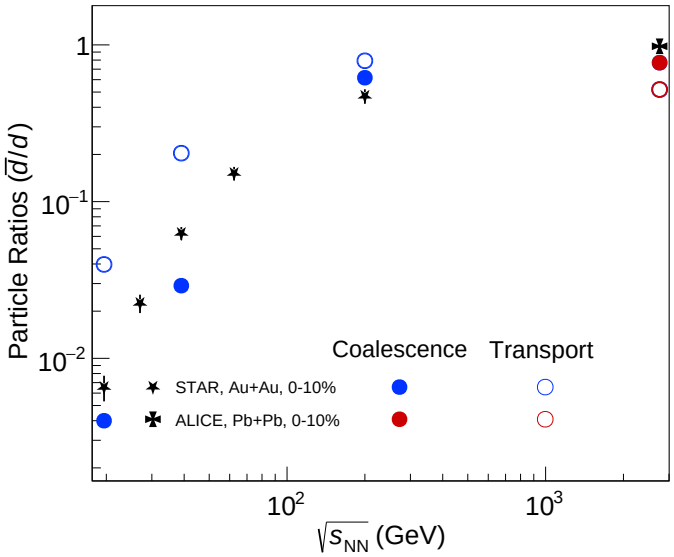

Figure 5.7: Particle ratios for anti-deuterons over deuterons as a function of center of mass energies from "Coalescence" and "Transport" modes. Experimental measurment of $\bar{\mathrm{d}}/\mathrm{d}$ ratios from the STAR and ALICE experiments for the central Au–Au collisions at $\sqrt{s_{\mathrm{NN}}}$ = 19.6 GeV, 39 GeV, 200 GeV and central Pb–Pb collisions at $\sqrt{s_{\mathrm{NN}}}$ = 2.76 TeV are also shown [212, 213]

and 39 GeV, the model exhibits a deviation across p_{T} that follows a similar pattern to that observed for deuterons. The model slightly overestimates the experimental data at low p_{T} and underestimates at larger values. However, the behaviour changes for tritons in Au–Au collisions at $\sqrt{s_{\mathrm{NN}}}$ = 200 GeV, giving a harder spectra when compared to the data. The helium-3 spectra for Pb–Pb collisions at $\sqrt{s_{\mathrm{NN}}}$ = 2.76 TeV is well described, with a slight overestimation for $p_{\mathrm{T}} < 3.5$ GeV/c.

5.5.2 Particle yield ratios

The p_{T}-integrated yields for (anti-)deuterons, tritons and helium-3s (d, $\bar{\mathrm{d}}$ and ^{3}H, ^{3}He) are calculated for central Au–Au collisions at $\sqrt{s_{\mathrm{NN}}}$ = 19.6, 39, 200 GeV and Pb–Pb collisions at $\sqrt{s_{\mathrm{NN}}}$ = 2.76 TeV at mid-rapidity via "Coalescence" and "Transport" modes. Figure 5.7 shows the $\bar{\mathrm{d}}/\mathrm{d}$ ratios as a function of center of mass energy compared to experimental measurements. Both modes are able to qualitatively describe the trend of energy dependence of d and $\bar{\mathrm{d}}$ production successfully at the respective RHIC and LHC energies[212]. Quantitatively, the "Transport" mode systematically overestimates the experimental data for Au–Au collisions from $\sqrt{s_{\mathrm{NN}}}$ = 19.6 to 200 GeV, but largely underestimates the value for Pb–Pb collisions at $\sqrt{s_{\mathrm{NN}}}$ = 2.76 TeV. The "Coalescence" mode underestimates the ratios for Au–Au collisions at $\sqrt{s_{\mathrm{NN}}}$ = 19.6 and 39 GeV, and

slightly overestimates for $\sqrt{s_{\rm NN}}$ = 200 GeV. The value at $\sqrt{s_{\rm NN}}$ = 2.76 TeV (Pb–Pb) is slightly underestimated.

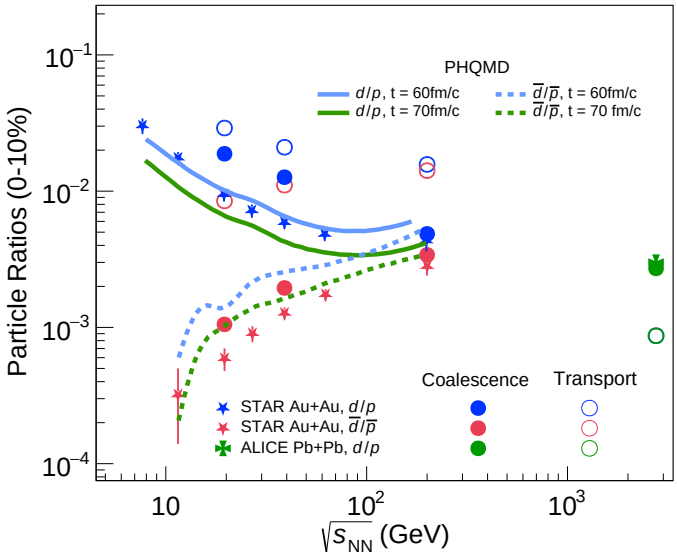

Figure 5.8: Particle ratios for deuterons over protons and anti-deuterons over anti-protons as a function of the center of mass energies from "Coalescence" and "Transport" modes. Solid lines are predictions from the PHQMD model [223]. Experimental measurement of d/p and $\bar{\rm d}/\bar{\rm p}$ ratios from the STAR and ALICE experiments for the central Au–Au collisions at $\sqrt{s_{\rm NN}}$ = 19.6 GeV, 39 GeV, 200 GeV and central Pb–Pb collisions at $\sqrt{s_{\rm NN}}$ = 2.76 TeV are also shown [212, 213].

The d($\bar{\rm d}$) over p($\bar{\rm p}$) ratios are presented in Figure 5.8 as a function of center of mass energy. Both modes capture the trends for d/p and $\bar{\rm d}/\bar{\rm p}$ in Au–Au collisions. However, there are substantial quantitative discrepancies between the model predictions and the experimental data. In particular, the "Transport" mode significantly overestimates the yield ratios compared to the experimental measurements, indicating a large deviation from the data [212]. The "Coalescence" mode overestimates the values, especially at $\sqrt{s_{\rm NN}}$ = 19.6 and 39 GeV, but gives a good description for $\sqrt{s_{\rm NN}}$ = 200 GeV and 2.76 TeV [213]. For completeness, the additional model comparisons from [223] are added to Figure 5.8. The predictions from the light nuclei cluster production with a PHQMD approach show a comprehensive study with different cluster freezeout times or "physical" times. The d/p ratio is well described for t = 60 fm/c for Au–Au collisions. The $\bar{\rm d}/\bar{\rm p}$ ratios for t = 70 fm/c are closer to data and consistent with the "Coalescence" predictions. However, this is accredited to an over-predicted $\bar{\rm d}$ yield by the model [223].

In Figure 5.9, the ^{3}H, ^{3}He $p_{\rm T}$-integrated yields over p and d yields for central (0-10%) Au–Au [216] and Pb–Pb collisions with "Coalescence" mode are presented [213]. All the ratios show the dependence with center of mass energy, and capture the trend of the

experimental results. The ^{3}H/p ratios are slightly overestimated for Au–Au collisions, but the ^{3}He/p ratio for Pb–Pb collisions is well described. The ^{3}H/d and ^{3}He/d values at 0-10% are also closely compatible with the experimental measurements [213, 216].

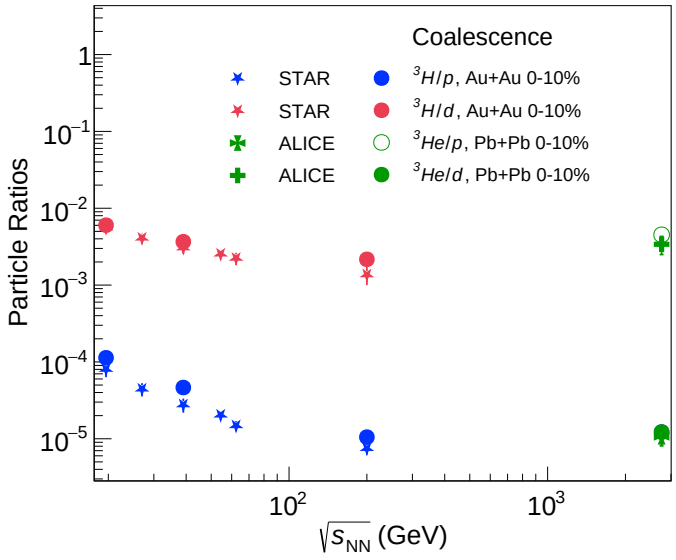

Figure 5.9: Particle ratios from the "Coalescence" mode for triton over proton and deuteron for 0-10% central Au–Au and Pb–Pb collisions, helium-3 over deuteron for 0-10% central Pb–Pb collisions and helium-3 over proton for 0-20% central Pb–Pb collisions. Experimental measurement of ^{3}H/p, ^{3}H/d, ^{3}He/p, ^{3}He/d ratios from the STAR and ALICE experiments for the central Au–Au collisions at $\sqrt{s_{\rm NN}}$ = 19.6 GeV, 39 GeV, 200 GeV and central Pb–Pb collisions at $\sqrt{s_{\rm NN}}$ = 2.76 TeV are also shown [213, 216].

It can be concluded that while there are some discrepancies between the "Coalescence" model's $p_{\rm T}$-differential and $p_{\rm T}$-integrated yields of light nuclei and experimental measurements from a quantitative standpoint, the model is still able to provide a reliable qualitative description of light nuclei yields as a function of $p_{\rm T}$ and center of mass energy. Moreover, the light nuclei yields are accurately reproduced by the coalescence model for higher collision energies. These findings demonstrate the effectiveness of a simple phase space coalescence over AMPT's "Transport" approach in light nuclei production. The model's ability to offer a comprehensive explanation of experimental data with only a few tuning parameters is particularly noteworthy. Moving forward, these results can be further refined by leveraging the enhanced capabilities of the updated string melting AMPT model.

5.5.3 Coalescence parameter

The coalescence parameter (B_2) values as a function of $p_{\rm T}$ are calculated for d($\bar{\rm d}$) in central Au–Au and Pb–Pb collisions at $\sqrt{s_{\rm NN}}$ = 39 GeV and 2.76 TeV respectively, us-

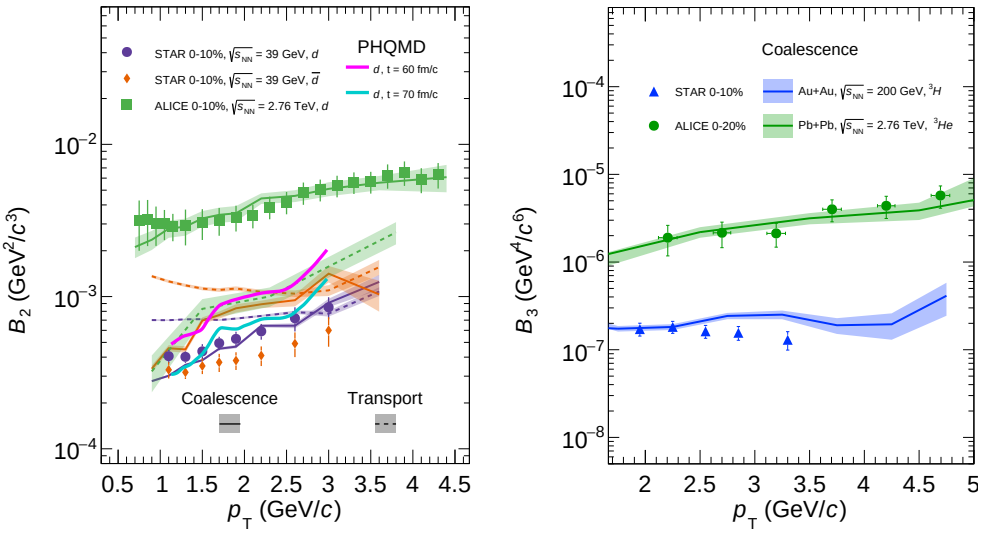

Figure 5.10: (Left) The B_2 parameter versus p_T of deuterons and anti-deuterons in central (0-10%) Au–Au collisions at $\sqrt{s_{NN}}$ = 39 GeV and central Pb–Pb collisions at $\sqrt{s_{NN}}$ = 2.76 TeV from "Coalescence" (solid lines) and "Transport" (dashed lines) modes. Predictions from the PHQMD model are superimposed [223]. (Right) The B_3 parameter versus p_T for triton and helium-3 in central (0-10%) Au–Au collisions at $\sqrt{s_{NN}}$ = 200 GeV and central (0-20%) Pb–Pb collisions at $\sqrt{s_{NN}}$ = 2.76 TeV from "Coalescence" (solid lines) mode. The results are compared to experimental measurements (symbols) from STAR and ALICE [212, 213, 254].

ing equation 5.3. The left panel of Figure 5.10 shows the results from "Coalescence" and "Transport" modes compared to experimental measurements [212, 213]. The "Coalescence" mode is promising in reproducing the increasing p_T dependence of deuteron B_2 for central Au–Au collisions at $\sqrt{s_{NN}}$ = 39 GeV and 2.76 TeV. For deuterons, the model predictions are compatible with the experimental results for Au–Au as well as Pb–Pb collisions. The anti-deuterons at $\sqrt{s_{NN}}$ = 39 GeV (Au–Au) shows an overestimated B_2 vs p_T with a finite slope. The "Transport" mode is unable to reproduce the increasing dependence of B_2 with p_T for Au–Au collisions. Both deuteron and anti-deuteron results are largely overestimated by "Transport" mode for $\sqrt{s_{NN}}$ = 39 GeV (Au–Au). For Pb–Pb collisions, the "Transport" mode is able to reproduce the increasing trend with p_T. However, the results are underestimated when compared to the experimental measurements [213]. The highlight of these results is the ability of the "Coalescence" mode to reproduce the increasing trend of B_2 with p_T. The PHQMD model results for deuteron B_2 for Au–Au collisions at $\sqrt{s_{NN}}$ = 39 GeV also successfully reproduces the increasing trend with p_T, for cluster freezeout time t = 70 fm/c [223]. A lower freezeout time (t = 60 fm/c) overestimates the values. Moreover, the simple coalescence model outperforms in quantitative estimation

of the B_2 for deuterons.

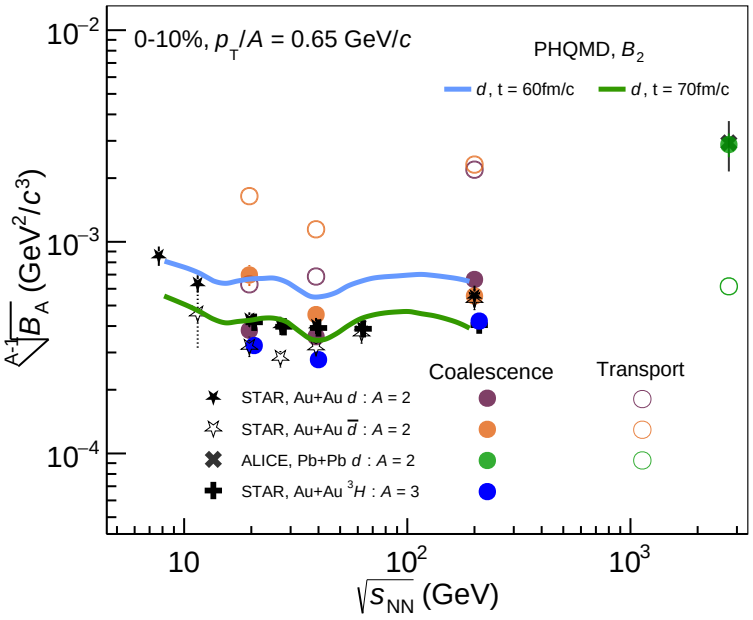

Figure 5.11: Coalescence parameter B_2 and $\sqrt{B_3}$ as a function of $\sqrt{s_{NN}}$ for p_T/A = 0.65 GeV/c in central (0-10%) Au–Au and Pb–Pb collisions for "Coalescence" and "Transport" modes. Solid lines are predictions from the PHQMD model [223]. The results are compared with measurements from the STAR and ALICE experiments. [212, 213, 254].

Furthermore, the B_3 values as a function of p_T for central collisions at $\sqrt{s_{NN}}$ = 200 GeV (Au–Au) and 2.76 TeV (Pb–Pb) from the "Coalescence" mode are presented on the right panel of Figure 5.10. The predictions are fairly close to the experimental data for 0-20% central Pb–Pb collisions [213] and 0-10% central Au–Au collisions [254], respectively. The trend of B_3 as a function of p_T is quantitatively reproduced for helium-3 with good agreement with the experimental results. On the other hand, the data for triton B_3 shows a flat or decreasing dependence with p_T, whereas the model shows somewhat of an increasing trend.

Figure 5.11 reports the B_A as a function of center of mass energies for d, $\bar{\text{d}}$ and ^{3}H, ^{3}He for central Au–Au and Pb–Pb collisions. The values are obtained for p_T/A = 0.65 GeV/c, which is 1.3 GeV/c for deuterons and 1.95 GeV/c for triton and helium-3. The B_2 of deuterons from "Coalescence" shows a good match within uncertainties with the experimental results [212] across $\sqrt{s_{NN}}$. The points for anti-deuterons at $\sqrt{s_{NN}}$ = 19.6 and 39 GeV are systematically overestimated and appear higher than the B_2 for deuteron. For $\sqrt{s_{NN}}$ = 200 GeV (Au–Au), the anti-deuteron B_2 falls within the uncertainties of the experimental results, nearly superimposed over the B_2 of the deuteron. The "Transport" mode, overestimates the coalescence parameter for both deuteron and anti-deuteron in Au–

Au collisions. The same is underestimated in Pb–Pb collisions. The PHQMD predictions also show the deuteron B_2 as a function of collision energy in Au–Au collisions [223]. Out of the two freezeout times, t = 70 fm/c shows a better agreement to the experimental measurements. The B_3 for tritons in Au–Au collisions are also shown and compared to experimental measurements from STAR [254]. The results at $\sqrt{s_{\rm NN}}$ = 200 GeV is accurately described by the model, whereas at $\sqrt{s_{\rm NN}}$ = 19.6 and 39 GeV, the values are slightly underestimated.

5.6 Enhancement of deuteron coalescence probability in jets

This section is based on a study inspired by an ALICE measurement; providing some interesting ground on the likelihood of (anti-)deuteron production in jets [255]. With the help of event topology variables, the deuteron was observed to have a higher chance of production via coalescence in jets. Previous work on jet-associated deuteron production by ALICE via angular correlations of deuterons and charged particles also showed a higher population of deuterons around a jet [256]. Due to the collimated nature of jets, the "in-jet" nucleons produced from the fragmentation processes are strongly correlated in phase space. As a result, the nucleons that are close in space are also close in momenta. This correlation is absent for "out-of-jet" nucleons that belong to the underlying event (UE). In a coalescence scenario, the "in-jet" nucleons with phase space vicinity will have a larger chance to form a deuteron and, therefore, carry a higher probability than "out-of-jet" nucleons. A Wigner coalescence afterburner (detailed description provided in Section 5.3.2) is developed for this work, coupled to PYTHIA8 [88, 149] for pp collisions at $\sqrt{s}$ = 13 TeV. To dive deeper into the microscopic aspects, spatial degrees of freedom for the nucleons are fed into PYTHIA8 from femtoscopic measurements by ALICE. Following the prescription described in Section 5.3.2.2 nucleon emission sources with effects from resonance decays are embedded into PYTHIA8 with source sizes measured by ALICE in high multiplicity (HM) pp collisions [110, 237]. The event shapes are classified as jetty and isotropic using transverse spherocity ($S_{\rm O}$), in the same form as described in Equation 4.4.

The Monash 2013 tune in PYTHIA8 [88] is chosen to reproduce the event multiplicities in pp collisions at $\sqrt{s}$ = 13 TeV. The charged-particle multiplicity distributions from PYTHIA8 in the SPD ($|\eta| < 0.8$) and V0 (or V0M) acceptance ($-3.7 < \eta < -1.7$ and $2.8 < \eta < 5.1$) of ALICE for pp collisions at $\sqrt{s}$ = 13 TeV are presented on the left panel of Figure 5.12. For both acceptances, the distributions are presented by scaling the event multiplicity to the average multiplicity ($N_{\rm ch}/\langle N_{\rm ch}\rangle$) which represents the fractional cross-section with the minimum-bias cross-section in pp collisions. The PYTHIA8 predictions reasonably describe the experimental results [206, 257]. The right panel of Figure 5.12 show the $S_{\rm O}$ distribution from PYTHIA8, compared to ALICE measurements for 0-1%

minimum bias (MB I) multiplicity in SPD and V0M acceptances [202]. The events with at least ten tracks are chosen to calculate S_{O}. PYTHIA8 with the Monash tune describes the S_{O} distribution for both acceptance ranges in the respective multiplicity classes. In addition, the analysis is extended to a high multiplicity selection (HM I) corresponding to 0-0.17% of the MB cross-section.

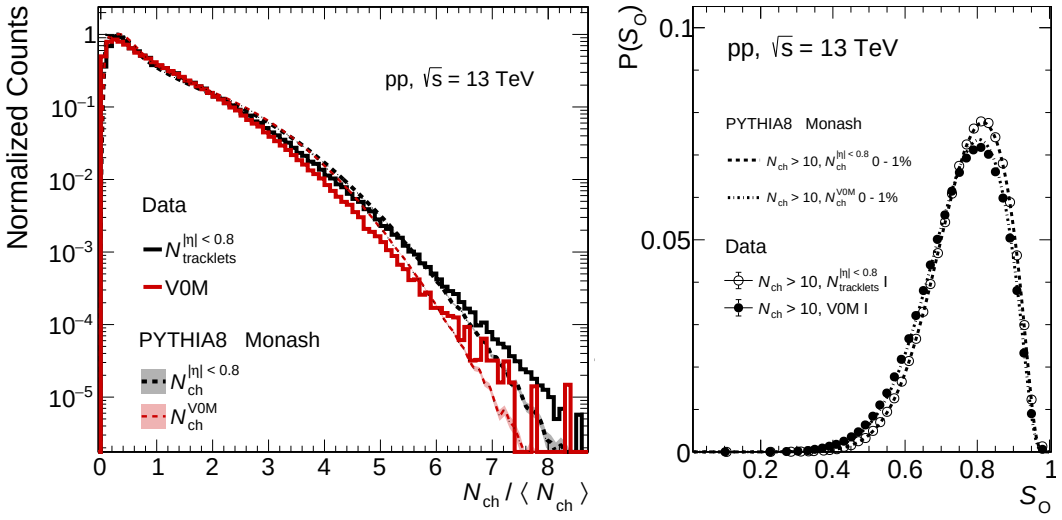

Figure 5.12: (Left) Charged-particle multiplicity distributions from PYTHIA8 + Monash (dotted lines) for pp collisions at $\sqrt{s}$ = 13 TeV. Data from ALICE (solid lines) for the midrapidity multiplicity estimator ($N^{|\eta|<0.8}_{\mathrm{tracklet}}$) and the V0M detector are presented for comparison [206, 257]. (Right) Transverse spherocity distributions from PYTHIA8 + Monash (lines) for pp collisions at $\sqrt{s}$ = 13 TeV. Data points from ALICE (markers) in the 0-1% multiplicity for the midrapidity estimator ($N^{|\eta|<0.8}_{\mathrm{tracklet}}$ I) and the V0M detector (V0M I) with events having $N_{\mathrm{ch}} > 10$ are presented for comparison [202].

5.6.1 Transverse momentum spectra

The transverse momentum (p_{T}) distribution of (anti-)protons and (anti-)deuterons via coalescence are presented in Figure 5.13, for MB I and HM I multiplicity classes in pp collisions at $\sqrt{s}$ = 13 TeV at midrapidity ($|y| < 0.5$). The (anti-)protons from PYTHIA8 in the MB I class reproduce the data quantitatively, showing good agreement with the V0M estimator and slightly overestimating for the midrapidity estimator for $p_{\mathrm{T}} > 4$ GeV/c. The HM I (anti-)protons from PYTHIA8 are slightly underestimated by the V0M multiplicity selection but quantitatively captured by the midrapidity estimator, showing a similar overestimation as MB I [103, 258].

The coalescence model predictions with the single Gaussian wave function shown in the central panel of Figure 5.13, are underestimated when compared to experimental

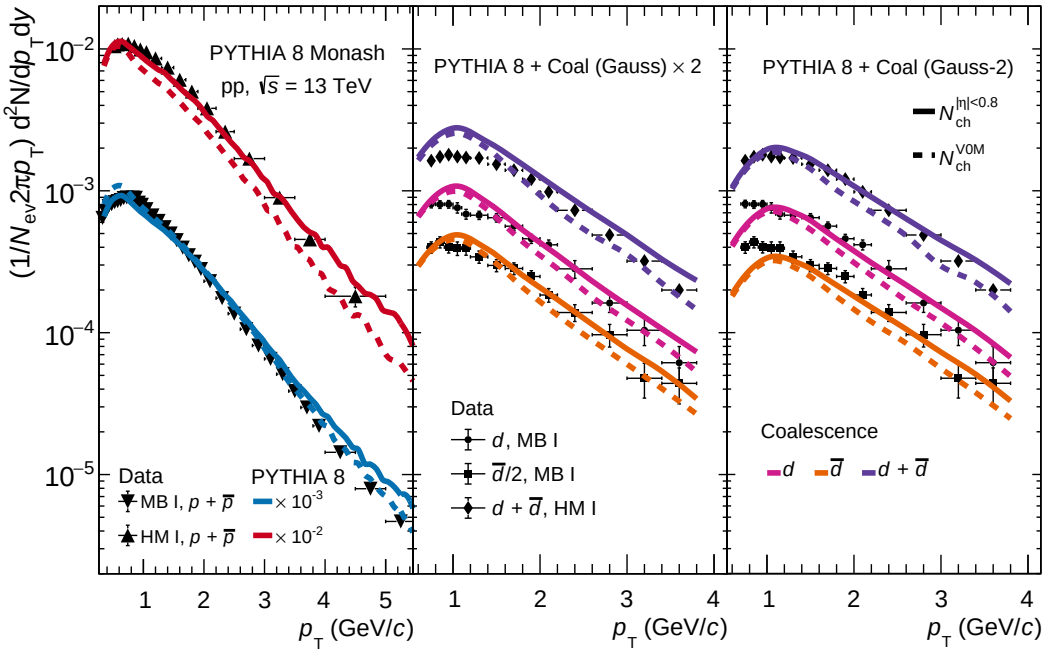

Figure 5.13: Transverse momentum spectra of (anti-)protons from PYTHIA8, and deuterons and anti-deuterons from pp collisions at $\sqrt{s} = 13$ TeV with PYTHIA8 + Coalescence in MB I and HM I class at midrapidity ($|y| < 0.5$) in two detector acceptances; (Left) Predictions from PYTHIA8 Monash in MB I and HM I multiplicity classes; (Center) Predictions from a single Gaussian deuteron wave function scaled twice to their actual values; (Right) Predictions from a two-Gaussian deuteron wave function. Results are compared to measurements from ALICE in respective multiplicity intervals [103, 258, 259].

measurements from ALICE and are scaled twice to their actual values for better visualization [103, 259]. The predictions for the MB I deuterons and anti-deuterons show a deviation from the experimental measurements at low p_{T} and slightly underestimates at intermediate to high p_{T}. Both multiplicity estimators provide a reasonable description of the p_{T} spectra of the (anti-)deuterons. The (anti-)deuterons from the HM I sample are also compared to the coalescence model predictions. The disagreement at low p_{T} is largely visible here, with a reasonable description of the shape from intermediate to high p_{T}. In this case, the (anti-)deuterons from $N_{\mathrm{ch}}^{|\eta|<0.8}$ multiplicity sample show a slight overestimation at intermediate to high p_{T}.

The right panel of Figure 5.13 presents the model predictions employing the two-Gaussian function as the deuteron wave function. The invariant yields as a function of p_{T} are nicely described for $p_{\mathrm{T}} > 1.25$ GeV/c and deviate at low p_{T}, similar to the single Gaussian case for MB I and HM I. However, the two-Gaussian model provides a quantitative estimation

of the yields. The results from the midrapidity multiplicity estimator show a reasonable agreement with the ALICE measurements [103]. It is worth noting that through the nature of coalescence, the shapes of the (anti-)deuteron distributions inherit the characteristics of the (anti-)proton, or, more precisely, the (anti-)nucleon momentum distribution. In addition, the distinct shape predicted by the model at low p_{T} is an artifact of the Wigner probability density associated with the deuteron wave function and the (anti-)nucleon momenta. Moreover, the inconsistencies seen between the multiplicity estimators and the multiplicity classes for the (anti-)proton production from PYTHIA8 also translate to the (anti-)deuteron distribution.

$N_{\mathrm{ch}}^{\lvert\eta\rvert<0.8}$	S_{O} selection	
	Jetty (0 - 20%)	Isotropic (80 - 100%)
MB I (0 - 1%)	0.665	0.851
HM I (0 - 0.17%)	0.689	0.862

Table 5.2: S_{O} selection for "jetty" and "isotropic" class on different multiplicity classes at midrapidity.

The description of the (anti-)deuteron p_{T} spectra is an important test of the adopted coalescence formalism with its underlying assumptions and the microscopic details of the emission source model. The deuteron wave function is relevant in this problem; the two-Gaussian form fitted to the Hulthén wave function gives a quantitative estimation of the p_{T}-differential yields over the single Gaussian form. A proper combination of the source model and the light nuclei wave function provides a cohesive description of the coalescence mechanisms of these nuclear clusters.

The (anti-)deuteron yields are extracted at midrapidity into different classes of S_{O} and $N_{\mathrm{ch}}^{\lvert\eta\rvert<0.8}$ as described in Table 5.2. The p_{T} spectra of (anti-)protons and (anti-)deuterons from each of these selections are shown in Figure 5.14 for the single and double Gaussian wave functions. The "jetty" ("isotropic") (anti-)protons and (anti-)deuterons show hardening (softening) of the spectra at high (low) p_{T} when compared to the S_{O} integrated p_{T} spectra at MB I multiplicity. The "jetty" (anti-)deuterons in HM I are affected by statistical uncertainties at intermediate to high p_{T}, which makes the same observation inconclusive. It is clear that for separate S_{O} intervals, the (anti-)deuteron yields share the behavior of (anti-)proton yields. These trends present the nature of the production of protons and deuterons in different event topologies; the harder event carries more protons at high-p_{T} and vice versa.

5.6.2 Coalescence parameter

In Figure 5.15, the coalescence parameter, B_2 as a function of p_{T} at midrapidity, is presented. The coalescence parameter is calculated using Equation 5.3 and shown for

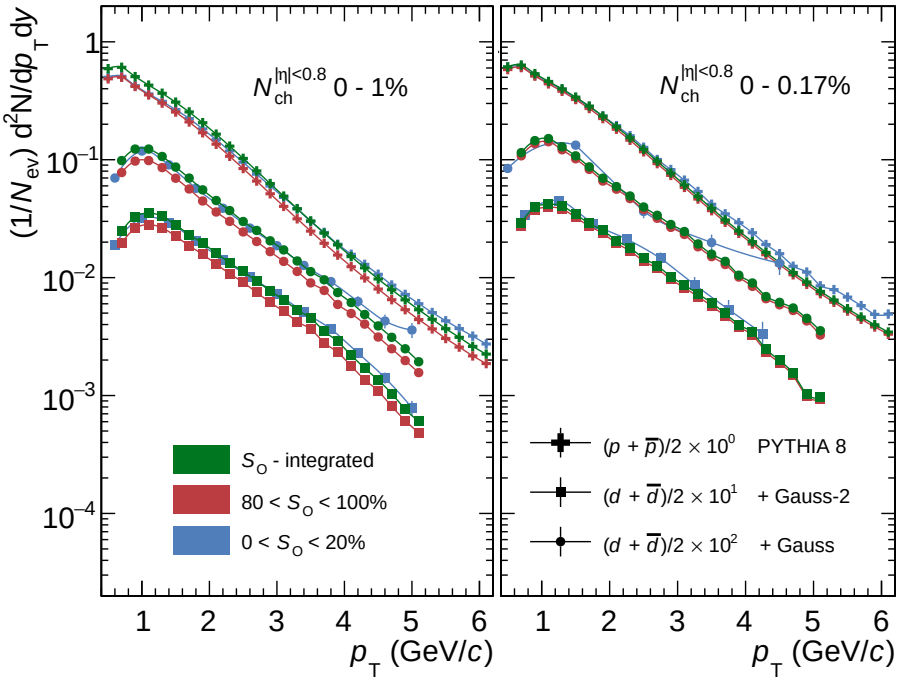

Figure 5.14: Transverse momentum spectra of (anti)-protons with PYTHIA8 and (anti-)deuterons with PYTHIA8 + Coalescence in "jetty", "isotropic", and S_O-integrated intervals at midrapidity ($|y| < 0.5$) in pp collisions at $\sqrt{s} = 13$ TeV. Predictions from the model are presented in (Left) MB I and (Right) HM I multiplicity interval.

0–20%, 80–100%, and integrated S_O in MB I and HM I multiplicities. In both multiplicity intervals, the "jetty" deuterons show a slightly higher B_2, which increases with increasing p_T. Although noticeable, the difference between the three S_O cases is insignificant. The quoted ALICE measurements belong to the S_O-integrated interval, which is supported by the calculations from the model [103, 259]. These results also show that the "jetty", "isotropic", and the integrated case are close or comparable, which can be accredited to the contribution of the UE at high multiplicities. The UE plays a dominant role in deuteron production.

The degree of enhancement of the B_2 for "jetty" deuterons is not as significant as the one reported by ALICE, where the "in-jet" deuterons show a B_2 10 times more than those of the UE [255]. In the ALICE measurement, the "in-jet" deuterons (region towards the jet) are separated by subtracting the UE contributions (region away from the jet) from the (anti-)deuterons closer to the jet. This removes the contribution of the UE deuterons in the region towards the jet and keeps the deuterons that originate solely from the jet fragmentation. This procedure can be repeated for the deuterons in S_O intervals by subtracting the "isotropic" deuterons from the "jetty" ones. These isolated (anti-)deuterons are produced from the coalescence of correlated (anti-)nucleon pairs that are produced in

the jet fragmentation processes in events that carry a "jetty" topology. However, one must be cautious as the deuterons would belong to different events from being truly separated by S_{O} without knowing the actual contribution of the UE in a S_{O} class. To approximate this, the average number of MPIs ($\langle N_{\mathrm{MPI}} \rangle$) is calculated for 0–20% and 80–100% S_{O} intervals. The relative contribution of $\langle N_{\mathrm{MPI}} \rangle$ in "jetty" to "isotropic" events is taken as a weight for the "isotropic" (anti-)deuteron p_{T} distribution. The "in-jet" deuterons are then approximated by taking the difference of "jetty" and the weighted "isotropic" distribution. At high multiplicities, where the contribution of MPI is large, there is a small difference between the number of MPIs between a jetty and an isotropic event. The relative contribution from MPIs in "jetty" to "isotropic" events is calculated to be $\approx 90 - 95\%$.

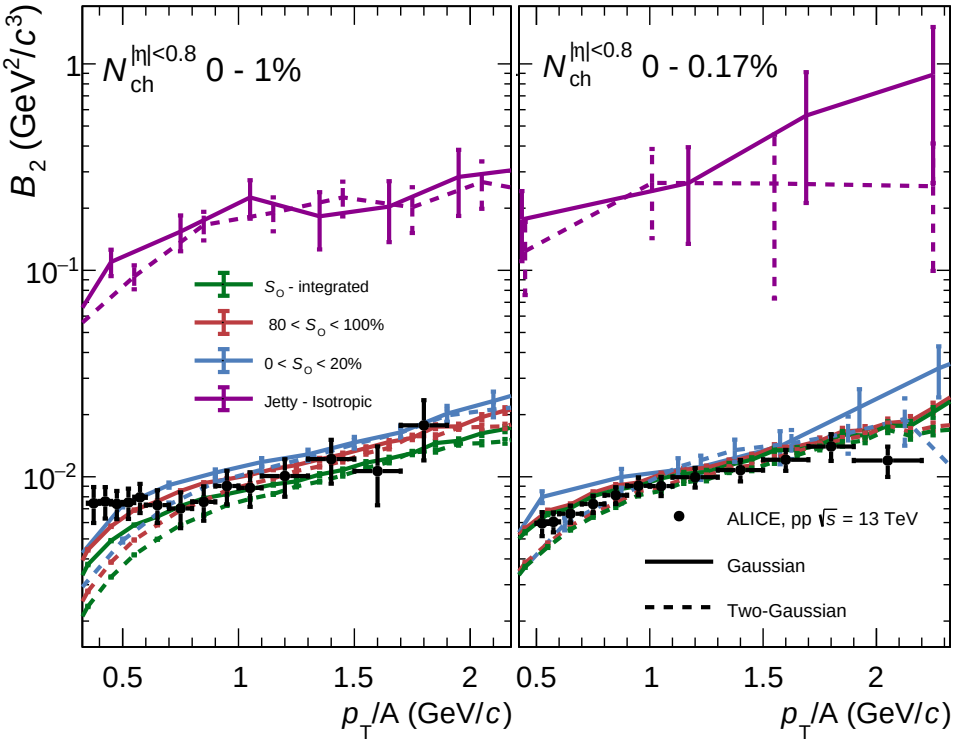

Figure 5.15: Coalescence parameter of (anti-)deuterons B_2 as a function of proton transverse momentum at midrapidity ($|y| < 0.5$) in pp collisions at $\sqrt{s} = 13$ TeV in (Left) MB I and (Right) HM I multiplicity interval. Solid and dashed lines represent the predictions from single and double Gaussian wave functions respectively. The results are compared to experimental measurements from ALICE [103, 259].

Figure 5.15 shows the (anti-)deuteron coalescence parameter for "jetty-isotropic" events. In both multiplicity intervals, the B_2 of "jetty"-"isotropic" deuterons is much higher than the individual S_{O} classes, showing an apparent "enhancement". The predictions from both models are compatible with one another. The "jetty"- "isotropic" B_2 is ten times to the S_{O}

integrated B_2 for the MB I multiplicity and up to 25 times for the HM I multiplicity class. However, the statistical uncertainties for the HM I "in-jet" deuterons are too large to draw a conclusive estimate of the enhancement. Although a quantitative comparison with ALICE measurements cannot be made as the multiplicity selections are different, the observations made on the enhancement of the coalescence probability in this study are quite transparent. With this enhancement in B_2, it is also seen that the strong spatio-momenta correlations between the coalescing nucleons are restored by removing the "isotropic" or UE deuterons from the "jetty" deuterons that contain an amalgamation of deuterons from both UE and jet fragmentation.

The results on (anti-)deuteron B_2 corroborate the claim on B_2 enhancement for "in-jet" deuterons and the observations on the same performed by ALICE [255]. Although the separation of "in-jet" deuterons is performed in an approximate manner, the motivation behind this work is supported by the results showing a clear enhancement of B_2 for "in-jet" deuterons compared to the ones belonging to the UE. It also shows that (anti-)deuteron production is dominated by the UE in pp collisions. Additionally, a finite p_{T} dependence of B_2 is observed in the MB I multiplicity class results, portraying a similar trend to the spectra from the UE. The same cannot be concluded for the HM class due to high statistical uncertainties.

5.7 Probing light nuclei formation with femtoscopy and anisotropic flow

This section is based on a study on femtoscopy of nucleons and light nuclei in heavy-ion collisions [233]. Due to its bound nature, light nuclei states are an ideal probe for performing two-particle correlations and femtoscopy [260, 261]. Understanding the interaction of these many-nucleon systems can assist in the realization of the intricacies of nucleon-nucleon interactions, as well as the EoS of neutron stars [93, 94]. The objective is to investigate coalescence as the primary nuclei production mechanism with validation from femtoscopic measurements. Preliminary results from STAR show that the size of the emission source of the nucleon/nuclei pairs from the femtoscopic correlations shows a decreasing trend with the centrality in Au–Au collisions [262]. This is due to the source sizes being non-trivially affected by the colliding matters' expansion time, radially and longitudinally. The measurement of emission space-time geometry of particles can assist in drawing a clearer description of the collective nature of expansion in heavy-ion collisions. The convolution between femtoscopy and collectivity of light nuclei production brings together a cohesive point of discussion about their production mechanism. Microscopic transport models such as UrQMD [155], AMPT [156], and more recent SMASH [167] are developed with one of many goals to interpret the collective nature of expansion from the generated anisotropies in non-central heavy-ion collisions. In such cases, the azimuthal angular distribution (ϕ) can be decomposed into a Fourier expansion, with each

harmonic corresponding to a flow component; directed flow $v_1 = \langle \cos \phi \rangle$ and elliptic flow $v_2 = \langle \cos 2\phi \rangle$ corresponding to first and second harmonics respectively [263, 264].

Experimental evidence suggests that protons' elliptic flow coefficient is below zero at center of mass energies around and below 3 GeV [265]. Depending on the time scale of expansion in low energy collisions, the expanding matter can be blocked by the spectators in the reaction plane [266]. Subsequently, this leads to a "squeeze-out" effect if the blockage time from the spectators is more, forcing the emission out-of-plane [267, 268]. This "effect" is arguably connected to a softening or hardening of the EoS, which the models exploit to explain the experimental measurements [269–272]. Fluid dynamical treatment with a 'soft' EoS fails to explain the negative elliptic flow. Here, the importance of mean-field interactions could be drawn out, which, in addition to the EoS, is an established approach to explain the flow of protons at low energies [268, 273–276]. Many transport models can achieve this by parameterizing the Skyrme mean-field potential between the nucleons based on the "stiffness" of the EoS. Calculations with SMASH and UrQMD at low energies have reported success in reproducing experimental data from HADES and STAR of light nuclei flow with the application of a hard EoS [170, 179].

For this work, Au–Au collisions at $\sqrt{s_{\mathrm{NN}}} = 3$ GeV are generated using SMASH [167]. The Wigner coalescence model (described in Section 5.3) is used to produce all the light nuclei species. For completeness, the event generation is performed with two prescriptions (i) a hard EoS mean field parameterization of the Skyrme potential in SMASH, and (ii) a hybrid treatment, where a fluid dynamical evolution is carried out with the vHLLE package [168, 169, 171]. The momentum correlations of p–d and d–d states are carried out with the correlation afterburner (CRAB) [224] for different Au–Au collision centralities. Moreover, the hadronic evolution in SMASH is propagated to two different freeze-out or last collision times (20 fm/c and 30 fm/c), corresponding to two cluster formation times for p–d and d–d clusters. The source sizes of these clusters are extracted by fitting the Lednický-Lyuboshits (LL) model [242, 243], with a Gaussian ansatz for the source. By varying the last collision time of the nucleons, an attempt is made to gain insight into the formation times from the emission sizes of these clusters. The results are also supplemented with the directed and elliptic flow of light clusters (d, t(^{3}H), ^{3}He) in mid-central Au–Au collisions.

5.7.1 Correlation functions

Figure 5.16 and 5.17 shows the predictions of momentum correlation functions from SMASH + Coal + CRAB fitted to the LL model, of p − d and d − d pairs in different collision centralities with single and double Gaussian wave functions, respectively. SMASH is configured in two ways, viz., with hydro and with a hard EoS. The correlation distributions are obtained from the CRAB afterburner, which takes in the nucleon (nuclei) phase-space from SMASH (SMASH + Coal). As CRAB is not designed for p − d correlations, the

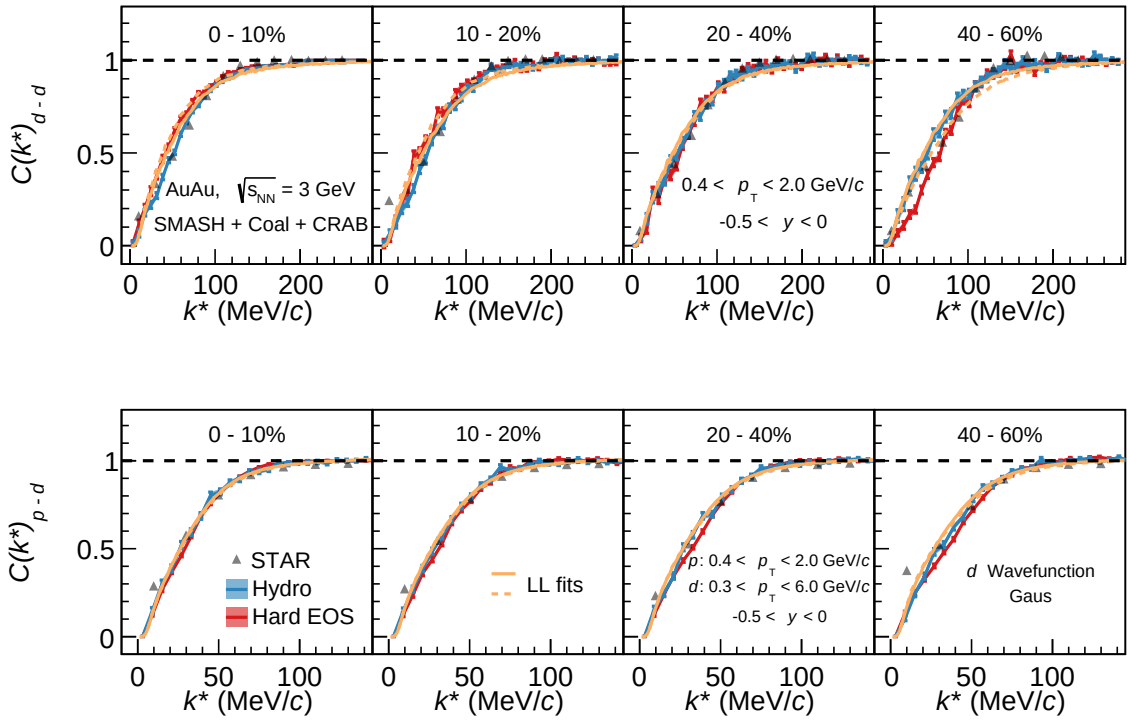

Figure 5.16: Momentum correlation of (Bottom) p – d and (Top) d – d pairs in Au–Au collisions at $\sqrt{s_{NN}}$ = 3 GeV with a single Gaussian function as the deuteron wavefunction in different centralities from SMASH + Coal + CRAB, compared to STAR preliminaries [262]. Predictions are presented for hydro and hard EoS SMASH fitted with the LL model shown in solid and dashed red lines, respectively.

potential for p – d interactions is adapted from [277]. The correlations are tested on two cluster formation times 20 and 30 fm/c up to which SMASH hadronic cascade is evolved and at which point the coalescence of nucleon pairs is carried out. The p – d and d – d femtoscopy results presented in Figure 5.16 and 5.17 are for cluster formation times 20 fm/c and 30 fm/c, respectively, for hydro and hard EoS SMASH. The results are compared to the preliminary measurements from STAR [262]. Except at 40-60% centrality, where a deviation between the hydro and hard EoS is noticed, the results show excellent agreement with the data for p – d and d – d correlations. A closer look reveals that the hydro predictions are slightly better than the hard EoS selection, especially noticeable for d – d pairs at peripheral collisions. However, no noticeable differences are observed for the two choices of deuteron wave functions.

The source sizes of the p – d and d – d pairs are extracted to gain quantitative insight and compare the formation times. The source sizes are extracted by fitting the LL model to the correlation distributions, assuming a Gaussian emission source. In addition, the LL

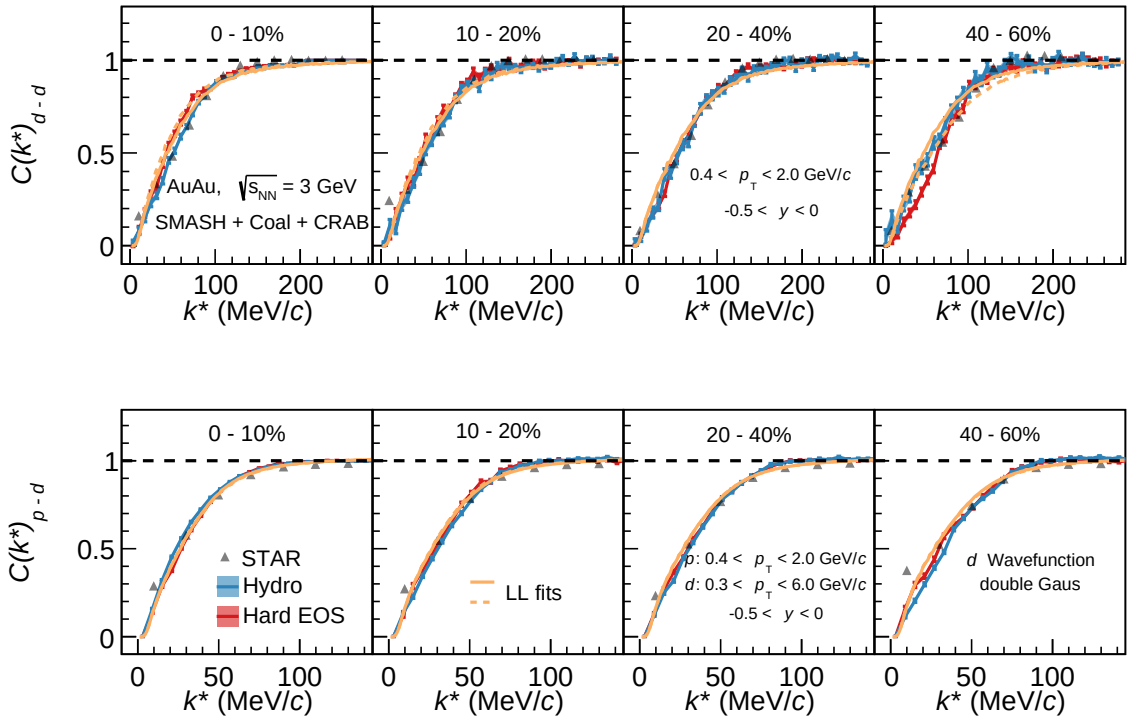

Figure 5.17: Momentum correlation of (Bottom) p – d and (Top) d – d pairs in Au–Au collisions at $\sqrt{s_{NN}}$ = 3 GeV with a double Gaussian function as the deuteron wavefunction in different centralities from SMASH + Coal + CRAB, compared to STAR preliminaries [262]. Predictions are presented for hydro and hard EoS SMASH fitted with the LL model shown in solid and dashed red lines, respectively.

model considers a smoothness approximation, which holds true for heavy-ion collisions. Moreover, to employ LL fits the deuteron is assumed to be a point particle. The fits are performed on the SMASH + Coal + CRAB results, as well as on the STAR preliminary measurements [262]. In Figure 5.18, the fits to the SMASH + Coal + CRAB outputs are reported across different centralities for p – d and d – d correlation functions for hydro and hard EoS configurations. The source sizes reported in Figure 5.18 show a decreasing dependence with centrality for the STAR data. The p – d cluster source sizes are larger, lying between 3 – 3.5 fm, in contrast to 1.8 – 2 fm for the d – d system. The SMASH + Coal + CRAB results for p – d pairs are well reproduced at 20 fm/c for hydro, with a slight underestimation by the hard EoS. At 30 fm/c, the source sizes overestimate the data, showing deviations upto 30%. The results for d – d pairs also predict the decreasing trend of source sizes with centrality, affirmed by the experimental results. Here, the scale of disagreement between the cluster formation times is less compared to the p – d pairs. Hydro SMASH offers the closest description at 30 fm/c. The hard EoS show 10% overestimation for central collisions, with closer description at mid-central to peripheral

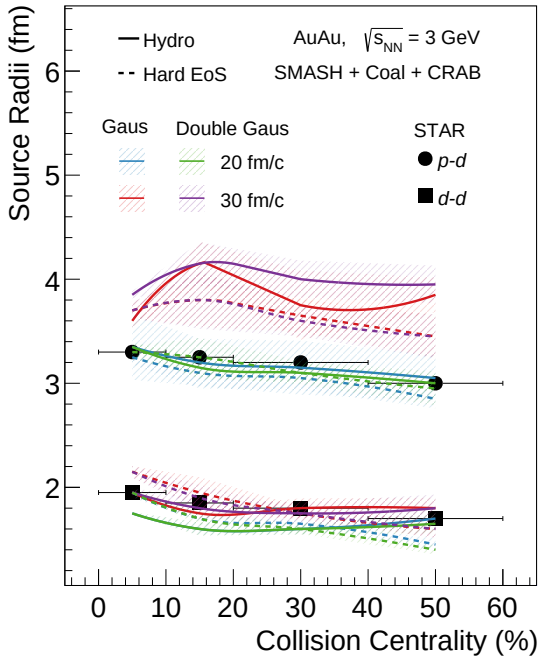

Figure 5.18: Source radius extracted from LL fits to p − d and d − d correlation functions from STAR preliminaries [262], and from two cluster formation times in hydro (solid lines) and hard EoS (dashed lines) SMASH + Coal and two choices of the deuteron wave function.

collisions. At 20 fm/c, the source radii are slightly lower than 30 fm/c, except at 40-60% for hydro. The radii from different wave function treatments, within uncertainties, show negligible deviation.

Even with finely spaced cluster formation times, variation in the p − d and d − d correlations is observed, which gets reflected in the emission source radii. Based on the agreement with the data, a cluster time at 30 fm/c for the deuteron is closer to describing the emission of d − d pairs, whereas a shorter time between 20–30 fm/c is preferred for the proton and deuteron pairs for the p − d cluster. This noteworthy observation indicates the formation time of differently populated baryon clusters formed in these heavy-ion collisions.

5.7.2 Anisotropic flow

Focusing on estimating the azimuthal anisotropies of light nuclei in 10-40% central Au–Au collisions at $\sqrt{s_{\rm NN}}$ = 3 GeV, the directed (v_1) and elliptic flow (v_2) coefficients of deuterons, triton, and helium-3 are calculated and compared with the extensive set of measurements performed by STAR collaboration [278]. Similar to source estimation, the flow coefficients

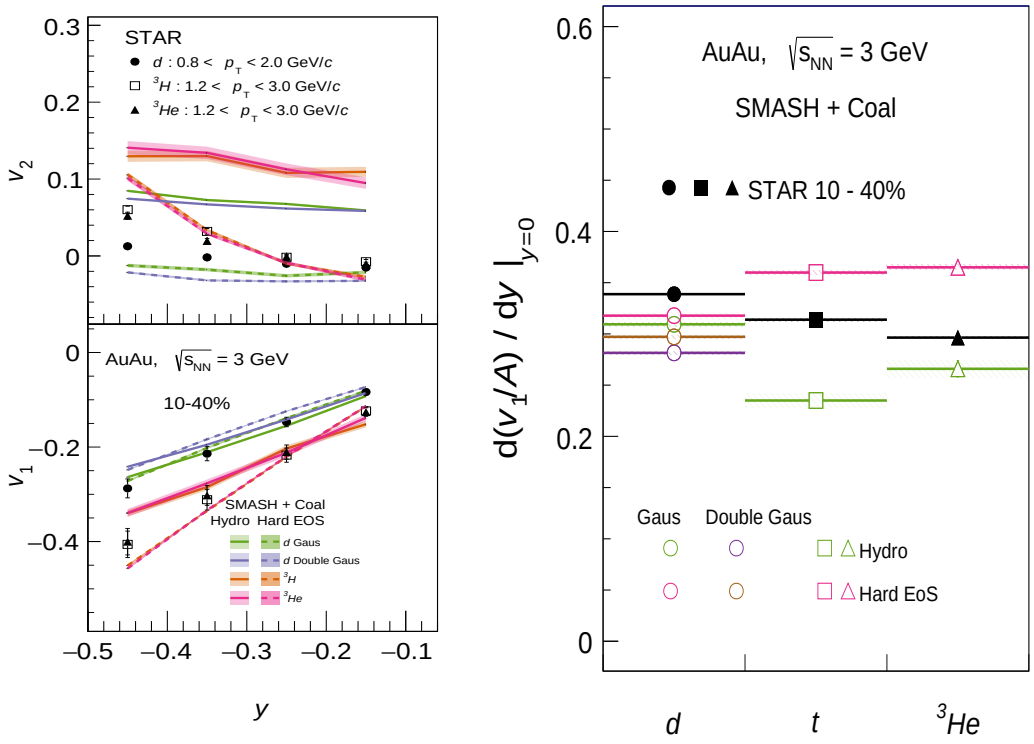

Figure 5.19: (Left) Elliptic flow (v_2) and directed flow (v_1) of deuterons, tritons and helium-3 produced in non-central Au–Au collisions as function of rapidity using SMASH + Coal. (Right) $\mathrm{d}v_1/\mathrm{d}y$ of deuterons, tritons and helium-3 produced in non-central Au–Au collisions using SMASH + Coal. Results are compared to experimental measurements from STAR [278].

are estimated for two variants of SMASH. The last collision time is taken from comparing the correlation functions from the previous subsection. The kinematic selections are kept the same as reported by the STAR measurements. The rapidity dependence of these flow coefficients, especially v_1, can reveal insights into the longitudinal dynamics of the collision. The left panel of Figure 5.19 presents the dependence of v_1 and v_2 of light nuclei as a function of rapidity (y), in specific p_T regions ($0.8 < p_\mathrm{T} < 2.0$ GeV/c for deuteron and $1.2 < p_\mathrm{T} < 3.0$ GeV/c for triton/helium-3). Here, the coefficients of all species show considerable sensitivity to different SMASH modes, in particular, v_2. The hydro SMASH mode overestimates the measured v_2 of all light nuclei species by almost factor 2.

In addition to this and, more importantly, the SMASH + Coal + hydro variant fails to describe the negative values of v_2 (out-of-plane flow) at central rapidity intervals. It is worth noting that the hydro mode appears to reproduce the trend of v_2. On the contrary, SMASH + Coal + hard EoS reproduce the negative values and reasonably describe the

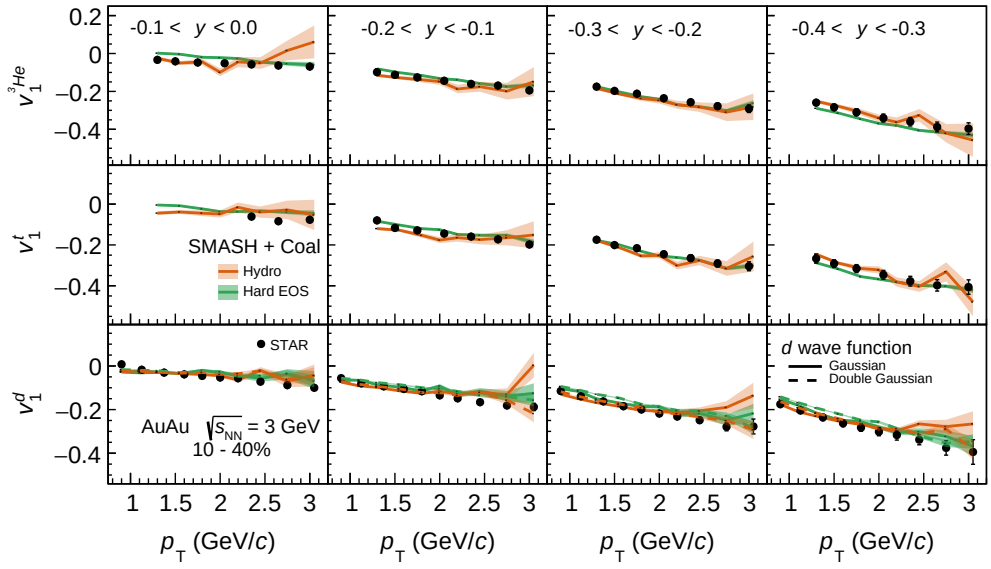

Figure 5.20: Directed flow (v_1) as function of p_T of (Bottom) deuterons, (Middle) tritons and (Top) helium-3 produced in non-central Au–Au collisions using SMASH and their comparison with experimental measurements from STAR [278].

light nuclei v_2 measurement at central rapidity; however, they slightly underestimate forward rapidities. This is possibly due to an effect of spectators or fragments from beam remnants that have an increasing rapidity dependence. An account of mean-field contributions seems to help describe the v_2 at such low beam energy. The deuteron results with the double Gaussian wavefunction treatment show a slight underestimation of the v_2 in both hydro and hard EoS configurations. An account of mean-field contributions from hardening of the EoS seems to explain the 'squeeze-out' and out-of-plane emission of the deuteron, describing light nuclei v_2 at such low beam energy. In retrospect, the v_1 of light nuclei is qualitatively described by both modes of SMASH. Here, the double Gaussian configuration slightly overestimates the data than the single Gaussian treatment. Hard EoS provides a closer description of the rapidity dependence of deuteron v_1, as compared to hydro. This is a consequence of the different phase space treatment in the two modes, leading to an effect from more low momenta deuterons from spectators. This observation is more apparent for triton and helium-3, where the hydro and Hard EoS modes under and overestimate towards increasing rapidity ($-0.4 < y < -0.3$), respectively. However, both hydro mode and hard EoS reproduce the mass ordering in both v_1 and v_2 as observed in experimental measurement.

The slope of directed flow ($\mathrm{d}v_1/\mathrm{d}y$) is an interesting observable for the investigation since it is sensitive to the underlying EoS and one of the candidates to provide insights

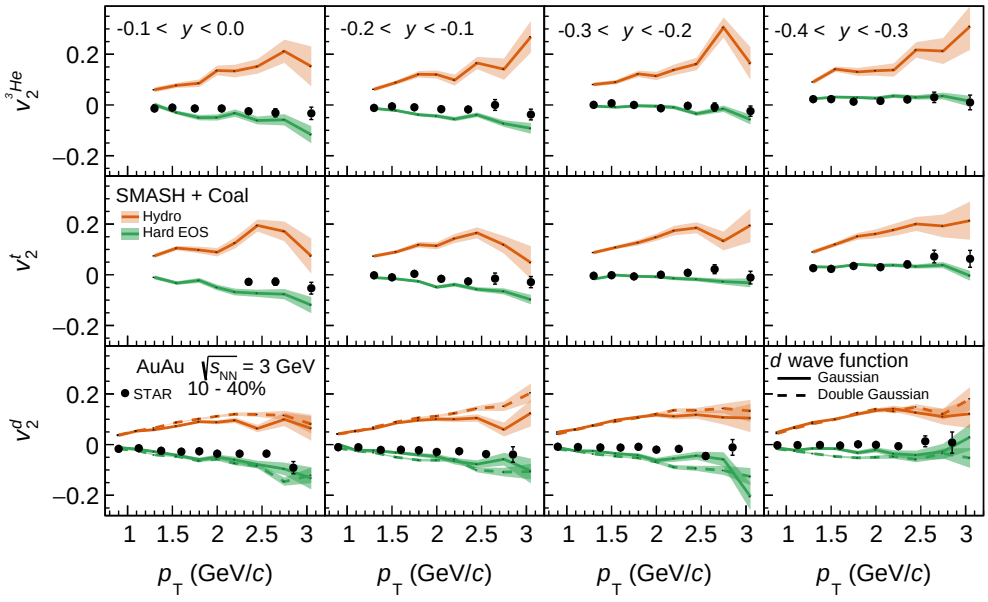

Figure 5.21: Elliptic flow (v_2) as function of p_T of (Bottom) deuterons, (Middle) tritons and (Top) helium-3 produced in non-central Au–Au collisions using SMASH and their comparison with experimental measurements from STAR [278].

about the dynamics of the QCD medium. As mentioned above, both modes of SMASH describe the v_1 slope; however, a quantitative comparison is performed with experimental measurements. On the right panel of Figure 5.19, the dv_1/dy of light nuclei with hydro and hard EoS SMASH are presented and compared with STAR measurements [278]. The slope is estimated by fitting the v_1 within the rapidity window, $-0.5 < y < 0.0$, using a first-order polynomial scaled to the respective mass numbers.The slopes corresponding to the deuterons from single Gaussian Wigner coalescence, and hard EoS configuration are closer to the experimental results, showing about 6% deviation, while the hydro results show a larger deviation ~9%. A systematic decrease in the slope upto 9% is noted for the deuterons with double Gaussian than the single Gaussian coalescence. On the other hand, the slopes for triton and helium deviate on either side of the data, creating a band with hard EoS and hydro with deviation up to ~ 25%.

Moving forward, the transverse momentum dependence of directed flow coefficient (v_1) of d, t(^{3}H), and ^{3}He as a function of p_T in different rapidity intervals is shown in Figure 5.20. SMASH modes, hard EoS, and hydro agree with the measurements across the whole p_T range from 1 to 3 GeV/c and rapidity intervals. The p_T dependence of elliptic flow coefficients (v_2) of light nuclei in different rapidity regions are shown in Figure 5.21. The SMASH modes show deviations similar to the results in Figure 5.19, with a positive v_2 and increasing with p_T for d, t(^{3}H), and ^{3}He with hydro turned on. However, the failure

of hydro in reproducing the sign suggests that SMASH + Coal + hydro at a low center of mass energies may not be enough to describe the "squeeze-out" of colliding matter that eventually leads to a negative flow. The hard EoS reproduces this phenomenon well across p_{T} and rapidity region, asserting the importance of the mean-field approach. Similar calculations of these flow coefficients are carried out using different last collision times to check the robustness of the results, and it is found that they do not change the message of the findings. For the specific case of the deuteron, the two wavefunction treatments do not show any discernible difference in the p_{T} dependent flow coefficient results.

In the literature [266] and [170], it has been argued that at low energies, neither soft nor hard EoS describe the v_1 and v_2 together convincingly. However, unlike hard EoS, soft EoS fails to explain the rapidity and p_{T} dependence of both v_1 and v_2. Since different transport model approaches have various underlying degrees of freedom, different conclusions regarding mean-field interaction strengths can be drawn. It has already been seen that existing FOPI data [269] is nicely explained by soft EoS [273], and approaches with a hard EoS over UrQMD shows agreement with the NA49 and HADES measurements [179, 270, 271].

Chapter 6

Summary

This thesis explores two primary areas of ultra-relativistic hadronic and heavy-ion collisions. The first objective is focused on the measurement of charm production as a function of event activity, by reconstructing D-mesons in pp collisions with ALICE at the LHC. These measurements test pQCD predictions and hadronization mechanisms of heavy quarks (charm and beauty) in pp collisions. The event variables of choice are charged-particle multiplicity and transverse spherocity. The D-meson self normalized yields are calculated with the extracted raw yields in a given interval of event multiplicity or spherocity corrected by the reconstruction efficiencies over the corresponding quantity in the integrated multiplicity or spherocity interval.

The second objective centers on light (anti-)nuclei production in heavy-ion collisions via coalescence, aimed at improving the understanding of low-energy nucleon-nucleon interactions. The coalescence model is based on the ansatz that light nuclei form from closely spaced proton-neutron pairs in phase space. The model successfully predicted deuteron, triton, and helium-3 production and was refined using a Wigner coalescence approach for in-jet deuteron production and to study femtoscopy of light nuclei, emphasizing coalescence as a key production mechanism.

Charm production in pp collisions with ALICE

D-mesons production versus charged-particle multiplicity

The prompt D-meson self-normalized yields in pp collisions at $\sqrt{s}$ = 13 TeV shows a stronger than linear trend as a function of relative charged-particle multiplicity. The trends become steeper with increasing p_{T}. The stronger than linear trend is accredited to the auto-correlation effects between the hard scattering process and the measured charged-particle multiplicity. The results show good agreement with the similar measurement in collisions at $\sqrt{s}$ = 7 TeV, and provide improved precision at high multiplicities. The

D-meson yields are also compared to self-normalized yields of J/ψ mesons and electrons from heavy-flavour hadron decays performed in pp collisions at $\sqrt{s}$ = 13 TeV, in compatible p_{T} intervals and acceptances.

Predictions from EPOS3 with a hydrodynamic evolution show a good agreement with the D-meson measurements, while EPOS3 without a hydrodynamic treatment and 3-Pomeron CGC model underestimates and overestimates the data, respectively. Moreover, an extensive study with PYTHIA8 is performed with Monash and CR beyond leading colour approximation tunes. While no noticeable differences are observed between the tunes, the importance of MPI and CR in event generation is laid out. This claim is supported by the extended study performed with and without MPI or CR. In conclusion, a combination of MPI and CR is essential to reproduce the production of charged-particles in pp collisions.

D-mesons production versus transverse spherocity

The self-normalized yields of prompt D-mesons are computed in three multiplicity intervals, which is fixed during the calculation of transverse spherocity of the event. The transverse spherocity values are converted into quantiles, categorizing the events to jetty and isotropic topologies. The yields in each multiplicity interval as a function of S_{O}-Quantiles suggest a similar trend, with high p_{T} D-mesons dominating in the jetty sector, declining in population with increasing isotropy. On the other hand, the low p_{T} D-mesons are suppressed in jetty events, showing a slow rise with isotropic events. The predictions from PYTHIA8 Monash and CR-BLC tunes show good agreement with the measurements in all p_{T} and multiplicity intervals.

Light nuclei synthesis via coalescence

Light (anti-)nuclei production with AMPT

This study analyzes light nuclei (d, ^{3}H, ^{3}He) production in central Au–Au collisions at $\sqrt{s_{\mathrm{NN}}}$ = 19.6, 39, 200 GeV, and Pb–Pb collisions at $\sqrt{s_{\mathrm{NN}}}$ = 2.76 TeV using a AMPT-driven 'box' coalescence model. The results show that the coalescence model outperforms the kinetic implementation of $\mathrm{d}(\bar{\mathrm{d}})$ production in AMPT and closely matches PHQMD results. The string melting AMPT model under the "Coalescence" mode struggles with $\mathrm{p}(\bar{\mathrm{p}})$ p_{T} spectra at $\sqrt{s_{\mathrm{NN}}}$ = 19.6, 39 GeV but performs well at $\sqrt{s_{\mathrm{NN}}}$ = 200 GeV and 2.76 TeV. For $\mathrm{p}(\bar{\mathrm{p}})$ yields, the "Transport" mode shows better agreement across all energies. "Coalescence" mode describes the yields of d, ^{3}H, ^{3}He well at $\sqrt{s_{\mathrm{NN}}}$ = 200 GeV and 2.76 TeV, with deviations at lower energies, while the "Transport" mode overestimates $\mathrm{d}(\bar{\mathrm{d}})$ yields across all energies.

The "Coalescence" results match experimentally measured $\mathrm{d}(\bar{\mathrm{d}})/\mathrm{p}(\bar{\mathrm{p}})$, $\bar{\mathrm{d}}/\bar{\mathrm{d}}$ ratios at $\sqrt{s_{\mathrm{NN}}}$ =

200 GeV and 2.76 TeV and ^{3}H(^{3}He)/d ratios across all energies. The "Transport" model overestimates $\mathrm{d}(\bar{\mathrm{d}})/\mathrm{p}(\bar{\mathrm{p}})$ and $\bar{\mathrm{d}}/\bar{\mathrm{d}}$ ratios for Au–Au and underestimates them for Pb–Pb collisions. The coalescence parameters B_2 and B_3 are well-described by "Coalescence" mode, especially for deuterons at RHIC and LHC energies. The model matches B_3 for ^{3}H at $\sqrt{s_{\mathrm{NN}}}$ = 2.76 TeV but struggles with ^{3}He at $\sqrt{s_{\mathrm{NN}}}$ = 200 GeV. At fixed p_{T}, the anti-deuteron B_2 at $\sqrt{s_{\mathrm{NN}}}$ = 19.6 and 39 GeV is overestimated by both "Coalescence" and "Transport" mode, but fits well for "Coalescence" at $\sqrt{s_{\mathrm{NN}}}$ = 200 GeV. B_3 values for ^{3}H and ^{3}He are well reproduced at $\sqrt{s_{\mathrm{NN}}}$ = 200 GeV and 2.76 TeV.

Enhancement of deuteron coalescence probability in jets

This study examines the production mechanism of (anti-)deuteron in pp collisions at midrapidity using an advanced coalescence model. This model is based on the Wigner probability density of a deuteron wave function and incorporates the emission source size in pp collisions. Based on femtoscopic measurements from ALICE, the relative distances between nucleons as a function of transverse mass are used as spatial inputs. The model also considers resonance decays and their contributions to nucleon production, using a modified Gaussian to account for mixed decay topologies. The resonance-source model is integrated into the PYTHIA8 event generator.

The deuteron wavefunction is approximated to a Gaussian distribution. In addition, a double Gaussian form is utilized, parameterized to the Hulthén wavefunction. The single Gaussian underestimates the experimental measurements of deuteron yields, while the double Gaussian provides a precise estimation. An event-shape differential study using transverse spherocity is investigated on deuteron production in "jetty" and "isotropic" spherocity classes at high multiplicities. (Anti-)Deuterons in "jetty" topologies show a comparable B_2 with the UE deuterons, stating that soft processes dominate in deuteron production. Subtracting UE contributions from "jetty" events highlights the enhancement of B_2, suggesting favorable coalescence conditions in-jets.

Probing light nuclei formation with femtoscopy and anisotropic flow

This study investigates the momentum correlation function of nucleons and light nuclei to understand their production times and sensitivity to initial anisotropy in heavy-ion collisions. The SMASH transport model generates the nucleon phase space in Au–Au collisions at $\sqrt{s_{\mathrm{NN}}}$ = 3 GeV, from which light nuclei states are produced through a coalescence afterburner. SMASH operates in hybrid and mean-field configurations.

Protons and deuterons from coalescence are fed into the CRAB afterburner to generate p–d and d–d momentum correlations. These correlations obtained for different collision centralities and compared to STAR preliminary measurements. The LL model, assuming

a Gaussian emission source is fitted to the correlation functions to estimate the emission source size of these states. The emission source radius of p–d and d–d states decreases from central to peripheral collisions, showing excellent agreement with experimental data and highlighting the importance of coalescence in light nuclei formation. A difference of 10 fm/c in cluster formation times is observed between p–d and d–d clusters, indicating sensitivity to formation times during medium evolution. The findings do not changes between the treatment of the deuteron wavefunction.

The directed and elliptic flow coefficients of d, ^{3}H, ^{3}He from coalescence are analyzed for mid-central Au–Au collisions at $\sqrt{s_{\rm NN}}$ = 3 GeV. A mean-field potential approach is compared to a hybrid approach in low-energy Au–Au collisions. Both approaches show no noticeable differences for the directed flow of light nuclei but differ significantly for v_2 and do not depend on cluster formation times. The mean-field treatment with a hard EoS parameterization precisely describes the data, whereas SMASH with a soft EoS fails to describe the rapidity and $p_{\rm T}$ dependence of elliptic flow coefficients.

Future prospects

A wealth of new measurements in heavy-flavour production await with the new high luminosity data being collected by ALICE during the Run-3. With the upgraded ITS3 and TPC, ALICE aims for a significant rate capability, leading to high signal significance. Moreover with Machine Learning techniques in the heavy-flavour reconstruction will allow for a highly efficient signal reconstruction. This will allow for measurements that could disentangle the effects between charm and beauty. Besides performance the newly collected data will provide more precise differential measurements, giving a clearer picture of heavy-quark hadronization mechanisms. With the possible formation of QGP droplets in small systems, more insight into heavy-quark participation in collectivity could be obtained. These measurements are expected in the immediate future at the LHC.

The study with coalescence effectively draws out the conclusion of it being a viable mechanism of light nuclei production in collision experiments. This approach can be extended to the production of hyper-nuclei and exotic states that lack in precise experimental measurements. Further research using state-of-the-art wavefunctions and precise femtoscopy studies will deepen understanding of light nuclei production and dynamics via coalescence as a whole. Measurements of their production in beam energy scans can shed light on the energy dependence and formation times of different nucleon or nuclei emission sources. New measurements in light and hypernuclei species is forseen with dedicated future heavy-ion experiments at Compressed Baryonic Matter (CBM), FAIR and Multi-Purpose Detector (MPD), NICA. Validating these new results in different regimes of the QCD phase diagram will provide more insight into nucleon-nucleon interactions and the formation mechanisms of different nuclei clusters.

Bibliography

[1] Quantum Diaries, https://www.quantumdiaries.org/2014/03/14/the-standard-model-a-beautiful-but-flawed-theory/.

[2] Steven Weinberg. A Model of Leptons. *Phys. Rev. Lett.*, 19:1264–1266, 1967. doi: 10.1103/PhysRevLett.19.1264.

[3] S. L. Glashow. Partial Symmetries of Weak Interactions. *Nucl. Phys.*, 22:579–588, 1961. doi: 10.1016/0029-5582(61)90469-2.

[4] Abdus Salam. Weak and Electromagnetic Interactions. *Conf. Proc. C*, 680519: 367–377, 1968. doi: 10.1142/9789812795915_0034.

[5] Jeffrey Goldstone, Abdus Salam, and Steven Weinberg. Broken Symmetries. *Phys. Rev.*, 127:965–970, 1962. doi: 10.1103/PhysRev.127.965.

[6] F. Englert and R. Brout. Broken Symmetry and the Mass of Gauge Vector Mesons. *Phys. Rev. Lett.*, 13:321–323, 1964. doi: 10.1103/PhysRevLett.13.321.

[7] Sidney R. Coleman and Erick J. Weinberg. Radiative Corrections as the Origin of Spontaneous Symmetry Breaking. *Phys. Rev. D*, 7:1888–1910, 1973. doi: 10.1103/PhysRevD.7.1888.

[8] Peter W. Higgs. Broken symmetries, massless particles and gauge fields. *Phys. Lett.*, 12:132–133, 1964. doi: 10.1016/0031-9163(64)91136-9.

[9] Peter W. Higgs. Broken Symmetries and the Masses of Gauge Bosons. *Phys. Rev. Lett.*, 13:508–509, 1964. doi: 10.1103/PhysRevLett.13.508.

[10] G. Arnison et al. Experimental Observation of Lepton Pairs of Invariant Mass Around 95-GeV/c**2 at the CERN SPS Collider. *Phys. Lett. B*, 126:398–410, 1983. doi: 10.1016/0370-2693(83)90188-0.

[11] G. Arnison et al. Experimental Observation of Isolated Large Transverse Energy Electrons with Associated Missing Energy at $\sqrt{s}$ = 540 GeV. *Phys. Lett. B*, 122: 103–116, 1983. doi: 10.1016/0370-2693(83)91177-2.

[12] Frank Wilczek. Quantum Chromodynamics (QCD): The Modern Theory of the Strong Interaction. *Ann. Rev. Nucl. Part. Sci.*, 32:177–209, 1982. doi: 10.1146/annurev.ns.32.120182.001141.

[13] H. David Politzer. Reliable Perturbative Results for Strong Interactions? *Phys. Rev. Lett.*, 30:1346–1349, 1973. doi: 10.1103/PhysRevLett.30.1346.

[14] Georges Aad et al. Observation of a new particle in the search for the Standard Model Higgs boson with the ATLAS detector at the LHC. *Phys. Lett. B*, 716:1–29, 2012. doi: 10.1016/j.physletb.2012.08.020.

[15] Y. Ashie et al. Evidence for an oscillatory signature in atmospheric neutrino oscillation. *Phys. Rev. Lett.*, 93:101801, 2004. doi: 10.1103/PhysRevLett.93.101801.

[16] A. D. Sakharov. Violation of CP Invariance, C asymmetry, and baryon asymmetry of the universe. *Pisma Zh. Eksp. Teor. Fiz.*, 5:32–35, 1967. doi: 10.1070/PU1991v034n05ABEH002497.

[17] Gianfranco Bertone, Dan Hooper, and Joseph Silk. Particle dark matter: Evidence, candidates and constraints. *Phys. Rept.*, 405:279–390, 2005. doi: 10.1016/j.physrep.2004.08.031.

[18] Lisa Randall and Raman Sundrum. A Large mass hierarchy from a small extra dimension. *Phys. Rev. Lett.*, 83:3370–3373, 1999. doi: 10.1103/PhysRevLett.83.3370.

[19] Juan Martin Maldacena. The Large N limit of superconformal field theories and supergravity. *Adv. Theor. Math. Phys.*, 2:231–252, 1998. doi: 10.4310/ATMP.1998.v2.n2.a1.

[20] Particle Data Group. Review of Particle Physics. *Progress of Theoretical and Experimental Physics*, 2022(8):083C01, 08 2022. ISSN 2050-3911. doi: 10.1093/ptep/ptac097. URL https://doi.org/10.1093/ptep/ptac097.

[21] David J. Gross and Frank Wilczek. Ultraviolet Behavior of Nonabelian Gauge Theories. *Phys. Rev. Lett.*, 30:1343–1346, 1973. doi: 10.1103/PhysRevLett.30.1343.

[22] F. Halzen and Alan D. Martin. *QUARKS AND LEPTONS: AN INTRODUCTORY COURSE IN MODERN PARTICLE PHYSICS*. 1984. ISBN 978-0-471-88741-6.

[23] Yuri V. Kovchegov and Eugene Levin. *Quantum Chromodynamics at High Energy*, volume 33. Oxford University Press, 2013. ISBN 978-1-009-29144-6, 978-1-009-29141-5, 978-1-009-29142-2, 978-0-521-11257-4, 978-1-139-55768-9. doi: 10.1017/9781009291446.

[24] Murray Gell-Mann. A Schematic Model of Baryons and Mesons. *Phys. Lett.*, 8: 214–215, 1964. doi: 10.1016/S0031-9163(64)92001-3.

[25] Guido Altarelli and G. Parisi. Asymptotic Freedom in Parton Language. *Nucl. Phys. B*, 126:298–318, 1977. doi: 10.1016/0550-3213(77)90384-4.

[26] D. J. Gross and Frank Wilczek. Asymptotically Free Gauge Theories - I. *Phys. Rev. D*, 8:3633–3652, 1973. doi: 10.1103/PhysRevD.8.3633.

[27] H. David Politzer. Asymptotic Freedom: An Approach to Strong Interactions. *Phys. Rept.*, 14:129–180, 1974. doi: 10.1016/0370-1573(74)90014-3.

[28] Kenneth G. Wilson. Confinement of Quarks. *Phys. Rev. D*, 10:2445–2459, 1974. doi: 10.1103/PhysRevD.10.2445.

[29] Roderick V. Reid, Jr. Local phenomenological nucleon-nucleon potentials. *Annals Phys.*, 50:411–448, 1968. doi: 10.1016/0003-4916(68)90126-7.

[30] A. Bazavov et al. The chiral and deconfinement aspects of the QCD transition. *Phys. Rev. D*, 85:054503, 2012. doi: 10.1103/PhysRevD.85.054503.

[31] Gines Martinez. Advances in Quark Gluon Plasma. 4 2013.

[32] Kenji Fukushima and Tetsuo Hatsuda. The phase diagram of dense QCD. *Rept. Prog. Phys.*, 74:014001, 2011. doi: 10.1088/0034-4885/74/1/014001.

[33] T. Hatsuda and T. Kunihiro. Critical Phenomena Associated with Chiral Symmetry Breaking and Restoration in QCD. *Prog. Theor. Phys.*, 74:765, 1985. doi: 10.1143/PTP.74.765.

[34] Misha A. Stephanov, K. Rajagopal, and Edward V. Shuryak. Event-by-event fluctuations in heavy ion collisions and the QCD critical point. *Phys. Rev. D*, 60:114028, 1999. doi: 10.1103/PhysRevD.60.114028.

[35] Mark G. Alford, Andreas Schmitt, Krishna Rajagopal, and Thomas Schäfer. Color superconductivity in dense quark matter. *Rev. Mod. Phys.*, 80:1455–1515, 2008. doi: 10.1103/RevModPhys.80.1455.

[36] Edward V. Shuryak. Quantum Chromodynamics and the Theory of Superdense Matter. *Phys. Rept.*, 61:71–158, 1980. doi: 10.1016/0370-1573(80)90105-2.

[37] K. Yagi, T. Hatsuda, and Y. Miake. *Quark-gluon plasma: From big bang to little bang*, volume 23. 2005.

[38] C. Y. Wong. *Introduction to high-energy heavy ion collisions*. 1995. ISBN 978-981-02-0263-7.

[39] J. D. Bjorken. Highly Relativistic Nucleus-Nucleus Collisions: The Central Rapidity Region. *Phys. Rev. D*, 27:140–151, 1983. doi: 10.1103/PhysRevD.27.140.

[40] Wit Busza, Krishna Rajagopal, and Wilke van der Schee. Heavy Ion Collisions: The Big Picture, and the Big Questions. *Ann. Rev. Nucl. Part. Sci.*, 68:339–376, 2018. doi: 10.1146/annurev-nucl-101917-020852.

[41] J. Barrette et al. Observation of anisotropic event shapes and transverse flow in Au + Au collisions at AGS energy. *Phys. Rev. Lett.*, 73:2532–2535, 1994. doi: 10.1103/PhysRevLett.73.2532.

[42] M. C. Abreu et al. Evidence for deconfinement of quarks and gluons from the J / psi suppression pattern measured in Pb + Pb collisions at the CERN SPS. *Phys. Lett. B*, 477:28–36, 2000. doi: 10.1016/S0370-2693(00)00237-9.

[43] John Adams et al. Experimental and theoretical challenges in the search for the quark gluon plasma: The STAR Collaboration's critical assessment of the evidence from RHIC collisions. *Nucl. Phys. A*, 757:102–183, 2005. doi: 10.1016/j.nuclphysa.2005.03.085.

[44] K. Aamodt et al. The ALICE experiment at the CERN LHC. *JINST*, 3:S08002, 2008. doi: 10.1088/1748-0221/3/08/S08002.

[45] Jaroslav Adam et al. Enhanced production of multi-strange hadrons in high-multiplicity proton-proton collisions. *Nature Phys.*, 13:535–539, 2017. doi: 10.1038/nphys4111.

[46] Vardan Khachatryan et al. Evidence for collectivity in pp collisions at the LHC. *Phys. Lett. B*, 765:193–220, 2017. doi: 10.1016/j.physletb.2016.12.009.

[47] Jaroslav Adam et al. Centrality Dependence of the Charged-Particle Multiplicity Density at Midrapidity in Pb-Pb Collisions at $\sqrt{s_{\mathrm{NN}}}$ = 5.02 TeV. *Phys. Rev. Lett.*, 116(22):222302, 2016. doi: 10.1103/PhysRevLett.116.222302.

[48] Johann Rafelski and Berndt Muller. Strangeness Production in the Quark - Gluon Plasma. *Phys. Rev. Lett.*, 48:1066, 1982. doi: 10.1103/PhysRevLett.48.1066. [Erratum: Phys.Rev.Lett. 56, 2334 (1986)].

[49] G. Agakishiev et al. Strangeness Enhancement in Cu+Cu and Au+Au Collisions at $\sqrt{s_{NN}}$ = 200 GeV. *Phys. Rev. Lett.*, 108:072301, 2012. doi: 10.1103/PhysRevLett.108.072301.

[50] E. Andersen et al. Strangeness enhancement at mid-rapidity in Pb Pb collisions at 158-A-GeV/c. *Phys. Lett. B*, 449:401–406, 1999. doi: 10.1016/S0370-2693(99)00140-9.

[51] Betty Bezverkhny Abelev et al. Multi-strange baryon production at mid-rapidity in Pb-Pb collisions at $\sqrt{s_{NN}}$ = 2.76 TeV. *Phys. Lett. B*, 728:216–227, 2014. doi: 10.1016/j.physletb.2014.05.052. [Erratum: Phys.Lett.B 734, 409–410 (2014)].

[52] S. Acharya et al. Transverse momentum spectra and nuclear modification factors of charged particles in pp, p-Pb and Pb-Pb collisions at the LHC. *JHEP*, 11:013, 2018. doi: 10.1007/JHEP11(2018)013.

[53] Vardan Khachatryan et al. Charged-particle nuclear modification factors in PbPb and pPb collisions at $\sqrt{s_{\mathrm{N\,N}}}$ = 5.02 TeV. *JHEP*, 04:039, 2017. doi: 10.1007/JHEP04(2017)039.

[54] Vardan Khachatryan et al. Nuclear Effects on the Transverse Momentum Spectra of Charged Particles in pPb Collisions at $\sqrt{s_{\mathrm{NN}}}$ = 5.02 TeV. *Eur. Phys. J. C*, 75(5): 237, 2015. doi: 10.1140/epjc/s10052-015-3435-4.

[55] Jaroslav Adam et al. Measurement of jet suppression in central Pb-Pb collisions at $\sqrt{s_{\mathrm{NN}}}$ = 2.76 TeV. *Phys. Lett. B*, 746:1–14, 2015. doi: 10.1016/j.physletb.2015.04.039.

[56] Georges Aad et al. Measurements of the Nuclear Modification Factor for Jets in Pb+Pb Collisions at $\sqrt{s_{\mathrm{NN}}}$ = 2.76 TeV with the ATLAS Detector. *Phys. Rev. Lett.*, 114(7):072302, 2015. doi: 10.1103/PhysRevLett.114.072302.

[57] Vardan Khachatryan et al. Measurement of inclusive jet cross sections in pp and PbPb collisions at $\sqrt{s_{NN}}$ = 2.76 TeV. *Phys. Rev. C*, 96(1):015202, 2017. doi: 10.1103/PhysRevC.96.015202.

[58] R. J. Glauber. Lectures on Theoretical Physics,. *Interscience*, 1:315, 1959.

[59] Michael L. Miller, Klaus Reygers, Stephen J. Sanders, and Peter Steinberg. Glauber modeling in high energy nuclear collisions. *Ann. Rev. Nucl. Part. Sci.*, 57:205–243, 2007. doi: 10.1146/annurev.nucl.57.090506.123020.

[60] Albert M Sirunyan et al. Measurement of nuclear modification factors of Υ(1S), Υ(2S), and Υ(3S) mesons in PbPb collisions at $\sqrt{s_{\mathrm{NN}}}$ = 5.02 TeV. *Phys. Lett. B*, 790:270–293, 2019. doi: 10.1016/j.physletb.2019.01.006.

[61] Jaroslav Adam et al. Differential studies of inclusive J/ψ and ψ(2S) production at forward rapidity in Pb-Pb collisions at $\sqrt{s_{\mathrm{NN}}}$ = 2.76 TeV. *JHEP*, 05:179, 2016. doi: 10.1007/JHEP05(2016)179.

[62] A. Adare et al. J/ψ suppression at forward rapidity in Au+Au collisions at $\sqrt{s_{NN}}$ = 200 GeV. *Phys. Rev. C*, 84:054912, 2011. doi: 10.1103/PhysRevC.84.054912.

[63] T. Matsui and H. Satz. J/ψ Suppression by Quark-Gluon Plasma Formation. *Phys. Lett. B*, 178:416–422, 1986. doi: 10.1016/0370-2693(86)91404-8.

[64] M. C. Abreu et al. Results from the NA50 experiment on J / psi suppression in Pb Pb collisions at the CERN SPS. *Nucl. Phys. B Proc. Suppl.*, 92:43–54, 2001. doi: 10.1016/S0920-5632(00)01018-5.

[65] S. S. Adler et al. J / psi production in Au Au collisions at s(NN)**(1/2) = 200-GeV at the Relativistic Heavy Ion Collider. *Phys. Rev. C*, 69:014901, 2004. doi: 10.1103/PhysRevC.69.014901.

[66] P. Braun-Munzinger and J. Stachel. (Non)thermal aspects of charmonium production and a new look at J / psi suppression. *Phys. Lett. B*, 490:196–202, 2000. doi: 10.1016/S0370-2693(00)00991-6.

[67] Robert L. Thews, Martin Schroedter, and Johann Rafelski. Enhanced J/ψ production in deconfined quark matter. *Phys. Rev. C*, 63:054905, 2001. doi: 10.1103/PhysRevC.63.054905.

[68] Xiaojian Du and Ralf Rapp. Sequential Regeneration of Charmonia in Heavy-Ion Collisions. *Nucl. Phys. A*, 943:147–158, 2015. doi: 10.1016/j.nuclphysa.2015.09.006.

[69] S. Acharya et al. Anisotropic flow of identified particles in Pb-Pb collisions at $\sqrt{s}_{\mathrm{NN}}$ = 5.02 TeV. *JHEP*, 09:006, 2018. doi: 10.1007/JHEP09(2018)006.

[70] S. Voloshin and Y. Zhang. Flow study in relativistic nuclear collisions by Fourier expansion of Azimuthal particle distributions. *Z. Phys. C*, 70:665–672, 1996. doi: 10.1007/s002880050141.

[71] John C. Collins, Davison E. Soper, and George F. Sterman. Factorization of Hard Processes in QCD. *Adv. Ser. Direct. High Energy Phys.*, 5:1–91, 1989. doi: 10.1142/9789814503266_0001.

[72] J. Pumplin, D. R. Stump, J. Huston, H. L. Lai, Pavel M. Nadolsky, and W. K. Tung. New generation of parton distributions with uncertainties from global QCD analysis. *JHEP*, 07:012, 2002. doi: 10.1088/1126-6708/2002/07/012.

[73] Sayipjamal Dulat, Tie-Jiun Hou, Jun Gao, Marco Guzzi, Joey Huston, Pavel Nadolsky, Jon Pumplin, Carl Schmidt, Daniel Stump, and C. P. Yuan. New parton distribution functions from a global analysis of quantum chromodynamics. *Phys. Rev. D*, 93(3):033006, 2016. doi: 10.1103/PhysRevD.93.033006.

[74] V. G. Kartvelishvili, A. K. Likhoded, and V. A. Petrov. On the Fragmentation Functions of Heavy Quarks Into Hadrons. *Phys. Lett. B*, 78:615–617, 1978. doi: 10.1016/0370-2693(78)90653-6.

[75] Richard D. Ball et al. Parton distributions from high-precision collider data. *Eur. Phys. J. C*, 77(10):663, 2017. doi: 10.1140/epjc/s10052-017-5199-5.

[76] Matteo Cacciari, Paolo Nason, and Carlo Oleari. A Study of heavy flavored meson fragmentation functions in e+ e- annihilation. *JHEP*, 04:006, 2006. doi: 10.1088/1126-6708/2006/04/006.

[77] Matteo Cacciari, Mario Greco, and Paolo Nason. The p_T spectrum in heavy-flavour hadroproduction. *JHEP*, 05:007, 1998. doi: 10.1088/1126-6708/1998/05/007.

[78] Matteo Cacciari, Stefano Frixione, Nicolas Houdeau, Michelangelo L. Mangano, Paolo Nason, and Giovanni Ridolfi. Theoretical predictions for charm and bottom production at the LHC. *JHEP*, 10:137, 2012. doi: 10.1007/JHEP10(2012)137.

[79] M. Benzke, M. V. Garzelli, B. Kniehl, G. Kramer, S. Moch, and G. Sigl. Prompt neutrinos from atmospheric charm in the general-mass variable-flavor-number scheme. *JHEP*, 12:021, 2017. doi: 10.1007/JHEP12(2017)021.

[80] G. Kramer and H. Spiesberger. Study of heavy meson production in p–Pb collisions at $\sqrt{S}$= 5.02 TeV in the general-mass variable-flavour-number scheme. *Nucl. Phys. B*, 925:415–430, 2017. doi: 10.1016/j.nuclphysb.2017.10.016.

[81] Stefano Catani, Simone Devoto, Massimiliano Grazzini, Stefan Kallweit, and Javier Mazzitelli. Bottom-quark production at hadron colliders: fully differential predictions in NNLO QCD. *JHEP*, 03:029, 2021. doi: 10.1007/JHEP03(2021)029.

[82] Shreyasi Acharya et al. Measurement of D^0 , D^+ , D^{*+} and D_s^+ production in pp collisions at $\sqrt{s}$ = 5.02 TeV with ALICE. *Eur. Phys. J. C*, 79(5):388, 2019. doi: 10.1140/epjc/s10052-019-6873-6.

[83] Shreyasi Acharya et al. Λ_c^+ production in pp and in p-Pb collisions at $\sqrt{s_{NN}}$=5.02 TeV. *Phys. Rev. C*, 104(5):054905, 2021. doi: 10.1103/PhysRevC.104.054905.

[84] G. Alexander et al. A Study of charm hadron production in Z0 —> c anti-c and Z0 —> b anti-b decays at LEP. *Z. Phys. C*, 72:1–16, 1996. doi: 10.1007/s002880050218.

[85] M. Niiyama et al. Production cross sections of hyperons and charmed baryons from e^+e^- annihilation near $\sqrt{s}$ = 10.52~GeV. *Phys. Rev. D*, 97(7):072005, 2018. doi: 10.1103/PhysRevD.97.072005.

[86] Stefano Frixione, Paolo Nason, and Giovanni Ridolfi. A Positive-weight next-to-leading-order Monte Carlo for heavy flavour hadroproduction. *JHEP*, 09:126, 2007. doi: 10.1088/1126-6708/2007/09/126.

[87] Torbjorn Sjostrand, Stephen Mrenna, and Peter Z. Skands. PYTHIA 6.4 Physics and Manual. *JHEP*, 05:026, 2006. doi: 10.1088/1126-6708/2006/05/026.

[88] Peter Skands, Stefano Carrazza, and Juan Rojo. Tuning PYTHIA 8.1: the Monash 2013 Tune. *Eur. Phys. J. C*, 74(8):3024, 2014. doi: 10.1140/epjc/s10052-014-3024-y.

[89] Johannes Bellm et al. Herwig 7.0/Herwig++ 3.0 release note. *Eur. Phys. J. C*, 76 (4):196, 2016. doi: 10.1140/epjc/s10052-016-4018-8.

[90] E. G. Kessler, Jr. The Deuteron Binding Energy and the Neutron Mass. *Phys. Lett. A*, 255:221, 1999. doi: 10.1016/S0375-9601(99)00078-X.

[91] C. Van Der Leun and C. Alderliesten. The deuteron binding energy. *Nucl. Phys. A*, 380:261–269, 1982. doi: 10.1016/0375-9474(82)90105-1.

[92] C. Drischler, J. W. Holt, and C. Wellenhofer. Chiral Effective Field Theory and the High-Density Nuclear Equation of State. *Ann. Rev. Nucl. Part. Sci.*, 71:403–432, 2021. doi: 10.1146/annurev-nucl-102419-041903.

[93] A. Akmal, V. R. Pandharipande, and D. G. Ravenhall. The Equation of state of nucleon matter and neutron star structure. *Phys. Rev. C*, 58:1804–1828, 1998. doi: 10.1103/PhysRevC.58.1804.

[94] J. M. Lattimer. Neutron Stars and the Nuclear Matter Equation of State. *Ann. Rev. Nucl. Part. Sci.*, 71:433–464, 2021. doi: 10.1146/annurev-nucl-102419-124827.

[95] Shreyasi Acharya et al. Production of ^{4}He and $^4\overline{\mathrm{He}}$ in Pb-Pb collisions at $\sqrt{s_{\mathrm{NN}}}$ = 2.76 TeV at the LHC. *Nucl. Phys. A*, 971:1–20, 2018. doi: 10.1016/j.nuclphysa.2017.12.004.

[96] Volodymyr Vovchenko and Horst Stoecker. Thermal-FIST: A package for heavy-ion collisions and hadronic equation of state. *Comput. Phys. Commun.*, 244:295–310, 2019. doi: 10.1016/j.cpc.2019.06.024.

[97] A. Andronic, P. Braun-Munzinger, and J. Stachel. Hadron production in central nucleus-nucleus collisions at chemical freeze-out. *Nucl. Phys. A*, 772:167–199, 2006. doi: 10.1016/j.nuclphysa.2006.03.012.

[98] Michele Floris. Hadron yields and the phase diagram of strongly interacting matter. *Nucl. Phys. A*, 931:103–112, 2014. doi: 10.1016/j.nuclphysa.2014.09.002.

[99] A. Andronic, P. Braun-Munzinger, J. Stachel, and H. Stocker. Production of light nuclei, hypernuclei and their antiparticles in relativistic nuclear collisions. *Phys. Lett. B*, 697:203–207, 2011. doi: 10.1016/j.physletb.2011.01.053.

[100] A. Andronic, F. Beutler, P. Braun-Munzinger, K. Redlich, and J. Stachel. Thermal description of hadron production in e+e- collisions revisited. *Phys. Lett. B*, 675: 312–318, 2009. doi: 10.1016/j.physletb.2009.04.024.

[101] J. Cleymans, K. Redlich, and E. Suhonen. Canonical description of strangeness conservation and particle production. *Z. Phys. C*, 51:137–141, 1991. doi: 10.1007/BF01579571.

[102] Shreyasi Acharya et al. Multiplicity dependence of (anti-)deuteron production in pp collisions at $\sqrt{s}$ = 7 TeV. *Phys. Lett. B*, 794:50–63, 2019. doi: 10.1016/j.physletb.2019.05.028.

[103] Shreyasi Acharya et al. Production of light (anti)nuclei in pp collisions at $\sqrt{s}$ = 13 TeV. *JHEP*, 01:106, 2022. doi: 10.1007/JHEP01(2022)106.

[104] H. Sato and K. Yazaki. On the coalescence model for high-energy nuclear reactions. *Phys. Lett. B*, 98:153–157, 1981. doi: 10.1016/0370-2693(81)90976-X.

[105] Joseph I. Kapusta. Mechanisms for deuteron production in relativistic nuclear collisions. *Phys. Rev. C*, 21:1301–1310, 1980. doi: 10.1103/PhysRevC.21.1301.

[106] N. Shah, Y. G. Ma, J. H. Chen, and S. Zhang. Production of multistrange hadrons, light nuclei and hypertriton in central Au+Au collisions at $\sqrt{s_{NN}}$ = 11.5 and 200 GeV. *Phys. Lett. B*, 754:6–10, 2016. doi: 10.1016/j.physletb.2016.01.005.

[107] Paula Hillmann, Katharina Käfer, Jan Steinheimer, Volodymyr Vovchenko, and Marcus Bleicher. Coalescence, the thermal model and multi-fragmentation: the energy and volume dependence of light nuclei production in heavy ion collisions. *J. Phys. G*, 49(5):055107, 2022. doi: 10.1088/1361-6471/ac5dfc.

[108] Yoshini Bailung, Neha Shah, and Ankhi Roy. Exploring light nuclei production at RHIC and LHC energies with A Multi-Phase Transport model and a coalescence afterburner. *Nucl. Phys. A*, 1037:122701, 2023. doi: 10.1016/j.nuclphysa.2023.122701.

[109] M. Kachelrieß, S. Ostapchenko, and J. Tjemsland. Alternative coalescence model for deuteron, tritium, helium-3 and their antinuclei. *Eur. Phys. J. A*, 56(1):4, 2020. doi: 10.1140/epja/s10050-019-00007-9.

[110] Maximilian Mahlein, Luca Barioglio, Francesca Bellini, Laura Fabbietti, Chiara Pinto, Bhawani Singh, and Sushanta Tripathy. A realistic coalescence model for deuteron production. *Eur. Phys. J. C*, 83(9):804, 2023. doi: 10.1140/epjc/s10052-023-11972-3.

[111] Yoshini Bailung, Neha Shah, and Ankhi Roy. Searching for enhancement in coalescence of in-jet (anti-)deuterons in proton-proton collisions. *Phys. Rev. C*, 109 (4):044908, 2024. doi: 10.1103/PhysRevC.109.044908.

[112] *LEP design report*. Report. CERN, Geneva, 1984. URL http://cds.cern.ch/record/102083. Copies shelved as reports in LEP, PS and SPS libraries.

[113] G. Aad et al. The ATLAS Experiment at the CERN Large Hadron Collider. *JINST*, 3:S08003, 2008. doi: 10.1088/1748-0221/3/08/S08003.

[114] S. Chatrchyan et al. The CMS Experiment at the CERN LHC. *JINST*, 3:S08004, 2008. doi: 10.1088/1748-0221/3/08/S08004.

[115] A. Augusto Alves, Jr. et al. The LHCb Detector at the LHC. *JINST*, 3:S08005, 2008. doi: 10.1088/1748-0221/3/08/S08005.

[116] Linear accelerator 2. 2012. URL https://cds.cern.ch/record/1997427.

[117] The Proton Synchrotron Booster. 2012. URL https://cds.cern.ch/record/1997372.

[118] G. K. Green and Ernest D. Courant. *The Proton Synchrotron*, pages 218–340. Springer Berlin Heidelberg, Berlin, Heidelberg, 1959. ISBN 978-3-642-45926-9. doi: 10.1007/978-3-642-45926-9_6. URL https://doi.org/10.1007/978-3-642-45926-9_6.

[119] Linear accelerator 3. 2012. URL http://cds.cern.ch/record/1997426.

[120] The Low Energy Ion Ring. 2012. URL https://cds.cern.ch/record/1997352.

[121] CERN optics repository, https://acc-models.web.cern.ch/acc-models/structure/.

[122] ALICE Figure Repository, https://alice-figure.web.cern.ch/, .

[123] K Aamodt et al. Alignment of the ALICE Inner Tracking System with cosmic-ray tracks. *JINST*, 5:P03003, 2010. doi: 10.1088/1748-0221/5/03/P03003.

[124] G. Dellacasa et al. ALICE: Technical design report of the time projection chamber. 1 2000.

[125] J. Alme et al. The ALICE TPC, a large 3-dimensional tracking device with fast readout for ultra-high multiplicity events. *Nucl. Instrum. Meth. A*, 622:316–367, 2010. doi: 10.1016/j.nima.2010.04.042.

[126] Antonin Maire. *Production des baryons multi-étranges au LHC dans les collisions proton-proton avec l'expérience ALICE*. PhD thesis, Strasbourg U., 2011.

[127] G. Dellacasa et al. ALICE technical design report of the time-of-flight system (TOF). 2 2000.

[128] A. Akindinov et al. Performance of the ALICE Time-Of-Flight detector at the LHC. *Eur. Phys. J. Plus*, 128:44, 2013. doi: 10.1140/epjp/i2013-13044-x.

[129] E. Abbas et al. Performance of the ALICE VZERO system. *JINST*, 8:P10016, 2013. doi: 10.1088/1748-0221/8/10/P10016.

[130] F. Carena et al. The ALICE data acquisition system. *Nucl. Instrum. Meth. A*, 741: 130–162, 2014. doi: 10.1016/j.nima.2013.12.015.

[131] Christian Wolfgang Fabjan, L Jirdén, V Lindestruth, Lodovico Riccati, D Rorich, Pierre Van de Vyvre, O Villalobos Baillie, and Hans de Groot. *ALICE trigger data-acquisition high-level trigger and control system: Technical Design Report*. Technical design report. ALICE. CERN, Geneva, 2004. URL https://cds.cern.ch/record/684651.

[132] J. Conrad, J. G. Contreras, and C. E. Jorgensen. Minimum bias triggers in proton-proton collisions with VZERO and pixel detectors. 2005.

[133] LHC computing Grid. Technical design report. 6 2005.

[134] Worldwide lhc computing grid, https://wlcg-public.web.cern.ch/.

[135] ALICE environment, https://alien.web.cern.ch/, .

[136] R. Brun and F. Rademakers. ROOT: An object oriented data analysis framework. *Nucl. Instrum. Meth. A*, 389:81–86, 1997. doi: 10.1016/S0168-9002(97)00048-X.

[137] AliROOT, https://alice-offline.web.cern.ch/, .

[138] P. Buncic, M. Krzewicki, and P. Vande Vyvre. Technical Design Report for the Upgrade of the Online-Offline Computing System. 4 2015.

[139] Betty Bezverkhny Abelev et al. Performance of the ALICE Experiment at the CERN LHC. *Int. J. Mod. Phys. A*, 29:1430044, 2014. doi: 10.1142/S0217751X14300440.

[140] R. Fruhwirth. Application of Kalman filtering to track and vertex fitting. *Nucl. Instrum. Meth. A*, 262:444–450, 1987. doi: 10.1016/0168-9002(87)90887-4.

[141] Veikko Karimäki. Effective Vertex Fitting. 6 1997.

[142] Bo Andersson. *The Lund Model*, volume 7 of *Cambridge Monographs on Particle Physics, Nuclear Physics and Cosmology*. Cambridge University Press, 7 2023. ISBN 978-1-009-40129-6, 978-1-009-40125-8, 978-1-009-40128-9, 978-0-521-01734-3, 978-0-521-42094-5, 978-0-511-88149-7. doi: 10.1017/9781009401296.

[143] Bo Andersson, G. Gustafson, G. Ingelman, and T. Sjostrand. Parton Fragmentation and String Dynamics. *Phys. Rept.*, 97:31–145, 1983. doi: 10.1016/0370-1573(83)90080-7.

[144] Silvia Ferreres-Solé and Torbjörn Sjöstrand. The space–time structure of hadronization in the Lund model. *Eur. Phys. J. C*, 78(11):983, 2018. doi: 10.1140/epjc/s10052-018-6459-8.

[145] Jesper R. Christiansen and Peter Z. Skands. String Formation Beyond Leading Colour. *JHEP*, 08:003, 2015. doi: 10.1007/JHEP08(2015)003.

[146] Patrik Eden and Gosta Gustafson. Baryon production in the string fragmentation picture. *Z. Phys. C*, 75:41–49, 1997. doi: 10.1007/s002880050445.

[147] Torbjorn Sjostrand, Patrik Eden, Christer Friberg, Leif Lonnblad, Gabriela Miu, Stephen Mrenna, and Emanuel Norrbin. High-energy physics event generation with PYTHIA 6.1. *Comput. Phys. Commun.*, 135:238–259, 2001. doi: 10.1016/S0010-4655(00)00236-8.

[148] Torbjorn Sjostrand, Stephen Mrenna, and Peter Z. Skands. A Brief Introduction to PYTHIA 8.1. *Comput. Phys. Commun.*, 178:852–867, 2008. doi: 10.1016/j.cpc.2008.01.036.

[149] Christian Bierlich et al. A comprehensive guide to the physics and usage of PYTHIA 8.3. *SciPost Phys. Codeb.*, 2022:8, 2022. doi: 10.21468/SciPostPhysCodeb.8.

[150] Paolo Bartalini and Jonathan Richard Gaunt, editors. *Multiple Parton Interactions at the LHC*, volume 29. WSP, 2019. ISBN 978-981-322-775-0, 978-981-322-777-4. doi: 10.1142/10646.

[151] P. D. B. Collins. *An Introduction to Regge Theory and High Energy Physics*. Cambridge Monographs on Mathematical Physics. Cambridge University Press, 7 2023. ISBN 978-1-009-40326-9, 978-1-009-40329-0, 978-1-009-40328-3, 978-0-521-11035-8. doi: 10.1017/9781009403269.

[152] Scott McDonald, Chun Shen, Francois Fillion-Gourdeau, Sangyong Jeon, and Charles Gale. Hydrodynamic predictions for Pb+Pb collisions at 5.02 TeV. *Phys. Rev. C*, 95(6):064913, 2017. doi: 10.1103/PhysRevC.95.064913.

[153] Wenbin Zhao, Hao-jie Xu, and Huichao Song. Collective flow in 2.76 A TeV and 5.02 A TeV Pb+Pb collisions. *Eur. Phys. J. C*, 77(9):645, 2017. doi: 10.1140/epjc/s10052-017-5186-x.

[154] H. Sorge, Horst Stoecker, and W. Greiner. RELATIVISTIC QUANTUM MOLECULAR DYNAMICS APPROACH TO NUCLEAR COLLISIONS AT ULTRA-RELATIVISTIC ENERGIES. *Nucl. Phys. A*, 498:567C–576C, 1989. doi: 10.1016/0375-9474(89)90641-6.

[155] S. A. Bass et al. Microscopic models for ultrarelativistic heavy ion collisions. *Prog. Part. Nucl. Phys.*, 41:255–369, 1998. doi: 10.1016/S0146-6410(98)00058-1.

[156] Zi-Wei Lin, Che Ming Ko, Bao-An Li, Bin Zhang, and Subrata Pal. A Multi-phase transport model for relativistic heavy ion collisions. *Phys. Rev. C*, 72:064901, 2005. doi: 10.1103/PhysRevC.72.064901.

[157] Xin-Nian Wang and Miklos Gyulassy. HIJING: A Monte Carlo model for multiple jet production in p p, p A and A A collisions. *Phys. Rev. D*, 44:3501–3516, 1991. doi: 10.1103/PhysRevD.44.3501.

[158] Xin-Nian Wang. Role of multiple mini - jets in high-energy hadronic reactions. *Phys. Rev. D*, 43:104–112, 1991. doi: 10.1103/PhysRevD.43.104.

[159] D. W. Duke and J. F. Owens. Q**2 Dependent Parametrizations of Parton Distribution Functions. *Phys. Rev. D*, 30:49–54, 1984. doi: 10.1103/PhysRevD.30.49.

[160] Xin-Nian Wang and Miklos Gyulassy. Energy and centrality dependence of rapidity densities at RHIC. *Phys. Rev. Lett.*, 86:3496–3499, 2001. doi: 10.1103/PhysRevLett.86.3496.

[161] Zi-wei Lin and C. M. Ko. Partonic effects on the elliptic flow at RHIC. *Phys. Rev. C*, 65:034904, 2002. doi: 10.1103/PhysRevC.65.034904.

[162] Bin Zhang. ZPC 1.0.1: A Parton cascade for ultrarelativistic heavy ion collisions. *Comput. Phys. Commun.*, 109:193–206, 1998. doi: 10.1016/S0010-4655(98)00010-1.

[163] Bao-An Li and Che Ming Ko. Formation of superdense hadronic matter in high-energy heavy ion collisions. *Phys. Rev. C*, 52:2037–2063, 1995. doi: 10.1103/PhysRevC.52.2037.

[164] Zi-wei Lin, S. Pal, C. M. Ko, Bao-An Li, and Bin Zhang. Charged particle rapidity distributions at relativistic energies. *Phys. Rev. C*, 64:011902, 2001. doi: 10.1103/PhysRevC.64.011902.

[165] Subrata Pal, C. M. Ko, and Zi-wei Lin. Multistrange baryon production in relativistic heavy ion collisions. *Nucl. Phys. A*, 730:143–159, 2004. doi: 10.1016/j.nuclphysa.2003.10.013.

[166] Subrata Pal, C. M. Ko, and Zi-wei Lin. Phi meson production in relativistic heavy ion collisions. *Nucl. Phys. A*, 707:525–539, 2002. doi: 10.1016/S0375-9474(02)00992-2.

[167] J. Weil et al. Particle production and equilibrium properties within a new hadron transport approach for heavy-ion collisions. *Phys. Rev. C*, 94(5):054905, 2016. doi: 10.1103/PhysRevC.94.054905.

[168] SMASH vHLLE Hybrid, https://github.com/smash-transport/smash-vhlle-hybrid.

[169] Anna Schäfer, Iurii Karpenko, Xiang-Yu Wu, Jan Hammelmann, and Hannah Elfner. Particle production in a hybrid approach for a beam energy scan of Au+Au/Pb+Pb collisions between $\sqrt{s_{\mathrm{NN}}}$ = 4.3 GeV and $\sqrt{s_{\mathrm{NN}}}$ = 200.0 GeV. *Eur. Phys. J. A*, 58 (11):230, 2022. doi: 10.1140/epja/s10050-022-00872-x.

[170] Justin Mohs, Martha Ege, Hannah Elfner, and Markus Mayer. Collective flow at SIS energies within a hadronic transport approach: Influence of light nuclei formation and equation of state. *Phys. Rev. C*, 105(3):034906, 2022. doi: 10.1103/PhysRevC.105.034906.

[171] Iu. Karpenko, P. Huovinen, and M. Bleicher. A 3+1 dimensional viscous hydrodynamic code for relativistic heavy ion collisions. *Comput. Phys. Commun.*, 185:3016–3027, 2014. doi: 10.1016/j.cpc.2014.07.010.

[172] G. S. Denicol, S. Jeon, and C. Gale. Transport Coefficients of Bulk Viscous Pressure in the 14-moment approximation. *Phys. Rev. C*, 90(2):024912, 2014. doi: 10.1103/PhysRevC.90.024912.

[173] S. Ryu, J. F. Paquet, C. Shen, G. S. Denicol, B. Schenke, S. Jeon, and C. Gale. Importance of the Bulk Viscosity of QCD in Ultrarelativistic Heavy-Ion Collisions. *Phys. Rev. Lett.*, 115(13):132301, 2015. doi: 10.1103/PhysRevLett.115.132301.

[174] J. Steinheimer, S. Schramm, and H. Stocker. An Effective chiral Hadron-Quark Equation of State. *J. Phys. G*, 38:035001, 2011. doi: 10.1088/0954-3899/38/3/035001.

[175] Pasi Huovinen and Hannah Petersen. Particlization in hybrid models. *Eur. Phys. J. A*, 48:171, 2012. doi: 10.1140/epja/i2012-12171-9.

[176] SMASH Hadron Sampler, https://github.com/smash-transport/smash-hadron-sampler.

[177] Fred Cooper and Graham Frye. Comment on the Single Particle Distribution in the Hydrodynamic and Statistical Thermodynamic Models of Multiparticle Production. *Phys. Rev. D*, 10:186, 1974. doi: 10.1103/PhysRevD.10.186.

[178] C. Hartnack, Rajeev K. Puri, J. Aichelin, J. Konopka, S. A. Bass, Horst Stoecker, and W. Greiner. Modeling the many body dynamics of heavy ion collisions: Present status and future perspective. *Eur. Phys. J. A*, 1:151–169, 1998. doi: 10.1007/s100500050045.

[179] Paula Hillmann, Jan Steinheimer, Tom Reichert, Vincent Gaebel, Marcus Bleicher, Sukanya Sombun, Christoph Herold, and Ayut Limphirat. First, second, third and fourth flow harmonics of deuterons and protons in Au+Au reactions at 1.23 AGeV. *J. Phys. G*, 47(5):055101, 2020. doi: 10.1088/1361-6471/ab6fcf.

[180] M. Aguilar-Benitez et al. Comparative Properties of 400-GeV/c Proton - Proton Interactions With and Without Charm Production. *Z. Phys. C*, 41:191, 1988. doi: 10.1007/BF01566916.

[181] B. Abelev et al. J/ψ Production as a Function of Charged Particle Multiplicity in pp Collisions at $\sqrt{s}$ = 7 TeV. *Phys. Lett. B*, 712:165–175, 2012. doi: 10.1016/j.physletb.2012.04.052.

[182] Betty Abelev et al. Underlying Event measurements in pp collisions at $\sqrt{s}$ = 0.9 and 7 TeV with the ALICE experiment at the LHC. *JHEP*, 07:116, 2012. doi: 10.1007/JHEP07(2012)116.

[183] Serguei Chatrchyan et al. Jet and Underlying Event Properties as a Function of Charged-Particle Multiplicity in Proton–Proton Collisions at $\sqrt{s}$ = 7 TeV. *Eur. Phys. J. C*, 73(12):2674, 2013. doi: 10.1140/epjc/s10052-013-2674-5.

[184] Jaroslav Adam et al. Measurement of charm and beauty production at central rapidity versus charged-particle multiplicity in proton-proton collisions at $\sqrt{s}$ = 7 TeV. *JHEP*, 09:148, 2015. doi: 10.1007/JHEP09(2015)148.

[185] S. G. Weber, A. Dubla, A. Andronic, and A. Morsch. Elucidating the multiplicity dependence of J/ψ production in proton–proton collisions with PYTHIA8. *Eur. Phys. J. C*, 79(1):36, 2019. doi: 10.1140/epjc/s10052-018-6531-4.

[186] Shreyasi Acharya et al. Inclusive and multiplicity dependent production of electrons from heavy-flavour hadron decays in pp and p-Pb collisions. *JHEP*, 08:006, 2023. doi: 10.1007/JHEP08(2023)006.

[187] Andrea Banfi, Gavin P. Salam, and Giulia Zanderighi. Phenomenology of event shapes at hadron colliders. *JHEP*, 06:038, 2010. doi: 10.1007/JHEP06(2010)038.

[188] Andrea Banfi, Gavin P. Salam, and Giulia Zanderighi. Resummed event shapes at hadron - hadron colliders. *JHEP*, 08:062, 2004. doi: 10.1088/1126-6708/2004/08/062.

[189] Eleazar Cuautle, Raul Jimenez, Ivonne Maldonado, Antonio Ortiz, Guy Paic, and Edgar Perez. Disentangling the soft and hard components of the pp collisions using the sphero(i)city approach. 4 2014.

[190] T. Akesson et al. The Dominance of Jets at Large Transverse Energy in a Full Azimuth Hadron Calorimeter at ISR Energies. *Phys. Lett. B*, 128:354–360, 1983. doi: 10.1016/0370-2693(83)90274-5.

[191] R. Ansari et al. Jet Measures and Hadronic Event Shapes at the CERN $\bar{p}p$ Collider. *Z. Phys. C*, 36:175, 1987. doi: 10.1007/BF01579132.

[192] T. Aaltonen et al. Measurement of Event Shapes in Proton-Antiproton Collisions at Center-of-Mass Energy 1.96 TeV. *Phys. Rev. D*, 83:112007, 2011. doi: 10.1103/PhysRevD.83.112007.

[193] S. Chekanov et al. Measurement of event shapes in deep inelastic scattering at HERA. *Eur. Phys. J. C*, 27:531–545, 2003. doi: 10.1140/epjc/s2003-01148-x.

[194] P. Achard et al. Determination of $alpha_s$ from hadronic event shapes in e^+e^- annihilation at 192-GeV <= $\sqrt{s}$ <= 208-GeV. *Phys. Lett. B*, 536:217–228, 2002. doi: 10.1016/S0370-2693(02)01814-2.

[195] J. Abdallah et al. The Measurement of alpha(s) from event shapes with the DELPHI detector at the highest LEP energies. *Eur. Phys. J. C*, 37:1–23, 2004. doi: 10.1140/epjc/s2004-01889-x.

[196] Betty Abelev et al. Transverse sphericity of primary charged particles in minimum bias proton-proton collisions at $\sqrt{s}$ = 0.9, 2.76 and 7 TeV. *Eur. Phys. J. C*, 72:2124, 2012. doi: 10.1140/epjc/s10052-012-2124-9.

[197] Georges Aad et al. Measurement of charged-particle event shape variables in $\sqrt{s}$ = 7 TeV proton-proton interactions with the ATLAS detector. *Phys. Rev. D*, 88 (3):032004, 2013. doi: 10.1103/PhysRevD.88.032004.

[198] Jaroslav Adam et al. Pseudorapidity and transverse-momentum distributions of charged particles in proton–proton collisions at $\sqrt{s}$ = 13 TeV. *Phys. Lett. B*, 753: 319–329, 2016. doi: 10.1016/j.physletb.2015.12.030.

[199] Shreyasi Acharya et al. Observation of a multiplicity dependence in the pT-differential charm baryon-to-meson ratios in proton–proton collisions at s=13 TeV. *Phys. Lett. B*, 829:137065, 2022. doi: 10.1016/j.physletb.2022.137065.

[200] G. Dissertori, F. Moortgat, and M. A. Weber. Hadronic Event-Shape Variables at CMS. In *34th International Conference on High Energy Physics*, 10 2008.

[201] Shreyasi Acharya et al. Charged-particle production as a function of multiplicity and transverse spherocity in pp collisions at $\sqrt{s}$ = 5.02 and 13 TeV. *Eur. Phys. J. C*, 79(10):857, 2019. doi: 10.1140/epjc/s10052-019-7350-y.

[202] Shreyasi Acharya et al. Light-flavor particle production in high-multiplicity pp collisions at $\sqrt{s}$= 13 TeV as a function of transverse spherocity. *JHEP*, 05:184, 2024. doi: 10.1007/JHEP05(2024)184.

[203] Antonio Ortiz, Guy Paić, and Eleazar Cuautle. Mid-rapidity charged hadron transverse spherocity in pp collisions simulated with Pythia. *Nucl. Phys. A*, 941:78–86, 2015. doi: 10.1016/j.nuclphysa.2015.05.010.

[204] Gavin P. Salam. Towards Jetography. *Eur. Phys. J. C*, 67:637–686, 2010. doi: 10.1140/epjc/s10052-010-1314-6.

[205] Daan Leermakers. Systematic study of track quality cuts at ALICE. 2015. URL https://cds.cern.ch/record/2045797.

[206] Shreyasi Acharya et al. Pseudorapidity distributions of charged particles as a function of mid- and forward rapidity multiplicities in pp collisions at $\sqrt{s}$ = 5.02, 7 and 13 TeV. *Eur. Phys. J. C*, 81(7):630, 2021. doi: 10.1140/epjc/s10052-021-09349-5.

[207] Shreyasi Acharya et al. Multiplicity dependence of J/ψ production at midrapidity in pp collisions at $\sqrt{s}$ = 13 TeV. *Phys. Lett. B*, 810:135758, 2020. doi: 10.1016/j.physletb.2020.135758.

[208] K. Werner, B. Guiot, Iu. Karpenko, and T. Pierog. Analysing radial flow features in p-Pb and p-p collisions at several TeV by studying identified particle production in EPOS3. *Phys. Rev. C*, 89(6):064903, 2014. doi: 10.1103/PhysRevC.89.064903.

[209] Ivan Schmidt and Marat Siddikov. Production mechanisms of open-heavy flavor mesons. *Phys. Rev. D*, 101(9):094020, 2020. doi: 10.1103/PhysRevD.101.094020.

[210] B. Alper et al. Large angle production of stable particles heavier than the proton and a search for quarks at the cern intersecting storage rings. *Phys. Lett. B*, 46: 265–268, 1973. doi: 10.1016/0370-2693(73)90700-4.

[211] S. Henning et al. Production of Deuterons and anti-Deuterons in Proton Proton Collisions at the CERN ISR. *Lett. Nuovo Cim.*, 21:189, 1978. doi: 10.1007/BF02822248.

[212] Jaroslav Adam et al. Beam energy dependence of (anti-)deuteron production in Au + Au collisions at the BNL Relativistic Heavy Ion Collider. *Phys. Rev. C*, 99(6): 064905, 2019. doi: 10.1103/PhysRevC.99.064905.

[213] Jaroslav Adam et al. Production of light nuclei and anti-nuclei in pp and Pb-Pb collisions at energies available at the CERN Large Hadron Collider. *Phys. Rev. C*, 93(2):024917, 2016. doi: 10.1103/PhysRevC.93.024917.

[214] Jaroslav Adam et al. ${}^{3}_{\Lambda}\mathrm{H}$ and ${}^{3}_{\bar{\Lambda}}\overline{\mathrm{H}}$ production in Pb-Pb collisions at $\sqrt{s_{\mathrm{NN}}} = 2.76$ TeV. *Phys. Lett. B*, 754:360–372, 2016. doi: 10.1016/j.physletb.2016.01.040.

[215] H. Agakishiev et al. Observation of the antimatter helium-4 nucleus. *Nature*, 473: 353, 2011. doi: 10.1038/nature10079. [Erratum: Nature 475, 412 (2011)].

[216] Muhammad Abdulhamid et al. Beam Energy Dependence of Triton Production and Yield Ratio ($\mathrm{N}_t \times \mathrm{N}_p/\mathrm{N}_d^2$) in Au+Au Collisions at RHIC. *Phys. Rev. Lett.*, 130: 202301, 2023. doi: 10.1103/PhysRevLett.130.202301.

[217] Peter Braun-Munzinger, Benjamin Dönigus, and Nicole Löher. ALICE investigates 'snowballs in hell'. *CERN Courier*, 55(7):26–30, 2015. URL https://cds.cern.ch/record/2232490.

[218] J. Cleymans, S. Kabana, I. Kraus, H. Oeschler, K. Redlich, and N. Sharma. Antimatter production in proton-proton and heavy-ion collisions at ultrarelativistic energies. *Phys. Rev. C*, 84:054916, 2011. doi: 10.1103/PhysRevC.84.054916.

[219] J. Steinheimer, K. Gudima, A. Botvina, I. Mishustin, M. Bleicher, and H. Stocker. Hypernuclei, dibaryon and antinuclei production in high energy heavy ion collisions: Thermal production versus Coalescence. *Phys. Lett. B*, 714:85–91, 2012. doi: 10.1016/j.physletb.2012.06.069.

[220] J. Aichelin. 'Quantum' molecular dynamics: A Dynamical microscopic n body approach to investigate fragment formation and the nuclear equation of state in heavy ion collisions. *Phys. Rept.*, 202:233–360, 1991. doi: 10.1016/0370-1573(91)90094-3.

[221] Jan Staudenmaier, Dmytro Oliinychenko, Juan M. Torres-Rincon, and Hannah Elfner. Deuteron production in relativistic heavy ion collisions via stochastic multiparticle reactions. *Phys. Rev. C*, 104(3):034908, 2021. doi: 10.1103/PhysRevC.104.034908.

[222] Dmytro Oliinychenko, Chun Shen, and Volker Koch. Deuteron production in AuAu collisions at $\sqrt{s_{NN}}$ =7–200 GeV via pion catalysis. *Phys. Rev. C*, 103(3):034913, 2021. doi: 10.1103/PhysRevC.103.034913.

[223] Susanne Gläßel, Viktar Kireyeu, Vadim Voronyuk, Jörg Aichelin, Christoph Blume, Elena Bratkovskaya, Gabriele Coci, Vadim Kolesnikov, and Michael Winn. Cluster and hypercluster production in relativistic heavy-ion collisions within the parton-hadron-quantum-molecular-dynamics approach. *Phys. Rev. C*, 105(1):014908, 2022. doi: 10.1103/PhysRevC.105.014908.

[224] Correlation AfterBurner (CRAB), https://web.pa.msu.edu/people/pratts/freecodes/crab/home.html.

[225] Carl B. Dover, Ulrich W. Heinz, Ekkard Schnedermann, and Joszef Zimanyi. Relativistic coalescence model for high-energy nuclear collisions. *Phys. Rev. C*, 44: 1636–1654, 1991. doi: 10.1103/PhysRevC.44.1636.

[226] Supplemental material: afterburner for generating light (anti-)nuclei with QCD-inspired event generators in pp collisions. 2017.

[227] Wenbin Zhao, Kai-jia Sun, Che Ming Ko, and Xiaofeng Luo. Multiplicity scaling of light nuclei production in relativistic heavy-ion collisions. *Phys. Lett. B*, 820: 136571, 2021. doi: 10.1016/j.physletb.2021.136571.

[228] Yongseok Oh, Zi-Wei Lin, and Che Ming Ko. Deuteron production and elliptic flow in relativistic heavy ion collisions. *Phys. Rev. C*, 80:064902, 2009. doi: 10.1103/PhysRevC.80.064902.

[229] Michael Annan Lisa, Scott Pratt, Ron Soltz, and Urs Wiedemann. Femtoscopy in relativistic heavy ion collisions. *Ann. Rev. Nucl. Part. Sci.*, 55:357–402, 2005. doi: 10.1146/annurev.nucl.55.090704.151533.

[230] K. Aamodt et al. Two-pion Bose-Einstein correlations in central Pb-Pb collisions at $\sqrt{s_{NN}}$ = 2.76 TeV. *Phys. Lett. B*, 696:328–337, 2011. doi: 10.1016/j.physletb.2010.12.053.

[231] Shreyasi Acharya et al. p-p, p-Λ and Λ-Λ correlations studied via femtoscopy in pp reactions at $\sqrt{s}$ = 7 TeV. *Phys. Rev. C*, 99(2):024001, 2019. doi: 10.1103/PhysRevC.99.024001.

[232] Yin Xia, Jun Xu, Bao-An Li, and Wen-Qing Shen. Spin transport in intermediate-energy heavy-ion collisions as a probe of in-medium spin–orbit interactions. *Nucl. Phys. A*, 955:41–57, 2016. doi: 10.1016/j.nuclphysa.2016.06.001.

[233] Yoshini Bailung, Sudhir Pandurang Rode, Neha Shah, and Ankhi Roy. Probing coalescence of light nuclei via femtoscopy and azimuthal anisotropies. *Phys. Rev. C*, 111(1):014911, 2025. doi: 10.1103/PhysRevC.111.014911.

[234] Francesca Bellini and Alexander Philipp Kalweit. Testing production scenarios for (anti-)(hyper-)nuclei and exotica at energies available at the CERN Large Hadron Collider. *Phys. Rev. C*, 99(5):054905, 2019. doi: 10.1103/PhysRevC.99.054905.

[235] M. Kachelriess, S. Ostapchenko, and J. Tjemsland. On nuclear coalescence in small interacting systems. *Eur. Phys. J. A*, 57(5):167, 2021. doi: 10.1140/epja/s10050-021-00469-w.

[236] M. Kachelriess, S. Ostapchenko, and J. Tjemsland. Effect of nonequal emission times and space-time correlations on (anti-) nuclei production. *Phys. Rev. C*, 108 (2):024903, 2023. doi: 10.1103/PhysRevC.108.024903.

[237] Shreyasi Acharya et al. Search for a common baryon source in high-multiplicity pp collisions at the LHC. *Phys. Lett. B*, 811:135849, 2020. doi: 10.1016/j.physletb.2020.135849.

[238] S. E. Koonin. Proton Pictures of High-Energy Nuclear Collisions. *Phys. Lett. B*, 70:43–47, 1977. doi: 10.1016/0370-2693(77)90340-9.

[239] R. Hanbury Brown and R. Q. Twiss. A New type of interferometer for use in radio astronomy. *Phil. Mag. Ser. 7*, 45:663–682, 1954. doi: 10.1080/14786440708520475.

[240] M. Gyulassy, S. K. Kauffmann, and L. W. Wilson. Pion Interferometry of Nuclear Collisions. 1. Theory. *Phys. Rev. C*, 20:2267–2292, 1979. doi: 10.1103/PhysRevC.20.2267.

[241] D. H. Boal, C. K. Gelbke, and B. K. Jennings. Intensity interferometry in subatomic physics. *Rev. Mod. Phys.*, 62:553–602, 1990. doi: 10.1103/RevModPhys.62.553.

[242] R. Lednicky and V. L. Lyuboshits. Final State Interaction Effect on Pairing Correlations Between Particles with Small Relative Momenta. *Yad. Fiz.*, 35:1316–1330, 1981.

[243] R. Lednicky. Notes on correlation femtoscopy. *Phys. Atom. Nucl.*, 71:1572–1578, 2008. doi: 10.1134/S1063778808090123.

[244] L. Adamczyk et al. Measurement of Interaction between Antiprotons. *Nature*, 527: 345–348, 2015. doi: 10.1038/nature15724.

[245] R. Lednicky. Correlation femtoscopy of multiparticle processes. *Phys. Atom. Nucl.*, 67:72–82, 2004. doi: 10.1134/1.1644010.

[246] J. Aichelin, E. Bratkovskaya, A. Le Fèvre, V. Kireyeu, V. Kolesnikov, Y. Leifels, V. Voronyuk, and G. Coci. Parton-hadron-quantum-molecular dynamics: A novel microscopic n -body transport approach for heavy-ion collisions, dynamical cluster formation, and hypernuclei production. *Phys. Rev. C*, 101(4):044905, 2020. doi: 10.1103/PhysRevC.101.044905.

[247] Rajeev K. Puri and Joerg Aichelin. Simulated annealing clusterization algorithm for studying the multifragmentation. *J. Comput. Phys.*, 162:245–266, 2000. doi: 10.1006/jcph.2000.6534.

[248] M. M. Aggarwal et al. An Experimental Exploration of the QCD Phase Diagram: The Search for the Critical Point and the Onset of De-confinement. 7 2010.

[249] Betty Bezverkhny Abelev et al. Multiplicity dependence of the average transverse momentum in pp, p-Pb, and Pb-Pb collisions at the LHC. *Phys. Lett. B*, 727: 371–380, 2013. doi: 10.1016/j.physletb.2013.10.054.

[250] L. Adamczyk et al. Elliptic flow of identified hadrons in Au+Au collisions at $\sqrt{s_{NN}}$ = 7.7-62.4 GeV. *Phys. Rev. C*, 88:014902, 2013. doi: 10.1103/PhysRevC.88.014902.

[251] B. I. Abelev et al. Energy dependence of pi+-, p and anti-p transverse momentum spectra for Au+Au collisions at s(NN)**(1/2) = 62.4 and 200-GeV. *Phys. Lett. B*, 655:104–113, 2007. doi: 10.1016/j.physletb.2007.06.035.

[252] L. Adamczyk et al. Bulk Properties of the Medium Produced in Relativistic Heavy-Ion Collisions from the Beam Energy Scan Program. *Phys. Rev. C*, 96(4):044904, 2017. doi: 10.1103/PhysRevC.96.044904.

[253] Betty Abelev et al. Centrality dependence of π, K, p production in Pb-Pb collisions at $\sqrt{s_{NN}}$ = 2.76 TeV. *Phys. Rev. C*, 88:044910, 2013. doi: 10.1103/PhysRevC.88.044910.

[254] Dingwei Zhang. Light Nuclei (d, t) Production in Au + Au Collisions at $\sqrt{s_{NN}}$ = 7.7-200GeV. *Nucl. Phys. A*, 1005:121825, 2021. doi: 10.1016/j.nuclphysa.2020.121825.

[255] Shreyasi Acharya et al. Enhanced Deuteron Coalescence Probability in Jets. *Phys. Rev. Lett.*, 131(4):042301, 2023. doi: 10.1103/PhysRevLett.131.042301.

[256] Shreyasi Acharya et al. Jet-associated deuteron production in pp collisions at s=13 TeV. *Phys. Lett. B*, 819:136440, 2021. doi: 10.1016/j.physletb.2021.136440.

[257] Shreyasi Acharya et al. Multiplicity dependence of (multi-)strange hadron production in proton-proton collisions at $\sqrt{s}$ = 13 TeV. *Eur. Phys. J. C*, 80(2):167, 2020. doi: 10.1140/epjc/s10052-020-7673-8.

[258] Shreyasi Acharya et al. Multiplicity dependence of π, K, and p production in pp collisions at $\sqrt{s}$ = 13 TeV. *Eur. Phys. J. C*, 80(8):693, 2020. doi: 10.1140/epjc/s10052-020-8125-1.

[259] S. Acharya et al. (Anti-)deuteron production in pp collisions at $\sqrt{s}$ = 13 TeV. *Eur. Phys. J. C*, 80(9):889, 2020. doi: 10.1140/epjc/s10052-020-8256-4.

[260] Shreyasi Acharya et al. Exploring the strong interaction of three-body systems at the LHC. 8 2023.

[261] R. Kotte et al. On the space-time difference of proton and composite particle emission in central heavy ion reactions at 400-A/MeV. *Eur. Phys. J. A*, 6:185–195, 1999. doi: 10.1007/s100500050333.

[262] Ke Mi. Femtoscopy of Proton, Light Nuclei, and Strange Hadrons in Au+Au Collisions at STAR. *Acta Phys. Polon. Supp.*, 16(1):1–A91, 2023. doi: 10.5506/APhysPolBSupp.16.1-A91.

[263] Arthur M. Poskanzer and S. A. Voloshin. Methods for analyzing anisotropic flow in relativistic nuclear collisions. *Phys. Rev. C*, 58:1671–1678, 1998. doi: 10.1103/PhysRevC.58.1671.

[264] J. Adams et al. Azimuthal anisotropy in Au+Au collisions at s(NN)**(1/2) = 200-GeV. *Phys. Rev. C*, 72:014904, 2005. doi: 10.1103/PhysRevC.72.014904.

[265] C. Pinkenburg et al. Elliptic flow: Transition from out-of-plane to in-plane emission in Au + Au collisions. *Phys. Rev. Lett.*, 83:1295–1298, 1999. doi: 10.1103/PhysRevLett.83.1295.

[266] Pawel Danielewicz, Roy Lacey, and William G. Lynch. Determination of the equation of state of dense matter. *Science*, 298:1592–1596, 2002. doi: 10.1126/science.1078070.

[267] P. Danielewicz, Roy A. Lacey, P. B. Gossiaux, C. Pinkenburg, P. Chung, J. M. Alexander, and R. L. McGrath. Disappearance of elliptic flow: a new probe for the nuclear equation of state. *Phys. Rev. Lett.*, 81:2438–2441, 1998. doi: 10.1103/PhysRevLett.81.2438.

[268] Yasushi Nara and Akira Ohnishi. Mean-field update in the JAM microscopic transport model: Mean-field effects on collective flow in high-energy heavy-ion collisions at sNN=2–20 GeV energies. *Phys. Rev. C*, 105(1):014911, 2022. doi: 10.1103/PhysRevC.105.014911.

[269] W. Reisdorf et al. Systematics of azimuthal asymmetries in heavy ion collisions in the 1 A GeV regime. *Nucl. Phys. A*, 876:1–60, 2012. doi: 10.1016/j.nuclphysa.2011.12.006.

[270] Hannah Petersen, Qingfeng Li, Xianglei Zhu, and Marcus Bleicher. Directed and elliptic flow in heavy ion collisions at GSI-FAIR and CERN-SPS. *Phys. Rev. C*, 74:064908, 2006. doi: 10.1103/PhysRevC.74.064908.

[271] Paula Hillmann, Jan Steinheimer, and Marcus Bleicher. Directed, elliptic and triangular flow of protons in Au+Au reactions at 1.23 A GeV: a theoretical analysis of the recent HADES data. *J. Phys. G*, 45(8):085101, 2018. doi: 10.1088/1361-6471/aac96f.

[272] V. P. Konchakovski, W. Cassing, Yu. B. Ivanov, and V. D. Toneev. Examination of the directed flow puzzle in heavy-ion collisions. *Phys. Rev. C*, 90(1):014903, 2014. doi: 10.1103/PhysRevC.90.014903.

[273] J. Aichelin, A. Rosenhauer, G. Peilert, Horst Stoecker, and W. Greiner. Importance of Momentum Dependent Interactions for the Extraction of the Nuclear Equation of State From High-energy Heavy Ion Collisions. *Phys. Rev. Lett.*, 58:1926–1929, 1987. doi: 10.1103/PhysRevLett.58.1926.

[274] M. Isse, A. Ohnishi, N. Otuka, P. K. Sahu, and Y. Nara. Mean-field effects on collective flows in high-energy heavy-ion collisions from AGS to SPS energies. *Phys. Rev. C*, 72:064908, 2005. doi: 10.1103/PhysRevC.72.064908.

[275] A. Le Fèvre, Y. Leifels, C. Hartnack, and J. Aichelin. Origin of elliptic flow and its dependence on the equation of state in heavy ion reactions at intermediate energies. *Phys. Rev. C*, 98(3):034901, 2018. doi: 10.1103/PhysRevC.98.034901.

[276] Yasushi Nara, Harri Niemi, Jan Steinheimer, and Horst Stöcker. Equation of state dependence of directed flow in a microscopic transport model. *Phys. Lett. B*, 769:543–548, 2017. doi: 10.1016/j.physletb.2017.02.020.

[277] Byron K. Jennings, David H. Boal, and Julian C. Shillcock. Two-particle correlation functions in the thermal model and nuclear interferometry descriptions. *Phys. Rev. C*, 33:1303–1306, 1986. doi: 10.1103/PhysRevC.33.1303.

[278] M. S. Abdallah et al. Light nuclei collectivity from $\sqrt{s_{NN}} = 3$ GeV Au+Au collisions at RHIC. *Phys. Lett. B*, 827:136941, 2022. doi: 10.1016/j.physletb.2022.136941.